



MOLECULAR PHOCATODES AND PHOTOANODES FOR LIGHT DRIVEN WATER SPLITTING

Sergi Grau Abarca

ADVERTIMENT. L'accés als continguts d'aquesta tesi doctoral i la seva utilització ha de respectar els drets de la persona autora. Pot ser utilitzada per a consulta o estudi personal, així com en activitats o materials d'investigació i docència en els termes establerts a l'art. 32 del Text Refós de la Llei de Propietat Intel·lectual (RDL 1/1996). Per altres utilitzacions es requereix l'autorització prèvia i expressa de la persona autora. En qualsevol cas, en la utilització dels seus continguts caldrà indicar de forma clara el nom i cognoms de la persona autora i el títol de la tesi doctoral. No s'autoritza la seva reproducció o altres formes d'explotació efectuades amb finalitats de lucre ni la seva comunicació pública des d'un lloc aliè al servei TDX. Tampoc s'autoritza la presentació del seu contingut en una finestra o marc aliè a TDX (framing). Aquesta reserva de drets afecta tant als continguts de la tesi com als seus resums i índexs.

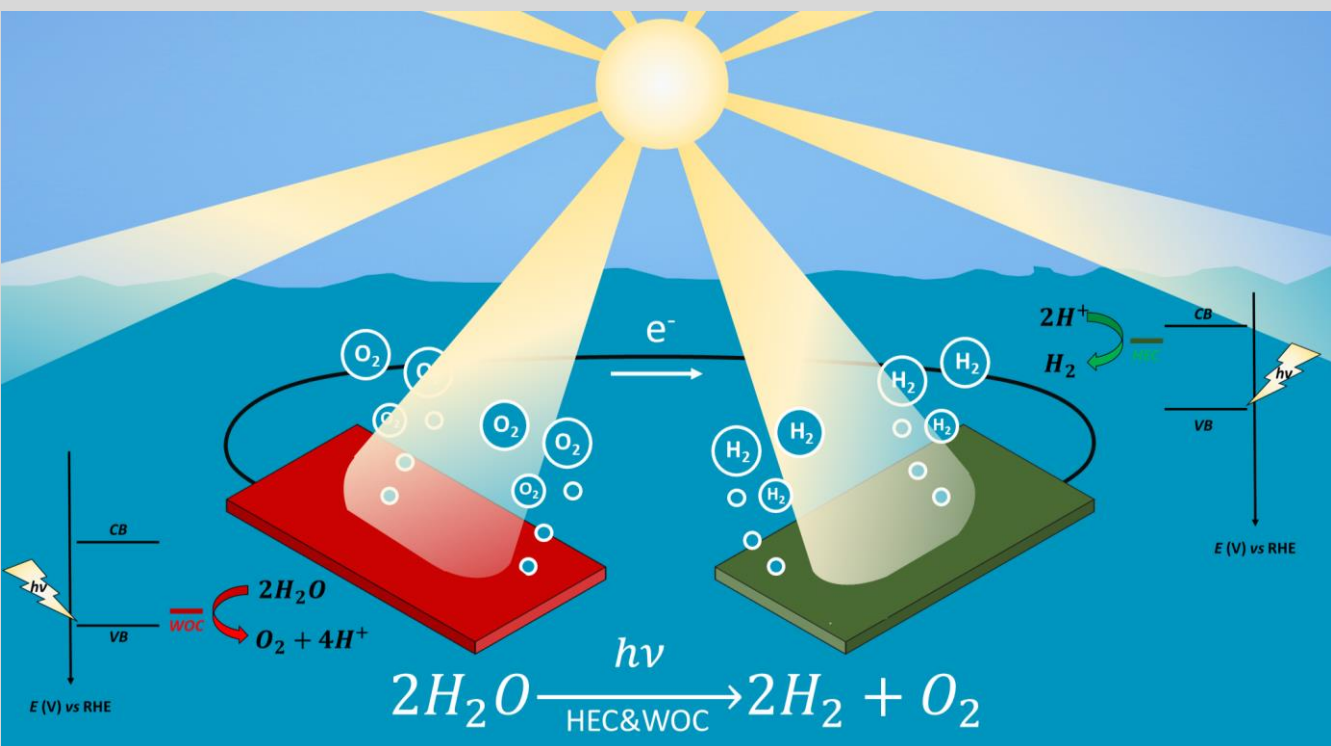
ADVERTENCIA. El acceso a los contenidos de esta tesis doctoral y su utilización debe respetar los derechos de la persona autora. Puede ser utilizada para consulta o estudio personal, así como en actividades o materiales de investigación y docencia en los términos establecidos en el art. 32 del Texto Refundido de la Ley de Propiedad Intelectual (RDL 1/1996). Para otros usos se requiere la autorización previa y expresa de la persona autora. En cualquier caso, en la utilización de sus contenidos se deberá indicar de forma clara el nombre y apellidos de la persona autora y el título de la tesis doctoral. No se autoriza su reproducción u otras formas de explotación efectuadas con fines lucrativos ni su comunicación pública desde un sitio ajeno al servicio TDR. Tampoco se autoriza la presentación de su contenido en una ventana o marco ajeno a TDR (framing). Esta reserva de derechos afecta tanto al contenido de la tesis como a sus resúmenes e índices.

WARNING. Access to the contents of this doctoral thesis and its use must respect the rights of the author. It can be used for reference or private study, as well as research and learning activities or materials in the terms established by the 32nd article of the Spanish Consolidated Copyright Act (RDL 1/1996). Express and previous authorization of the author is required for any other uses. In any case, when using its content, full name of the author and title of the thesis must be clearly indicated. Reproduction or other forms of for profit use or public communication from outside TDX service is not allowed. Presentation of its content in a window or frame external to TDX (framing) is not authorized either. These rights affect both the content of the thesis and its abstracts and indexes.



Molecular photoanodes and photocathodes for light induced water splitting

Sergi Grau Abarca



UNIVERSITAT ROVIRA I VIRGILI

MOLECULAR PHOCATODES AND PHOTOANODES FOR LIGHT DRIVEN WATER SPLITTING

Sergi Grau Abarca

UNIVERSITAT ROVIRA I VIRGILI

MOLECULAR PHOCATODES AND PHOTOANODES FOR LIGHT DRIVEN WATER SPLITTING

Sergi Grau Abarca

Sergi Grau Abarca

Molecular photoanodes and photocathodes for light induced water splitting

DOCTORAL THESIS

Supervised by

Prof. Antoni Llobet and Dr. Carolina Gimbert

Institute of Chemical Research of Catalonia



Tarragona

2019

UNIVERSITAT ROVIRA I VIRGILI

MOLECULAR PHOCATODES AND PHOTOANODES FOR LIGHT DRIVEN WATER SPLITTING

Sergi Grau Abarca



ICIQ - Institut Català d'Investigació Química

Avinguda Països Catalans 16,

43007 Tarragona (Spain)

Prof. Antoni Llobet, Group Leader at the Institute of Chemical Research of Catalonia and Dr. Carolina Gimbert,

We STATE that the present study, entitled "Molecular photoanodes and photocathodes for light induced water splitting" presented by Sergi Grau Abarca for the award of the degree of Doctor, has been carried out under our supervision in our group at the Institute of Chemical Research of Catalonia and that it fulfills all the requirements to be eligible for the International Doctor Distinction.

Tarragona, June 4th, 2019

Doctoral Thesis Supervisors

Prof. Antoni Llobet

Dr. Carolina Gimbert

Acknowledgments

Arribats a aquest punt del camí, és moment de mirar enrere i agrair a tota la gent que ha fet possible la realització d'aquesta tesi.

En primer lloc, vull donar les gràcies als meus directors, en Toni i la Carolina. Gràcies per guiar-me durant aquest viatge de quatre anys. Sense els vostres consells i supervisió fa temps que hagués naufragat i abandonat el camí. Gràcies per ensenyar-me tot el que he après i per transferir-me l'entusiasme i la passió que sentiu per la Química. Vull agrair especialment a la Carolina la paciència que ha tingut amb mi durant tot aquest temps, especialment als inicis, quan no tenia molt clar de què anava tot això. Espero ser el primer d'una llarga llista de doctorands sota la teva tutela (així com espero que sempre te'n recordis del primer, a poder ser, de les coses bones).

Vull mostrar el meu agraïment a la meva família, a la meva mare Lourdes, al meu pare Albert i a la meva germana Marina. Gràcies per aguantar lo inaguantable i per compartir totes i cadascunes de les alegries viscudes. Haver arribat fins aquí només és una senyal que com m'heu educat. Gràcies per deixar ben clar que a casa mai ha faltat un cèntim per estudiar o per comprar llibres. Gràcies per haver-me transmès l'amor pel coneixement ja sigui de ciències o de lletres, però sobretot gràcies per haver-me ensenyat a ser bona persona, part d'aquesta tesi es vostra.

I would like to acknowledge to all Antoni Llobet Group members for the supporting in the hard moments, for the research advices and for laughing about my stupid jokes. Thanks to Roc, Lorenzo, Sam, CJ, Serena, Sayantan, Abi, Asmaul, Primavera, Natalia, Martetas, Yuanyuan, Tingting, Jan O., Jan H., Laura, Ludo, Andrew and Martina. Without all of you, this journey would have been a nightmare.

I would like to give a special acknowledge to Marine and Leonie for their excellent work on the synthesis of the ligands during their master stay in our group and Navid to continue their work. Half of Chapter 4 is also yours.

I perquè aquesta feina no la fem sols, i sense el personal de l'Àrea de suport a la recerca no arribaríem ni la meitat de lluny, també vull mostrar el meu

agraïment a les unitats de ChromTAE, X-ray Diffraction, Chemical Reaction Technologies, Spectroscopics and Kinetics i Photophysics Unit, en especial a les Martes, en Fernando i en Javier, tan pel suport científic com pels consells més mundans. També vull agrair a en Xavier i en Jose Luís dels tallers de vidre i mecànic per arreglar i fabricar tot el que he necessitat durant aquests quatre anys. A en Xavier Blanch també li vull agrair tota la formació de seguretat rebuda al llarg d'aquests anys, al cap i a la fi, no tothom té la oportunitat de fer de bomber totalment equipat per un dia...

Todo buen viaje empieza y acaba en el mismo sitio, pero en el recorrido tienes la oportunidad de visitar diferentes centros y conocer a diferentes personas. Me gustaría agradecer al profesor Juanjo Vilatela de IMDEA Materiales y a todo su grupo por acogerme una semana y mostrarme su magnífica nanofibra de carbono, en especial a Alicia por cuidar de mí y enseñarme Madrid y Getafe.

Parte de este viaje también me ha llevado, en alguna ocasión, a visitar el IREC para fabricar los fantásticos fotocátodos con los que he realizado el capítulo 5 de esta tesis, bajo la supervisión de Dr. Edgardo Saucedo y el profesor Alejandro Pérez. Muchísimas gracias por implicarme en la fabricación de estos y por contestar a todas y cada una de mis dudas. También quiero agradecer a Dr. Sergio Giraldo su ayuda y colaboración en este proyecto.

One of the last places where this journey has taken me was Göttingen, for a stay of three months under the supervision of professor Franc Meyer. Thank you so much for hosting me in your group. It was the first time in my life that I was living abroad, but thanks to Jana, Göttingen was like my second house, I left a small part of me there and I will always be happy to visit this charming city again. Vielen Dank, Jana. Ich werde mich immer an die Zeit erinnern, die wir zusammen in Göttingen verbracht haben.

M'agradaria també agrair als amics de tota la vida el seu suport en els moments més difícils del doctorat, sobretot en el darrer tram, els vostres ànims m'han donat l'energia necessària per acabar la tesi. Moltes gràcies Albert, Guillem, Oscar, Joel, Angel, Arnau i Jordi. Vull fer especial al·lusió a la contribució de'n Victor en qualitat de dissenyador gràfic, per ajudar-me amb el disseny de la tesi recomenant-me les tipografies, que ve a ser com si a un químic li demanes el nombre atòmic del berili o del oxigen. També vull agrair als inseparables amics

que vaig fer a la carrera i que a dia d'avui ho segueixen sent, gràcies Edu, Laia, Raul i Gemma. Sense tots vosaltres no hagués aguantat ni la meitat del camí!

Y como no todo es trabajo, pero en el trabajo os he conocido, muchísimas gracias a Marta, Víctor, Funes, Elena, Adiran y Bruna por haber hecho de esta experiencia en Tarragona una de las mejores etapas de mi vida. Gracias por las cenas, las salidas y las cervecitas en la plaza del mercado, pero sobretodo por vuestro cariño y vuestra amistad.

Para ir acabando, me gustaría agradecer especialmente a los Chaches todo lo que me han aguantado, lo mucho que me han ayudado, y sobretodo por lo mucho que nos hemos reído. Sé que con vosotros dos, aunque haya miles de kilómetros de distancia o que pasemos lustros sin vernos las caras, siempre seguiremos queriéndonos y siendo amigos. Muchas gracias Pablo (y Marta) y Marcos por haberme hecho sentir tan querido y por perdonar todos mis arrebatos.

M'agradaria agrair també la contribució d'un gran amic en la persona que sóc ara. Moltes gràcies Jose per intentar fer-me millor, no passa un sol dia sense que me'n recordi de tu. M'hagués agradat molt veure la teva tesi i que tu veiessis la meva.

Finalment, vull agrair a la persona més important de la meva vida el fet d'haver-me aguantat tot aquest temps i haver-me donat motius per ser millor persona. Sense tu no hagués estat capaç d'acabar tot això. Sense tu haver vingut a Tarragona no hagués estat ni la meitat d'interessant, tan sols hagués estat feina. Sense tu ara mateix no sabia viure. Gràcies per formar part de la meva vida Vanessa.

The work performed in the present doctoral thesis has been possible thanks to the Institute of Chemical Research of Catalonia (ICIQ) and the funding of: MINECO and FEDER (CTQ2016-80058-R, CTQ2015-73028 EXP, SEV 2013-0319) and PhD Fellowship in the Frame of a Mobility Programme with the Georg-August-Universität Göttingen (ICIQ's Severo Ochoa Excellence Accreditation 2014-2018).



List of publications

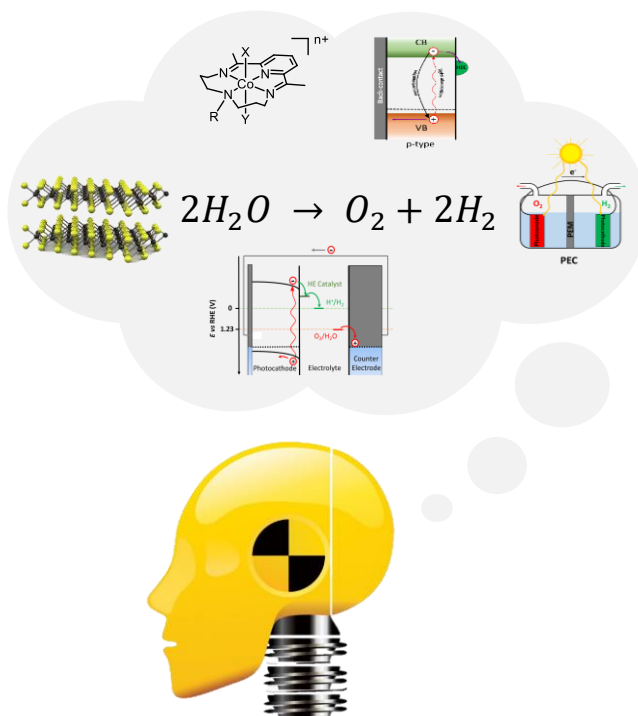
1-“Magnetically-actuated mesoporous nanowires for enhanced heterogeneous catalysis” Serra, Albert; Grau, Sergi; Gimbert-Suriñach, Carolina; Sort, Jordi; Nogues, Josep; Valles, Elisa. *Applied Catalysis B: Environmental*, 2017, 217, 81-91.

2-“A hybrid molecular photoanode for efficient light-induced water oxidation” Sergi Grau, Serena Berardi, Alicia Moya, Roc Matheu, Vito Cristino, Juan Jose Vilatela, Carlo A. Bignozzi, Stefano Caramori, Carolina Gimbert-Suriñach and Antoni Llobet. *Sustainable Energy Fuels*, 2018, 2, 1979.

3-“Can Ni Complexes Behave as Molecular Water Oxidation Catalysts?” Garrido-Barros, Pablo; Grau, Sergi; Drouet, Samuel; Benet-Buchholz, Jordi; Gimbert-Suriñach, Carolina; Llobet, Antoni. *ACS Catalysis*, 2019, 9, (5), 3936-3945.

Abstract

Chapter 1 General introduction

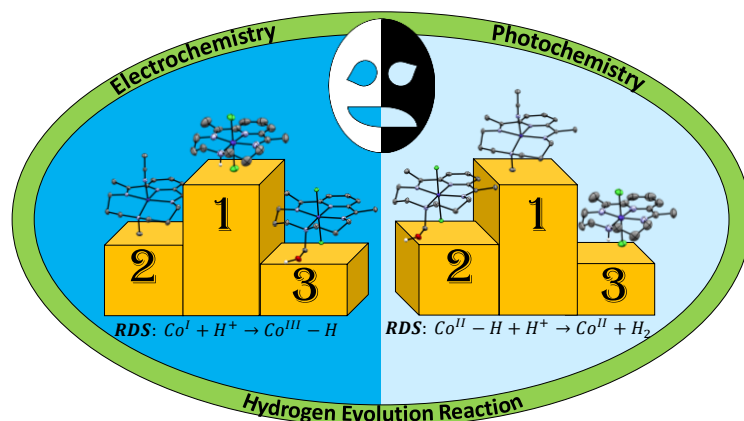


This chapter contains the motivation for the research done during the elaboration of this thesis, providing general information to the reader in the field of study. Firstly, an introduction on how we generate energy nowadays and its consequences for our planet. Then, a discussion on how scientists inspired by nature, developed alternatives to produce clean fuels including artificial photosynthesis is presented. A description of the historical development of the molecular catalysts for proton reduction to generate hydrogen gas and water oxidation to generate oxygen gas as well as the basic principles on semiconductors and available systems for water splitting will be provided. Finally some strategies to anchor molecular catalysts onto different substrates will be discussed.

Chapter 2 Objectives

According to the state-of-the-art in the field of artificial photosynthesis presented in Chapter 1, the main objectives are exposed in the present chapter.

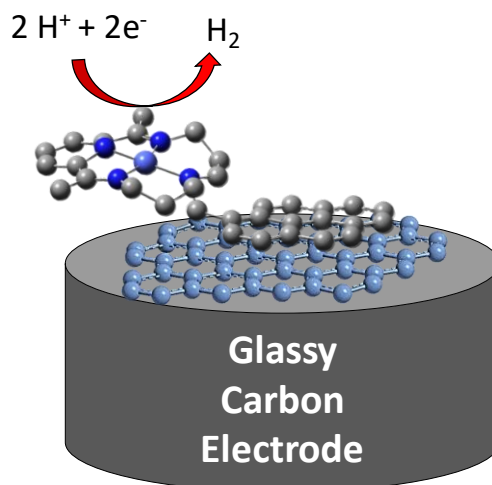
Chapter 3 Factors influencing hydrogen evolution (photo)catalysis in macrocyclic cobalt complexes



Chapter 3 explores the role of the proton relay in the second coordination sphere of cobalt macrocycle complexes that are active for the proton reduction reaction. The substitution of the proton in the amine in a macrocyclic ligand scaffold changes basicity of the corresponding Co hydrides, which are key intermediates in the catalysis thus strongly influencing catalytic properties. We found that electrochemical and photochemical proton reduction operates *via* different catalytic pathways, whose rate determining steps were identified through complementary computational studies.

Chapter 4

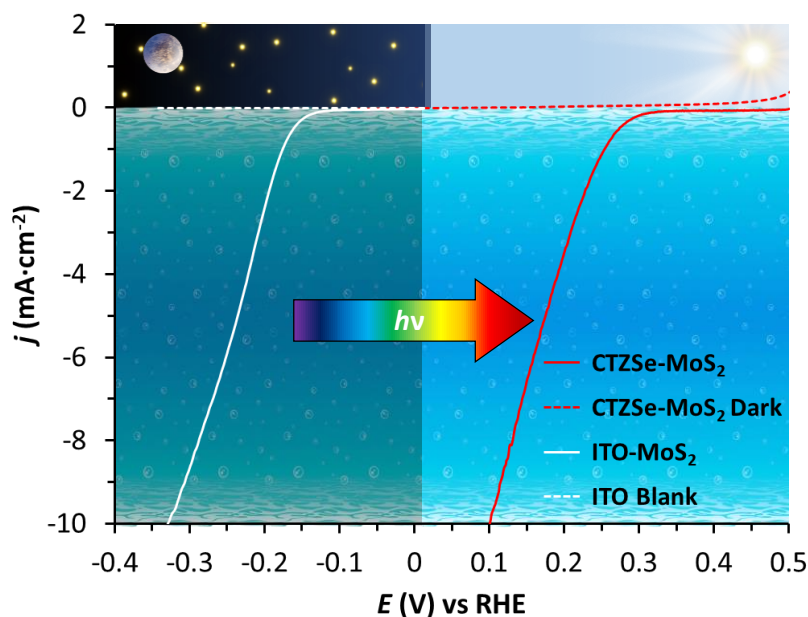
A molecular cathode for hydrogen evolution catalysis



A cobalt macrocyclic complex bearing a pyrene moiety in the ligand scaffold was developed for proton reduction. Its electrochemical properties have been characterized showing important differences in its catalytic properties compared to its analogous catalyst without the pyrene group. The catalyst has been used to prepare molecular cathodes by anchoring it on graphene powder by π - π stacking. A solid state analysis as well as an electrochemical study of the complex in solution and on the electrode reveal a strong interaction between the dangling pyrene group and the Co metal center which strongly affects its catalytic properties. By using different electrochemical techniques we were able to determine the onset potential of the electrode as well as the faradaic efficiency of the overall catalytic process.

Chapter 5

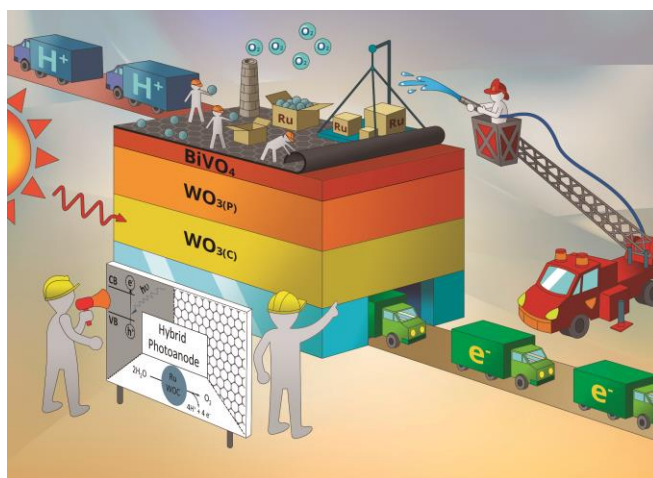
Photocathodes based on $\text{Cu}_2\text{ZnSnSe}_4$ for the Hydrogen Evolution Reaction



A methodology to electrodeposit amorphous MoS₂ on ITO electrodes have been developed that allows us to functionalize p-type semiconductor kesterite (CZTSe) very active for proton reduction catalysis. The prepared non-noble metal photocathode features an excellent performance in pH 2, able to reach $-10 \text{ mA}\cdot\text{cm}^{-2}$ at 100 mV before the thermodynamic potential. Moreover, the photocathode is able to sustain high current densities without any loss in activity for at least one hour.

Chapter 6

A molecular catalyst enhances water oxidation of heterostructured $\text{WO}_3/\text{BiVO}_4$ based photoanodes



The catalytic activity towards water oxidation of a heterostructured $\text{WO}_3/\text{BiVO}_4$ based photoanode has been carried out by the addition of a carbon nanotube fiber decorated with the state-of-the-art molecular catalysts for water oxidation, increasing the photocurrent at low potentials where the bare material can not oxidize water at all. The photoelectrochemical experiment probed that the molecular catalyst is producing oxygen from water. A detailed EIS study of the photoanode has been done, providing a valuable information to rationalize the electrical properties that affect the photoelectrochemical performance.

Chapter 7

General conclusions

Chapter 8

Annexes

Table of Contents

Acknowledgments	7
List of publications	11
Abstract	13
Chapter 1	21
General Introduction.....	21
Chapter 2	73
Objectives	73
Chapter 3	77
Factors influencing hydrogen evolution (photo)catalysis in macrocyclic cobalt complexes.....	77
Chapter 4	129
A molecular cathode for hydrogen evolution catalysis.....	129
Chapter 5	185
Photocathodes based on $\text{Cu}_2\text{ZnSnSe}_4$ for the HER.....	185
Chapter 6	223
A hybrid molecular photoanode for efficient light-induced water oxidation	223
Chapter 7	2655
General Conclusions	2655
Annexes	271

Chapter

1

General Introduction

This chapter contains the motivation for the research that has been done during the elaboration of this thesis, providing general information to the reader in the field of study. Firstly, an introduction on how we generate energy nowadays and its consequences for our planet. Then, a discussion on how scientists inspired by nature, developed alternatives to produce clean fuels including artificial photosynthesis is presented. A description of the historical development of the molecular catalysts for proton reduction to generate hydrogen gas and water oxidation to generate oxygen gas as well as the basic principles on semiconductors and available systems for water splitting will be provided. Finally, some strategies to anchor molecular catalysts onto diferent substrates will be discussed by showing some examples from the literature.

General Introduction

1.1 Global energy concern



Since the industrial revolution, humankind mainly uses fossil fuels like coal, natural gas and oil as a source of energy to carry on industrial processes, mobility and daily life. The exponential growth of world's population, the fast development of the emerging countries as well as the changes in the life style of our society is leading to a rapid increase in worldwide energy consumption.¹ Despite the fact that fossil fuels are limited, the most important problems of using it is the emission of greenhouse gases and pollutants, the scientific worldwide community is concerned about this effect in our atmosphere and world warming.²

In 2018, the world energy consumption was 14301 Mtoe (Millions Tons of Oil Equivalence), corresponding to an increase of 2.3% (respect to 2017), almost nearly twice the average rate of growth since 2010.³ This increase was mainly supplied by fossil fuels (nearly 70%), especially natural gas (43%) (Figure 1). Renewable energy was also increasing, but not enough to meet even with only the electrical demands around the world.

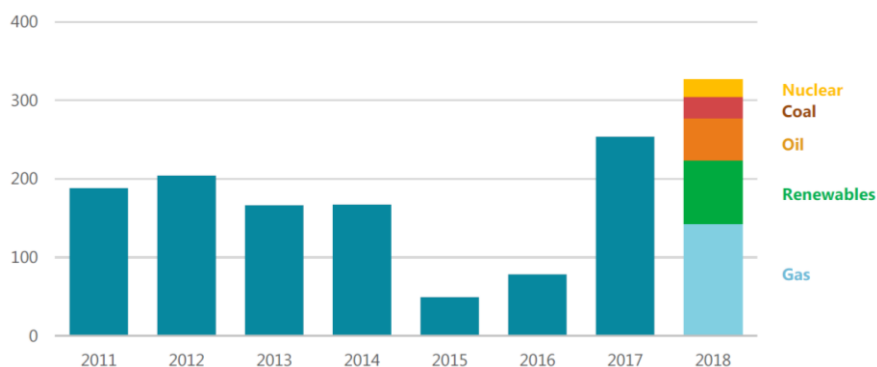


Figure 1. Average annual global primary energy demand growth by fuel, 2010-2018.³

In this scenario, under constant increasing energy demand supplied mainly by fossil fuels, the amount of atmospheric CO₂ is also increasing (Figure 2). The global energy-related CO₂ emissions rose 1.7%, reaching 33.1 Gt, the highest value record until now. In 2018, the averaged CO₂ atmospheric concentration was 407.4 ppm (pre-industrial levels were ranged about 180-280 ppm).

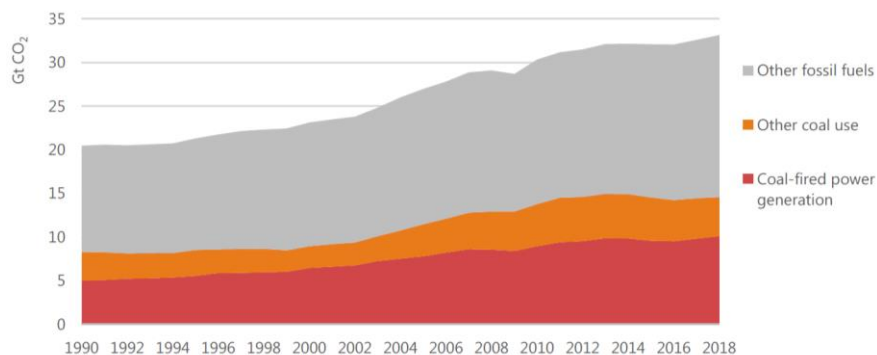


Figure 2. Global energy-related carbon dioxide emissions by source, 1990-2018.³

It is estimated that the human activities are the responsible of approximately 1.0 °C of the global world warming from the pre-industrial levels due to anthropogenic emissions (CO₂, other greenhouse gasses, aerosols, etc.), and their effects will persist for centuries.⁴ According to the predictions based on current warming rate, we will reach 1.5 °C between 2030 and 2052 (Figure 3, horizontal orange segment).

The global world warming very likely will cause long-term changes in climate system, such as rise in the sea level, changes in temperatures in land and oceans, disappearance of ecosystems and migrations of humans and animals.⁴ Moreover, the reserves of fossil fuels known nowadays will run out during this century (around 50 years for oil and natural gas, more than 130 for coal),⁵ thus the transition from fossil fuels to new energy production based on renewable and sustainable systems is imperative.

General Introduction

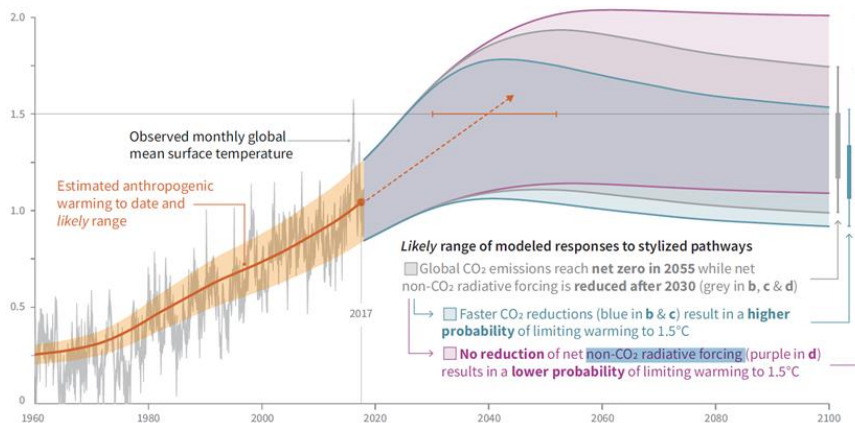


Figure 3. Global warming relative to 1850-1900 ($^{\circ}\text{C}$).⁴

Nowadays, there are carbon-free alternatives for energy production, such as nuclear, solar, wind, hydroelectric, geothermal and biomass. These more sustainable alternatives can produce electric energy efficiently, but the long-time storage of this is still an unresolved problem. Electrical energy can be stored in different ways, like pumped hydroelectric and compressed air systems, flywheels, thermal energy storage and batteries. These systems are able to store electrical energy when the production overcome the demand, but require expensive facilities and they need an electrical connection to the general electric power grid to supply the stored energy.^{6,7} There are other options to store the electrical energy such as batteries. Inside the batteries, lithium batteries is the most used in our daily life and have been improving in the last decade, but still being expensive, heavy and suffer undesired discharge over the time.⁸

Solar energy has been in the spotlight of scientific community as sustainable and clean energy source due the energy of the sunlight that reach the surface of our planet in one hour is 3 orders of magnitude bigger than humankind energy consumption in one year.⁹ Solar energy that reaches the Earth's surface is sensitive to various factors such as; location (altitude and latitude), time of day/year, orientation of the surface and weather conditions. This however, can be harvested in practically any part of the world, and is more equally distributed natural resource than fossil fuels (oil, coal, natural gas, uranium, etc.). On the other hand, nowadays the solar energy is mainly used to generate

electrical power or heating water and both energies cannot be stored efficiently.

In 2018, renewable energies covered close to 45% of the electricity energy growth, suppling over 25% of the world electric energy consumption.³ Inside this group, Photovoltaic (PV) electricity generation is one of the most used, growing 31% last year.³

To meet the objective to reduce the global world warming, decrease the anthropogenic green house emissions and develop an efficient, renewable and environmentally friendly new energy system, humankind needs to find a way to store energy efficiently.



General Introduction

1.2 Natural and artificial photosynthesis

Nature has been storing energy of the sunlight in chemical bonds for billions of years, using a process known as natural photosynthesis (eq. 1). This sophisticated process done by green plants and algae, consists in the formation of sugars and starches from water and atmospheric CO₂ using the energy of the sunlight, releasing O₂ as a side product. These carbohydrates will fuel other biological process when the organism needs the energy.¹⁰⁻¹³

From the electrochemical point of view, the general reaction for the specific case of formation of glucose (eq. 1) can be divided in two half-reactions, water oxidation and CO₂ reduction (eq. 2 and 3 respectively):

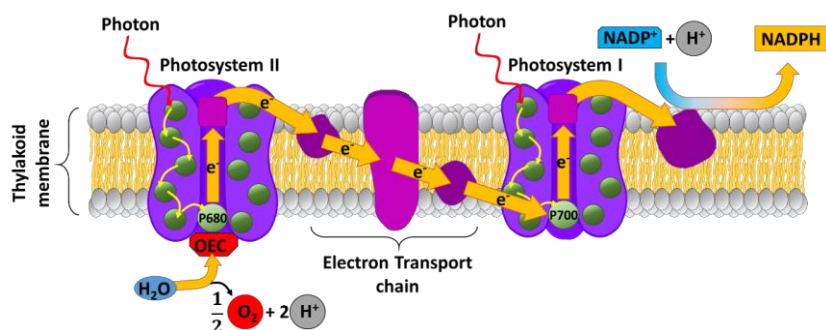
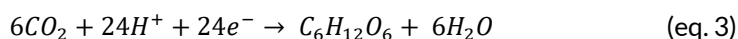
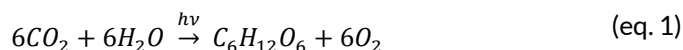


Figure 4. Schematic representation of PSII and PSI and the electron transport along the thylakoid membrane.

The photosynthesis process starts with the absorption of the photons by proteins called chlorophyll P700 and P680 in photosystems I and II respectively (PSI and PSII) located in the thylakoid membrane in higher green plants (Figure 4). The excited P680* transfers an electron to pheophytin, the



first member of the electron transport chain, that carries electrons from PSII to PSI. The high oxidizing $P680^+$ subtract one electron from the Oxygen-Evolving center (OEC, Figure 5), which is the responsible for the oxygen evolution reaction (OER). This process is mediated by tyrosine residue and is repeated four times to oxidize a water molecule (eq. 2) and release molecular oxygen and four protons. In PSI, the excited $P700^*$ is oxidized to reduce $NADP^+$ to NADPH (Nicotinamide Adenine Dinucleotide Phosphate) that lately will reduce CO_2 into carbohydrates. Finally, the electrons carried from PSII to PSI are used to reduce $P700^+$. At the same time, the protons (H^+) generated from OER creates a H^+ concentration gradient across the thylakoid membrane that is used by ATP synthase to produce ATP (Adenosine Triphosphate) from ADP (Adenosine Diphosphate) and phosphates.

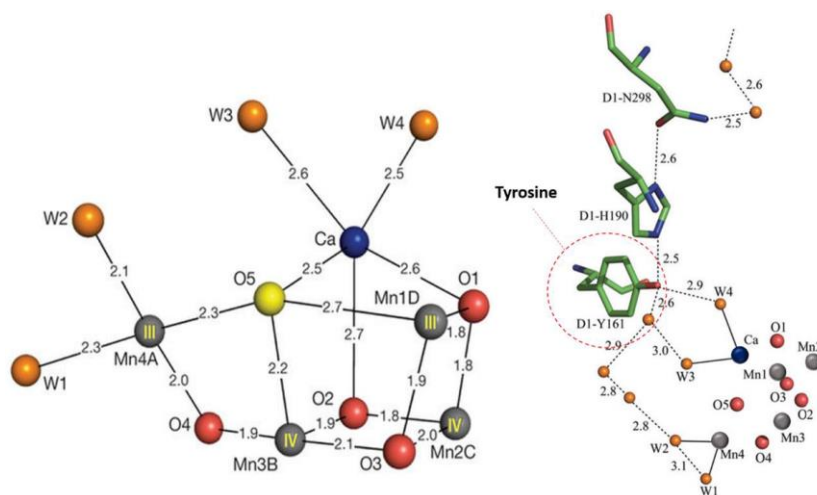


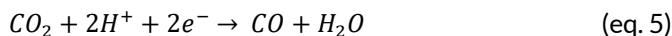
Figure 5. Structure of the Mn_4CaO_5 cluster of the OEC from PSII. (Left) Distances (\AA) between metal atoms and oxo bridges or water molecules. Colour code: Mn, grey; Ca, blue; O bridge, red and yellow; O (H_2O), orange. (Right) Representation of the environment around tyrosine residue involved in the oxidation of the Mn_4CaO_5 cluster.^{14,15} Colour code : Mn, grey; Ca, blue; O bridge, red; O (H_2O),orange.

General Introduction



The core of the OEC comprises a Mn_4CaO_5 cluster where three Mn atoms and one Ca atom are linked by oxo groups forming a cubane like structure, whereas the fourth Mn atom is outside of the cubane structure.^{14,15} Mn4A (Figure 5, left) is linked to other two Mn atoms inside the cubane through di- μ -oxo bridge. The OEC core is surrounded by a framework of amino acids residues and water molecules.^{16,17}

Inspired by nature, artificial photosynthesis has emerged as a promising technology that mimics the natural photosynthesis, harvesting the solar energy into chemical bonds. The process generally involves the oxidation of the water (eq. 2) to obtain electrons and protons that are used to reduce other small molecules obtaining the so called solar fuel. The most common reductive reactions carried on by artificial photosynthesis are hydrogen evolution reaction (eq. 4, HER) to generate molecular hydrogen, CO_2 reduction (eq. 5)¹⁸ to obtain CO (or other carbohydrates such as methanol, formaldehyde, etc.) and N_2 reduction to obtain ammonia (eq. 6).¹⁹



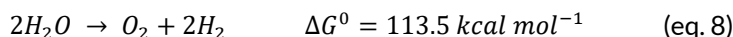
1.3 Water splitting devices

1.3.1 Thermodynamics and kinetics requirements

The water splitting overall reaction is a non-spontaneous and endergonic reaction (so thermodynamically uphill). The free energy associated to this reaction can be easily calculated by using the following formula:

$$\Delta G^0 = -nF\Delta E^0 \quad (\text{eq. 7})$$

Where ΔG^0 is the free energy of the process, n the number of electrons involved in the process, F is faraday constant ($96485 \text{ C}\cdot\text{mol}^{-1}$) and ΔE^0 is the difference between two half reactions' standard potentials of i) proton reduction (eq. 4) and ii) water oxidation (eq. 2). This allows us to calculate the energy required to split water into molecular oxygen and hydrogen:



The previous equation regards only to the thermodynamics of the reaction and doesn't take into account the extra energy required to overcome the kinetic barrier of both half reactions (usually between 0.3 and 0.6 V).^{20,21} Thus, the final energy input required to split one mole of water is increased up to 168.71 kcal mol⁻¹ (assuming an overpotential of 0.6 V).

1.3.2 Technical requirements

From the technical point of view, there are some requirements that any device designed for light driven water splitting need to fulfill:

- An external energy input, since the water splitting is a thermodynamic demanding reaction (eq. 7). To keep the process with zero emissions, this input must come from sunlight.
- A strategy to minimize the energy required to carry out the two half reactions (water oxidation and proton reduction) as well as to speed it up as much as possible.
- Separation of the products obtained from the overall process.



General Introduction

The first requirement can be accomplished using light absorbers, which can be a semiconductor (SC), an organic dye or a transition metal complex. When the light interact with the light absorber, the valence electrons are excited to the conduction band of the SC or to the lowest unoccupied molecular orbital (LUMO) of the molecule and eventually they are transferred to promote the necessary chemical transformations.

For the second requirement it is necessary to use robust and fast catalysts that are specifically active for the water oxidation or proton reduction reactions. They are responsible for the reduction of the kinetic barrier associated with the chemical process. Many catalysts in the form of nanoparticles, films or molecular entities have been reported for both half-reactions and this field is still being widely investigated by the scientific community.²²⁻²⁴

Finally, the third requirement can be accomplished by separating physically each half-reaction in two compartments by a semipermeable membrane, obtaining the products separately.

1.3.3 Designs for water splitting devices

There are several strategies to build light driven water splitting devices that can be divided into three different groups, as shown in the Figure 6: photovoltaic(PV)-assisted electrolysis systems (also called PV-electrolyzers), photoelectrochemical cell (PEC) systems and mixed colloid photocatalytic systems.²⁵

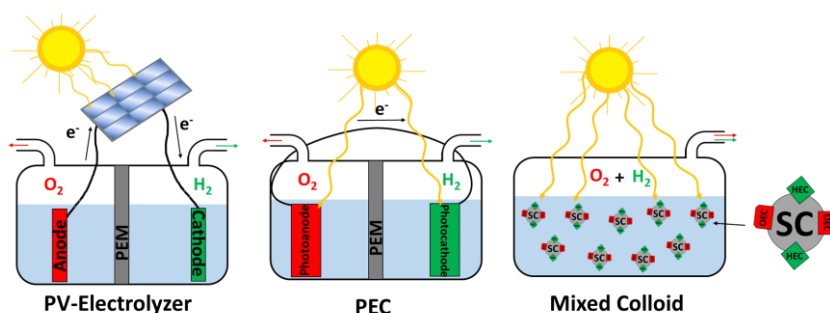


Figure 6. Designs of artificial photosynthetic devices.

PV-assisted electrolysis systems are based on mature technologies and consist in a PV cell connected to an electrolyzer composed by an anode and a cathode functionalized with heterogeneous catalysts that are immersed in the electrolyte solution. In this system, the light absorption and the redox reactions are separated and completely independent. One of the advantages of this system is that their components can be optimized separately but for efficient performance, the materials required are too expensive to be cost-competitive. Only systems with Solar-to-Hydrogen (STH) efficiencies close to the theoretical limit (>25%) could be economically competitive.^{26,27}

In the other extreme, we find the mixed colloid photocatalytic systems, where the light absorption and the redox reactions are integrated. The semiconductor particles are modified with catalysts for both redox reactions, so following the photoexcitation, OER and HER happens simultaneously in the same semiconductor particle. To be economically competitive, this system requires small STH (5-10%) although they are still in a proof-of-concept stage with a reported STH between 1-3%.^{25,28}

Finally, the PEC systems consist of at least one photoelectrode made of suitable semiconductor functionalized with heterogeneous catalysts for the desired reaction. In PEC the photoelectrode/electrolyte junction is the key for efficient coordination of the different processes, which are:


- i) light absorption
- ii) charge separation
- iii) chemical reactions

In these processes good alignment of the energies of conduction and valence bands with working potentials of the catalysts are critical as described later in this chapter. There are several configurations for PEC water splitting systems and the most common ones consist of using either i) one photoelectrode and one dark counter electrode (see Figure 8) or ii) two photoelectrodes in tandem.²⁹⁻³¹ One of the advantages of this kind of systems is that the photoelectrodes can be optimized separately and require intermediate STH efficiencies of 10-15% to be economically competitive.



General Introduction

1.3.4 Harvesting the light



Light can interact with matter in three different ways: reflection, refraction and absorption. The first two interactions are phenomena where the light change its wavefront direction when it founds an interface media (two different mediums with different refractive index). If the wavefront goes back to the medium where it comes we talk about reflection, but if the wavefront pass to the other medium then we talk about refraction. In both cases, the light conserves its energy. Materials or molecules that absorb light do so because the energy associated to the photon is enough to promote one electron from its ground state to an excited state (from one molecular orbital to another with higher in energy). In this kind of interactions, matter absorbs the energy of the photons.

Usually, the materials/molecules that absorb the light, release the absorbed energy in form of heat (non-radiative decay) or light (radiative decay) to recover its ground state. However, some materials such as semiconductors, can produce work with light's absorbed energy. According to its electrical conductivity, the materials can be divided in conductors, insulators and semiconductors. Conductor materials are usually made of metallic atoms (or alloys). In a conductive metallic crystal, the orbitals of each atom are overlapped with its neighbors. Since the Pauli exclusion principle dictates that no more than one electron can have the same quantum numbers inside the crystal, the orbitals are split resulting in a "continuum" in energy (actually is formed by discrete values very close to each other) of the molecular orbitals. The electrons with higher energy are "delocalized" inside the crystal and can move "freely" when they are excited from one atom to another because they have access to other orbitals. On the other hand, insulators have a huge difference in energy from the ground state and the excited state (>9 eV), making impossible in practice to promote one electron to another orbital higher in energy. In solid-state physics, the set of occupied molecular orbitals created by valence atomic orbitals is called Valance Band (VB) and the mostly empty molecular orbitals create the Conduction Band (CB). The energy difference between highest part of the VB and the lowest of the CB is called Band Gap (E_g).³² The energy where you have 50% of chances to find a populated state is called Fermi level (E_F).³³ In conductors, this Fermi level lays inside one of the bands, while in insulators lays inside the band gap. The electronic

structure of semiconductors is in between conductors and isolators. They have a band gap, but its energy is much smaller than insulators and the electrons from VB can be promoted to CB in some conditions. In metals, the electrons are the charge carriers responsible for the electric conductivity. In comparison, semiconductors utilise the vacancy that is left from the one electron promotion, called the “hole”. This can move in the lattice of the semiconductor as this hole can be occupied by another electron from neighbouring bands, leaving another hole in a different position of the crystallographic lattice.

Ideally, a crystalline semiconductor without any defect has the same numbers of electrons in the CB than holes in the VB (called intrinsic semiconductors), and usually have a low conductivity.³² To increase its conductivity, these materials can be doped by introducing atoms into the lattice with elements with differing valance electrons. Adding atoms with more valance electrons results in a n-type semiconductor (more electrons in the CB than holes in the VB) while adding atoms with less valance electrons result in a p-type semiconductor (more holes in VB than electrons in the CB). Hence, in a n-type semiconductor, the major charge carriers are electrons, and the minor charge carriers are holes while in a p-type semiconductor is the opposite.

When one semiconductor is under light, the photons with higher energy than the band gap ($h\nu > E_g$) are absorbed by the semiconductor, promoting one electron from the VB to the CB and leaving one hole in the VB (Figure 7, top, red arrow). In photovoltaics cells, the energy of the promoted electrons are used to create electrical power but this energy can also be used to promote chemical reactions. To use efficiently the electron-hole pair created by the absorption of a photon, it is necessary to separate them since the electron tends to decay returning to the VB in a process called recombination (Figure 7, top, black arrow).³² There are many approaches for charge separation, the most common is the use of p-n junctions. As described above, the n-type semiconductors have partially occupied states in the CB, thus its E_F lays near to the CB. On the other hand, p-type has a lack of electrons, and the CB is empty with the E_F close to the VB. When (electron rich) n-type and (hole rich) p-type are in contact in absence of light or external bias, their E_F reach an equilibrium by filling the holes of the p-type semiconductor with the free electrons from the n-type semiconductor, creating a depletion layer or space charge region. This new distribution of the charges creates an electric field through the



General Introduction

junction as depicted in the Figure 7 (bottom). The potential difference across the junction actually helps to separate physically the created electron-hole pairs since they feel an opposite force inside the same electric field (they have opposite charge), minimizing the recombination. With the proper architecture, the minor carriers will move to the interface photoelectrode-electrolyte to meet with the heterogeneous catalysts to promote the electrochemical reaction, while the major carriers will move to the back-contact of the photoelectrode (i.e. electrical connection of the photoelectrode with the rest of the system).

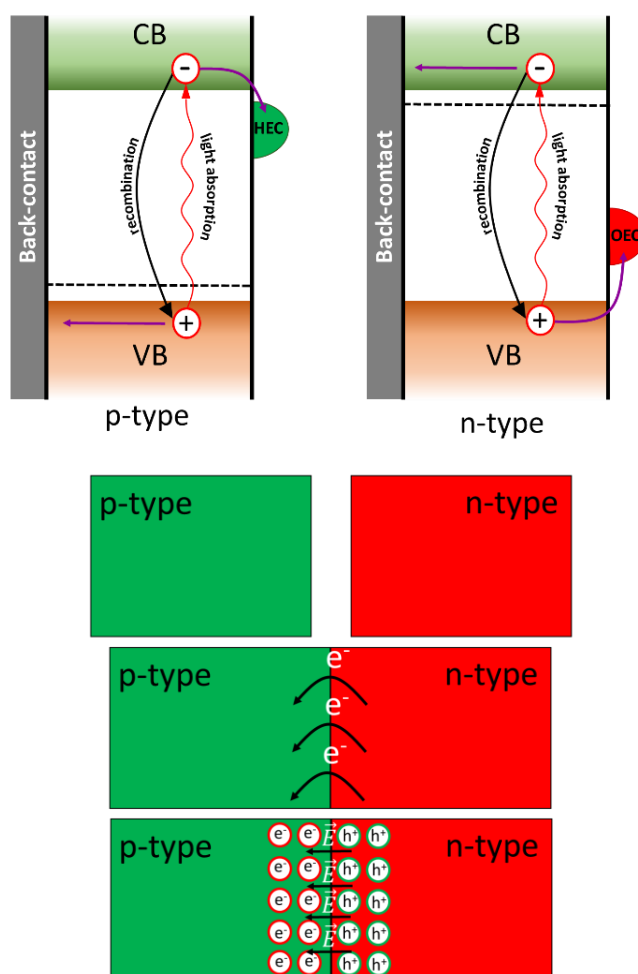


Figure 7. Top) Diagram of the movement of the minor and major carriers in a semiconductor under illumination. Bottom) Representation of a p-n junction before the union (top), during the charge equilibration (middle) and in equilibrium (bottom).

1.3.5 Storing energy of light into chemical bonds

In photoelectrochemical water splitting systems, the electron-hole pairs are used in the proton reduction and water oxidation reactions in the interface electrolyte-photoelectrode. P-type semiconductors are used to build photocathodes and the excited electrons from the CB are used in proton reduction, while the n-type semiconductors are used for photoanodes, and their holes in the valence band are used in water oxidation (Figure 8).

There are a wide number of suitable semiconductors that can be implemented in a photoelectrochemical cell for the two water-splitting half-reactions, however in the last decade the researchers have focused on the development of earth abundant and non-toxic materials to prepare photoelectrodes. Despite the fact that composition and technology used to prepare photoelectrodes has an impact on the price of the device, the first imperative requirement for choosing a semiconductor is to fulfill the thermodynamic principle, thus there should be a suitable alignment between the semiconductor bands and the electrochemical potential of the desired reaction. Selected p-type material as a photocathode for HER, should have the CB above the electrochemical potential of the proton reduction, while a n-type semiconductor for OER should have the VB below the water oxidation potential. When catalysts are used to accelerate the chemical reaction, the redox potentials of the specific catalysts also need to align to the band position and thermodynamic potential of the reaction (Figure 8). This requirement is necessary to ensure that once the electron-hole pair are generated and separated, they have enough driving force to reduce the heterogeneous hydrogen evolving catalyst (HEC) in photocathode's surface and/or oxidize the heterogeneous water oxidation catalyst (WOC) in the photoanode's surface.



General Introduction

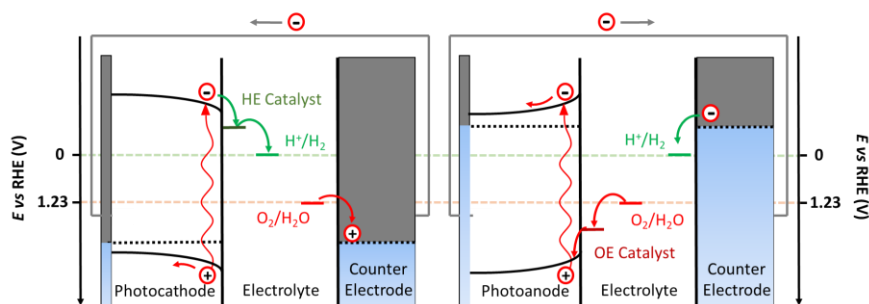


Figure 8. Schematics of PEC water splitting systems under illumination using a photocathode for proton reduction and counter electrode (left) and photoanode for water oxidation to dioxygen and counter electrode (right). Black dashed lines indicate the E_F . The electrocatalyst on the counter electrode was omitted for clarity. In the y axis, the potential of the two half reaction involved are indicated.

1.3.6 n-type and p-type semiconductors for light driven water splitting

There are several SC available to be used as photoelectrodes for light driven water splitting. Nevertheless, some consideration have to be taken into account for fabricating practical photoelectrodes:

- Position of the CB and VB: as previously discussed, CB should be more negative than H^+/H_2 couple while the VB should be more positive than H_2O/O_2 couple.
- The SC should be able to absorb most of the solar spectrum in order to increase as much as possible the solar to fuel conversion efficiency. For this propose E_g higher than 3 eV are considered not useful for this application.
- The material must be stable in the electrolyte (aqueous solution) to ensure the long term stability of the device.
- The material have to be composed of earth-abundant, cheap and non-toxic materials.

It is important to highlight, that up to date, there is no semiconductor material that can fulfill all the requirements mentioned above.

Figure 9 contains the energetic diagram of selected semiconductor materials that have been used in water splitting photoelectrochemical cells. Among all the suitable materials to prepare photocathodes (p-type semiconductors), metal oxides semiconductors usually feature the advantage of easy preparation. Binary metal oxides present metal vacancy defects, resulting in a

p-type conductivity and although can be made by earth-abundant and low-cost elements, usually show a low absorption coefficients and poor charge-carrier mobility. One example of p-type metal oxide is Cu_2O , with a $E_g = 1.9\text{-}2.2$ eV, a theoretical 18% solar-to-fuel conversion efficiency, easy electrochemical preparation³⁴ and the CB 0.7 eV more negative than proton reduction potential, this material is being widely studied (Figure 9). One of the main problems of this SC is that its self-oxidation (to form CuO) and self-reduction (to form metallic Cu) potentials are within the band gap. Thus, in order to avoid the degradation, the material is usually protected by heterojunctions. Paracchino *et al.* covered Cu_2O with Al:ZnO/TiO_2 by Atomic Layer Deposition (ALD) with Pt nanoparticles as HEC, reaching -7.6 $\text{mA}\cdot\text{cm}^{-2}$ at the thermodynamic potential in pH 7.³⁵ Morales-Guio *et al.* reported the same material using MoS_2 as HEC in pH 14, reaching -6.3 $\text{mA}\cdot\text{cm}^{-2}$ at 0 V vs RHE. In these conditions the photocathode was able to sustain HER for 10 hours proving the robustness of the protective heterojunction.³⁶

Another family of p-type SC is the copper-based chalcogenides such as $\text{CuIn}_x\text{Ga}_{1-x}\text{Se}_2$ (CIGSe) and kesterites $\text{Cu}_2\text{ZnSn(S/Se)}_4$ (CZTS/Se), with a high absorption coefficients ($\sim 10^5$ cm^{-1}) and narrow band gap (1.0-1.68 eV and 1.0-1.5 eV, respectively) have been widely investigated in solid state PV field.³⁷⁻⁴⁰ Their p-type conduction is due to the vacancies of Cu in the crystalline structure and are usually obtained by sulfuration/selenation of the sputtered or electroplated stacked metals (Cu/In/Ga for CIGS and Cu/Zn/Sn for CZT(S/Se)). The best performance either in photovoltaic or in PEC applications, are always combined with n-type SC to create p-n heterojunction (usually CdS, but more recently In_2S_3 or ZnS are also used). Due to the poor stability of CdS during HER, the photocathode is protected by metal oxide layers such as ZnO, Al_2O_3 or TiO_2 . Yokoyama *et al.* prepared a CIGS/CdS/Pt photocathode able to reach -12.0 $\text{mA}\cdot\text{cm}^{-2}$ at 0 V vs RHE.⁴¹ The same group also reported a CZTS/CdS/ TiO_2 /Pt photocathode able to reach -9.0 $\text{mA}\cdot\text{cm}^{-2}$ at 0 V vs RHE in pH 9.5.⁴² Although the kesterites are not so good as the well developed CIGS (much more mature technology) they are made by earth-abundant materials (In and Ga are not earth-abundant), and in the last years their performances have been improving.

Some examples of n-type SC suitable to prepare photoanodes are WO_3 and BiVO_4 . BiVO_4 started to attract great interest since Kudo and coworker



General Introduction



reported its activity towards OER under visible light.⁴³ With a $E_g = 2.4$ eV and VB 1.2 eV more positive than the water oxidation potential this material is a good candidate for preparing photoanodes for OER. The main drawback of this material is its low carrier mobility ($\sim 4.4 \cdot 10^{-2} \text{ cm}^2 \text{V}^{-1} \text{s}^{-1}$), 1-2 orders of magnitude lower than other metal oxide SC. Its CB mainly consist in the V 3d orbitals. Vanadium ions are located in the non-interconnected VO_4 tetrahedrons, thus the electrons have to jump these tetrahedrons to be transferred.⁴⁴ Due to the low mobility of the carriers, the recombination of the photogenerated electron-hole pair is high. To reduce it, a common strategy is the use of dopants and co-catalysts. Luo and Zou reported that Mo^{6+} and W^{6+} as the most effective dopants.⁴⁵ Krol *et al.* prepared a multilayered $\text{BiVO}_4/\text{WO}_3$ and after the annealing process, a W^{6+} doped BiVO_4 with a gradient dopant concentration were obtained, resulting in a better conductivity and charge separation and thus, a better photoelectrochemical performance towards OER.³¹ $\text{WO}_3/\text{BiVO}_4$ composites have been also reported, with enhanced performance compared to bare BiVO_4 due to their good band alignment (Figure 9) and the good electrical properties of WO_3 and the better light absorbance of BiVO_4 .⁴⁶ As co-catalysts, the most common used are Co oxides⁴⁷ and $\text{NiOOH}/\text{FeOOH}$. Park *et al.* prepared a nanostructured $\text{WO}_3/\text{BiVO}_4$ with $\text{NiOOH}/\text{FeOOH}$ as water oxidation co-catalyst, reaching $5.35 \text{ mA} \cdot \text{cm}^{-2}$ at 1.23V vs RHE in pH 7 under 1 sun illumination.⁴⁸

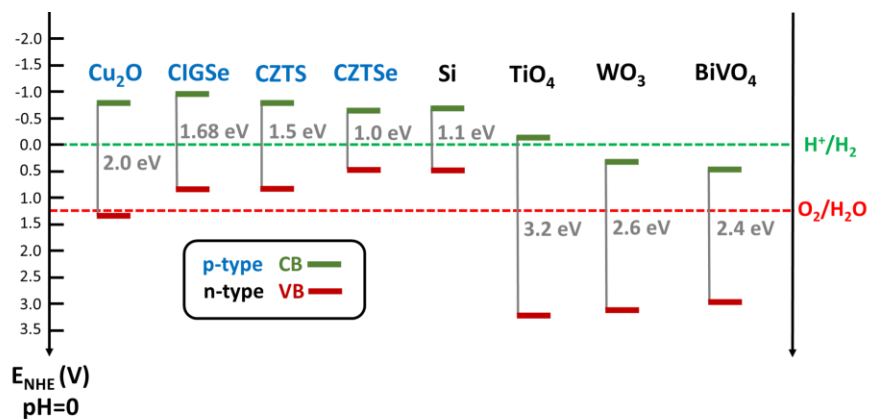


Figure 9. Energy diagram with the relative positions of CB and VB of selected p-type and n-type semiconductors.

General Introduction

1.4 Catalysts for water splitting

1.4.1 Evaluating Molecular catalysts



A good catalyst for HER or OER should be robust and work with a high activity under low overpotential. To evaluate these properties we need to define turnover number (TON), turnover frequency (TOF) and electrochemical overpotential (η):

- TON is a dimensionless parameter that evaluates the robustness of a molecular catalyst, defined by the number of catalytic cycles that one molecule of catalyst can perform before it deactivates. The bigger the value, the more robust and stable the catalyst is. To calculate it is necessary to know accurately the amount of catalyst and product, using the following formula:

$$TON = \frac{n_{Product}}{n_{CAT}}$$

Where $n_{Product}$ and n_{CAT} are the number of mols of product and catalyst respectively.

- TOF is a parameter that evaluates how fast a catalyst is. More specifically, it gives the number of catalytic cycles per catalytic center per unit of time. Its units are $time^{-1}$ (usually s^{-1}) and is calculated with the following formula:

$$TOF = \frac{TON}{\Delta t}$$

Where Δt is the lapse of time considered. It is important to notice that TOF depends on k_{obs} of the reaction and its value changes with the concentration of the substrate, thus usually the TOF is reported at the early stages of the catalysis. Sometimes initial TOF (TOF_i) or maximum TOF (TOF_{max}) are reported.

- The electrochemical overpotential (η) as used in this thesis is the difference between the thermodynamic potential and the actual potential at which the desired reaction takes place, defined by:

$$\eta = E - E^0$$

Where E is the applied potential and E^0 is the thermodynamic potential of the reaction.

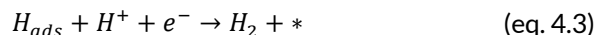
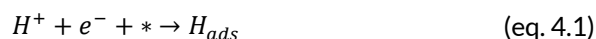


1.4.2 Hydrogen Evolution Reaction

The formation of one molecule of H_2 from water (or protons) is a relatively simple reaction where only two protons and two electrons are necessary (eq. 4), and its associated kinetic barrier is small compared to that of OER. Since it's impossible to unlink any redox half reaction from its counterpart, the electrochemical potential for HE in standard conditions (*i.e.* pH=0, 1 atmosphere and 298.15 K) was used to reference all the electrochemical reactions. Thus, its electrochemical potential was set (for convention) as 0 V.

Among all kind of catalysts for HER, metallic platinum is the best. It operates in high catalytic rate with almost no overvoltage but it is scarce and expensive, making its application in a large-scale industrial application non-viable economically.⁴⁹

The general mechanism for proton reduction on heterogeneous bulk catalysts is depicted in Figure 10.⁵⁰ In-depth mechanistic studies have correlated the tafel slope (η vs $\log|j|$) with the rate determining step in the electrocatalytic proton reduction,⁵¹ assuming constant coverage of adsorbed H atoms over the range of potentials.



The process starts with the adsorption of a free proton from the media to an active site (*) coupled to a one electron reduction, called Volmer step or

General Introduction

discharge step (eq. 4.1). To evolve molecular hydrogen two possible mechanistic pathways can happen. The first one is known as the Tafel recombination step (eq. 4.2), where two adsorbed H atoms combine to form H_2 while the second one is called Heyrovsky step and involves another free proton that is reduced and simultaneously reacts with H_{ads} to release H_2 (eq. 4.3). A Tafel plot with ca. $120 \text{ mV} \cdot \text{decade}^{-1}$ slope indicates that the rate determining step is Volmer while a Tafel slope of 40 and $30 \text{ mV} \cdot \text{decade}^{-1}$ suggests that the rate determining step are Heyrovsky and Tafel steps, respectively.^{50,52,53}

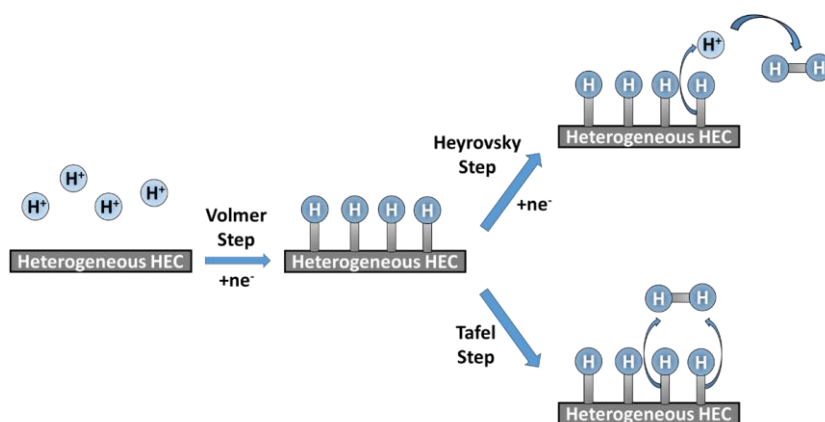


Figure 10. Schematic representation of the Volmer-Tafel and Volmer-Heyrovsky mechanisms for heterogeneous catalytic HER.

Catalysts based on earth abundant transition metals for HER have been widely investigated in order to find a substitute for Pt.⁵⁴ Nature brings us excellent examples to mimic: hydrogenases. Hydrogenases are enzymes based on iron and/or nickel that can reduce protons to H_2 with rates up to 10000 moles of hydrogen per mol of catalysts per second with negligible overpotential. They are classified according to the active-site metals and two prominent examples are [FeFe]-hydrogenases and [NiFe]-hydrogenases.⁵⁵⁻⁵⁷ The structure of these two hydrogenase's cofactors were solved during 1990s⁵⁸⁻⁶⁰, revealing that for [FeFe]-hydrogenase, the active center was a dinuclear Fe-Fe complex coordinated to CN^- , CO and azadithiolate ligands (Figure 11, left). The latter is key for the H-H bond formation step because it has been proposed to act as proton relay bringing an incoming proton close to the Fe-hydride intermediate



species (Figure 11, middle). One Fe ion is hexa-coordinated showing an ideal octahedral configuration and the other has only penta-coordination, leaving one vacancy used as active site. The active center of [NiFe]-hydrogenase was identified as an asymmetric Ni-Fe complex, where CN⁻ and CO ligands coordinate with Fe ion and Ni ion is in a high distorted square-planar configuration, coordinated by four cysteinyl ligands, two of which link both ions together. Both Fe and Ni sites leave one vacant position as active site (Figure 11, right).

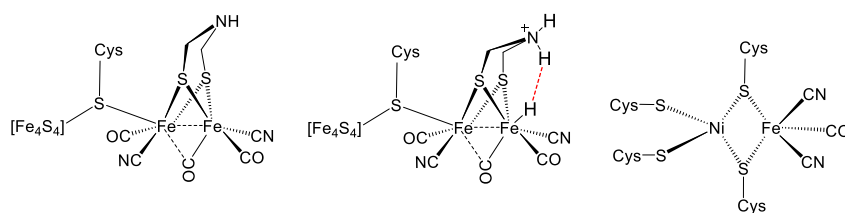


Figure 11. Structural representation of the active sites of [FeFe]-Hydrogenase (left), intermediate species derived from [FeFe]-Hydrogenase that leads to H-H bond formation (middle) and [NiFe]-Hydrogenase (right). Cys is cysteinylate.

Hydrogenases and their artificial derivatives have been extensively investigated revealing the structure and the catalytic mechanism of the active sites. A general catalytic mechanism for the hydrogen evolution at a metallic center M^{n+} is given in Figure 12.⁶¹⁻⁶⁴ The active metal center undergoes two consecutive or coupled electron and proton transfers to form a metal-hydride intermediate ($H-M^{n+}$ in Figure 12).²⁴ From this point, there are three possible pathways for the subsequent H_2 formation. The first one is an homolytic pathway, where two metal-hydrides react to generate molecular hydrogen via reductive elimination. The second is the heterolytic pathway where the metal-hydride is protonated to form H_2 . Alternatively, the metal-hydride can be further reduced and react with another reduced metal-hydride (homolytic) or be protonated to form H_2 (heterolytic). Determining the mechanism is often challenging due to the fact that several pathways can happen at the same time, or they can interconvert depending on the conditions of a given system, like pH.⁶⁵ Metal-hydride formation and H_2 generation can be facilitated by the

General Introduction

backbone of the ligands, placing proton relays in the first or second sphere coordination of the metal center, such as in the natural system.^{66,67}

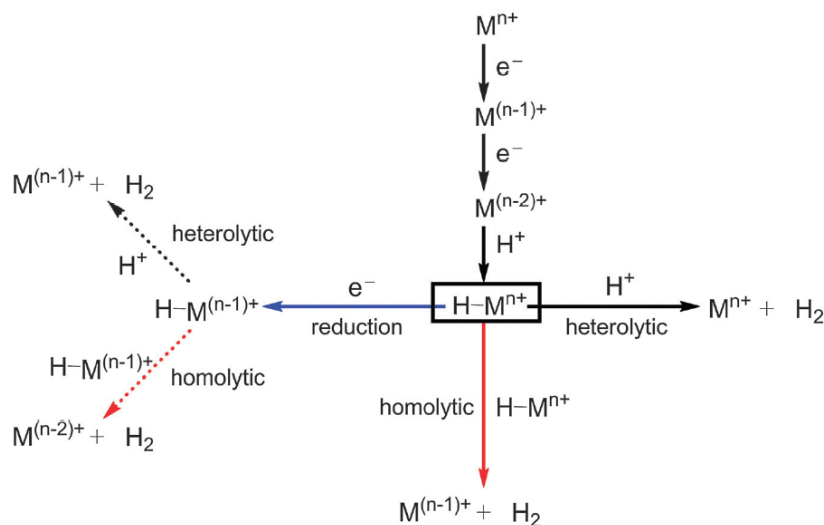


Figure 12. Proposed mechanistic pathways for hydrogen evolution catalysis at a metallic center M^{n+} .²⁴

This mechanistic information gives us some criteria for the rational design of new and better catalysts active for HER. Transition metal complexes are good candidates to act as hydrogen evolution catalysts because they can store electrons *via* multiple redox processes in the metal center and also because they contain ligands that can be specifically designed according to the reaction and mechanism requirements. One of the most important characteristic is that the metal complex should have available coordination positions and appropriate electronic structure to obtain a basic metal-hydride. The ligand should also stabilize low oxidation states of the metal center in order to minimize the overpotential needed for HER. Other strategies include redox tuning by using non-innocent redox ligands or including protonation sites integrated in the catalyst secondary sphere of the metal that could facilitate the H-H bond formation as it happens with the [FeFe]-hydrogenase cofactor (Figure 11, middle). Indeed, second coordination effects and the tertiary structure of proteins plays a crucial role controlling the availability of protons and electrons to the active center in natural hydrogenases.

Over the last decade, many studies have focused on the development of earth-abundant metal-based and cost-effective catalysts for HER, like Ni, Co, Fe and Mo.^{25,68,69} One example of heterogeneous HEC is Molybdenum disulfide (MoS₂, Figure 13), a transition metal dichalcogenide that can be found naturally in molybdenite (mineral). It's a layered solid widely used in the industry as a solid lubricant.⁷⁰ Like graphene layers in graphite, Mo-S-Mo stacked layers are assembled together by weak Van der Waals interactions in hexagonally packed structures, making the movement between layers relatively easy. Bulk MoS₂ has an indirect $E_g = 1.2$ eV⁷¹ while monolayer feature a direct band gap of 1.8 eV⁷² and presents four poly-types: 1T MoS₂, 1H MoS₂, 2H MoS₂ and 3R MoS₂. Its catalytic properties are widely studied for two reactions: hydrodesulfurization (HDS) and HER. There are many experimental and theoretical studies about the electrochemical properties of MoS₂ towards HER, and the results confirm that the catalytic active sites are the crystallographic edges while the basal planes are catalytically inert.⁷³⁻⁷⁵ The catalytic properties of the active site in MoS₂ are comparable to the noble metals, for this reason this material has been drawn great attentions due to their low cost and high chemical stability. One of the focus of this research is to try to synthesize a "rich in active sites" MoS₂. There are several synthetic approaches to obtain nanostructured MoS₂, divided in physical and chemical methods. Inside the physical methods we found techniques such as microwave plasma, laser ablation, arc discharge, sputtering and pulsed-laser vaporization. The most used chemical methods are chemical vapor deposition, solvothermal process and sonochemical synthesis.⁷⁰ There are two ways to improve the catalytic activity of the MoS₂: **i)** increase the intrinsic activity of the active sites by optimizing the binding energy of hydrogen (H_{ads}) and improve the electronic conductivity, or **ii)** increasing the density of the active sites.

One approach used to enhance the intrinsic catalytic activity of MoS₂ is the doping of the material by some promoters, such as Ni, Co, Au, Zn, Pt and C in order to modify the free energy of the proton absorption (being $\Delta G_H = 0$ eV the optimal value), as well as to improve the electrical conductivity with appropriate materials as catalyst supports.^{74,76-78} Another approach is to synthesize MoS₂ nanostructures with different architectures (nanoparticles, flakes, open flowers, nanotubes, mesoporous films, etc.) in order to increase (or expose to the electrolyte) more catalytic sites (*i.e* more edges per mol).^{73,74,79-}



General Introduction

⁸⁶ Until now, only crystalline structures were considered in the discussion but it is worth mentioning that in late 90's, amorphous MoS₂ started to be in the scientific community spot since its electrochemical performance towards HER was much higher than bulk crystalline MoS₂ and its easy preparation by electrodeposition.⁸⁷⁻⁹³ The reason for the enhanced activity of amorphous MoS₂ is still nowadays not clear, the most plausible hypothesis is that the amorphous MoS₂ has many defect sites, where there are coordinately and structurally unsaturated sulfur atoms, where hydrogen atoms can be absorbed.⁹¹ New investigations suggest that active sites of amorphous MoS₂ could differ from the crystalline MoS₂ edges.⁹⁴

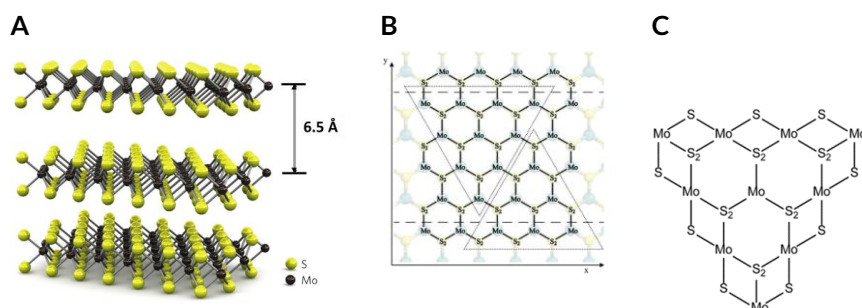


Figure 13. A) Three-dimensional representation of the structure of MoS₂.⁹⁵ B) Top view of the 2D MoS₂ sheet. The two horizontal dashed lines indicate terminations along the (10 $\bar{1}$ 0) Mo-edge and ($\bar{1}$ 010) S-edge. The two triangles represent the terminations for Mo-edge and S-edge clusters. C) Schematic representation of the 50% S coverage Mo-edge cluster.⁹⁶

In the family of molecular catalysts, DuBois and co-workers developed Ni-complex with two 1,3-diethylphosphopropane (DEPP) ligands [Ni(DEPP)₂]²⁺ capable of reversible cleave H₂ in the presence of 2,3-dichloroaniline to form a nickel hydrate and the protonated dichloroaniline. Inspired by natural hydrogenases, an amine base was incorporated in the backbone structure to facilitate the proton transfer rate⁹⁷ resulting in a negative shift of 650 mV for the hydrogen oxidation but with a low reaction rate. In order to place the N-pendant base near to the Ni metal center, the 1,5-diaza-3,7-diphosphacyclooctanes ligands were synthesized (Figure 14).⁹⁸⁻¹⁰⁰ Further studies on the mechanism of catalytic H₂ generation revealed that three



different isomers were formed after two electron reduction and double protonation of the intermediates (A, B and C from Figure 14) and only A was active for HER.¹⁰¹ To avoid the formation of isomers B and C, the new ligand 1-aza-3,6-diphosphacycloheptane was synthesized with only one pendant N-base and forming a 7 member ring around the metal center (DuBois catalyst, Figure 14).¹⁰² The new complex showed a significant enhancement of the electrocatalytic performance with TOF values of 33000 s^{-1} at 0.63 V of overpotential using $[(\text{DMF})\text{H}](\text{OTf}) = 0.43\text{ M}$ in acetonitrile. This value increases until 106000 s^{-1} with the addition of the optimal amount of water. DuBois' nickel catalysts are the perfect example of how a deep insight into the mechanism of the catalytic cycle can provide information to correlate the structure and the activity of a given catalyst, obtaining valuable information to design rationally better molecular catalysts. DuBois catalysts featured a high activity and stability in organic solvents in the presence of strong acids, but on the other hand they only operate with such high rate under large overpotential ($\eta > 0.6\text{ V}$) in non-aqueous medium.

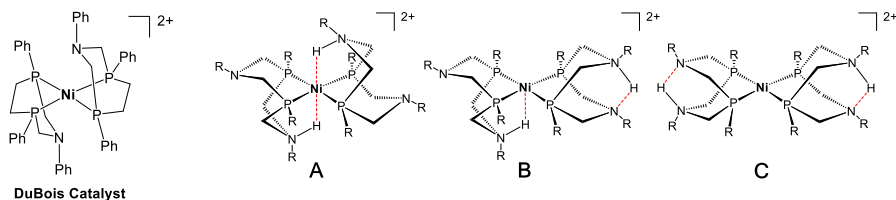


Figure 14. Left) DuBois catalyst. Right) Double protonated Ni^0 intermediates involved in HER (isomers A, B and C). Only isomer A is active for proton reduction.

1.4.1 Cobalt-based catalysts for HER

Even though there are no biological system that uses cobalt in the active center for HER, most of the reported small-molecule HEC stable in aqueous media employ this element. Cobalt complexes as HEC in electro and photochemical hydrogen generation have been in the spot of the researchers due to its rich redox chemistry and catalytic power. According to the ligands, Co-based catalysts for HER can be divided in eight groups: **i)** N_4 -macrocyclic complexes, **ii)** hexaamino complexes, **iii)** porphyrin complexes, **iv)** phthalocyanine complexes, **v)** cyclopentadienyl complexes, **vi)** cobalt glyoxime (also known as

General Introduction

cobaloximes) **vii**) polypyridine complexes and **viii**) cyclopentadienyl complexes.⁶⁸ Here, only groups **i**) macrocycles, **vi**) cobaloximes and **vii**) polypyridine complexes will be briefly commented due to their good performance for the HER in aqueous solutions.¹⁰³⁻¹⁰⁶



The first molecular HEC based on cobalt was reported by Fisher and Eisenberg in 1980 and was able to produce H₂ from protons with 80% of Faradaic efficiency in 2:1 water:acetonitrile mixture and pure water at -1.26 V and -1.36 V vs NHE on a Hg pool electrode (HEC 1, Figure 15).¹⁰⁵

Cobaloximes-type of complexes have been extensively studied as proton reduction catalyst in electro- and photochemical systems due its easy preparation, good catalytic activities in organic solvents and relatively low overpotential. One of the first examples is HEC 2 in Figure 15, reported of Connolly and Espenson in 1986.¹⁰⁷ Since then, the study of this family of compounds has brought to the field important insights to understand the HER mechanism in aprotic organic media in the presence of strong to moderate acids as a proton source but their lack of stability in neutral and acidic aqueous solutions has limited their use. Improvement of the stability of cobaloximes in water have been achieved by Peters and coworkers, who reported the electrocatalytic behavior of a family of complexes with modified ligand frameworks (HEC 2-5 in Figure 15).¹⁰⁸ In pH 2.2, HEC 3 and HEC 4 featured a catalytic current corresponding to the catalytic proton reduction while HEC 2 showed a wave before the catalytic current, assigned to Co^{II/I} couple. This fact suggested that HEC 2 operates *via* protonation of “Co⁰” species instead of protonation of Co^I species like HEC 3 and 4. Controlled potential experiments at -0.69 V vs NHE for two hours revealed that the HEC 3 was the most active catalyst, with 28 TON and a Faradaic efficiency of 81%. On the other hand, HEC 5 only reached 2 TON and a Faradaic efficiency of 30% in the same experimental conditions, suggesting that the complex decomposes to inactive species.

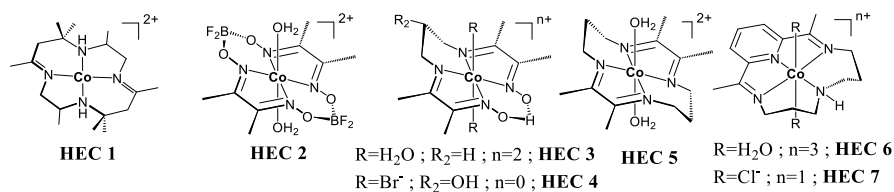


Figure 15. Structures of selected cobalt macrocycles and cobaloxime complexes actives for HER.



Complex HEC 6 in Figure 15 is another kind of molecular cobalt complexes containing a tetraazamacrocycle made of a pyridine and two imine groups. It was first used as HEC in 2011 by Lau and coworkers although the synthesis of the complex was reported by Brush and Long in 1970^{109,110}. Its electrocatalytic activity for proton reduction was tested in acetonitrile and aqueous solutions using p-cyanoanilinium and acetic acid as a proton source, respectively, with high Faradaic efficiency (>90%) and >50 TON in both media. Photochemical H₂ production was also carried out in a mixture of acetonitrile:water with [Ir^{III}(ppy)₂(bpy)]⁺ (where ppy is 2-phenylpyridine and bpy is 2,2'-bipyridine) as a photosensitizer, acetic acid as proton source and triethanolamine as a sacrificial electron donor, reaching 180 TON under visible light.¹¹¹ Peters *et al.* also studied the same cobalt complex electrochemically reaching 17 TON with 92% of faradaic yield.¹⁰⁸ Compared to cobaloximes derivatives, HEC 6 with a ligand scaffold containing a pyridine and two imine groups shows slightly more negative redox potential but higher Faradaic efficiencies suggesting better stability in aqueous solutions.

Later on, HEC 6 and 7 (which give the same active species after the substitution of the chlorido by aqua ligands) have been used by Collomb and coworkers as well as by our group in photochemical systems. In these systems ascorbic/ascorbate was used as both sacrificial electron donor and buffer and a plethora of different photosensitizers including [Ru(bpy)₃]²⁺,^{112,113} CdTe¹¹⁴ or CuInS₂ quantum dots¹¹⁵ as well as purely organic dyes.¹¹⁶ A breakthrough in elucidating the mechanism of the reaction for the HER by HEC 6 was reported in 2016 using state of the art x-ray transient absorption spectroscopy techniques (X-TAS). In this work, it was possible to trap intermediate species in the nano to micro-second time scale and to determine the rate-limiting step of the process for the system HEC 6/[Ru(bpy)₃]²⁺/ascorbate, which consists in the

General Introduction

protonation of the Co^{I} species to form the $\text{Co}^{\text{II}}\text{-H}$ species (Figure 12 and Figure 16), the latter is so reactive that remain elusive in the experimental time-scale resolution.¹¹⁷

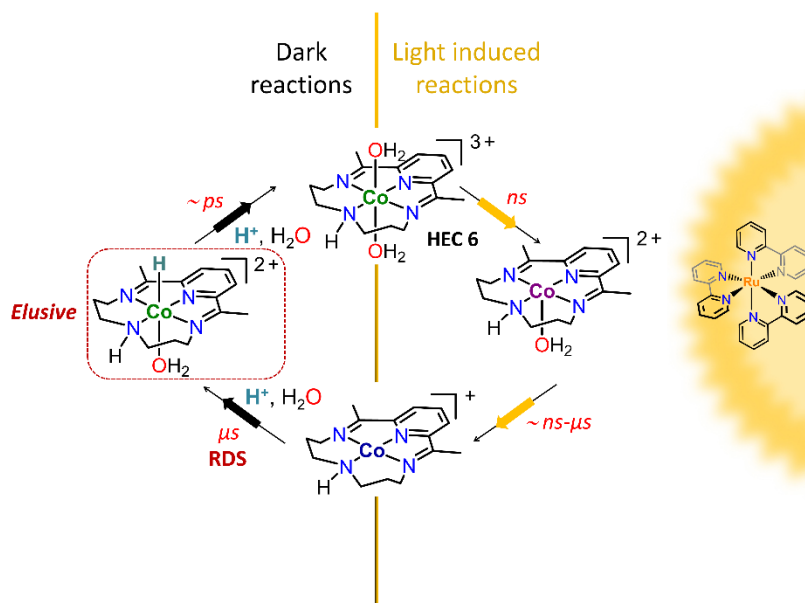


Figure 16. HER mechanism followed by catalyst HEC 6 under photochemical conditions using $[\text{Ru}(\text{bpy})_3]^{2+}$ as photosensitizer and ascorbic/ascorbate as both sacrificial electron donor and buffer.¹¹⁷

Polypyridine cobalt complexes are another important family of cobalt HEC, some of them able to reduce protons in neutral water media. For instance, HEC 11 in Figure 17 was reported to reduce protons from trifluoroacetic acid (TFA) in acetonitrile and 1:1 acetonitrile-water solutions at *ca.* -0.76 V vs NHE.¹⁰⁶ Chang and coworkers also reported a series of cobalt pentapyridine complexes capable to reduce protons in neutral pH (HEC 8-10).¹¹⁸ Electrochemical studies showed that all three catalysts featured a wave before the electrocatalytic wave assigned to the $\text{Co}^{\text{II/I}}$ couple. In controlled potential electrolysis experiments at -1.30 V vs NHE in pH 7 phosphate buffer, HEC 8 catalyzes proton reduction with 99% of Faradaic efficiency and reaching $5.5 \cdot 10^4$ TON in a lapse of 60 hours. The redox potential of these complexes can be tuned by changing the para-substituent on the axial pyridine ligand. For instance, the



$\text{Co}^{\text{II/I}}$ couple is at -1.0 V vs NHE when $\text{R}=\text{H}$ (HEC 8). When the para-substituent is replaced by an electro-withdrawing group, like $-\text{CF}_3$ (HEC17), the potential is shifted to -0.84 V . On the other hand, the potential is shifted to -1.12 V when is substituted by an electron-donor such as $-\text{NMe}_2$. Zhao and coworkers reported a similar penta-coordinated pyridyl-amine cobalt complex (HEC 13),¹¹⁹ able to reduce protons in neutral pH. Cyclic voltammetry experiments of HEC 13 in pH 7 phosphate buffer showed two waves assigned to the $\text{Co}^{\text{III/II}}$ and $\text{Co}^{\text{II/I}}$ couples before the onset of the catalysis at -1.2 V vs NHE. HEC 13 is reported to catalyze proton reduction with a 99% Faradaic efficiency and more than 300 TON in 1 hour of controlled potential electrolysis at -1.4 V vs NHE in pH 7 on a Hg pool electrode.

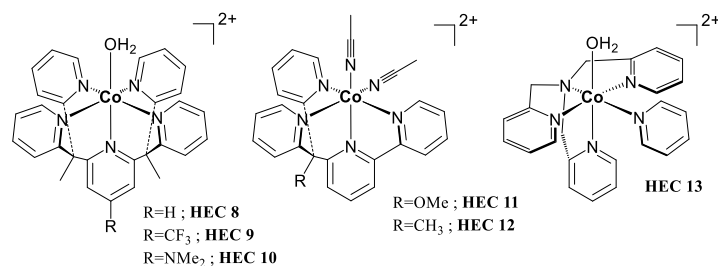


Figure 17: Structures of selected cobalt polypyridine complexes actives for HER.

1.5 Oxygen Evolution Reaction

The formation of one molecule of O_2 from water (eq. 2) requires the transfer of four electrons, the breakage of four O-H bonds and the formation of the double O=O bond. Due to its complexity, water oxidation half reaction is nowadays, the bottleneck process for developing artificial photosynthesis devices. OER is a thermodynamically demanding reaction ($E^0 = 1.23\text{ V}$ vs NHE at $\text{pH} = 0$) with a high associated kinetic barrier. Thus, a catalyst that can carry out the OER must be able to accumulate four oxidative charges and be stable in water at high oxidation states.¹²⁰

As already pointed out before for the HER, in order to design better catalyst it's very important to understand the mechanism of the reaction during the formation of O_2 . Indeed, the OER mechanism has been studied extensively

General Introduction

using kinetic studies, spectroscopic techniques, labeling experiments and DFT calculations in order to understand every step involved in the process. Two different mechanisms have been proposed for the O-O bond formation: interaction between two metal oxo M-O groups (I2M) and water nucleophilic attack (WNA) (Figure 18).^{121,122} In WNA, one water molecule acts as a nucleophile and attacks the electrophilic M-O species, facilitating the breakage of the M-O bond and the formation of M-O-OH (hydroperoxido species) and releasing O₂ after a posterior oxidation. In the I2M mechanism, two M-O units interact to form the O-O bond. In both cases, the formation of the O-O bond is the rate-determining step.

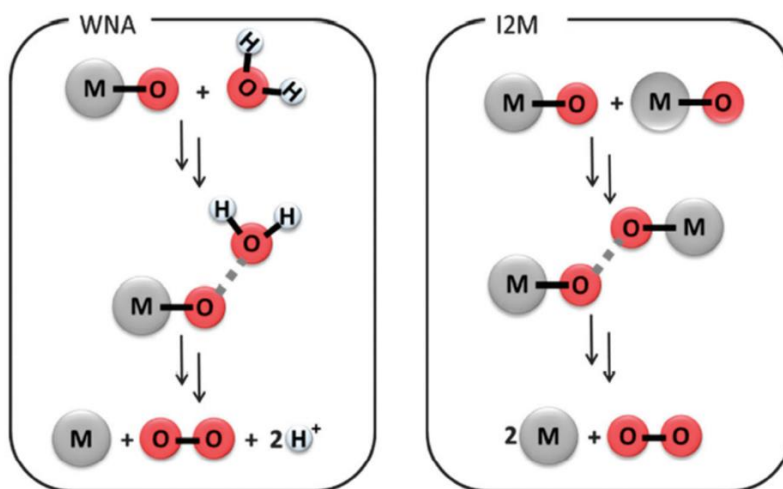


Figure 18: Proposed mechanistic pathways for O-O bond formation in oxygen evolution catalysis through metal-oxo M=O group. WNA: Water nucleophilic attack. I2M: interaction between two metal-oxo groups.

There's a plethora of heterogeneous and homogeneous catalysts that have been reported in the literature that can perform OER in many different forms: metal oxides films and nanoparticles,^{23,54,123-125} POMs,¹²⁶ MOFs¹²⁷⁻¹³⁰ and molecular catalysts.^{24,121,122,131-134} However, only a brief description of a ruthenium-based molecular catalyst will be discussed in this section.

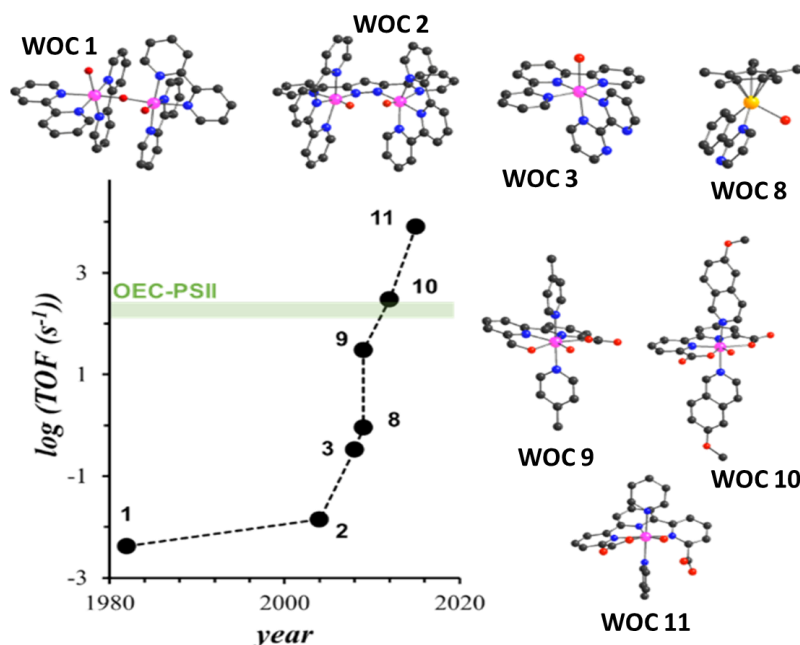


Figure 19. Evolution of the TOF of molecular Ru WOC in the last 40 years. The green line indicates the TOF of the oxygen evolution center present in the photosystem II. Color code: C, grey; Ru, pink; N, blue; O, red; Ir, orange.

Ruthenium is a second row transition metal with electronic configuration $[\text{Kr}] 4d^7 5s^1$, having access to a widely range of oxidation states, from +8 in RuO_4 to -2 in $[\text{Ru}(\text{CO})_4]^{2-}$ corresponding to d^0 and d^{10} electronic configuration. High oxidation states can be stabilized by using polypyridyl ligands, making molecular ruthenium complexes a good candidate as catalysts for oxygen evolution reaction. Figure 19 shows the evolution of ruthenium-based water oxidation catalysts, where the $\log(\text{TOF})$ of these catalysts is plotted versus year of it publication. The first example in the literature was a dinuclear Ru-complex WOC1, known as blue dimer, published by Meyer *et al.* in 1980's.^{135,136} In the last 10 years chemists achieved great improvements in the field, increasing more than 4 orders of magnitude the rate for water oxidation reaction (TOF) beating OEC from the natural photosystem II. The best WOC reported to date is the complex $[\text{Ru}(\text{tda})(\text{py})_2]$ (where tda is [2,2':6',2''-terpyridine]-6,6''-dicarboxylato and py is pyridine), WOC11 in Figure 19) that was published by our group in 2015.¹³⁴ The main characteristic of this catalyst

General Introduction

is that the Ru center is seven-coordinated at oxidation state IV, leaving one dangling carboxylate group in the second coordination sphere that assists the WNA step, lowering the activation free energy that leads to O-O bond formation. This catalyst have the impressive TOF of 8000s^{-1} calculated by foot of the wave analysis, the highest value reported until now.



1.6 Molecular (photo)electrodes

The study of catalysts in homogenous phase is very convenient due to all the available techniques to characterize intermediate species (specially spectroscopic techniques) that allow the researchers to study and get insights in the reaction mechanisms of a given molecular catalyst. This valuable information makes possible to correlate the structure and the catalytic activity and thus design new molecular catalysts more robust, efficient and fast. However, the applicability of homogeneous catalysts in photoelectrochemical cell for water splitting is null. For a solid state device is necessary to immobilize the molecular catalysts on the surface of the (photo)electrode by modifying the ligand scaffolds with appropriate functional groups that allow to attach the catalyst on the surface without changing its intrinsic activity. Several functional groups have been used to follow this strategy depending on the nature of the (photo)electrode material (metal, metal oxides, graphitic structures, etc.). In Figure 20 the most common functional groups used for this propose are shown.¹³⁷ Among them, phosphonates (a) and carboxylates (b) are the most extensively used linkages, although their stability in aqueous conditions is very poor. That is why the use of pyrene groups (e) has been recently taken as a good alternative to anchor molecular catalysts on graphitic type of substrates via π -stacking interactions. Another strategy is using diazonium salts (f) to make new C-C bonds on carbon surfaces.

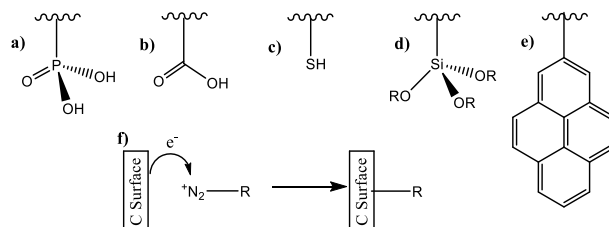


Figure 20. Different binding moieties to link catalyst on electrodes surfaces: a) phosphonic acid, b) carboxylic acid, c) thiol, d) silane, e) pyrene, f) diazonium salt.

There are many examples in the literature that use heterogeneous catalysts for HER and OER, but only few examples of (photo)electrodes with immobilized molecular catalysts while is true that the interest in this field was growing during the last decade.¹³⁸

Reisner and coworkers reported a modified HEC 3 that features a doubly phosphonated propanediyl bridgehead in the equatorial diimine-dioxime ligand and immobilized it onto meso-ITO and meso-FTO electrodes.¹³⁹ The double linkage guarantee a strong attachment of the catalyst on the metal oxide surface. The meso-FTO electrode showed a 10-14 TON (based on surface coverage of the molecular catalysts, that was estimated *ca.* $\Gamma = 1.50 \cdot 10^{-7} \text{ mol} \cdot \text{cm}^{-2}$) under controlled potential electrolysis at -0.7 V vs NHE during 12 hours in pH 7. Later, the same group reported a p-type silicon protected by mesoporous TiO_2 . The protective layer also increase the surface area allowing to load more catalyst, which was functionalized by modified DuBois catalysts with phosphonate moieties. The resulting photocathode was able to perform 1000 TON in 24 hours in pH 4.5 acetate buffer at 0 V vs RHE under 1 sun illumination.¹⁴⁰ Moore and Sharp also immobilize Dubois catalysts onto p-type Si and GaP wafers.¹⁴¹ Another molecular photocathode electrode reported by Moore *et al.* consisted in inducing the photopolymerization of 4-vinylpyridine with UV light on GaP wafers.¹⁴² Covering the semiconductor surface with this approach provides a polymer chain with multiple pyridine moieties that later on were used to link the molecular HEC (in this case of the family of cobaloximes). Under 1 sun illumination, this photocathode reached $2.4 \text{ mA} \cdot \text{cm}^{-2}$ at +310 mV before the thermodynamic H^+/H_2 potential. One withdrawal of this anchoring system is that the molecular catalysts releases its

General Introduction

axial ligands (pyridine) during the catalytic cycle (Co^{I} species tend to show a square planar geometry), resulting in a decrease in the catalytic current.



Artero *et al.* reported a molecular electrode by decorating Multi-Wall Carbon Nanotubes (MWCNT) with poly-4-(2-aminoethyl)phenylene by electroreduction of its aryldiazonium salt precursor, and later a modified cobaloxime was attached covalently to the MWCNT through amide linkages generated with the reaction of the immobilized amines in MWCNT and the activated esters in the Co complex (Figure 21, top).⁶¹ With a surface coverage of the molecular catalyst of $ca. 4.5 \times 10^{-9} \text{ mol} \cdot \text{cm}^{-2}$ these electrodes featured 55000 TON at pH 4.5 acetate buffer for 7 hours at -0.59 V vs RHE. Using the similar anchoring approach, the same group linked successfully the Ni DuBois catalyst on MWCNT capable to reduce protons to molecular hydrogen with very low overpotential (20mV) in pH 0 (Figure 21, middle).¹⁴³ The prepared electrode was able to held controlled potential electrolysis at -0.3 V vs NHE for 10 hours without degradation, reaching 100000 TON (according to the catalyst surface coverage of $ca. 1.5 \cdot 10^{-9} \text{ mols} \cdot \text{cm}^{-2}$).

Our group also reported a molecular electrode by dropcasting a dispersion of carbon nanotubes (CNT) decorated with $[\text{Ru}(\text{tda})(\text{L})_2]$ complex (where L is 4-(pyren-1-yl)pyridine), a derivative of WOC11 in Figure 19.¹⁴⁴ The catalyst was anchored onto the CNT surface by π -stacking due to the pyrene moiety of the axial ligand (L). The electrodes prepared with these catalysts exhibit the stunning TON of 10^6 in pH 7 at 1.45 V vs NHE without any sign of degradation. The same catalyst attached to CNT was used as WOC in a n-type Si photoanode protected by TiO_2 and sputtered carbon, reaching $1 \text{ mA} \cdot \text{cm}^{-2}$ in pH 7 at 1.07 V vs NHE (Figure 21, bottom).¹⁴⁵ Another molecular photoanode was reported by Wu and coworkers, where they use a n-type BiVO_4 photoanode functionalized with a Co^{III} -porphyrin.¹⁴⁶ The molecular catalyst was attached by a covalent bond between the $-\text{COOH}$ moieties and the Al_2O_3 protective layer. This modification enhanced the photocurrent at the thermodynamic potential, reaching almost $2 \text{ mA} \cdot \text{cm}^{-2}$ in pH 6.8 phosphate buffer under 1 sun illumination. Controlled potencial electrolysis for 4 hours at 1.4 V vs RHE revealed a Faradaic yield of 80%. However, the true molecular nature of the real catalyst was never proven.

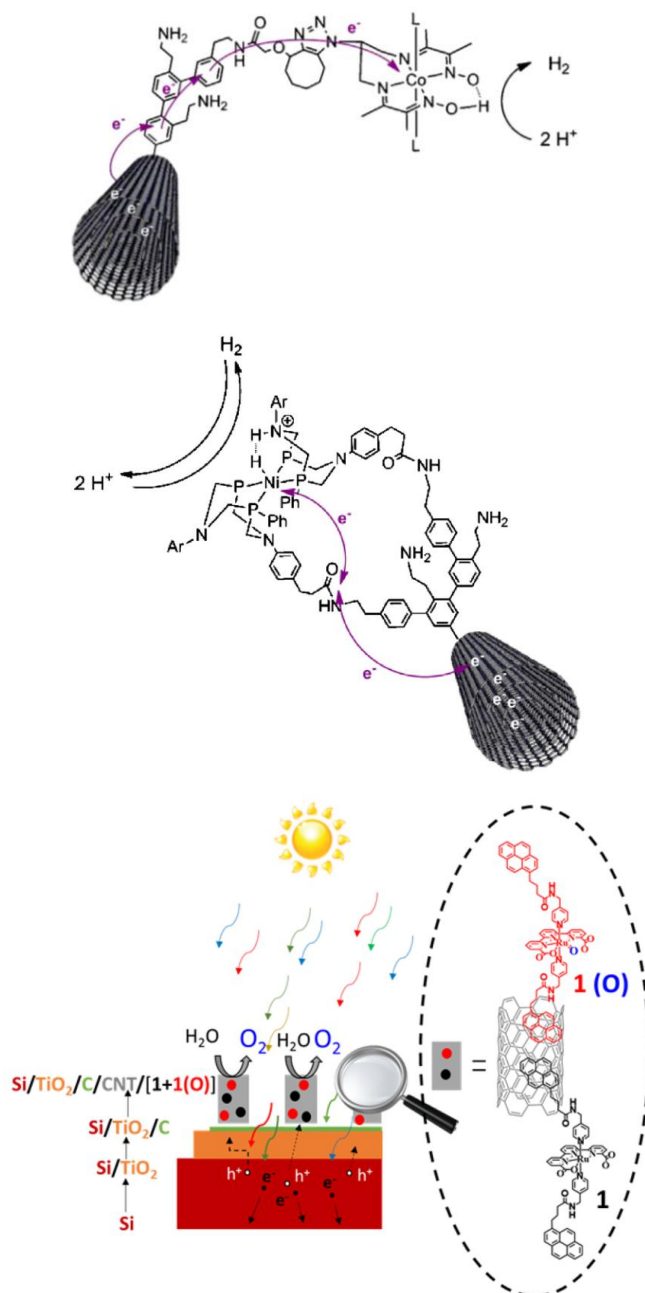



Figure 21. Architecture of relevant molecular (photo)electrodes reported in the literature. **Top:** Covalently attached cobaloxime HEC derivative on MWCNT.⁶¹ **Middle:** Covalently attached Ni DuBois HEC derivative on MWCNT.¹⁴³ **Bottom:** Molecular catalyst derived from WOC11 attached by π - π stacking to a MWCNT on a n-Si/TiO₂/C photoanode.¹⁴⁵

General Introduction


1.7 References

- 
- (1) Gupta, C. L. Role of Renewable Energy Technologies in Generating Sustainable Livelihoods. *Renew. Sustain. Energy Rev.* **2003**, *7* (2), 155–174. [https://doi.org/10.1016/S1364-0321\(03\)00006-6](https://doi.org/10.1016/S1364-0321(03)00006-6).
 - (2) Bernstein, L.; Bosch, P.; Canziani, O.; Chen, Z.; Christ, R.; Davidson, O.; Hare, W.; Huq, S.; Karoly, D.; Kattsov, V.; et al. *Climate Change 2007 - IPCC Synthesis Report - A Report of the Intergovernmental Panel on Climate Change*; 2007. <https://doi.org/10.1256/004316502320517344>.
 - (3) IEA. *Global Energy & CO₂ Status Report*; 2018.
 - (4) Masson-Delmotte, V.; Zhai, P.; Pörtner, H.-O.; Roberts, D.; Skea, J.; Shukla, P. R.; Pirani, A.; Moufouma-Okia, W.; Péan, C.; Pidcock, R.; et al. *Global Warming of 1.5°C An IPCC Special Report*; 2018; Vol. 265.
 - (5) BP Statistical Review of World Energy. *Statistical Review of World Energy June 2018*; BP p.l.c., 1 St James's Square, London, SW1Y 4PD, UK, 2018.
 - (6) Grossmann, W. D.; Grossmann, I.; Steininger, K. W. Solar Electricity Generation across Large Geographic Areas, Part II: A Pan-American Energy System Based on Solar. *Renew. Sustain. Energy Rev.* **2014**, *32*, 983–993. <https://doi.org/10.1016/j.rser.2014.01.003>.
 - (7) Nathan S. Lewis. Research Opportunities to Advance Solar Energy Utilization. *Science* (80-.). **2016**, *351* (6271), 353–364. <https://doi.org/10.1126/science.aad1920.22>.
 - (8) Nitta, N.; Wu, F.; Lee, J. T.; Yushin, G. Li-Ion Battery Materials: Present and Future. *Mater. Today* **2015**, *18* (5), 252–264. <https://doi.org/10.1016/j.mattod.2014.10.040>.
 - (9) UNDP. *World Energy Assessment: Energy and the Challanhe of Sustainability*; United Nations Development Programme Bureau for Development Policy One United Nations Plaza New York, NY 10017, 2000. <https://doi.org/10.2105/ajph.64.12.1166-b>.
 - (10) McEvoy, J. P.; Brudvig, G. W. Water-Splitting Chemistry of Photosystem II. *Chem. Rev.* **2006**, *106* (11), 4455–4483. <https://doi.org/10.1021/cr0204294>.
 - (11) Romain, S.; Vigara, L.; Llobet, A. Oxygen-Oxygen Bond Formation Pathways Promoted by Ruthenium Complexes. *Acc. Chem. Res.* **2009**, *42* (12), 1944–1953. <https://doi.org/10.1021/ar900240w>.
 - (12) Kärkäs, M. D.; Verho, O.; Johnston, E. V.; Åkermark, B. Artificial Photosynthesis: Molecular Systems for Catalytic Water Oxidation. *Chem. Rev.* **2014**, *114* (24), 11863–12001. <https://doi.org/10.1021/cr400572f>.

- (13) Nelson, N.; Ben-Shem, A. The Complex Architecture of Oxygenic Photosynthesis. *Nat. Rev. Mol. Cell Biol.* **2004**, *5* (12), 971–982. <https://doi.org/10.1038/nrm1525>.
- (14) Suga, M.; Akita, F.; Hirata, K.; Ueno, G.; Murakami, H.; Nakajima, Y.; Shimizu, T.; Yamashita, K.; Yamamoto, M.; Ago, H.; et al. Native Structure of Photosystem II at 1.95Å^o Resolution Viewed by Femtosecond X-Ray Pulses. *Nature* **2015**, *517* (7532), 99–103. <https://doi.org/10.1038/nature13991>.
- (15) Umena, Y.; Kawakami, K.; Shen, J. R.; Kamiya, N. Crystal Structure of Oxygen-Evolving Photosystem II at a Resolution of 1.9Å. *Nature* **2011**, *473* (7345), 55–60. <https://doi.org/10.1038/nature09913>.
- (16) Glöckner, C.; Kern, J.; Broser, M.; Zouni, A.; Yachandra, V.; Yano, J. Structural Changes of the Oxygen-Evolving Complex in Photosystem II during the Catalytic Cycle. *J. Biol. Chem.* **2013**, *288* (31), 22607–22620. <https://doi.org/10.1074/jbc.M113.476622>.
- (17) Blomberg, M. R. A.; Borowski, T.; Himo, F.; Liao, R.-Z.; Siegbahn, P. E. M. Quantum Chemical Studies of Mechanisms for Metalloenzymes. *Chem. Rev.* **2014**, *114* (7), 3601–3658. <https://doi.org/10.1021/cr400388t>.
- (18) Appel, A. M.; Bercaw, J. E.; Bocarsly, A. B.; Dobbek, H.; DuBois, D. L.; Dupuis, M.; Ferry, J. G.; Fujita, E.; Hille, R.; Kenis, P. J. A.; et al. Frontiers, Opportunities, and Challenges in Biochemical and Chemical Catalysis of CO₂ Fixation. *Chem. Rev.* **2013**, *113* (8), 6621–6658. <https://doi.org/10.1021/cr300463y>.
- (19) Schrock, R. R. Reduction of Dinitrogen. *Proc. Natl. Acad. Sci.* **2006**, *103* (46), 17087–17087. <https://doi.org/10.1073/pnas.0603633103>.
- (20) Murphy, A.; Barnes, P.; Randeniya, L.; Plumb, I.; Grey, I.; Horne, M.; Glasscock, J. Efficiency of Solar Water Splitting Using Semiconductor Electrodes. *Int. J. Hydrogen Energy* **2006**, *31* (14), 1999–2017. <https://doi.org/10.1016/j.ijhydene.2006.01.014>.
- (21) Bard, A. J.; Faulkner, L. R. *Electrochemical Methods, Fundamentals and Applications*, 2nd ed.; Wiley, 2001; Vol. 60. <https://doi.org/10.1021/ed060pa25.1>.
- (22) Faber, M. S.; Jin, S. Earth-Abundant Inorganic Electrocatalysts and Their Nanostructures for Energy Conversion Applications. *Energy Environ. Sci.* **2014**, *7* (11), 3519–3542. <https://doi.org/10.1039/c4ee01760a>.
- (23) Montoya, J. H.; Seitz, L. C.; Chakthranont, P.; Vojvodic, A.; Jaramillo, T. F.; Nørskov, J. K. Materials for Solar Fuels and Chemicals. *Nat. Mater.* **2016**, *16* (1), 70–81. <https://doi.org/10.1038/nmat4778>.
- (24) Berardi, S.; Drouet, S.; Francàs, L.; Gimbert-Suriñach, C.; Guttentag, M.;



General Introduction

- 
- Richmond, C.; Stoll, T.; Llobet, A. Molecular Artificial Photosynthesis. *Chem. Soc. Rev.* **2014**, *43* (22), 7501–7519. <https://doi.org/10.1039/c3cs60405e>.
- (25) McKone, J. R.; Lewis, N. S.; Gray, H. B. Will Solar-Driven Water-Splitting Devices See the Light of Day? *Chem. Mater.* **2014**, *26* (1), 407–414. <https://doi.org/10.1021/cm4021518>.
- (26) Bonke, S. A.; Wiechen, M.; MacFarlane, D. R.; Spiccia, L. Renewable Fuels from Concentrated Solar Power: Towards Practical Artificial Photosynthesis. *Energy Environ. Sci.* **2015**, *8* (9), 2791–2796. <https://doi.org/10.1039/c5ee02214b>.
- (27) Jia, J.; Seitz, L. C.; Benck, J. D.; Huo, Y.; Chen, Y.; Ng, J. W. D.; Bilir, T.; Harris, J. S.; Jaramillo, T. F. Solar Water Splitting by Photovoltaic-Electrolysis with a Solar-to-Hydrogen Efficiency over 30%. *Nat. Commun.* **2016**, *7* (May), 1–6. <https://doi.org/10.1038/ncomms13237>.
- (28) Fabian, D. M.; Hu, S.; Singh, N.; Houle, F. A.; Hisatomi, T.; Domen, K.; Osterloh, F. E.; Ardo, S. Particle Suspension Reactors and Materials for Solar-Driven Water Splitting. *Energy Environ. Sci.* **2015**, *8* (10), 2825–2850. <https://doi.org/10.1039/c5ee01434d>.
- (29) Hisatomi, T.; Domen, K. Introductory Lecture: Sunlight-Driven Water Splitting and Carbon Dioxide Reduction by Heterogeneous Semiconductor Systems as Key Processes in Artificial Photosynthesis. *Faraday Discuss.* **2017**, *198*, 11–35. <https://doi.org/10.1039/c6fd00221h>.
- (30) Lin, C.-Y.; Lai, Y.-H.; Mersch, D.; Reisner, E. Cu₂O/NiOx Nanocomposite as an Inexpensive Photocathode in Photoelectrochemical Water Splitting. *Chem. Sci.* **2012**, *3* (12), 3482. <https://doi.org/10.1039/c2sc20874a>.
- (31) Borno, P.; Abdi, F. F.; Tilley, S. D.; Dam, B.; van de Krol, R.; Graetzel, M.; Sivula, K. A Bismuth Vanadate–Cuprous Oxide Tandem Cell for Overall Solar Water Splitting. *J. Phys. Chem. C* **2014**, *118* (30), 16959–16966. <https://doi.org/10.1021/jp500441h>.
- (32) Sze, S. M.; Ng, K. K. *Physics of Semiconductor Devices*, Third Edit.; John Wiley & Sons, Inc.: Hoboken, New Jersey, 2007.
- (33) Chen, Z.; Dinh, H. N.; Miller, E. *Photoelectrochemical Water Splitting Standards, Experimental Methods, and Protocols*; 2013. <https://doi.org/10.2533/chimia.2007.815>.
- (34) Zhang, Z.; Wang, P. Highly Stable Copper Oxide Composite as an Effective Photocathode for Water Splitting via a Facile Electrochemical Synthesis Strategy. *J. Mater. Chem.* **2012**, *22* (6), 2456–2464. <https://doi.org/10.1039/C1JM14478B>.
- (35) Paracchino, A.; Laporte, V.; Sivula, K.; Grätzel, M.; Thimsen, E. Highly

- Active Oxide Photocathode for Photoelectrochemical Water Reduction. *Nat. Mater.* **2011**, *10* (6), 456–461. <https://doi.org/10.1038/nmat3017>.
- (36) Morales-Guio, C. G.; Liardet, L.; Mayer, M. T.; Tilley, S. D.; Grätzel, M.; Hu, X. Photoelectrochemical Hydrogen Production in Alkaline Solutions Using Cu₂O Coated with Earth-Abundant Hydrogen Evolution Catalysts. *Angew. Chemie - Int. Ed.* **2015**, *54* (2), 664–667. <https://doi.org/10.1002/anie.201410569>.
- (37) Neuschitzer, M.; Sanchez, Y.; Olar, T.; Thersleff, T.; Lopez-Marino, S.; Oliva, F.; Espindola-Rodriguez, M.; Xie, H.; Placidi, M.; Izquierdo-Roca, V.; et al. Complex Surface Chemistry of Kesterites: Cu/Zn Reordering after Low Temperature Postdeposition Annealing and Its Role in High Performance Devices. *Chem. Mater.* **2015**, *27* (15), 5279–5287. <https://doi.org/10.1021/acs.chemmater.5b01473>.
- (38) Neuschitzer, M.; Moises, E.-R.; Guc, M.; Prieto, J.; Giraldo, S.; Forbes, I.; Alejandro, P.-R.; Saucedo, E. Revealing the Beneficial Effects of Ge Doping on Cu₂ZnSnSe₄ Thin Film Solar Cells. *J Mater Chem* **2018**, *6* (25), 11759–11772. <https://doi.org/10.1039/C8TA02551G>.
- (39) Giraldo, S.; Neuschitzer, M.; Thersleff, T.; L opez-Marino, S.; S anchez, Y.; Xie, H.; Colina, M.; Placidi, M.; Pistor, P.; Izquierdo-Roca, V.; et al. Large Efficiency Improvement in Cu₂ZnSnSe₄ Solar Cells by Introducing a Superficial Ge Nanolayer. *Adv. Energy Mater.* **2015**, *5* (21), 1501070. <https://doi.org/10.1002/aenm.201501070>.
- (40) Neuschitzer, M.; Sanchez, Y.; Olar, T.; Thersleff, T.; Lopez-Marino, S.; Oliva, F.; Espindola-Rodriguez, M.; Xie, H.; Placidi, M.; Izquierdo-Roca, V.; et al. Complex Surface Chemistry of Kesterites: Cu/Zn Reordering after Low Temperature Postdeposition Annealing and Its Role in High Performance Devices. *Chem. Mater.* **2015**, *27* (15), 5279–5287. <https://doi.org/10.1021/acs.chemmater.5b01473>.
- (41) Yokoyama, D.; Minegishi, T.; Maeda, K.; Katayama, M.; Kubota, J.; Yamada, A.; Konagai, M.; Domen, K. Photoelectrochemical Water Splitting Using a Cu(In,Ga)Se₂ Thin Film. *Electrochem. commun.* **2010**, *12* (6), 851–853. <https://doi.org/10.1016/j.elecom.2010.04.004>.
- (42) Yokoyama, D.; Minegishi, T.; Jimbo, K.; Hisatomi, T.; Ma, G.; Katayama, M.; Kubota, J.; Katagiri, H.; Domen, K. H₂ Evolution from Water on Modified Cu₂ZnSnS₄ Photoelectrode under Solar Light. *Appl. Phys. Express* **2010**, *3* (10), 2–4. <https://doi.org/10.1143/APEX.3.101202>.
- (43) Kudo, A.; Ueda, K.; Kato, H.; Mikami, I. Photocatalytic O₂ Evolution under Visible Light Irradiation on BiVO₄ in Aqueous AgNO₃ Solution. *Catal. Letters* **1998**, *53* (3/4), 229–230. <https://doi.org/10.1023/A:1019034728816>.
- (44) Liang, Y.; Tsubota, T.; Mooij, L. P. A.; van de Krol, R. Highly Improved Quantum Efficiencies for Thin Film BiVO₄ Photoanodes. *J. Phys. Chem. C*



General Introduction

- 2011**, *115* (35), 17594–17598. <https://doi.org/10.1021/jp203004v>.
- (45) Luo, W.; Yang, Z.; Li, Z.; Zhang, J.; Liu, J.; Zhao, Z.; Wang, Z.; Yan, S.; Yu, T.; Zou, Z. Solar Hydrogen Generation from Seawater with a Modified BiVO₄ Photoanode. *Energy Environ. Sci.* **2011**, *4* (10), 4046–4051. <https://doi.org/10.1039/c1ee01812d>.
- (46) Hong, S. J.; Lee, S.; Jang, J. S.; Lee, J. S. Heterojunction BiVO₄/WO₃ Electrodes for Enhanced Photoactivity of Water Oxidation. *Energy Environ. Sci.* **2011**, *4* (5), 1781. <https://doi.org/10.1039/c0ee00743a>.
- (47) Pilli, S. K.; Furtak, T. E.; Brown, L. D.; Deutsch, T. G.; Turner, J. A.; Herring, A. M. Cobalt-Phosphate (Co-Pi) Catalyst Modified Mo-Doped BiVO₄ Photoelectrodes for Solar Water Oxidation. *Energy Environ. Sci.* **2011**, *4* (12), 5028. <https://doi.org/10.1039/c1ee02444b>.
- (48) Shi, X.; Choi, I. Y.; Zhang, K.; Kwon, J.; Kim, D. Y.; Lee, J. K.; Oh, S. H.; Kim, J. K.; Park, J. H. Efficient Photoelectrochemical Hydrogen Production from Bismuth Vanadate-Decorated Tungsten Trioxide Helix Nanostructures. *Nat. Commun.* **2014**, *5* (1), 4775. <https://doi.org/10.1038/ncomms5775>.
- (49) Gordon, R. B.; Bertram, M.; Graedel, T. E. Metal Stocks and Sustainability. *Proc. Natl. Acad. Sci.* **2006**, *103* (5), 1209–1214. <https://doi.org/10.1073/pnas.0509498103>.
- (50) Conway, B. E.; Tilak, B. V. Interfacial Processes Involving Electrocatalytic Evolution and Oxidation of H₂, and the Role of Chemisorbed H. *Electrochim. Acta* **2002**, *47* (22-23), 3571–3594. [https://doi.org/10.1016/S0013-4686\(02\)00329-8](https://doi.org/10.1016/S0013-4686(02)00329-8).
- (51) Bockris, J. O.; Potter, E. C. The Mechanism of the Cathodic Hydrogen Evolution Reaction. *J. Electrochem. Soc.* **1952**, *99* (4), 169. <https://doi.org/10.1149/1.2779692>.
- (52) Nørskov, J. K.; Bligaard, T.; Logadottir, A.; Kitchin, J. R.; Chen, J. G.; Pandelov, S.; Stimming, U. Trends in the Exchange Current for Hydrogen Evolution. *J. Electrochem. Soc.* **2005**, *152* (3), J23. <https://doi.org/10.1149/1.1856988>.
- (53) Nørskov, J. K.; Bligaard, T.; Logadottir, A.; Kitchin, J. R.; Chen, J. G.; Pandelov, S.; Stimming, U. Response to “Comment on ‘Trends in the Exchange Current for Hydrogen Evolution’ [J. Electrochem. Soc., 152, J23 (2005)].” *J. Electrochem. Soc.* **2006**, *153* (12), L33. <https://doi.org/10.1149/1.2358292>.
- (54) McCrory, C. C. L.; Jung, S.; Ferrer, I. M.; Chatman, S. M.; Peters, J. C.; Jaramillo, T. F. Benchmarking Hydrogen Evolving Reaction and Oxygen Evolving Reaction Electrocatalysts for Solar Water Splitting Devices. *J. Am. Chem. Soc.* **2015**, *137* (13), 4347–4357. <https://doi.org/10.1021/ja510442p>.

- (55) Frey, M. Hydrogenases: Hydrogen-Activating Enzymes. *ChemBioChem* **2002**, 3 (2-3), 153–160. [https://doi.org/10.1002/1439-7633\(20020301\)3:2/3<153::AID-CBIC153>3.0.CO;2-B](https://doi.org/10.1002/1439-7633(20020301)3:2/3<153::AID-CBIC153>3.0.CO;2-B).
- (56) Evans, D. J.; Pickett, C. J. Chemistry and the Hydrogenases. *Chem. Soc. Rev.* **2003**, 32 (5), 268. <https://doi.org/10.1039/b201317g>.
- (57) Armstrong, F. A. Hydrogenases: Active Site Puzzles and Progress. *Curr. Opin. Chem. Biol.* **2004**, 8 (2), 133–140. <https://doi.org/10.1016/j.cbpa.2004.02.004>.
- (58) Lubitz, W.; Ogata, H.; Rüdiger, O.; Reijerse, E. Hydrogenases. *Chem. Rev.* **2014**, 114 (8), 4081–4148. <https://doi.org/10.1021/cr4005814>.
- (59) Peters, J. W.; Schut, G. J.; Boyd, E. S.; Mulder, D. W.; Shepard, E. M.; Broderick, J. B.; King, P. W.; Adams, M. W. W. [FeFe]- and [NiFe]-Hydrogenase Diversity, Mechanism, and Maturation. *Biochim. Biophys. Acta - Mol. Cell Res.* **2015**, 1853 (6), 1350–1369. <https://doi.org/10.1016/j.bbamcr.2014.11.021>.
- (60) Fontecilla-Camps, J. C.; Volbeda, A.; Cavazza, C.; Nicolet, Y. Structure/Function Relationships of [NiFe]- and [FeFe]-Hydrogenases. *Chem. Rev.* **2007**, 107 (10), 4273–4303. <https://doi.org/10.1021/cr050195z>.
- (61) Baffert, C.; Artero, V.; Fontecave, M. Cobaloximes as Functional Models for Hydrogenases. 2. Proton Electroreduction Catalyzed by difluoroborylbis(dimethylglyoximate)cobalt(II) Complexes in Organic Media. *Inorg. Chem.* **2007**, 46 (5), 1817–1824. <https://doi.org/10.1021/ic061625m>.
- (62) Muckerman, J. T.; Fujita, E. Theoretical Studies of the Mechanism of Catalytic Hydrogen Production by a Cobaloxime. *Chem. Commun.* **2011**, 47 (46), 12456–12458. <https://doi.org/10.1039/c1cc15330g>.
- (63) Dempsey, J. L.; Winkler, J. R.; Gray, H. B. Mechanism of H₂ Evolution from a Photogenerated Hydridocobaloxime. *J. Am. Chem. Soc.* **2010**, 132 (47), 16774–16776. <https://doi.org/10.1021/ja109351h>.
- (64) Solis, B. H.; Hammes-Schiffer, S. Substituent Effects on Cobalt Diglyoxime Catalysts for Hydrogen Evolution. *J. Am. Chem. Soc.* **2011**, 133 (47), 19036–19039. <https://doi.org/10.1021/ja208091e>.
- (65) Koelle, U.; Paul, S. Electrochemical Reduction of Protonated Cyclopentadienylcobalt Phosphine Complexes. *Inorg. Chem.* **1986**, 25 (16), 2689–2694. <https://doi.org/10.1021/ic00236a007>.
- (66) Bernhardt, P. V.; Jones, L. A. Electrochemistry of Macrocyclic Cobalt(III/II) Hexamines: Electrocatalytic Hydrogen Evolution in Aqueous Solution. *Inorg. Chem.* **1999**, 38 (22), 5086–5090. <https://doi.org/10.1021/ic981425d>.



General Introduction

- (67) Karunadasa, H. I.; Montalvo, E.; Sun, Y.; Majda, M.; Long, J. R.; Chang, C. J. A Molecular MoS₂ Edge Site Mimic for Catalytic Hydrogen Generation. *Science* (80-.). **2012**, 335 (6069), 698–702. <https://doi.org/10.1126/science.1215868>.
- (68) Wang, M.; Chen, L.; Sun, L. Recent Progress in Electrochemical Hydrogen Production with Earth-Abundant Metal Complexes as Catalysts. *Energy Environ. Sci.* **2012**, 5 (5), 6763–6778. <https://doi.org/10.1039/c2ee03309g>.
- (69) Thoi, V. S.; Sun, Y.; Long, J. R.; Chang, C. J. Complexes of Earth-Abundant Metals for Catalytic Electrochemical Hydrogen Generation under Aqueous Conditions. *Chem. Soc. Rev.* **2013**, 42 (6), 2388–2400. <https://doi.org/10.1039/c2cs35272a>.
- (70) He, Z.; Que, W. Molybdenum Disulfide Nanomaterials: Structures, Properties, Synthesis and Recent Progress on Hydrogen Evolution Reaction. *Appl. Mater. Today* **2016**, 3, 23–56. <https://doi.org/10.1016/j.apmt.2016.02.001>.
- (71) Kam, K. K.; Parkinson, B. A. Detailed Photocurrent Spectroscopy of the Semiconducting Group VIB Transition Metal Dichalcogenides. *J. Phys. Chem. Chem.* **1982**, 86 (4), 463–467. <https://doi.org/10.1021/j100393a010>.
- (72) Mak, K. F.; Lee, C.; Hone, J.; Shan, J.; Heinz, T. F. Atomically Thin MoS₂: A New Direct-Gap Semiconductor. *Phys. Rev. Lett.* **2010**, 105 (13), 2–5. <https://doi.org/10.1103/PhysRevLett.105.136805>.
- (73) Li, Y.; Wang, H.; Xie, L.; Liang, Y.; Hong, G.; Dai, H. MoS₂ Nanoparticles Grown on Graphene: An Advanced Catalyst for the Hydrogen Evolution Reaction. *J. Am. Chem. Soc.* **2011**, 133 (19), 7296–7299. <https://doi.org/10.1021/ja201269b>.
- (74) Chorkendorff, I.; Jørgensen, K. P.; Nielsen, J. H.; Hinnemann, B.; Moses, P. G.; Nørskov, J. K.; Horch, S.; Bonde, J. Biomimetic Hydrogen Evolution: MoS₂ Nanoparticles as Catalyst for Hydrogen Evolution. *J. Am. Chem. Soc.* **2005**, 127 (15), 5308–5309. <https://doi.org/10.1021/ja0504690>.
- (75) Chorkendorff, I.; Bonde, J.; Jørgensen, K. P.; Horch, S.; Jaramillo, T. F.; Nielsen, J. H. Identification of Active Edge Sites for Electrochemical H₂ Evolution from MoS₂ Nanocatalysts. *Science* (80-.). **2007**, 317 (5834), 100–102. <https://doi.org/10.1126/science.1141483>.
- (76) Yoosuk, B.; Kim, J. H.; Song, C.; Ngamcharussrivichai, C.; Prasassarakich, P. Highly Active MoS₂, CoMoS₂ and NiMoS₂ Unsupported Catalysts Prepared by Hydrothermal Synthesis for Hydrodesulfurization of 4,6-Dimethyldibenzothiophene. *Catal. Today* **2008**, 130 (1), 14–23. <https://doi.org/10.1016/j.cattod.2007.07.003>.
- (77) Coulier, L.; Beer, V. H. J. De; Veen, J. a R. Van; Niemantsverdriet, J. W. On the Formation of Cobalt – Molybdenum Sulfides in Silica-Supported

- Hydrotreating Model Catalysts. *Top. Catal.* **2000**, *13*, 99–108.
- (78) Shi, Y.; Wang, J.; Wang, C.; Zhai, T. T.; Bao, W. J.; Xu, J. J.; Xia, X. H.; Chen, H. Y. Hot Electron of Au Nanorods Activates the Electrocatalysis of Hydrogen Evolution on MoS₂ Nanosheets. *J. Am. Chem. Soc.* **2015**, *137* (23), 7365–7370. <https://doi.org/10.1021/jacs.5b01732>.
- (79) Chang, Y. H.; Lin, C. T.; Chen, T. Y.; Hsu, C. L.; Lee, Y. H.; Zhang, W.; Wei, K. H.; Li, L. J. Highly Efficient Electrocatalytic Hydrogen Production by MoS_x Grown on Graphene-Protected 3D Ni Foams. *Adv. Mater.* **2013**, *25* (5), 756–760. <https://doi.org/10.1002/adma.201202920>.
- (80) Chang, L.; Yang, H.; Fu, W.; Zhang, J.; Yu, Q.; Zhu, H.; Chen, J.; Wei, R.; Sui, Y.; Pang, X.; et al. Simple Synthesis of MoS₂ Inorganic Fullerene-like Nanomaterials from MoS₂ Amorphous Nanoparticles. *Mater. Res. Bull.* **2008**, *43* (8-9), 2427–2433. <https://doi.org/10.1016/j.materresbull.2007.07.043>.
- (81) Lukowski, M. A.; Daniel, A. S.; Meng, F.; Forticaux, A.; Li, L.; Jin, S. Enhanced Hydrogen Evolution Catalysis from Chemically Exfoliated Metallic MoS₂ Nanosheets. *J. Am. Chem. Soc.* **2013**, *135* (28), 10274–10277. <https://doi.org/10.1021/ja404523s>.
- (82) Laursen, A. B.; Kegnæs, S.; Dahl, S.; Chorkendorff, I. Molybdenum Sulfides—efficient and Viable Materials for Electro- and Photoelectrocatalytic Hydrogen Evolution. *Energy Environ. Sci.* **2012**, *5* (2), 5577. <https://doi.org/10.1039/c2ee02618j>.
- (83) Li, D. J.; Maiti, U. N.; Lim, J.; Choi, D. S.; Lee, W. J.; Oh, Y.; Lee, G. Y.; Kim, S. O. Molybdenum Sulfide/N-Doped CNT Forest Hybrid Catalysts for High-Performance Hydrogen Evolution Reaction. *Nano Lett.* **2014**, *14* (3), 1228–1233. <https://doi.org/10.1021/nl404108a>.
- (84) Yu, Y.; Huang, S.-Y.; Li, Y.; Steinmann, S. N.; Yang, W.; Cao, L. Layer-Dependent Electrocatalysis of MoS₂ for Hydrogen Evolution. *Nano Lett.* **2014**, *14* (2), 553–558. <https://doi.org/10.1021/nl403620g>.
- (85) Gao, G.; Sun, Q.; Du, A. Activating Catalytic Inert Basal Plane of Molybdenum Disulfide to Optimize Hydrogen Evolution Activity via Defect Doping and Strain Engineering. *J. Phys. Chem. C* **2016**, *120* (30), 16761–16766. <https://doi.org/10.1021/acs.jpcc.6b04692>.
- (86) Kibsgaard, J.; Lauritsen, J. V.; Lægsgaard, E.; Clausen, B. S.; Topsøe, H.; Besenbacher, F. Cluster–Support Interactions and Morphology of MoS₂ Nanoclusters in a Graphite-Supported Hydrotreating Model Catalyst. *J. Am. Chem. Soc.* **2006**, *128* (42), 13950–13958. <https://doi.org/10.1021/ja0651106>.
- (87) Ponomarev, E. A.; Hodes, G. Electrochemical Deposition of MoS₂ Thin Films by Reduction of Tetrathiomolybdate. *Thin Solid Films* **1996**, *280*, 186–



General Introduction

- 189.
- (88) Abu-Yaron, A.; Lévy-Clément, C.; Katty, A.; Bastide, S.; Tenne, R. Influence of the Electrochemical Deposition Parameters on the Microstructure of MoS₂ Thin Films. *Thin Solid Films* **2000**, *361*, 223–228. [https://doi.org/10.1016/S0040-6090\(99\)00838-X](https://doi.org/10.1016/S0040-6090(99)00838-X).
- (89) Dukstiene, N.; Kazancev, K.; Prosvicvas, I.; Guobiene, A. Electrodeposition of Mo-Se Thin Films from a Sulfamic Electrolyte. *J. Solid State Electrochem.* **2004**, *8* (5), 330–336. <https://doi.org/10.1007/s10008-003-0457-x>.
- (90) Merki, D.; Fierro, S.; Vrabel, H.; Hu, X. Amorphous Molybdenum Sulfide Films as Catalysts for Electrochemical Hydrogen Production in Water. *Chem. Sci.* **2011**, *2* (7), 1262–1267. <https://doi.org/10.1039/c1sc00117e>.
- (91) Merki, D.; Hu, X. Recent Developments of Molybdenum and Tungsten Sulfides as Hydrogen Evolution Catalysts. *Energy Environ. Sci.* **2011**, *4* (10), 3878–3888. <https://doi.org/10.1039/c1ee01970h>.
- (92) Vrabel, H.; Hu, X. Growth and Activation of an Amorphous Molybdenum Sulfide Hydrogen Evolving Catalyst. *ACS Catal.* **2013**, *3* (9), 2002–2011. <https://doi.org/10.1021/cs400441u>.
- (93) Morales-Guio, C. G.; Hu, X. Amorphous Molybdenum Sulfides as Hydrogen Evolution Catalysts. *Acc. Chem. Res.* **2014**, *47* (8), 2671–2681. <https://doi.org/10.1021/ar5002022>.
- (94) Dubouis, N.; Yang, C.; Beer, R.; Ries, L.; Voiry, D.; Grimaud, A. Interfacial Interactions as an Electrochemical Tool to Understand Mo-Based Catalysts for the Hydrogen Evolution Reaction. *ACS Catal.* **2018**, *8* (2), 828–836. <https://doi.org/10.1021/acscatal.7b03684>.
- (95) Radisavljevic, B.; Radenovic, A.; Brivio, J.; Giacometti, V.; Kis, A. Single-Layer MoS₂ Transistors. *Nat. Nanotechnol.* **2011**, *6* (3), 147–150. <https://doi.org/10.1038/nnano.2010.279>.
- (96) Huang, Y.; Nielsen, R. J.; Goddard, W. A.; Soriaga, M. P. The Reaction Mechanism with Free Energy Barriers for Electrochemical Dihydrogen Evolution on MoS₂. *J. Am. Chem. Soc.* **2015**, *137* (20), 6692–6698. <https://doi.org/10.1021/jacs.5b03329>.
- (97) Curtis, C. J.; Miedaner, A.; Ciancanelli, R.; Ellis, W. W.; Noll, B. C.; Rakowski DuBois, M.; DuBois, D. L. [Ni(Et₂PCH₂NMeCH₂PEt₂)₂]²⁺ as a Functional Model for Hydrogenases. *Inorg. Chem.* **2003**, *42* (1), 216–227. <https://doi.org/10.1021/ic020610v>.
- (98) Wilson, A. D.; Newell, R. H.; McNevin, M. J.; Muckerman, J. T.; DuBois, M. R.; DuBois, D. L. Hydrogen Oxidation and Production Using Nickel-Based Molecular Catalysts with Positioned Proton Relays. *J. Am. Chem. Soc.*

- 2006, 128 (1), 358–366. <https://doi.org/10.1021/ja056442y>.
- (99) Fraze, K.; Wilson, A. D.; Appel, A. M.; Rakowski DuBois, M.; DuBois, D. L. Thermodynamic Properties of the Ni–H Bond in Complexes of the Type [HNi(P₂RN₂R')₂](BF₄) and Evaluation of Factors That Control Catalytic Activity for Hydrogen Oxidation/Production. *Organometallics* **2007**, 26 (16), 3918–3924. <https://doi.org/10.1021/om070143v>.
- (100) Wilson, A. D.; Shoemaker, R. K.; Miedaner, A.; Muckerman, J. T.; DuBois, D. L.; DuBois, M. R. Nature of Hydrogen Interactions with Ni(II) Complexes Containing Cyclic Phosphine Ligands with Pendant Nitrogen Bases. *Proc. Natl. Acad. Sci.* **2007**, 104 (17), 6951–6956. <https://doi.org/10.1073/pnas.0608928104>.
- (101) Rakowski DuBois, M.; DuBois, D. L. The Roles of the First and Second Coordination Spheres in the Design of Molecular Catalysts for H₂ Production and Oxidation. *Chem. Soc. Rev.* **2009**, 38 (1), 62–72. <https://doi.org/10.1039/B801197B>.
- (102) Helm, M. L.; Stewart, M. P.; Bullock, R. M.; DuBois, M. R.; DuBois, D. L. A Synthetic Nickel Electrocatalyst with a Turnover Frequency Above 100,000 s⁻¹ for H₂ Production. *Science (80-.)*. **2011**, 333 (6044), 863–866. <https://doi.org/10.1126/science.1205864>.
- (103) Losse, S.; Vos, J. G.; Rau, S. Catalytic Hydrogen Production at Cobalt Centres. *Coord. Chem. Rev.* **2010**, 254 (21-22), 2492–2504. <https://doi.org/10.1016/j.ccr.2010.06.004>.
- (104) Artero, V.; Chavarot-Kerlidou, M.; Fontecave, M. Splitting Water with Cobalt. *Angew. Chemie - Int. Ed.* **2011**, 50 (32), 7238–7266. <https://doi.org/10.1002/anie.201007987>.
- (105) Fisher, B.; Eisenberg, R. Electrocatalytic Reduction of Carbon Dioxide by Using Macrocycles of Nickel and Cobalt. *J. Am. Chem. Soc.* **1980**, 102 (24), 7361–7363. <https://doi.org/10.1021/ja00544a035>.
- (106) Bigi, J. P.; Hanna, T. E.; Harman, W. H.; Chang, A.; Chang, C. J. Electrocatalytic Reduction of Protons to Hydrogen by a Water-Compatible Cobalt Polypyridyl Platform. *Chem. Commun.* **2010**, 46 (6), 958–960. <https://doi.org/10.1039/b915846d>.
- (107) Connolly, P.; Espenson, J. H. Cobalt-Catalyzed Evolution of Molecular Hydrogen. *Inorg. Chem.* **1986**, 25 (16), 2684–2688. <https://doi.org/10.1021/ic00236a006>.
- (108) McCrory, C. C. L.; Uyeda, C.; Peters, J. C. Electrocatalytic Hydrogen Evolution in Acidic Water with Molecular Cobalt Tetraazamacrocycles. *J. Am. Chem. Soc.* **2012**, 134 (6), 3164–3170. <https://doi.org/10.1021/ja210661k>.



General Introduction

- (109) Long, K. M.; Busch, D. H. Cobalt(II) Complexes of the Quadridentate Macrocycle 2,12-Dimethyl-3,7,11,17-tetraazabicyclo[11.3.1]heptadecan-1(17),2,11,13,15-Pentaene. **1970**, 9 (3).
- (110) Long, K. M.; Busch, D. H. Cobalt(III) Complexes of the Tetridentate Macrocycle 2, 12-Dimethyl-3, 7,11, 17-Tetraazabi-Cyclo(11.3.1)heptadecan-1(17), 2,11,13, 15-Pentaene. *J. Coord. Chem.* **1974**, 4 (2), 113–123. <https://doi.org/10.1080/00958977408075888>.
- (111) Leung, C.-F.; Chen, Y.-Z.; Yu, H.-Q.; Yiu, S.-M.; Ko, C.-C.; Lau, T.-C. Electro and Photocatalytic Hydrogen Generation in Acetonitrile and Aqueous Solutions by a Cobalt Macrocylic Schiff-Base Complex. *Int. J. Hydrogen Energy* **2011**, 36 (18), 11640–11645. <https://doi.org/10.1016/j.ijhydene.2011.06.062>.
- (112) Molton, F.; Fortage, J.; Deronzier, A.; Blackman, A. G.; Stoll, T.; Collomb, M.-N.; Varma, S.; Castillo, C. E. Efficient Photocatalytic Hydrogen Production in Water Using a Cobalt(iii) Tetraaza-Macrocylic Catalyst: Electrochemical Generation of the Low-Valent Co(i) Species and Its Reactivity toward Proton Reduction. *Phys. Chem. Chem. Phys.* **2013**, 15 (40), 17544. <https://doi.org/10.1039/c3cp52641k>.
- (113) Gueret, R.; Castillo, C. E.; Rebarz, M.; Thomas, F.; Hargrove, A.-A.; Pécaut, J.; Sliwa, M.; Fortage, J.; Collomb, M.-N. Cobalt(III) Tetraaza-Macrocylic Complexes as Efficient Catalyst for Photoinduced Hydrogen Production in Water: Theoretical Investigation of the Electronic Structure of the Reduced Species and Mechanistic Insight. *J. Photochem. Photobiol. B Biol.* **2015**, 152, 82–94. <https://doi.org/10.1016/j.jphotobiol.2015.04.010>.
- (114) Gimbert-Suriñach, C.; Albero, J.; Stoll, T.; Fortage, J.; Collomb, M.-N.; Deronzier, A.; Palomares, E.; Llobet, A. Efficient and Limiting Reactions in Aqueous Light-Induced Hydrogen Evolution Systems Using Molecular Catalysts and Quantum Dots. *J. Am. Chem. Soc.* **2014**, 136 (21), 7655–7661. <https://doi.org/10.1021/ja501489h>.
- (115) Sandroni, M.; Gueret, R.; Wegner, K. D.; Reiss, P.; Fortage, J.; Aldakov, D.; Collomb, M. N. Cadmium-Free CuInS₂/ZnS Quantum Dots as Efficient and Robust Photosensitizers in Combination with a Molecular Catalyst for Visible Light-Driven H₂ Production in Water. *Energy Environ. Sci.* **2018**, 11 (7), 1752–1761. <https://doi.org/10.1039/c8ee00120k>.
- (116) Gueret, R.; Poulard, L.; Oshinowo, M.; Chauvin, J.; Dahmane, M.; Dupeyre, G.; Lainé, P. P.; Fortage, J.; Collomb, M. N. Challenging the [Ru(bpy)₃]²⁺ Photosensitizer with a Triazatriangulenium Robust Organic Dye for Visible-Light-Driven Hydrogen Production in Water. *ACS Catal.* **2018**, 8 (5), 3792–3802. <https://doi.org/10.1021/acscatal.7b04000>.
- (117) Moonshiram, D.; Gimbert-Suriñach, C.; Guda, A.; Picon, A.; Lehmann, C. S.; Zhang, X.; Doumy, G.; March, A. M.; Benet-Buchholz, J.; Soldatov, A.; et al. Tracking the Structural and Electronic Configurations of a Cobalt



- Proton Reduction Catalyst in Water. *J. Am. Chem. Soc.* **2016**, *138* (33), 10586–10596. <https://doi.org/10.1021/jacs.6b05680>.
- (118) Sun, Y.; Bigi, J. P.; Piro, N. A.; Tang, M. L.; Long, J. R.; Chang, C. J. Molecular Cobalt Pentapyridine Catalysts for Generating Hydrogen from Water. *J. Am. Chem. Soc.* **2011**, *133* (24), 9212–9215. <https://doi.org/10.1021/ja202743r>.
- (119) Singh, W. M.; Baine, T.; Kudo, S.; Tian, S.; Ma, X. A. N.; Zhou, H.; Deyonker, N. J.; Pham, T. C.; Bollinger, J. C.; Baker, D. L.; et al. Electrocatalytic and Photocatalytic Hydrogen Production in Aqueous Solution by a Molecular Cobalt Complex. *Angew. Chemie - Int. Ed.* **2012**, *51* (24), 5941–5944. <https://doi.org/10.1002/anie.201200082>.
- (120) Inoue, H.; Shimada, T.; Kou, Y.; Nabetani, Y.; Masui, D.; Takagi, S.; Tachibana, H. The Water Oxidation Bottleneck in Artificial Photosynthesis: How Can We Get through It? An Alternative Route Involving a Two-Electron Process. *ChemSusChem* **2011**, *4* (2), 173–179. <https://doi.org/10.1002/cssc.201000385>.
- (121) Sala, X.; Maji, S.; Bofill, R.; García-Antón, J.; Escriche, L.; Llobet, A. Molecular Water Oxidation Mechanisms Followed by Transition Metals: State of the Art. *Acc. Chem. Res.* **2014**, *47* (2), 504–516. <https://doi.org/10.1021/ar400169p>.
- (122) Garrido-Barros, P.; Gimbert-Suriñach, C.; Matheu, R.; Sala, X.; Llobet, A. How to Make an Efficient and Robust Molecular Catalyst for Water Oxidation. *Chem. Soc. Rev.* **2017**, *46* (20), 6088–6098. <https://doi.org/10.1039/c7cs00248c>.
- (123) Jayalakshmi, M.; Kim, W. Y.; Jung, K. D.; Joo, O. S. Electrochemical Characterization of Ni-Mo-Fe Composite Film in Alkali Solution. *Int. J. Electrochem. Sci.* **2008**, *3* (8), 908–917.
- (124) Merrill, M. D.; Dougherty, R. C. Metal Oxide Catalysts for the Evolution of O₂ from H₂O. *J. Phys. Chem. C* **2008**, *112* (10), 3655–3666. <https://doi.org/10.1021/jp710675m>.
- (125) Raj, I. A.; Vasu, K. I. Transition Metal-Based Hydrogen Electrodes in Alkaline Solution - Electrocatalysis on Nickel Based Binary Alloy Coatings. *J. Appl. Electrochem.* **1990**, *20* (1), 32–38. <https://doi.org/10.1007/BF01012468>.
- (126) Puntoriero, F.; La Ganga, G.; Sartorel, A.; Carraro, M.; Scorrano, G.; Bonchio, M.; Campagna, S. Photo-Induced Water Oxidation with Tetra-Nuclear Ruthenium Sensitizer and Catalyst: A Unique 4 × 4 Ruthenium Interplay Triggering High Efficiency with Low-Energy Visible Light. *Chem. Commun.* **2010**, *46* (26), 4725. <https://doi.org/10.1039/c0cc00444h>.
- (127) Wang, C.; Xie, Z.; Dekrafft, K. E.; Lin, W. Doping Metal-Organic



General Introduction

- Frameworks for Water Oxidation, Carbon Dioxide Reduction, and Organic Photocatalysis. *J. Am. Chem. Soc.* **2011**, *133* (34), 13445–13454. <https://doi.org/10.1021/ja203564w>.
- (128) Bhunia, A.; Johnson, B. A.; Czaplá-Masztafiak, J.; Sá, J.; Ott, S. Formal Water Oxidation Turnover Frequencies from MIL-101(Cr) Anchored Ru(bda) Depend on Oxidant Concentration. *Chem. Commun.* **2018**, *54* (56), 7770–7773. <https://doi.org/10.1039/c8cc02300j>.
- (129) Johnson, B. A.; Bhunia, A.; Ott, S. Electrocatalytic Water Oxidation by a Molecular Catalyst Incorporated into a Metal-Organic Framework Thin Film. *Dalt. Trans.* **2017**, *46* (5), 1382–1388. <https://doi.org/10.1039/c6dt03718f>.
- (130) Lin, S.; Pineda-Galvan, Y.; Maza, W. A.; Epley, C. C.; Zhu, J.; Kessinger, M. C.; Pushkar, Y.; Morris, A. J. Electrochemical Water Oxidation by a Catalyst-Modified Metal–Organic Framework Thin Film. *ChemSusChem* **2017**, *10* (3), 469. <https://doi.org/10.1002/cssc.201700107>.
- (131) Francàs, L.; Matheu, R.; Pastor, E.; Reynal, A.; Berardi, S.; Sala, X.; Llobet, A.; Durrant, J. R. Kinetic Analysis of an Efficient Molecular Light-Driven Water Oxidation System. *ACS Catal.* **2017**, *7* (8), 5142–5150. <https://doi.org/10.1021/acscatal.7b01357>.
- (132) Creus, J.; Matheu, R.; Peñafiel, I.; Moonshiram, D.; Blondeau, P.; Benet-Buchholz, J.; García-Antón, J.; Sala, X.; Godard, C.; Llobet, A. A Million Turnover Molecular Anode for Catalytic Water Oxidation. *Angew. Chemie - Int. Ed.* **2016**, *55* (49), 15382–15386. <https://doi.org/10.1002/anie.201609167>.
- (133) Deronzier, A.; Stoll, T.; Palomares, E.; Fortage, J.; Gimbert-Suriñach, C.; Llobet, A.; Collomb, M.-N.; Albero, J. Efficient and Limiting Reactions in Aqueous Light-Induced Hydrogen Evolution Systems Using Molecular Catalysts and Quantum Dots. *J. Am. Chem. Soc.* **2014**, *136* (21), 7655–7661. <https://doi.org/10.1021/ja501489h>.
- (134) Matheu, R.; Ertem, M. Z.; Benet-Buchholz, J.; Coronado, E.; Batista, V. S.; Sala, X.; Llobet, A. Intramolecular Proton Transfer Boosts Water Oxidation Catalyzed by a Ru Complex. *J. Am. Chem. Soc.* **2015**, *137* (33), 10786–10795. <https://doi.org/10.1021/jacs.5b06541>.
- (135) Gilbert, J. A.; Eggleston, D. S.; Murphy, W. R.; Geselowitz, D. A.; Gersten, S. W.; Hodgson, D. J.; Meyer, T. J. Structure and Redox Properties of the Water-Oxidation Catalyst [(bpy)₂(OH₂)RuORu(OH₂)(bpy)₂]. *J. Am. Chem. Soc.* **1985**, *107* (13), 3855–3864. <https://doi.org/10.1021/ja00299a017>.
- (136) Gersten, S. W.; Samuels, G. J.; Meyer, T. J. Catalytic Oxidation of Water by an Oxo-Bridged Ruthenium Dimer. *J. Am. Chem. Soc.* **1982**, *104* (14), 4029–4030. <https://doi.org/10.1021/ja00378a053>.

- (137) Reynal, A.; Durrant, J. R.; Pastor, E.; Orchard, K. L.; Willkomm, J.; Reisner, E. Dye-Sensitised Semiconductors Modified with Molecular Catalysts for Light-Driven H₂ Production. *Chem. Soc. Rev.* **2015**, *45* (1), 9–23. <https://doi.org/10.1039/c5cs00733j>.
- (138) Garrido-Barros, P.; Matheu, R.; Gimbert-Suriñach, C.; Llobet, A. Electronic, Mechanistic and Structural Factors That Influence the Performance of Molecular Water Oxidation Catalysts Anchored on Electrode Surfaces. *Curr. Opin. Electrochem.* **2019**. <https://doi.org/10.1016/j.coelec.2019.04.027>.
- (139) Muresan, N. M.; Willkomm, J.; Mersch, D.; Vaynzof, Y.; Reisner, E. Immobilization of a Molecular Cobaloxime Catalyst for Hydrogen Evolution on a Mesoporous Metal Oxide Electrode. *Angew. Chemie Int. Ed.* **2012**, *51* (51), 12749–12753. <https://doi.org/10.1002/anie.201207448>.
- (140) Leung, J. J.; Warnan, J.; Nam, D. H.; Zhang, J. Z.; Willkomm, J.; Reisner, E. Photoelectrocatalytic H₂ Evolution in Water with Molecular Catalysts Immobilised on P-Si via a Stabilising Mesoporous TiO₂ Interlayer. *Chem. Sci.* **2017**, *8* (7), 5172–5180. <https://doi.org/10.1039/C7SC01277B>.
- (141) Moore, G. F.; Sharp, I. D. A Noble-Metal-Free Hydrogen Evolution Catalyst Grafted to Visible Light-Absorbing Semiconductors. *J. Phys. Chem. Lett.* **2013**, *4* (4), 568–572. <https://doi.org/10.1021/jz400028z>.
- (142) Krawicz, A.; Yang, J.; Anzenberg, E.; Yano, J.; Sharp, I. D.; Moore, G. F. Photofunctional Construct That Interfaces Molecular Cobalt-Based Catalysts for H₂ Production to a Visible-Light-Absorbing Semiconductor. *J. Am. Chem. Soc.* **2013**, *135* (32), 11861–11868. <https://doi.org/10.1021/ja404158r>.
- (143) Le Goff, A.; Artero, V.; Jusselme, B.; Tran, P. D.; Guillet, N.; Metaye, R.; Fihri, A.; Palacin, S.; Fontecave, M. From Hydrogenases to Noble Metal-Free Catalytic Nanomaterials for H₂ Production and Uptake. *Science (80-.)*. **2009**, *326* (5958), 1384–1387. <https://doi.org/10.1126/science.1179773>.
- (144) Creus, J.; Moonshiram, D.; Benet-Buchholz, J.; Godard, C.; Matheu, R.; Llobet, A.; García-Antón, J.; Sala, X.; Blondeau, P.; Peñafiel, I. A Million Turnover Molecular Anode for Catalytic Water Oxidation. *Angew. Chemie Int. Ed.* **2016**, *55* (49), 15382–15386. <https://doi.org/10.1002/anie.201609167>.
- (145) Matheu, R.; Moreno-Hernandez, I. A.; Sala, X.; Gray, H. B.; Brunschwig, B. S.; Llobet, A.; Lewis, N. S. Photoelectrochemical Behavior of a Molecular Ru-Based Water-Oxidation Catalyst Bound to TiO₂-Protected Si Photoanodes. *J. Am. Chem. Soc.* **2017**, *139* (33), 11345–11348. <https://doi.org/10.1021/jacs.7b06800>.
- (146) Liu, B.; Li, J.; Wu, H. L.; Liu, W. Q.; Jiang, X.; Li, Z. J.; Chen, B.; Tung, C. H.; Wu, L. Z. Improved Photoelectrocatalytic Performance for Water Oxidation by Earth-Abundant Cobalt Molecular Porphyrin Complex-



General Introduction

Integrated BiVO₄ Photoanode. *ACS Appl. Mater. Interfaces* **2016**, 8 (28), 18577–18583. <https://doi.org/10.1021/acsami.6b04510>.



Chapter

2

Objectives

According to the state-of-the-art in the field of artificial photosynthesis presented in Chapter 1, the main objectives are exposed in the present chapter.

Objectives

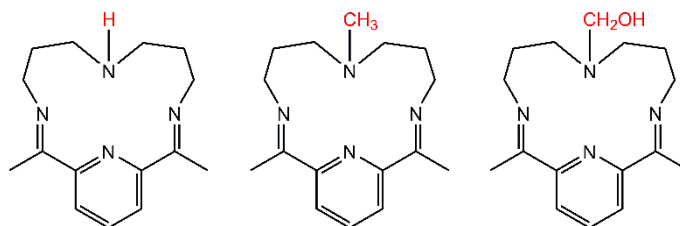
In the last decades, the interest in developing technologies to achieve the production of clean fuels, that are economically competitive to substitute the traditional fossil fuels have been increasing. Among all the possible options, technologies that takes the advantage of the free solar energy are the most promising choices. As already mentioned in the general introduction, artificial photosynthesis seems to be a good candidate to produce clean solar fuels from water and sunlight in large scale in the not so distant future. To make this possible it is mandatory to reduce the expenses of the material production by means of using cheap and abundant elements of the absorbers as well as to develop powerful and robust catalysts to carry out the oxygen evolution (OER) and hydrogen evolution (HER) half reactions. For these reasons, the general goal of the present thesis is to develop efficient and stable electrodes and photoelectrodes capable of performing water splitting with low overpotential.

The main goal mentioned above can be divided into the following specific objectives:

- **Objective 1:**

Develop homogeneous catalysts for the hydrogen evolution reaction made of materials that are more readily available than platinum, the best catalyst for HER known to date. The performance and mechanism of the reaction under electrochemical and photochemical conditions will be studied in detail with the aim of correlating their catalytic activity with their structure.

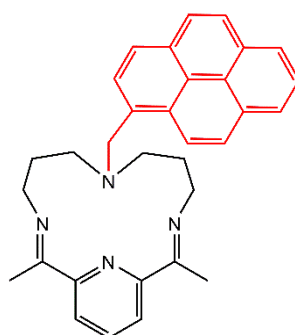
In particular, cobalt complexes containing the macrocyclic ligands shown in Chart 1 will be prepared. The role of proton relay groups in the second coordination sphere of the metal center (highlighted in red) will be the main focus of the mechanistic studies.



- **Objective 2:**

Synthesis and characterization of a hydrogen evolution catalyst based on a cobalt complex, that contains a pyrene moiety in order to decorate conductive graphitic materials *via* π - π stacking. The resulting hybrid electrode will be tested as an inexpensive molecular cathode for the HER..

The functionalized ligand is inspired by the active catalysts developed in the previous objective, as shown in Chart 2.



- **Objective 3:**

Preparation of a multilayered photocathode for HER based on p-type $\text{Cu}_2\text{ZnSnSe}_4$ semiconductor material with inexpensive non-noble based electrocatalysts for HER. In particular, the electrodeposition of MoS_2 on top of the photoabsorber will be explored and the activity and stability of the resulting photoelectrodes thoroughly tested.

- **Objective 4:**

Preparation of a molecular photoanode for OER based on n-type $\text{WO}_3/\text{BiVO}_4$ semiconductor materials, enhancing its catalytic activity by introducing a state-of-the-art molecular catalyst properly functionalized with a pyrene group. The use of an interlayer of carbon nanotube fiber between photoabsorber and catalytic centers will be explored.

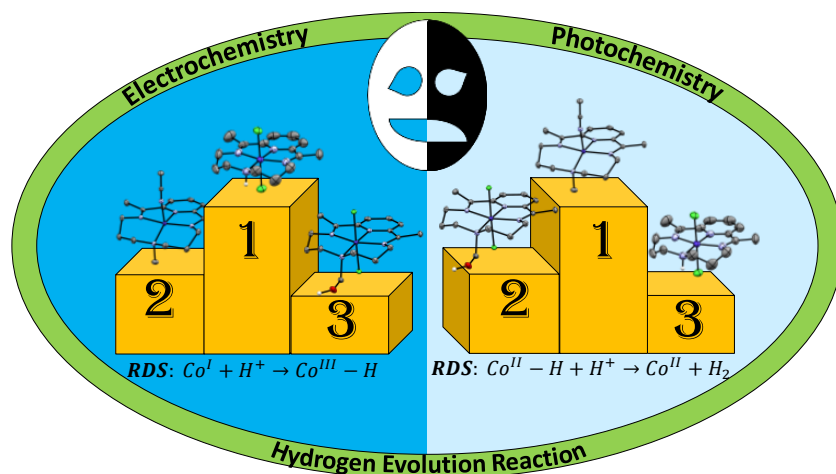
Chapter

3

Factors influencing hydrogen evolution (photo)catalysis in macrocyclic cobalt complexes

Chapter 3 explores the role of proton relays in the second coordination sphere of cobalt macrocyclic complexes that are active for the proton reduction reaction. The substitution of the proton in the amine in a macrocyclic ligand scaffold changes basicity of the corresponding Co hydrides, which are key intermediates in the catalysis thus strongly influencing catalytic properties. We found that electrochemical and photochemical proton reduction operates *via* different catalytic pathways, whose rate determining steps were identified through complementary computational studies.

Factors influencing HE (photo)catalysis in cobalt macrocycles



Abstract

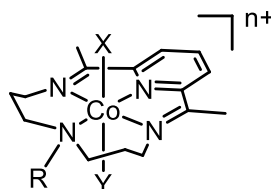
In this work, two new cobalt macrocyclic complexes active for HER were synthesized in order to study the role of proton relays by modifying the secondary amine for the methyl and the hydroxymethyl of one existing proton reduction catalyst. Electrochemical and photochemical experiments show that the modifications of the ligands affects the geometry and electron density of the metal center. These changes influence the calculated pK_a of the cobalt hydride species that are found to be the key intermediates towards the hydrogen evolution reaction. Here we propose two different catalytic pathways that explain the different behavior of these catalysts in electrochemical and photochemical hydrogen generation. The proposed mechanisms were calculated by density functional theory (DFT), finding that the rate determining step is the formation of $Co^{III}-H$ from Co^I in electrochemical experiments, while the rate determining step in photochemical experiments is the H-H bond formation.

Contributions:

Sergi Grau Abarca synthesized and characterized all the compounds, as well as carried out all the photochemical, electrochemical and spectroscopic experiments.

3.1 Introduction

The generation of hydrogen gas from light induced water splitting is a highly pursued process for its sustainable nature and high-energy storage capabilities of the hydrogen molecule.^{1,2} The development of catalysts based on transition metal complexes to perform the water reduction half-reaction is an active field that has given rise to a plethora of new compounds exploiting the tunable electronic effect of the ligands and their capacity to store multiple electrons on the metal site, the ligand or both.³⁻⁷ Another useful feature of molecular based hydrogen evolution catalysts (HEC) is the possibility to include proton relay groups in the second coordination sphere of the metal, thus facilitating the H-H bond formation step.⁸



- 1 R = H, X = Y = Cl, n = 1
- 2 R = CH₃, X = CH₃CN, Y = vacant, n = 2
- 3 R = CH₂OH, X = Y = Cl, n = 1

Figure 1. Cobalt hydrogen evolution catalysts studied in this work.

A prominent example of molecular hydrogen evolution catalyst is the cobalt macrocyclic complex **1** in Figure 1. It has shown extraordinary stability under catalytic turnover in acidic water, and has been successfully used in both electrocatalytic^{9,10} as well as photocatalytic systems in combination with metal

Factors influencing HE (photo)catalysis in cobalt macrocycles

based photosensitizers,¹⁰⁻¹² quantum dots^{13,14} and organic dyes.¹⁵ We have recently studied the mechanism followed by this catalyst under photocatalytic conditions with $[\text{Ru}(\text{bpy})_3]^{2+}$ photosensitizer and were able to determine the rate determining step of the process, which involved the formation of a key Co^{III} hydride ($\text{Co}^{\text{III}}\text{-H}$) intermediate.¹² One of the interesting features of **1** is the secondary amine group of the macrocyclic ligand that could be involved in the H-H bond formation step, as proposed for many other molecular hydrogen evolution catalyst, including the naturally occurring hydrogenases.⁸ In this work, we examine the role of proton relay groups in cobalt macrocyclic ligands derived from **1** by blocking the site with a methyl group or by positioning the proton relay further away from the metal center (**2** and **3** in Figure 1, respectively).



3.2 Results and Discussion

3.2.1 Synthesis, spectroscopic and structural characterization of 2-5

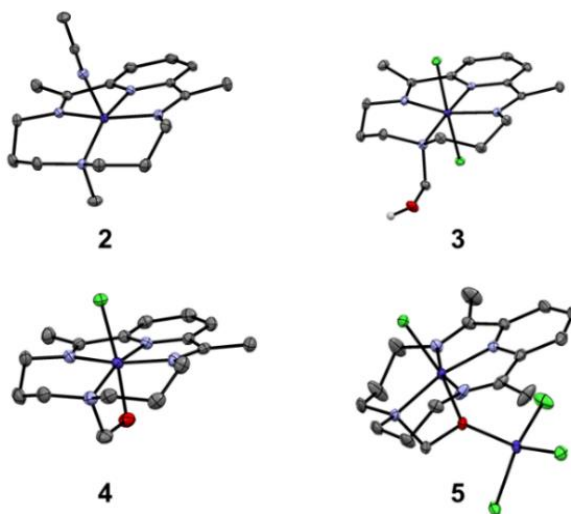


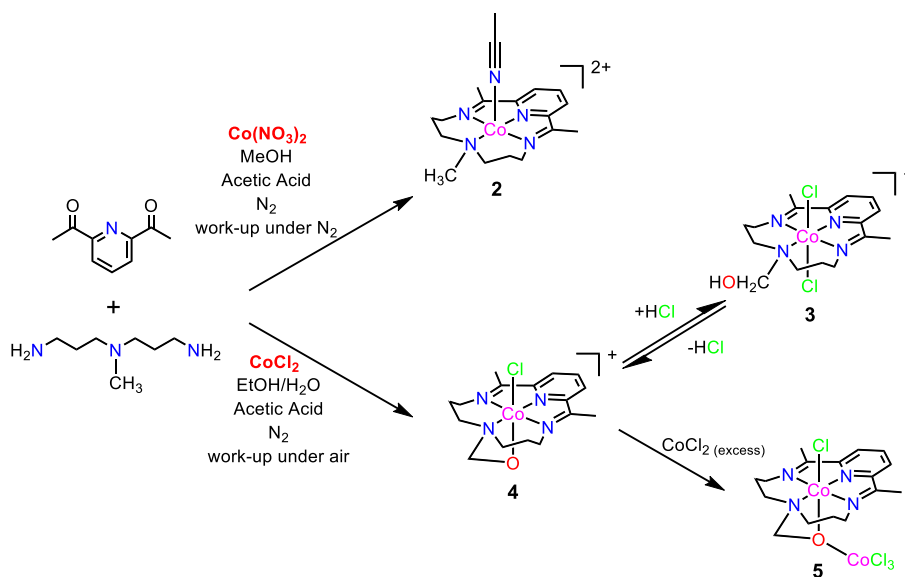
Figure 2. X-ray diffraction structures. ORTEP plots at 50% probability of cationic species **2**, **3**, **4** and neutral dinuclear complex. Only the H atom connected to hydroxomethyl group in **2** is shown. The rest of H atoms as well as counter ions and solvent molecules have been omitted for clarity.

Compounds **2** and **3** were prepared using a modified reported procedure.¹⁶ It consists of a one-step template synthesis starting from 2,6-diacetylpyridine and *N,N*-bis-(3-aminopropyl)-methylamine under nitrogen atmosphere (Scheme 1). Detailed synthetic procedures, spectroscopic and analytical characterization are described in the supporting information. Single crystals suitable for x-ray diffraction (XRD) studies were obtained and their ORTEP plots are shown in Figure 2. Compound **2** is a Co^{II} five-coordinated complex with distorted square-based pyramid geometry with an acetonitrile molecule occupying the axial position. This structure is analogous to that of the Co^{II} compound derived from **1**, with similar bond distances and angles.¹⁷ On the other hand, complex **3** is a Co^{III} six-coordinated compound with two chlorido



Factors influencing HE (photo)catalysis in cobalt macrocycles

ligands in the axial positions, which has very similar bond distances to those of **1**, with the same coordination sphere.^{10,12} The main difference between compounds **1** and **3** is the highly distorted octahedral geometry of **3** due to the repulsion between the chlorido and hydroxomethyl groups in *cis* relative position ($\alpha_1(\text{Cl}_{\text{cis}}\text{-Co-NH}) = 87.64^\circ$ vs $\alpha_3(\text{Cl}_{\text{cis}}\text{-Co-NCH}_2\text{OH}) = 94.31^\circ$). The dangling alcohol in the amino group of the macrocyclic ligand in **3** is prone to coordination, generating compound **4** in Figure 2. In the presence of excess cobalt chloride, precursor in the synthetic mixture, compound **4** evolves to the dicobalt complex **5** in Figure 2. In the presence of hydrochloric acid, derivatives **4** evolves to catalyst **3** (Scheme 1).



Scheme 1. Synthetic scheme for the synthesis of compounds 2-5.

3.2.2 Electrochemistry of 1-3 in organic media

The electrochemical properties of **2** and **3** were analyzed by cyclic voltammetry and spectroelectrochemical experiments in dimethylformamide (DMF) or acetonitrile (MeCN) (Figure 3, S1-S4 and Table S1). All complexes feature two chemically reversible metal centered one-electron waves which were assigned to the $\text{Co}^{\text{III/II}}$ and $\text{Co}^{\text{II/I}}$ couples. Compounds **1** and **3** show the same reduction potential values at $E_{1/2} = -0.37 \text{ V vs Fc}^+/\text{Fc}$ ($\Delta E = 69\text{-}80 \text{ mV}$) and $E_{1/2} = -0.88 \text{ V vs Fc}^+/\text{Fc}$ ($\Delta E = 57\text{-}79 \text{ mV}$), respectively. In contrast, both electrochemical events show a significant anodic shift for compound **2**, suggesting that the penta-coordinated structure, with a neutral acetonitrile ligand in the axial position, observed in the solid state is also maintained in solution ($E_a^1 = 0.71 \text{ V}$ and $E_c^1 = -0.04 \text{ V vs Fc}^+/\text{Fc}$ ($\Delta E = 752 \text{ mV}$) for $\text{Co}^{\text{III/II}}$ and $E_{1/2} = -0.71 \text{ V vs Fc}^+/\text{Fc}$ ($\Delta E = 58 \text{ mV}$) for $\text{Co}^{\text{II/I}}$). The high peak to peak separation for the $\text{Co}^{\text{III/II}}$ couple, particularly for complex **2**, is associated with a square mechanism involving ligand coordination, from square-based pyramid to octahedral geometry upon oxidation (Scheme S1). Finally, a third ligand based redox wave at $E_{1/2} \approx -1.65 \text{ V vs Fc}^+/\text{Fc}$ ($\Delta E = 70\text{-}110 \text{ mV}$) is observed for all the complexes, regardless of the substitution of the ligand on the amine group of the macrocyclic ligand.



Factors influencing HE (photo)catalysis in cobalt macrocycles

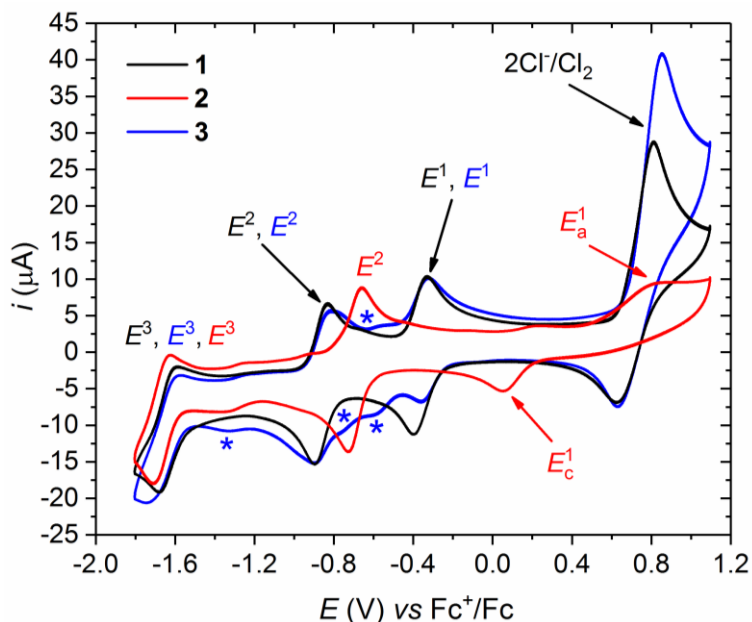


Figure 3. Cyclic voltammetry of compounds **1** (black), **2** (red) and **3** (blue) in DMF (0.1 M $[\text{Bu}_4\text{N}]\text{PF}_6$). $[\text{Complex}] = 1 \text{ mM}$; WE = Glassy Carbon disk; CE = Platinum disk; RE = AgNO_3/Ag (converted to Fc^+/Fc by adding +0.096 V as determined experimentally); scan rate = 100 mV/s. Blue asterisks (*) indicate species derived from compound **3**, likely related to the coordination abilities of the hydroxymethyl group (see compounds **4** and **5** in Scheme 1).

3.2.3 Electrochemistry and electrocatalysis of 1-3 in aqueous media

The axial acetonitrilo and chlorido ligands of **2** and **3** are exchanged by water in their aqueous solutions as demonstrated by UV-Vis spectroscopy experiments (Figure S5 and S6). The same substitution reaction was also observed in case of **1**.¹² Interestingly, the derivative compound **4** with the coordinated alcoxido group evolves to the same aqua complex derived for **3** as demonstrated by UV-Vis spectra in water. This is most likely due to the protonation of the alcoxido ligand in aqueous conditions (Figures S5 and S6).

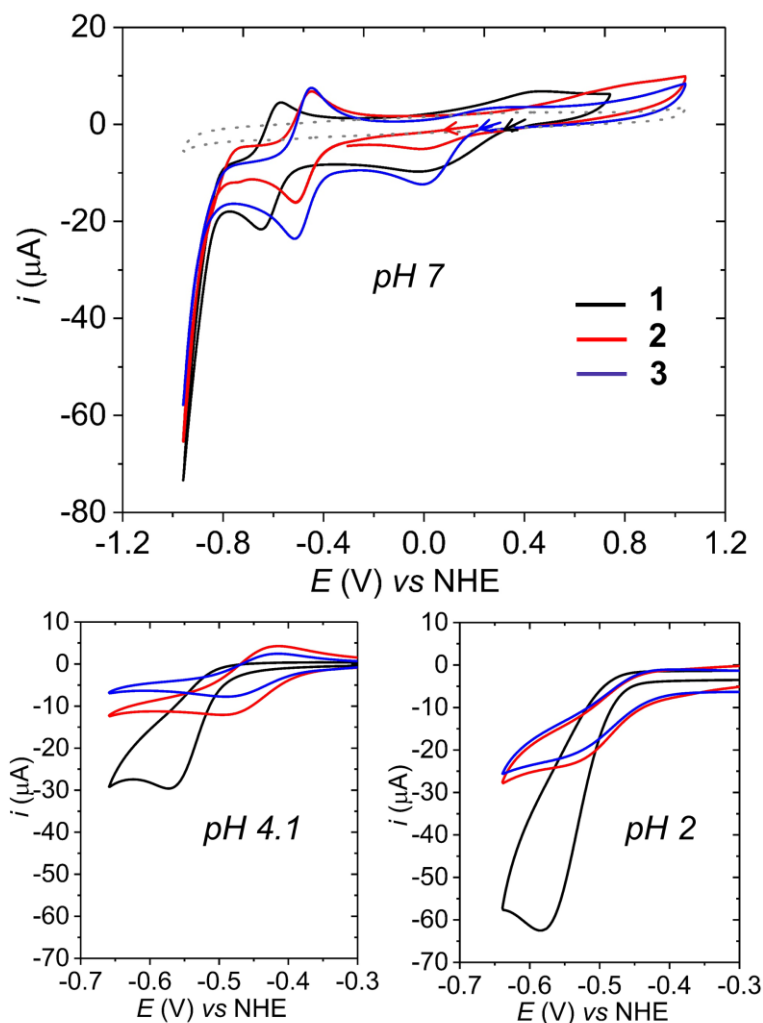


Figure 4. Cyclic voltammety experiments in pH 7, pH 4.1 and pH 2 of **1** (black), **2** (red) and **3** (blue). [Complex] = 1 mM; WE = glassy carbon disk; CE = Pt disk; RE = SCE (+0.241V vs NHE); scan rate = 100 mV/s.

Cyclic voltammety experiments of **2** and **3** in pH 7 show a reversible $\text{Co}^{\text{II/I}}$ redox couple at the same potential, i.e., $E_{1/2} = -0.51 \text{ V vs NHE}$ ($\Delta E = 65\text{--}71 \text{ mV}$), which is 100 mV anodically shifted to that of **1** ($E_{1/2} = -0.61 \text{ V vs NHE}$) ($\Delta E = 81 \text{ mV}$) (Figure 4 and Table 1). These results suggest that in aqueous solutions, **2** and **3** have the same coordination sphere at oxidation state +2,

Factors influencing HE (photo)catalysis in cobalt macrocycles

most likely a square-based pyramid with an aqua ligand in the axial position. A very broad, pH dependent wave associated with the $\text{Co}^{\text{III/II}}$ redox couple is also observed for compounds **1-3**, which is associated with a slow process involving significant changes in geometry upon changing the oxidation state of the Co center (Scheme S1, Figure S7 and Table S2). Upon lowering the pH to 4.1, the $\text{Co}^{\text{II/I}}$ of **1** becomes irreversible due to the proton reduction catalysis, which is already described in detail in the literature.^{11,13} In sharp contrast, the $\text{Co}^{\text{II/I}}$ couples of **2** and **3** are almost fully reversible at this pH, indicative of the low reactivity of their Co^{I} derivatives towards the formation of the $\text{Co}^{\text{III-H}}$ active species that are the gate to the hydrogen evolution catalytic cycle. The reactivity of these Co^{I} species increases at pH 2, when all complexes show catalytic waves with similar shape (Figure 4). Cyclic voltammetry experiments at variable scan rates show that catalyst **1** features a catalytic wave regardless of the scan rate (Figure S8). On the other hand, catalysts **2** and **3** show significant differences in the profile of the electrocatalytic wave upon changing the scan rate of the sweep (Figures S9-S10). If the experiment is performed at sufficiently slow scan rate (5 mV/s) it is possible to observe a catalytic wave at pH 4.5 for both catalysts. In addition, when performing the experiment at a sufficiently fast scan rate (500 mV/s) at pH 2, it is possible to avoid the catalytic behavior and recover the reversibility of the $\text{Co}^{\text{II/I}}$ redox couple. These results suggest that this protonation step is determining the catalytic performance of this type of catalysts. Indeed, calculated pK_a values of such species are in the range of -7.5 to -1.5, a measure of the high thermodynamic demand of this process (Table 1 and Table S3).¹⁸



Table 1. Reduction potentials for the $\text{Co}^{\text{III/I}}$ (E^1) and $\text{Co}^{\text{III/II-H}}$ (E^2) couples and pK_a values of the cobalt hydride species. See supporting information for the DFT calculation details of the presented values.

Catalyst	$E^1(\text{Co}^{\text{III/I}})^a$		$E^2(\text{Co}^{\text{III/II-H}})^a$	pK_a^{18} ($\text{Co}^{\text{n+}} - \text{H} \rightleftharpoons \text{Co}^{\text{n-2}} + \text{H}^+$)	
	Experimental ^b	Calculated ^c	Calculated ^d	$\text{Co}^{\text{III-H}}^e$	$\text{Co}^{\text{II-H}}^e$
1	-0.61 ($\Delta E = 71$ mV)	-0.61	-0.06	-7.5	12.0
2	-0.51 ($\Delta E = 65$ mV)	-0.61	-0.11	-6.7	12.5 ^f
3	-0.51 ($\Delta E = 71$ mV)	-0.55	-0.01	-6.6	11.8 ^f

^a Potentials reported versus NHE. ^b Values correspond to the $E_{1/2}$ values obtained from cyclic voltammetry experiments at pH 7 where no catalysis is observed, in parenthesis ΔE indicates the peak to peak separation between E_c and E_a waves. ^c DFT calculated values for the reduction of the penta-coordinated cobalt species with an aqua ligand in the axial position in cis orientation relative to the N-R group ($R = \text{H}$, **1**; $R = \text{CH}_3$, **2**; $R = \text{CH}_2\text{OH}$, **3**). ^d DFT calculated values for the penta-coordinated cobalt species with an hydrido ligand in the axial position in trans orientation relative to the N-R group ($R = \text{H}$, **1**; $R = \text{CH}_3$, **2**; $R = \text{CH}_2\text{OH}$, **3**). ^e DFT calculated values for the penta-coordinated cobalt species with an hydrido ligand in the axial position in trans orientation relative to the N-R group ($R = \text{H}$, **1**; $R = \text{CH}_3$, **2**; $R = \text{CH}_2\text{OH}$, **3**) to give a square planar cobalt species upon proton loss. See supporting information for details and complementary data (section 3.5.4).



3.2.4 Photocatalysis of 1-3

The photochemical water reduction activity of catalysts **2** and **3** were assessed in a thermostated 4 mL photoreactor at 25°C using $[\text{Ru}(\text{bpy})_3][\text{ClO}_4]_2$ as photosensitizer and a 1:1 mixture of ascorbic acid/sodium ascorbate as sacrificial electron donor and buffer at pH 4.1. A Xe lamp equipped with a UV light filter provided the light source calibrated to 1 sun intensity. The hydrogen gas evolution was then monitored with a Clark electrode. The profiles are shown in Figure 4, as well as the profile of reported catalyst **1** measured under the same experimental conditions for comparison purposes.

Factors influencing HE (photo)catalysis in cobalt macrocycles

Under photochemical conditions, the three catalysts show similar rates as deduced from the slopes of the hydrogen evolution profiles. Compound **2** is the fastest catalyst with a slightly steeper slope (Figure 5, red trace). Catalyst **3** has a similar catalytic rate but deactivates in less than 1h of reaction (Figure 5, blue trace). We attribute the fast deactivation of **3** to the reactivity of the dangling hydroxymethyl group that can coordinate the cobalt center, as proven by species **4** and **5** in Figure 2, which were isolated in reaction mixtures during the synthesis of **3**. Interestingly, catalyst **1** is the slowest but most stable catalyst (Figure 5, black trace), in contrast to the results observed under electrochemical conditions in Figure 3, which clearly show that the rate determining step of the reaction, that is, the protonation step of the Co^{I} , is faster for **1**.

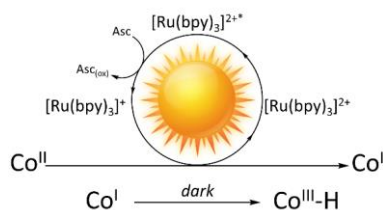
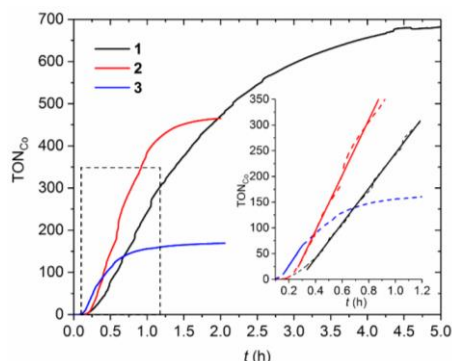


Figure 5. Hydrogen evolution photocatalysis in acidic water. $[\text{Complex}] = 0.05 \text{ mM}$; $[\text{Ru}(\text{bpy})_3][\text{ClO}_4]_2 = 0.5 \text{ mM}$; $[\text{ascorbic acid}] = [\text{sodium ascorbate}] = 0.55 \text{ M}$; $\text{pH} = 4.1$. Light intensity calibrated to 1 sun illumination, 100 mW/cm^2 . TON_{Co} = turnover number = mols of H_2 /mols of cobalt catalyst.

3.2.5 Mechanistic insights from experimental and computational studies

While electrocatalysis unambiguously determines the protonation of the Co^{I} intermediate as the rate determining step (rds) of the process, it is not obvious in the case of the photochemical reaction at pH 4.1, in which the relative kinetics of catalysts **1-3** follow a different trend (Figure 5). Thus, a different mechanistic pathway must be responsible for the hydrogen evolution reaction under these conditions. Over the time of the bulk photochemical experiments, reductive equivalents provided by photogenerated $[\text{Ru}(\text{bpy})_3]^+$ are available in excess. Therefore, a second reduction of the initial complex to generate a formal “ Co^0 ” species could take place. “ Co^0 ” species refers to a reduced species where the additional electron is shared between ligand and metal center (based on Mulliken charge population analysis, the additional electron is delocalized between the cobalt center and the coordinating nitrogen atoms, in particular with the pyridine (75-80% vs 10-15%, for Co and N respectively). Indeed, the reduction potential of the $[\text{Ru}(\text{bpy})_3]^{2+}/[\text{Ru}(\text{bpy})_3]^+$ couple is about 80 mV lower than the second reduction of complexes **1-3** as indicated by their respective cyclic voltammetry experiments in organic solvents ($E_{1/2} = -1.73$ V and $E_{1/2} \approx -1.65$ V vs Fc^+/Fc respectively, see Figures 3 and S11). The basicity of the doubly reduced species “ Co^0 ” is much higher and should react with protons to generate a $\text{Co}^{\text{II}}\text{-H}$ much faster than the monoreduced Co^{I} derivative to generate the $\text{Co}^{\text{III}}\text{-H}$ counterpart. Indeed, as shown in Table 1, calculated pK_a values of the Co^{II} hydride species are in the range of 11.8 to 12.5. In this scenario, the H-H bond formation must be the slowest step determining the rate of the catalytic cycle.



Factors influencing HE (photo)catalysis in cobalt macrocycles

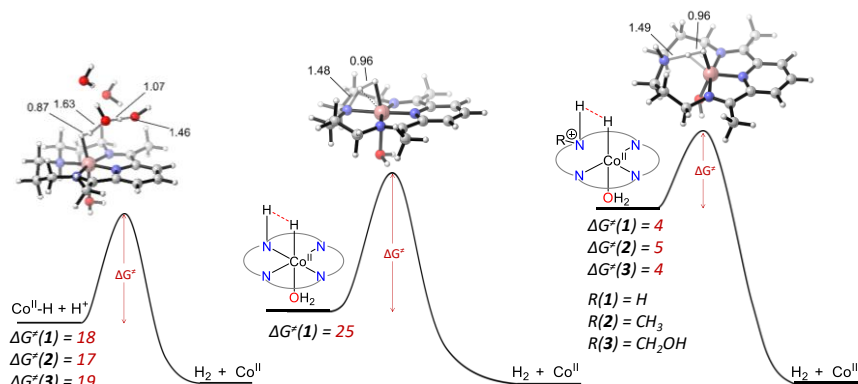


Figure 6. Intermolecular vs intramolecular H-H bond formation. Transition states relevant to the hydrogen evolution reaction by catalysts 1-3. The kinetic barriers (ΔG^\ddagger) are indicated for each catalyst in kcal/mol and representative drawings of each TS is given for 1. Note: it is important to highlight here that the relative energies of the starting compounds are not comparable and out of scale.

DFT calculations were carried out by Mr. Mauro Schilling and Professor Sandra Luber from University of Zurich (Institut für Physikalische Chemie). The methods and basis used to calculate redox potentials of key intermediates as well as transition states (TS) involved in the intermolecular H-H bond formation from $\text{Co}^{\text{II}}\text{-H}$ are described in SI. In addition, an intramolecular pathway involving the N-H group was also calculated for catalyst 1, which is the only compound with an available proton appended group in close proximity to the cobalt hydride. Finally, a third family of TS was considered where a putative protonated amine group $\text{H-N}^+\text{-R}$ is involved in the hydrogen formation step ($R = \text{H}, \text{CH}_3$ or CH_2OH for 1, 2 and 3 respectively).

Table 1 collects the theoretical reduction potentials of the $\text{Co}^{\text{III/II}}$ couple in the range of $E^1_{\text{calc}} = -0.61$ to -0.55 V that match well with the experimental values ($E^1_{\text{exp}} = -0.61$ to -0.51). We find that the reduction potential of the $\text{Co}^{\text{III}}\text{-H}$ intermediate to give a reduced $\text{Co}^{\text{II}}\text{-H}$ is more positive than the $\text{Co}^{\text{III/II}}$ couple for the three catalysts, suggesting that once the $\text{Co}^{\text{III}}\text{-H}$ is generated, it is immediately reduced ($E^2_{\text{calc}} = -0.11$ to -0.01 V, Table 1 and Table S3). The HER

mechanism via $\text{Co}^{\text{II}}\text{-H}$ has already been previously proposed for catalyst **1** under electrochemical conditions.¹¹

A model system using four hydrogen bonded water molecules were used to calculate the transition states for the intermolecular H-H bond formation with catalysts **1-3** from $\text{Co}^{\text{II}}\text{-H}$ (Figure 6, left). Two cobalt species were considered, one with square based pyramid and one with octahedral geometry containing an additional aqua ligand. Similar trends were observed for the two family of compounds and thus we will restrict our discussion to the penta-coordinated species, which are the most favorable ones according to previous structural data. As depicted in the left of Figure 6, the kinetic barriers to form hydrogen from the $\text{Co}^{\text{II}}\text{-H}$ with this model are around $\Delta G^\ddagger = 18$ kcal/mol. These values cannot distinguish catalytic rates between the three catalysts as they are essentially the same if one considers the inherent error of the calculations. However, these results are consistent with the similar slopes of the hydrogen evolution profiles obtained in the photochemical reactions of Figure 5 if we consider the H-H bond formation is considered as the rds. Interestingly, the proton source of the final hydrogen molecule is not coming from the water directly interacting with the hydride but from the furthest water molecule.

On the other hand, the intramolecular pathway involving the N-H group of **1** requires a much higher energy in the range of 24.8 to 30.0 kcal/mol, ruling out this catalytic pathway (Figure 6, center). In addition, we should emphasize here that the isomers with a relative cis configuration of the N-H group in regards to the $\text{Co}^{\text{II}}\text{-H}$ are higher in energy than the trans counterparts, used for the intermolecular mechanism, making this particular intramolecular pathway even less likely.

Interestingly, an intramolecular pathway involving a protonation of the macrocyclic amine (in the macrocyclic ligand) resulted in lower kinetic barriers for the three catalysts ($\Delta G^\ddagger = 4\text{-}5$ kcal/mol, Figure 6 right). This catalytic route involves an intermediate $\text{Co}^{\text{II}}\text{-H}$ species, where the amino group of the macrocyclic framework is decoordinates from the metal upon protonation.



Factors influencing HE (photo)catalysis in cobalt macrocycles

Although there are currently no experimental evidences supporting the formation of such an intermediate, this is certainly a possible catalytic route that should be taken into account for this family of compounds.

3.3 Conclusions

A thorough analysis of the hydrogen evolution catalytic behavior of **1**, **2** and **3** shows the intricate role of the macrocyclic ligand that occupies the equatorial position of our family of catalysts. First of all, the bulkiness and electronic properties of the substituent on the amine group of the macrocyclic frame determines the geometry and electronic density on the metal center as demonstrated by XRD studies summarized in Figure 2 and electrochemical properties in Figure 3. These changes have consequences in the pK_a of the cobalt hydride species that are key intermediates towards the hydrogen evolution reaction (Figure 7). In those catalytic systems where the $Co^{III}-H$ is involved, the protonation step from Co^I to $Co^{III}-H$ is the rds of the overall process, dictated by the low calculated pK_a of the hydrides (-7.5 to -1.5). This is the case of cyclic voltammetry experiments at pH higher than 2 where the concentration of protons is limited. In sharp contrast, this is not the case in photo induced catalysis using $[Ru(bpy)_3][ClO_4]_2$ as photosensitizer, which after photoactivation and reductive quenching by the ascorbate, has enough reducing power to generate a doubly reduced “ $Co(0)$ ” species (Figure 7, right). The latter can be quickly protonated to form the corresponding $Co^{II}-H$ with a much higher calculated pK_a (11.8 to 12.5). In this scenario, the H-H bond formation is the rds.



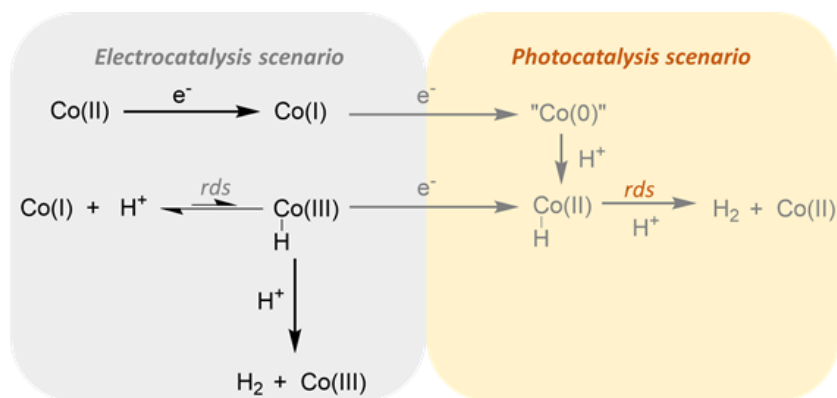


Figure 7. Catalytic pathways towards hydrogen evolution by catalysts 1-3.

A series of plausible transition states involving intermolecular as well as intramolecular pathways have been assessed. The flexibility and different relative positions (cis or trans) of the substituent in the amine group of the macrocyclic ligand offers a high degree of complexity to the studied system. After analysis of all the possibilities, two different mechanisms with Co^{II}-H key intermediate are proposed to contribute in the hydrogen evolution catalysis by 1, 2 and 3. The first one involves intermolecular H-H bond formation between the cobalt hydride and one proton of an incoming water molecule (Figure 6, left). The second one consists in the intramolecular interaction between an ammonium proton in the macrocyclic ligand and the cobalt hydride (Figure 5, right). The activation energies in both catalytic pathways do not differ significantly within the three complexes. These calculations are in full agreement with the experimental photocatalytic results in Figure 4 that show similar slopes for the hydrogen evolution profiles.



Factors influencing HE (photo)catalysis in cobalt macrocycles

3.4 References

- (1) McKone, J. R.; Lewis, N. S.; Gray, H. B. Will Solar-Driven Water-Splitting Devices See the Light of Day? *Chem. Mater.* **2014**, *26* (1), 407–414. <https://doi.org/10.1021/cm4021518>.
- (2) Nathan S. Lewis. Research Opportunities to Advance Solar Energy Utilization. *Science (80-.)*. **2016**, *351* (6271), 353–364. <https://doi.org/10.1126/science.aad1920.22>.
- (3) Du, P.; Eisenberg, R. Catalysts Made of Earth-Abundant Elements (Co, Ni, Fe) for Water Splitting: Recent Progress and Future Challenges. *Energy Environ. Sci.* **2012**, *5* (3), 6012–6021. <https://doi.org/10.1039/c2ee03250c>.
- (4) Eckenhoff, W. T.; Eisenberg, R. Molecular Systems for Light Driven Hydrogen Production. *Dalt. Trans.* **2012**, *41* (42), 13004–13021. <https://doi.org/10.1039/c2dt30823a>.
- (5) Berardi, S.; Drouet, S.; Francàs, L.; Gimbert-Suriñach, C.; Guttentag, M.; Richmond, C.; Stoll, T.; Llobet, A. Molecular Artificial Photosynthesis. *Chem. Soc. Rev.* **2014**, *43* (22), 7501–7519. <https://doi.org/10.1039/c3cs60405e>.
- (6) Artero, V.; Saveant, J. M. Toward the Rational Benchmarking of Homogeneous H₂-Evolving Catalysts. *Energy Environ. Sci.* **2014**, *7* (11), 3808–3814. <https://doi.org/10.1039/c4ee01709a>.
- (7) Khnayzer, R. S.; Thoi, V. S.; Nippe, M.; King, A. E.; Jurss, J. W.; El Roz, K. A.; Long, J. R.; Chang, C. J.; Castellano, F. N. Towards a Comprehensive Understanding of Visible-Light Photogeneration of Hydrogen from Water Using Cobalt(ii) Polypyridyl Catalysts. *Energy Environ. Sci.* **2014**, *7* (4), 1477–1488. <https://doi.org/10.1039/c3ee43982h>.
- (8) Helm, M. L.; Stewart, M. P.; Bullock, R. M.; DuBois, M. R.; DuBois, D. L. A Synthetic Nickel Electrocatalyst with a Turnover Frequency Above 100,000 s⁻¹ for H₂ Production. *Science (80-.)*. **2011**, *333* (6044), 863–866. <https://doi.org/10.1126/science.1205864>.
- (9) McCrory, C. C. L.; Uyeda, C.; Peters, J. C. Electrocatalytic Hydrogen Evolution in Acidic Water with Molecular Cobalt Tetraazamacrocycles. *J. Am. Chem. Soc.* **2012**, *134* (6), 3164–3170. <https://doi.org/10.1021/ja210661k>.
- (10) Leung, C.-F.; Chen, Y.-Z.; Yu, H.-Q.; Yiu, S.-M.; Ko, C.-C.; Lau, T.-C. Electro and Photocatalytic Hydrogen Generation in Acetonitrile and Aqueous Solutions by a Cobalt Macrocyclic Schiff-Base Complex. *Int. J. Hydrogen Energy* **2011**, *36* (18), 11640–11645. <https://doi.org/10.1016/j.ijhydene.2011.06.062>.



- (11) Molton, F.; Fortage, J.; Deronzier, A.; Blackman, A. G.; Stoll, T.; Collomb, M.-N.; Varma, S.; Castillo, C. E. Efficient Photocatalytic Hydrogen Production in Water Using a Cobalt(iii) Tetraaza-Macrocyclic Catalyst: Electrochemical Generation of the Low-Valent Co(i) Species and Its Reactivity toward Proton Reduction. *Phys. Chem. Chem. Phys.* **2013**, *15* (40), 17544. <https://doi.org/10.1039/c3cp52641k>.
- (12) Moonshiram, D.; Gimbert-Suriñach, C.; Guda, A.; Picon, A.; Lehmann, C. S.; Zhang, X.; Doumy, G.; March, A. M.; Benet-Buchholz, J.; Soldatov, A.; et al. Tracking the Structural and Electronic Configurations of a Cobalt Proton Reduction Catalyst in Water. *J. Am. Chem. Soc.* **2016**, *138* (33), 10586–10596. <https://doi.org/10.1021/jacs.6b05680>.
- (13) Gimbert-Suriñach, C.; Albero, J.; Stoll, T.; Fortage, J.; Collomb, M.-N.; Deronzier, A.; Palomares, E.; Lobet, A. Efficient and Limiting Reactions in Aqueous Light-Induced Hydrogen Evolution Systems Using Molecular Catalysts and Quantum Dots. *J. Am. Chem. Soc.* **2014**, *136* (21), 7655–7661. <https://doi.org/10.1021/ja501489h>.
- (14) Sandroni, M.; Gueret, R.; Wegner, K. D.; Reiss, P.; Fortage, J.; Aldakov, D.; Collomb, M. N. Cadmium-Free CuInS₂/ZnS Quantum Dots as Efficient and Robust Photosensitizers in Combination with a Molecular Catalyst for Visible Light-Driven H₂ Production in Water. *Energy Environ. Sci.* **2018**, *11* (7), 1752–1761. <https://doi.org/10.1039/c8ee00120k>.
- (15) Gueret, R.; Poulard, L.; Oshinowo, M.; Chauvin, J.; Dahmane, M.; Dupeyre, G.; Lainé, P. P.; Fortage, J.; Collomb, M. N. Challenging the [Ru(bpy)₃]²⁺ Photosensitizer with a Triazatriangulenium Robust Organic Dye for Visible-Light-Driven Hydrogen Production in Water. *ACS Catal.* **2018**, *8* (5), 3792–3802. <https://doi.org/10.1021/acscatal.7b04000>.
- (16) Poon, C.-K.; Liao, S. S. T. Structural and Mechanistic Studies of Coordination Compounds. Part 22. Preparation and Ligand-Substitution Kinetics of Some Trans-Di- Halogeno- and Trans-Halogenoisoithiocyanato-cobalt(III) Complexes of 2,12-Dimethyl- and 2,7,12-Trimethyl-3,7,11 ,17-Tetra. *J. Chem. Soc. Dalt. Transitions* **1978**, No. 1180, 1180–1185.
- (17) Lacy, D. C.; McCrory, C. C. L.; Peters, J. C. Studies of Cobalt-Mediated Electrocatalytic CO₂ Reduction Using a Redox-Active Ligand. *Inorg. Chem.* **2014**, *53* (10), 4980–4988. <https://doi.org/10.1021/ic403122j>.
- (18) Morris, R. H. Brønsted-Lowry Acid Strength of Metal Hydride and Dihydrogen Complexes. *Chem. Rev.* **2016**, *116* (15), 8588–8654. <https://doi.org/10.1021/acs.chemrev.5b00695>.



Factors influencing HE (photo)catalysis in cobalt macrocycles

3.5 Supporting Information

3.5.1. Materials and Methods

Reagents

All organic reagents, salts for buffers and metal precursors were purchased from Sigma-Aldrich and used without further purification, unless otherwise stated. Anhydrous solvents were taken from a solvent purification system (SPS®).

Electrochemistry methods and equipment

Glassy Carbon Disk electrodes, Platinum Disk Electrodes and reference electrodes (SCE and AgNO₃/Ag) were purchased from IJ-Cambria Ltd. Pads and alumina for polishing were also purchased from the same company.

Buffer solutions at pH 7 and pH 2 were prepared with Na₂HPO₄, NaH₂PO₄ and adjusted to 0.1 M ionic strength. Buffer solutions at pH 4.1 were prepared with ascorbic acid:sodium ascorbate mixtures 1:1 (0.55 M).

Cyclic voltammetry experiments were performed with a CHI660D potentiostat in a one-compartment cell, three electrode system using glassy carbon (GC) disk as working electrode, platinum disk as counter electrode and standard calomel electrode (SCE) or AgNO₃/Ag reference electrodes.

Spectroelectrochemistry

Spectroelectrochemistry experiments were performed in a custom-made Optically Transparent Thin Layer Electrochemical (OTTLE) cell (University of Reading) with platinum mesh working electrode, platinum wire counter electrode and silver wire pseudo-reference electrode.

UV-vis equipment

UV-Vis measurements were carried out on a Lambda 1050 PerkinElmer spectrophotometer equipped with a PMT, InGaAs and PbS detectors system, double beam optics, double monochromator and D2 and W light sources.



General Procedure for photochemical experiments

In a 20mL glass vial, a mixture of solid ascorbic acid (284.0 mg, 1.6×10^{-3} mol) and sodium ascorbate (326.9 mg, 1.6×10^{-3} mol) was added to a 2.9 mL aqueous solution containing $[\text{Ru}(\text{bpy})_3](\text{ClO}_4)_2$ (1.034×10^{-3} M). The mixture was sonicated and protected from the light until all the salts are dissolved. The solution was transferred in a water-jacketed 4 mL flask and 0.1mL of cobalt catalyst (**1**, **2** or **3**) were added (3×10^{-3} M) reaching a final composition of 0.55M of ascorbic acid and sodium ascorbate, 0.1mM of cobalt catalyst and 1mM of ruthenium photosensitizer. The flask was sealed with a septum and the mixture degased for 1 hour by bubbling nitrogen. A Clark hydrogen sensor was inserted in the cell and the mixture irradiated using a 150 W Xe Arc Lamp with a cut off filter ($\lambda > 400$ nm, 25 mm). The light intensity was calibrated to “1 sun” previous to the experiment and the temperature was maintained constant at 25 °C. At the end of the experiment, the cell was degased with nitrogen and calibrated adding known amounts of hydrogen.



Factors influencing HE (photo)catalysis in cobalt macrocycles

3.5.2 Synthetic procedures, electrochemical methods and additional characterization

Compound 1

2,6-diacetyl-pyridine (686 mg, 4.2 mmol) and $\text{CoCl}_2 \cdot 6\text{H}_2\text{O}$ (1 g, 4.2 mmol) were dissolved in degassed ethanol (6.3 mL) and heated to 75 °C under N_2 (deep blue solution). Degassed water (4.2 mL) were added and the mixture was stirred until everything were dissolved, giving a purple solution. 3,3'-diaminodipropylamine (0.59 mL, 4.2 mmol) was added dropwise. The colour turned to dark blue and the solution became cloudy upon addition of the amine. Glacial acetic acid (0.17 mL) was added to catalyze the condensation, giving a clear solution, which was kept at 75°C for 5 hours stirring under N_2 . At this time, the condensation was judged to be complete and mixture was cooled down to room temperature. A concentrated HCl aqueous solution (0.39 mL, 37 %, 4.62 mmol) was added, after which the solution turned to an orange/brown color. The mixture was aerated overnight affording a green solution. The volume was reduced on the rotary evaporator until 1 mL of water was left. Cold ethanol (7 mL) at -8 °C was added slowly and product **1** precipitated as green microcrystals. The green crystals were filtered off and washed with cold ethanol (565 mg, 1.33 mmols, 35%). Spectroscopic and electrochemistry measurements matched the data reported in the literature.¹

Compound 2

2,6-diacetyl-pyridine (326.4 mg, 2 mmol) and $\text{Co}(\text{NO}_3)_2 \cdot 6\text{H}_2\text{O}$ (582.06 mg, 2 mmol) were dissolved in degassed anhydrous methanol (10 mL) and heated to 75°C under N_2 and the reaction mixture stirred until everything was dissolved, giving a pink-red solution. 3,3-Diamino-*N*-methyldipropylamine (0.32 mL, 2 mmol) was added dropwise. The solution turned dark and cloudy upon addition of the amine. Glacial acetic acid (0.1 mL) was added to catalyze the imine condensation, forming a clear solution. The reaction mixture (dark red) was stirred and kept at 75°C for 5 hours under N_2 . After 5 hours, the condensation was complete. The reaction mixture was cooled down to room temperature, filtered under N_2 and transferred into a Schlenk flask containing a degassed methanolic solution of NaClO_4 (561.8 mg, 4 mmol). After a second filtration to remove a white solid, the filtered solution was dried under reduced pressure



and redissolved in degassed anhydrous acetonitrile. An orange powder precipitated by adding degassed diethylether to the acetonitrile solution (729 mg). The product was recrystallized dissolving the powder in acetonitrile (40 mL) and adding toluene (40 mL) very slowly (forming a layer). After 2-4 hours, dark orange crystals of compound **2** were obtained. The crystals were filtered under air and washed with toluene (522.3 mg, 0.914 mmol, 46%). Single crystals were obtained by slow diffusion of diethylether into an acetonitrile solution of **2**.

Anal. Calcd for $C_{18}H_{27}Cl_2CoN_5O_8$: C, 37.84; H, 4.76; N, 12.26. **Found**: C, 37.80; H, 4.36; N, 12.30. **ESI⁺-HRMS m/z**: calcd for $[M-CH_3CN]^+$ ($C_{16}H_{24}CoN_4^+$): m/z: 331.1333, found m/z: 331.1332.

Compound 3, 4 and 5

2,6-Diacetyl-pyridine (686 mg, 4.2 mmol) and $CoCl_2 \cdot 6H_2O$ (1 g, 4.2 mmol) were dissolved in degassed ethanol (6.3 mL) and heated to 75°C under N_2 (deep blue solution). Degassed water (4.2 mL) was added and the mixture was stirred until everything was dissolved, giving a purple solution. 3,3-Diamino-*N*-methylpropylamine (0.7 mL, 4.2 mmol) was added dropwise. The solution turned to dark blue and cloudy on addition of the amine. Glacial acetic acid (0.2 mL) was added to catalyze the condensation giving a clear solution, which was stirred and kept at 75°C for 5 hours under N_2 . At this point, the reaction mixture became dark red. After 5h, the condensation was judged to be complete and the mixture was cooled down to room temperature. A concentrated HCl aqueous solution (0.39 mL, 37%, 4.62 mmol) was added. The mixture was aerated overnight. The reaction mixture was dried under reduced pressure and the resulting solid is dissolved in the minimum volume of methanol (brown solution). Green solid precipitates when isopropanol is added dropwise. The solid was filtered and washed with isopropanol. The green powder was dissolved in water and acetone was added until the solution started to become cloudy. Then the solution was kept in the fridge overnight. The green solid was filtered and identified as compound **4** containing traces of compound **3** (572 mg, *ca.* 1.2 mmol, *ca.* 30%). Single crystals of **4** were obtained by slow diffusion of diethylether in a solution of **4** in methanol.

¹H NMR (500 MHz, D₂O-*d*₂) δ = 8.53 (dd, *J* = 8.4 and 7.3 Hz, 1H), 8.46 (d, *J* = 7.9 Hz, 2H), 5.27 (s, 2H), 4.21 (dt, *J* = 15 and 3.2 Hz, 2H), 3.81 (t, *J* = 13.7 Hz, 2H),



Factors influencing HE (photo)catalysis in cobalt macrocycles

3.51 (td, $J = 12.85$ and 2.6 Hz, 2H), 2.9 (s, 6H), 2.76 (dt, $J = 12.9$ and 3.1 Hz, 2H), 2.55-2.37 (m, 4H).

^{13}C NMR (126 MHz, $\text{D}_2\text{O}-d_2$) $\delta = 178.8, 157.7, 142.6, 127.8, 90.8, 56.1, 49.5, 24.9, 16.9$.

ESI⁺-HRMS m/z : calcd for $[\text{M}]^+$ ($\text{C}_{16}\text{H}_{23}\text{ClCoN}_4\text{O}^+$): m/z : 381.0892. Found m/z : 381.0887.

Compound 3 was prepared by adding 10 equivalents of hydrochloric acid to an aqueous solution of **4**. Dark green microcrystals can be obtained by adding acetone to the acidic mixture and cooling it down to -20°C overnight. Single crystals were obtained by slow diffusion of diethylether in a solution of **3** in methanol.

^1H NMR (400 MHz, $\text{MeOD}-d_4$) $\delta = 8.49$ (t, $J = 8.0$ Hz, 1H), 8.40 (d, $J = 8.0$ Hz, 2H), 4.60 (s, 2H), 3.96 (m, 2H), 3.64 (m, 2H), 3.54 (t, $J = 12.5$ Hz, 2H), 3.14 (dq, $J = 3.5, 1.5$ Hz, 2H), 2.81 (s, 6H), 2.35 (m, 2H), 2.10 (m, 2H).

^{13}C NMR (101 MHz, $\text{MeOD}-d_4$) $\delta = 179.6, 157.2, 141.5, 127.6, 82.5, 51.3, 50.4, 22.0, 16.7$.

Anal. Calcd for $\text{C}_{16}\text{H}_{24}\text{Cl}_3\text{CoN}_4\text{O}$: C, 42.36; H, 5.33; N, 12.35. Found: C, 41.19; H, 5.51; N, 12.14.

ESI⁺-HRMS m/z : calcd for $[\text{M}-\text{H},\text{Cl}]^+$ ($\text{C}_{16}\text{H}_{23}\text{ClCoN}_4\text{O}^+$): m/z : 381.0892, found m/z : 381.0887 (**3** converts into **4** in the MS chamber).

Single crystals of **Compound 5** were isolated from the methanolic solution of the first filtration during the synthesis of **4** described above. We attribute the formation of **5** to the presence of excess of CoCl_2 .

^1H NMR (400 MHz, $\text{MeOD}-d_4$) $\delta = 8.53$ (t, $J = 7.8$ Hz, 1H), 8.45 (d, $J = 7.8$ Hz, 2H), 5.30 (s, 2H), 4.20 (m, 2H), 3.81 (m, 2H), 3.52 (m, 2H), 2.89 (s, 6H), 2.75 (m, 2H), 2.56-2.36 (m, 4H). We attribute the broad bands observed in the ^1H NMR spectrum to the Co^{II} atom (particularly for the $-\text{CH}_2-$ group, the closest to the paramagnetic center).

Anal. Calcd for $\text{C}_{16}\text{H}_{23}\text{Cl}_4\text{Co}_2\text{N}_4\text{O}$: C, 35.13; H, 4.24; N, 10.24. Found: C, 35.18; H, 3.98; N, 10.14.

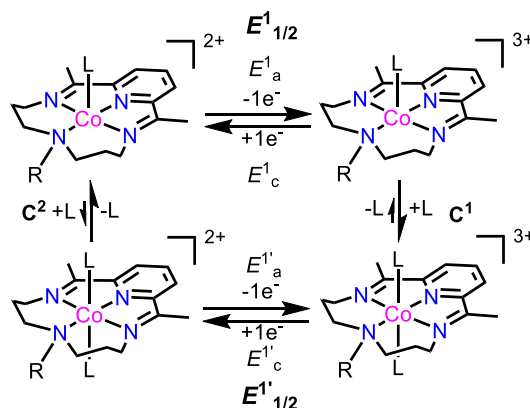


3.5.3. Figures Supporting Information

Table S1. Summary of electrochemistry data of compounds **1**, **2** and **3** in DMF (from Figure S1).

	$E^1(\text{Co}^{\text{III/II}})^a$		$E^2(\text{Co}^{\text{II/I}})^a$		$E^3(\text{L/L}')^a$	
	$E_{1/2}(\text{V})$	$\Delta E(\text{V})^b$	$E_{1/2}(\text{V})$	$\Delta E(\text{V})$	$E_{1/2}(\text{V})$	$\Delta E(\text{V})$
1	-0.37	0.069	-0.88	0.057	-1.64	0.07
2	$E^1_a = 0.799; E^1_c = 0.052^c$		-0.71	0.058	-1.66	0.07
3	-0.37	0.080	-0.88	0.079	-1.65	0.11

^aPotentials reported versus Fc^+/Fc . ^b ΔE indicates the peak to peak separation between E_c and E_a waves. ^cNot possible to calculate $E_{1/2}$ due to high peak to peak separation (square mechanism indicated in Scheme S2), instead the values of the E_c and E_a waves are given.



Scheme S1. Square mechanism associated with the high peak to peak separation between E_c and E_a of the $\text{Co}^{\text{III/II}}$ couple in the cyclic voltammetry experiments of Figure 1. $R = \text{H}, \text{CH}_3$ or CH_2OH ; $L = \text{MeCN}, \text{DMF}$ or H_2O .



Factors influencing HE (photo)catalysis in cobalt macrocycles

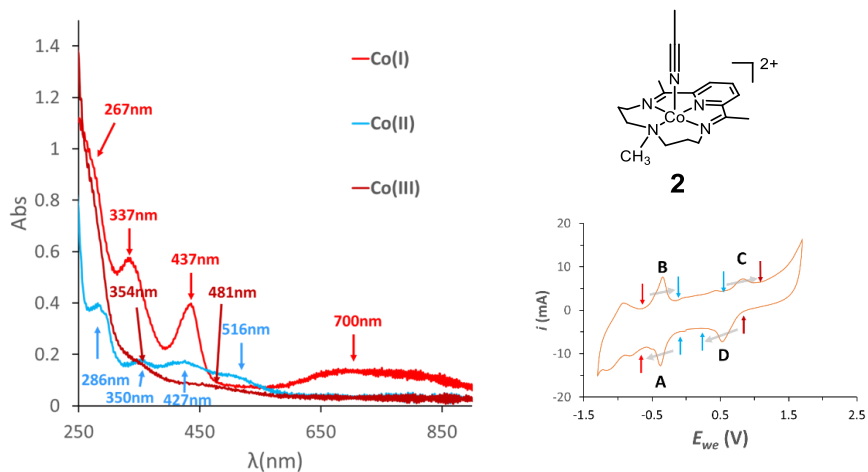


Figure S1. *Left*) UV-Vis spectra of **2** in acetonitrile at oxidation state Co^{III} (dark red), Co^{II} (blue) and Co^I (light red) generated electrochemically. *Right*) Molecular structure of **2** and its cyclic voltammogram experiment in the OTTLE cell (WE = Platinum mesh; CE = Platinum wire; RE: Silver pseudo-reference electrode; solvent = acetonitrile 0.1 M [Bu₄N]PF₆; [Co] = 2 mM; scan rate = 2 mV/s. Dark red, blue and light red arrows show the starting/ending of the UV-vis spectra acquisition. Grey arrows indicate the polarity of the scan.



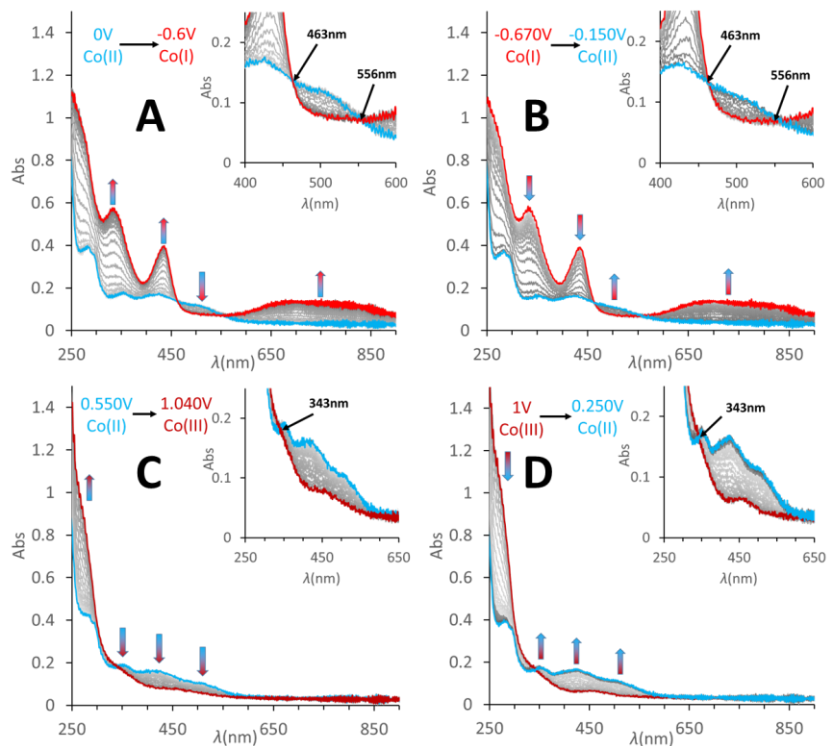


Figure S2. Spectroelectrochemistry of 2 in acetonitrile, associated with Figure S1.



Factors influencing HE (photo)catalysis in cobalt macrocycles

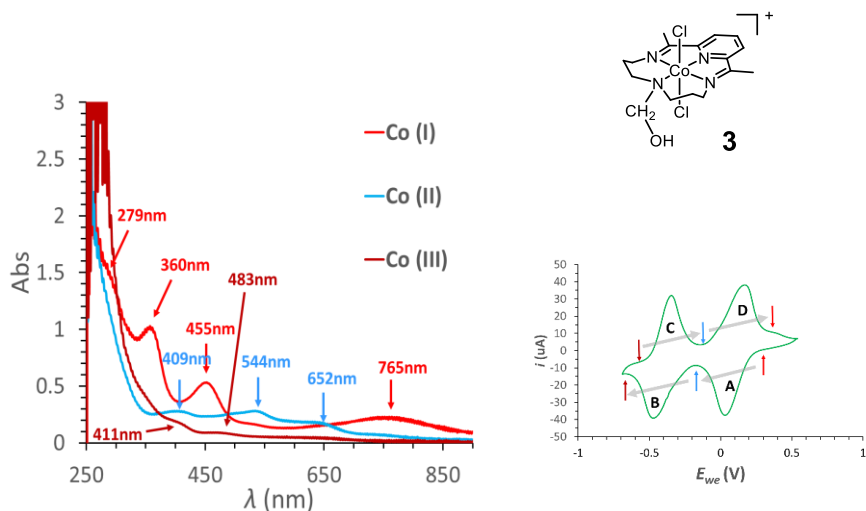


Figure S3. *Left*) UV-Vis spectra of **3** in dimethylformamide at oxidation state Co^{III} (dark red), Co^{II} (blue) and Co^I (light red) generated electrochemically. *Right*) Molecular structure of **3** and its cyclic voltammetry experiment in the OTTLE cell (WE = Platinum mesh; CE = Platinum wire; RE: Silver pseudo-reference electrode; solvent = DMF-0.1 M [Bu₄N]PF₆; [Co] = 2 mM; scan rate = 2 mV/s. Red, blue and purple arrows show the starting/ending of the UV-vis spectra acquisition. Grey arrows indicate the polarity of the scan.



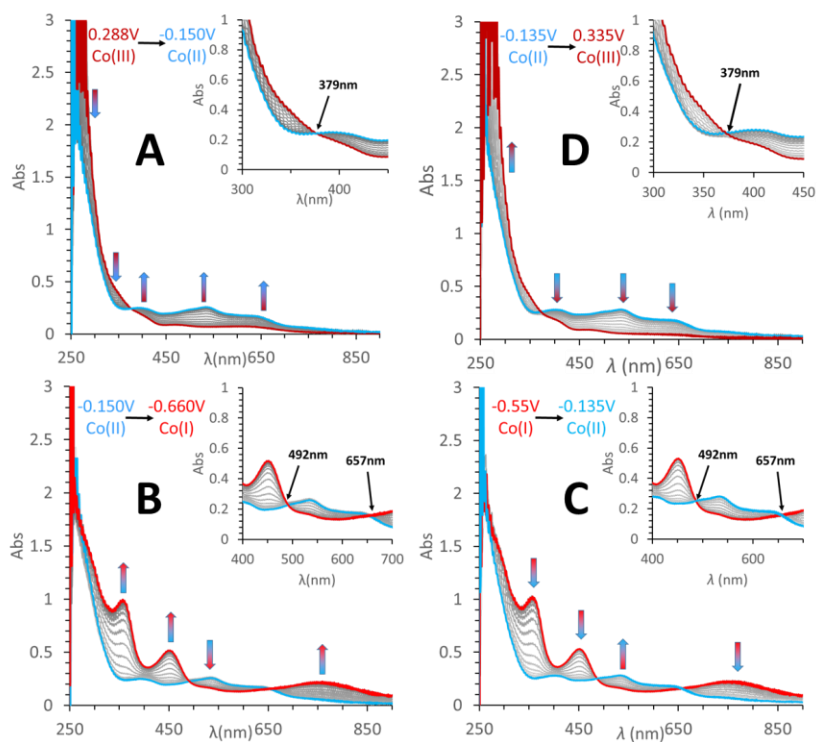


Figure S4. Spectroelectrochemistry of 3 in dimethylformamide, associated with Figure S3.



Factors influencing HE (photo)catalysis in cobalt macrocycles

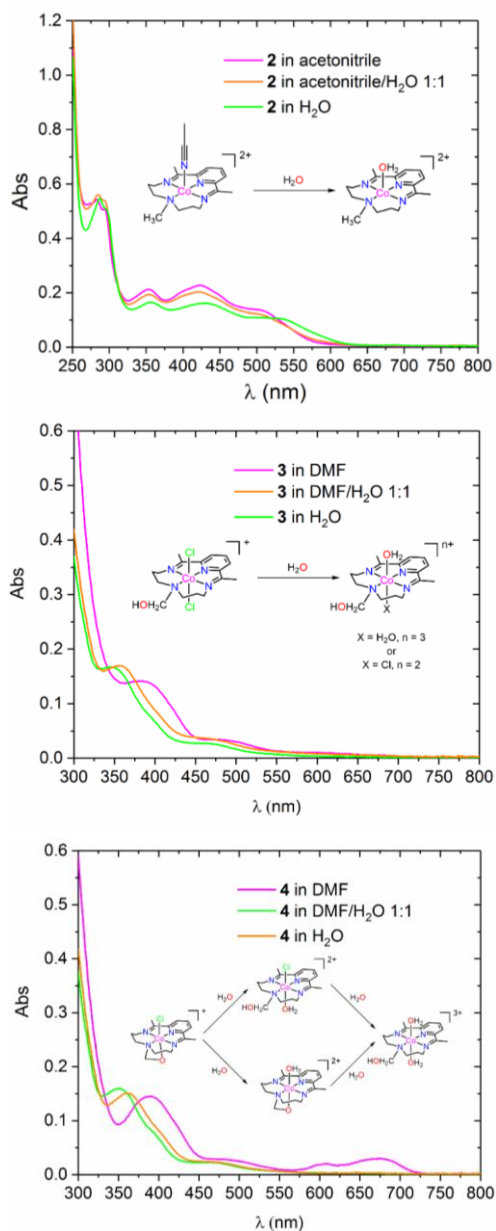


Figure S5. Top) UV-Vis spectra of 0.1 mM solutions of **2** in acetonitrile (pink), acetonitrile:H₂O 1:1 (orange) and water (green). **Middle)** UV-Vis spectra of 0.1 mM solutions of **3** in DMF (pink), DMF:H₂O 1:1 (orange) and water (green). **Bottom)** UV-Vis spectra of 0.1 mM solutions of **4** in DMF (pink), DMF:H₂O 1:1 (orange) and water (green).

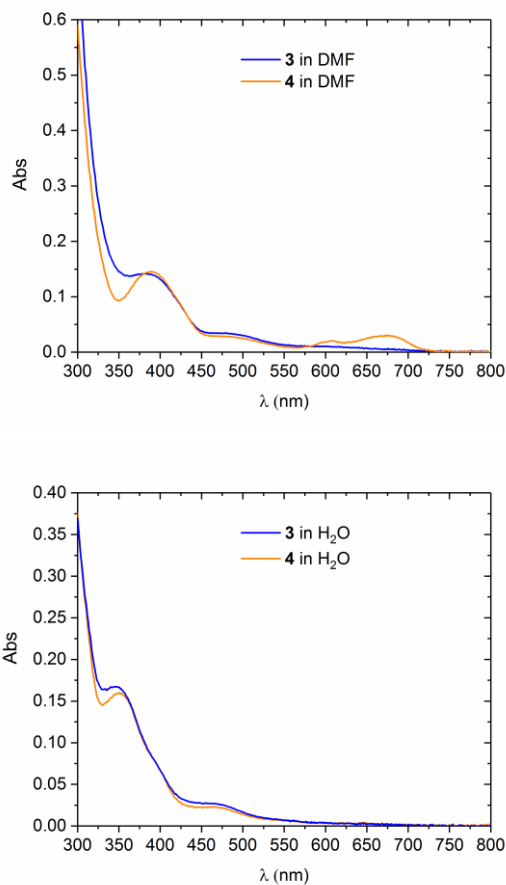


Figure S6. Overlapping of UV-Vis spectra of 0.1 mM solutions of **3** (blue) and **4** (orange) in DMF (Top) and water (Bottom).

Factors influencing HE (photo)catalysis in cobalt macrocycles

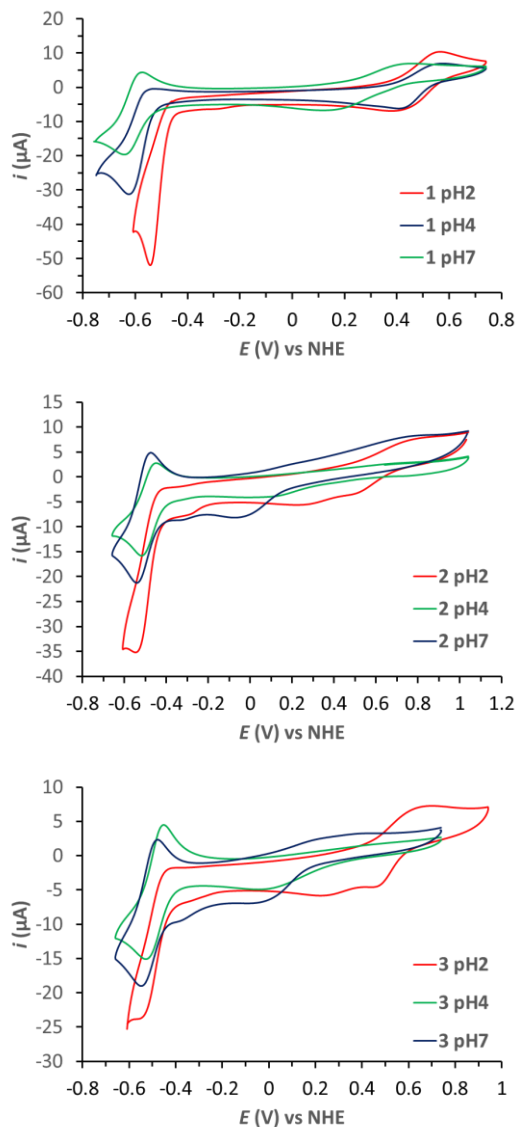


Figure S7. Cyclic voltammetry of compounds **1** (top), **2** (middle) and **3** (bottom) in aqueous conditions at different pHs. $[\text{Co}] = 1 \text{ mM}$; WE = Glassy Carbon disk; CE = Platinum disk; RE = SCE; scan rate = 100 mV/s.

Table S2. Summary of electrochemistry data of compounds **1**, **2** and **3** in aqueous conditions.

pH7	$E^1(\text{Co}^{\text{III/II}})^a$		$E^2(\text{Co}^{\text{II/I}})^a$		
	CAT	$E_{1/2}$ (V) ΔE (mV)	E_c (V)	E_a (V)	ΔE (mV)
1	-0.609	71	0.133	0.446	313
2	-0.509	65	-0.050	0.773	823
3	-0.512	71	-0.023	0.393	416

pH4	$E^1(\text{Co}^{\text{III/II}})^a$		$E^2(\text{Co}^{\text{II/I}})^a$		
	CAT	$E_{1/2}$ (V) ΔE (mV)	E_c (V)	E_a (V)	ΔE (mV)
1	^a	--	0.406	0.576	170
2	-0.484	67	0.105	0.654	549
3	-0.490	77	0.004	0.413	409

pH2	$E^1(\text{Co}^{\text{III/II}})^a$		$E^2(\text{Co}^{\text{II/I}})^a$			
	CAT	E_{cat} (V) ΔE (mV)	E_{c1} (V)	E_{c2} (V)	E_a (V)	ΔE (mV)
1	-0.543	--	0.386	--	0.566	180
2	-0.546	--	0.513 ^b	0.300 ^b	0.732	219-432
3	-0.555	--	0.461 ^b	0.241 ^b	0.644	183-403

^aCatalytic wave with $E_{cat} = -0.617\text{V}$ for **1**. ^bThe two waves E_{c1} and E_{c2} observed in the cathodic scan for catalysts **2** and **3** in pH 2 are attributed to derivatives with different coordination sphere (coordinated/decoordinated amine).



Factors influencing HE (photo)catalysis in cobalt macrocycles

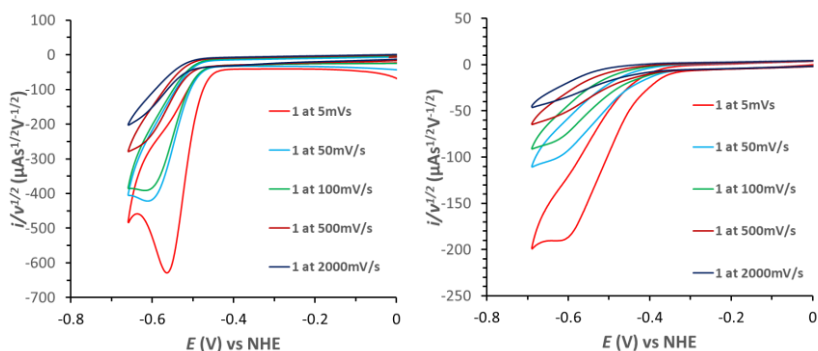


Figure S8. Plot of the $i/v^{1/2}$ vs E of **1** in pH 2 (left, phosphate buffer $I = 0.1M$) and pH 4.1 (right, $[NaHAsc/H_2Asc] = 1.1 M$ water solution). Scan rate from 5 to 2000 mV/s. WE: GC. CE: Pt disk. RE: SCE (converted to NHE by adding +0.241 V); WE: Glassy Carbon disk; CE: Platinum disk.

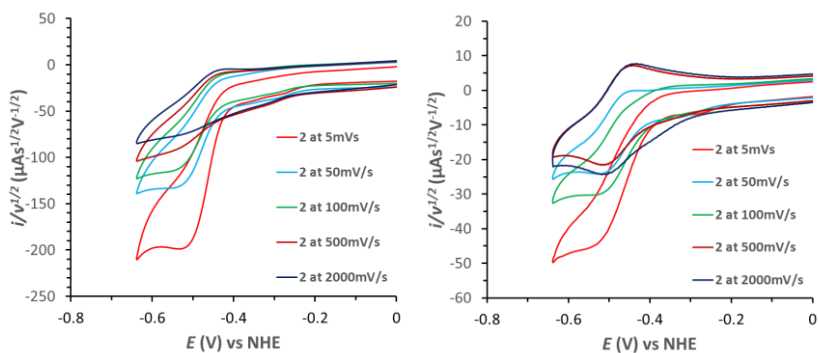


Figure S9. Plot of the $i/v^{1/2}$ vs E of **2** in pH 2 (left) (phosphate buffer $I=0.1M$) and pH 4.1 (right) ($[NaHAsc/H_2Asc]=1.1M$ water solution). Scan rate from 5 to 2000mV/s. RE: SCE (converted to NHE by adding +0.241V); WE: Glassy Carbon disk; CE: Platinum disk.

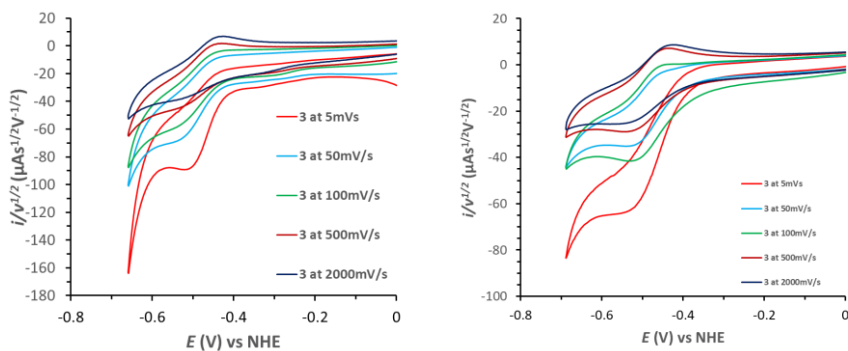


Figure S10. Plot of the $i/v^{1/2}$ vs E of **3** in pH 2 (left) (phosphate buffer $I=0.1M$) and pH 4.1 (right) ($[NaHAsc/H_2Asc]=1.1M$ water solution). Scan rate from 5 to 2000mV/s. RE: SCE (converted to NHE by adding +0.241V); WE: Glassy Carbon disk; CE: Platinum disk.

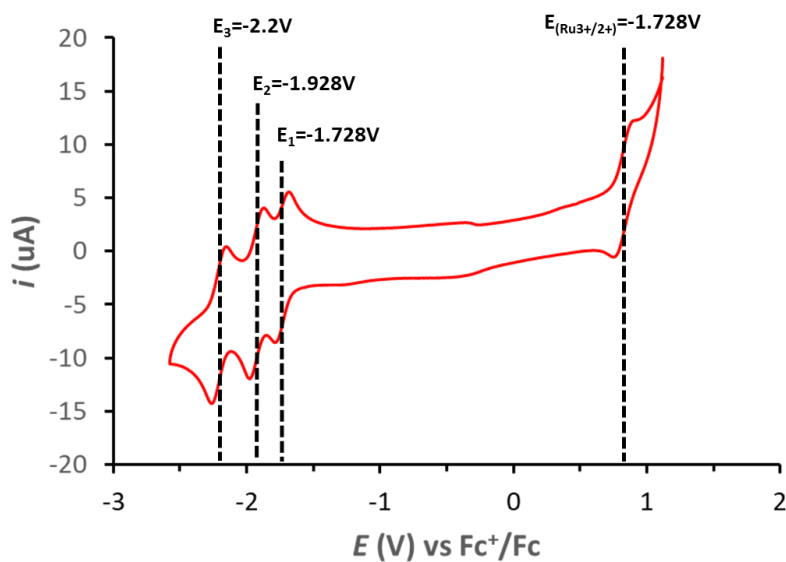


Figure S11. Cyclic Voltammetry of $[Ru(bpy)_3](ClO_4)_2$ in DMF-0.1 M $[Bu_4N]PF_6$. Scan rate 100mV/s. RE: Ag/AgNO₃ (converted to Fc^+/Fc by adding +0.096 V as determined experimentally). WE: Glassy Carbon disk; CE: Platinum disk.



Factors influencing HE (photo)catalysis in cobalt macrocycles

3.5.4. Density Functional Theory methods and additional data

Table S3. Reduction potentials for the Co^{II/I} (E^1) and Co^{III/II-H} (E^2) couples and pK_a values of the cobalt hydride species.

Catalyst	$E^1(\text{Co}^{\text{II/I}})^{\text{a}}$		$E^2(\text{Co}^{\text{III/II-H}})^{\text{a}}$		pK _a
	Experimental ^b	Theoretical ^c	Theoretical	Co ^{III} -H	
1	-0.61 ($\Delta E = 71$ mV)	-0.61	-0.06 ^d	-7.5 ^f	12.0 ^f
			-0.49 ^e	-1.5 ^g	
2	-0.51 ($\Delta E = 65$ mV)	-0.61	-0.11 ^d	-6.7 ^f	12.5 ^f
			-0.46 ^e	-2.7 ^g	
3	-0.51 ($\Delta E = 71$ mV)	-0.55	-0.01 ^d	-6.6 ^f	11.8 ^f
			-0.38 ^e	-3.6 ^g	

^aPotentials reported versus NHE. ^bValues correspond to the $E_{1/2}$ values obtained from cyclic voltammetry experiments at pH 7 where no catalysis is observed, in parenthesis ΔE indicates the peak to peak separation between E_c and E_a waves. ^cDFT calculated values for the reduction of the penta-coordinated cobalt species with an aqua ligand in the axial position in cis orientation relative to the N-R group (R = H, **1**; R = CH₃, **2**; R = CH₂OH, **3**). ^dDFT calculated values for the penta-coordinated cobalt species with an hydrido ligand in the axial position in trans orientation relative to the N-R group (R = H, **1**; R = CH₃, **2**; R = CH₂OH, **3**). ^eDFT calculated values for the octahedral cobalt species with aqua and hydrido ligands in the axial positions, the latter in trans orientation relative to the N-R group (R = H, **1**; R = CH₃, **2**; R = CH₂OH, **3**). ^fDFT calculated values for the penta-coordinated cobalt species with an hydrido ligand in the axial position in trans orientation relative to the N-R group (R = H, **1**; R = CH₃, **2**; R = CH₂OH, **3**) to give a square planar cobalt species upon proton loss. ^gDFT calculated values for the octahedral cobalt species with aqua and hydrido ligands in the axial positions, the latter in trans orientation relative to the N-R group (R = H, **1**; R = CH₃, **2**; R = CH₂OH, **3**) to give a penta-coordinated cobalt species upon proton loss.



Methods

All calculations were carried out by Mr Mauro Schilling in the S. Luber group in the University of Zürich, using the Turbomole software package (version 7.1)². Geometry optimizations and frequency analyses were performed employing unrestricted Kohn-Sham density functional theory by means of the BP86 exchange-correlation functional^{3,4}, the def2-TZVP basis set⁵, Grimme's D3 dispersion correction⁶ and the COSMO solvation model⁷ (dielectric constant $\epsilon = 80$ for water, default radii) (BP86-D3/def2-TZVP(COSMO)). Single-point energies were obtained at the B3LYP-D3/def2-TZVP(COSMO) level of theory^{8,9}.

All calculations were sped-up by means of the Resolution-of-the-Identity approach (RI-J, with its corresponding auxiliary basis sets¹⁰⁻¹²) and Multipole-Assisted-RI-J¹³ (MARIJ). The Gibbs free energy correction terms were at a pressure of 1~bar and a temperature of 298.15~K, without any scaling of the normal modes. Those terms are based on the description of a rigid-rotator within the harmonic approximation. Furthermore, Gibbs free energies were corrected for the change in standard state from 1~bar to 1~M by adding 1.9~kcal/mol (rsp. 1~bar to 55.6~M for water, i.e. 4.28~kcal/mol).

As the spin state of most intermediates and transitions states remain unknown, calculations were performed for a low-spin (lowest possible spin-state at a given charge) and high-spins state (two more unpaired electrons compared to the low-spin state). All reported free energies, reduction potentials or pK_a values were obtained for the lowest energy structures and sometimes contain a spin-flip. In cases where we found a spin-contamination of more than 10% (calculated vs theoretically expected), electronic energies were corrected according to:

$$E_{spin-corr} = \frac{E_S - aE_{(S+1)}}{1 - a}$$
$$a = \frac{\langle S_S^2 \rangle - S(S+1)}{\langle S_{(S+1)}^2 \rangle - S(S+1)}$$

Where S is the spin angular momentum, E_S and $E_{(S+1)}$ are the electronic energies (B3LYP-D3//def2-TZVP(COSMO)) obtained for their respective spin



Factors influencing HE (photo)catalysis in cobalt macrocycles

state. $\langle S_S^2 \rangle$ and $\langle S_{(S+1)}^2 \rangle$ are the squares of the total angular momentum calculated at the indicated level of theory^{14,15}.

Initial guesses for the transition state search were obtained from minimum energy pathways obtained by the Turbomole module *woelfling* using chain-of-states method¹⁶. Those guesses were further refined using the transition state optimization procedures implemented in Turbomole. Normal mode analysis was used to check that each transition state possesses exactly one imaginary mode, which represents the chemical reaction of interest. Further the transition mode was used to locate the associated reactant and product states. It is worth mentioning, that coordinated hydrogen (H_2) is often found to dissociate rather than to form a stable intermediate.

The standard reduction potentials were calculated according to:

$$\Delta E_{red}^{\circ} = \frac{\Delta G_{red}^{\circ}}{nF} - E_{SHE}^{absolute}$$

Where ΔG_{red}° is the free energy of the reduction, n is the number of electrons, F the Faraday constant, and $E_{SHE}^{absolute}$ the potential of the standard hydrogen electrode (SHE) taken as 4.28~V¹⁷.

Acidity constants were calculation according to:

$$pK_A = \frac{\Delta G_{diss}^{\circ}}{\ln(10) RT}$$

$$\Delta G_{diss}^{\circ} = G(A_{solv}^{-}) + G(H_{solv}^{+}) - G(AH_{solv})$$

Where ΔG_{diss}° is the standard free energy of the deprotonation, R the universal gas constant and T the temperature (298.15~K). $\Delta G_{solv}^{H^+}$ is taken from the experimental solvation free energy of a proton in water (265.9~kcal/mol)¹⁸. $G_{gas}^{H^+}$ is computed from the translational partition function (-6.3~kcal/mol)^{17,19}, the sum of the latter is equal to $G(H_{solv}^{+})$.

There are more advanced protocols to determine pK_a values and reduction potentials in the literature^{18,20-23}.



As we are not primarily interested in the absolute values but rather in the relative differences between structural isomers (penta or hexa-coordinated) as well as the difference between the three catalysts (CAT1, CAT2, and CAT3) we decided that a protocol analogously to one used by Call et al. would be sufficient¹⁷. Further, transition states for the intermolecular pathway could only be obtained when the geometries were optimized employing the COSMO solvation model. For the sake of consistency, we therefore refrained to optimize the structures of all the intermediates in the gas phase, as it would be required for some other protocols for the calculation of pK_A values and reduction potentials.

The relevant results of these calculations are given in Table S3 and in the main manuscript. The details are going to be publish in a separate thesis and in the form of a scientific paper in due course.



Factors influencing HE (photo)catalysis in cobalt macrocycles

3.5.5. X-ray diffraction (XRD) methods and additional data

Crystal preparation: Crystals of **2**, **3**, **4** and **5** were grown by slow diffusion of antisolvent into cataluyst solution (see synthetic procedures). The measured crystals were prepared under inert conditions immersed in perfluoropolyether as protecting oil for manipulation.

Data collection: Crystal structure determinations of **2**, **4** and **5** were carried out using a Apex DUO Kappa 4-axis goniometer equipped with an APPEX 2 4K CCD area detector, a Microfocus Source E025 luS using MoK α radiation (0.71073 Å), Quazar MX multilayer Optics as monochromator and a Oxford Cryosystems low temperature device Cryostream 700 plus ($T = -173\text{ }^{\circ}\text{C}$). Full-sphere data collection was used with ω and φ scans. *Programs used:* Data collection APEX-2¹, data reduction Bruker Saint² V/.60A and absorption correction SADABS³.

Crystal structure determination for compound **3** was carried out using a Rigaku diffractometer equipped with a Pilatus 200K area detector, a Rigaku MicroMax-007HF microfocus rotating anode with MoK α radiation, Confocal Max Flux optics and an Oxford Cryosystems low temperature device Cryostream 700 plus ($T = -173\text{ }^{\circ}\text{C}$). Full-sphere data collection was used with ω and φ scans. *Programs used:* Data collection and reduction with CrysAlisPro⁴ V/.60A and absorption correction with Scale3 Abspack scaling algorithm⁵.

¹ Data collection with APEX II v2014.9-0. Bruker (2014). Bruker AXS Inc., Madison, Wisconsin, USA.

² Data reduction with Bruker SAINT+ version V8.35A. Bruker (2013). Bruker AXS Inc., Madison, Wisconsin, USA.

³ SADABS: V2014/5 Bruker (2001). Bruker AXS Inc., Madison, Wisconsin, USA. Blessing, Acta Cryst. (1995) A51 33-38.

⁴ Data collection and reduction with CrysAlisPro 1.171.39.12b (Rigaku OD, 2015).

⁵ Empirical absorption correction using spherical harmonics implemented in Scale3 Abspack scaling algorithm, CrysAlisPro 1.171.39.12b (Rigaku OD, 2015).

Structure Solution and Refinement:

Crystal structure solution was achieved using the computer program SHELXT⁶. Visualization was performed with the program SHELXle⁷. Missing atoms were subsequently located from difference Fourier synthesis and added to the atom list. Least-squares refinement on F^2 using all measured intensities was carried out using the program SHELXL 2015⁸. All non-hydrogen atoms were refined including anisotropic displacement parameters.

Comments to the structures:

5: The asymmetric unit contains one molecule of the metal complex. The Cobalt atom is not coordinated as expected with two Chlorine atoms, it is coordinated to a Chlorine atom and to cobalt trichloride. In the structure one of the alkane chains is disordered in two orientations (ratio: 55:45). Compound **3:** The asymmetric unit contains one molecule of the metal complex and a Chlorine/Bromine-anion in a shared position with a relative occupancy of respectively 92:08. The structure contains two additional independent water molecules. **2:** The asymmetric unit contains one molecule of the metal complex coordinated to an acetonitrile molecule and two ClO_4^- -anions. **4:** The asymmetric unit contains one molecule of the metal complex and a ClO_4^- -anion. The ClO_4^- -anion is disordered in two orientations with a ratio of 59:41. The oxygen in the metal complex is coordinated to the Cobalt atom. It is not clear if this oxygen has a hydrogen atom bonded; but it could not be localized experimentally from the electron densities.



⁶ SHELXT; Sheldrick, G.M. *Acta Cryst.* **2015** A71, 3-8.

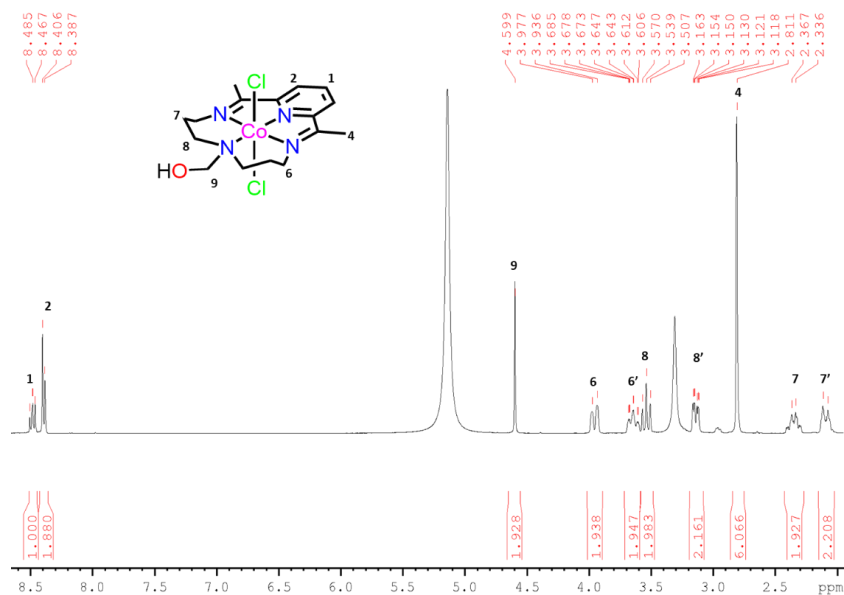
⁷ SHELXle; C.B. Huebschle, G.M. Sheldrick & B. Dittrich; *J.Appl.Cryst.* (2011) 44, 1281-1284.

⁸ SHELXL; Sheldrick, G.M. *Acta Cryst.* **2015** C71, 3-8. SHELXT.

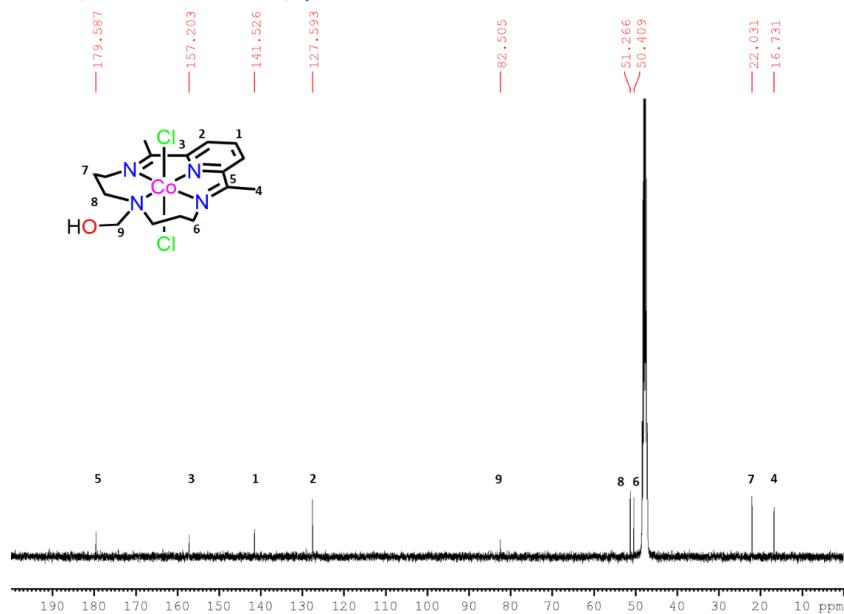
Factors influencing HE (photo)catalysis in cobalt macrocycles

3.5.6. NMR characterization of 3, 4 and 5

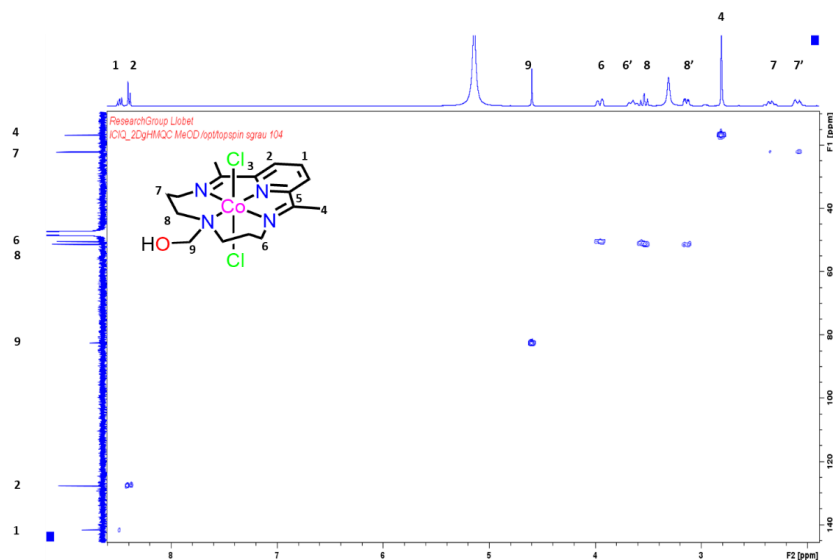
NMR spectra of 3



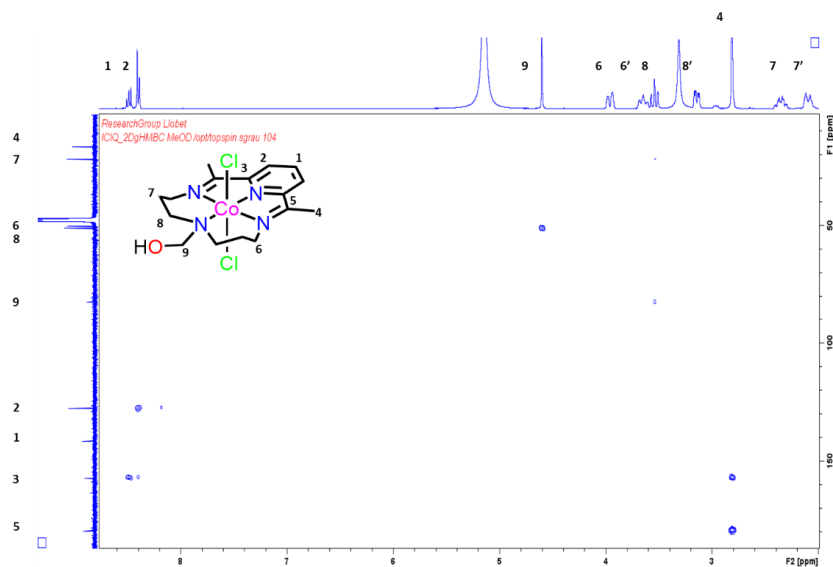
¹H NMR (400MHz, MeOD-d₄) spectrum of 3.



¹³C NMR (101MHz, MeOD-d₄) spectrum of 3.



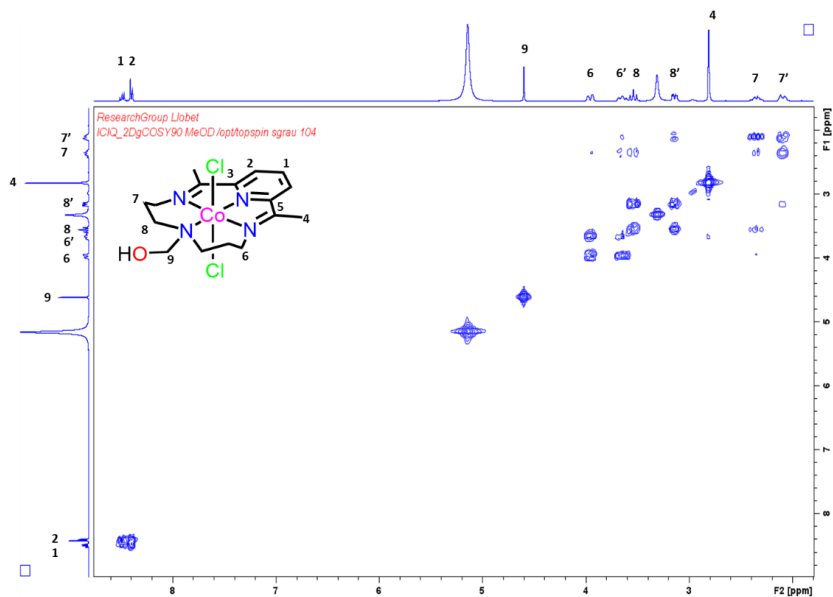
HSQC (400MHz, MeOD-d₄) spectrum of **3**.



HMBC (400MHz, MeOD-d₄) spectrum of **3**.



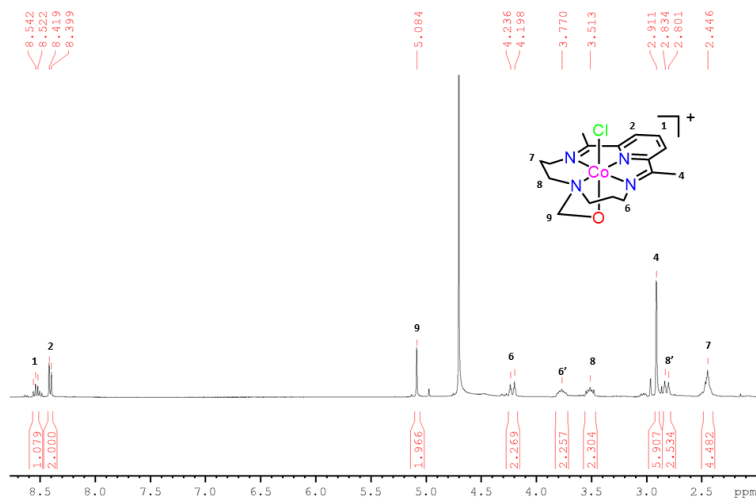
Factors influencing HE (photo)catalysis in cobalt macrocycles



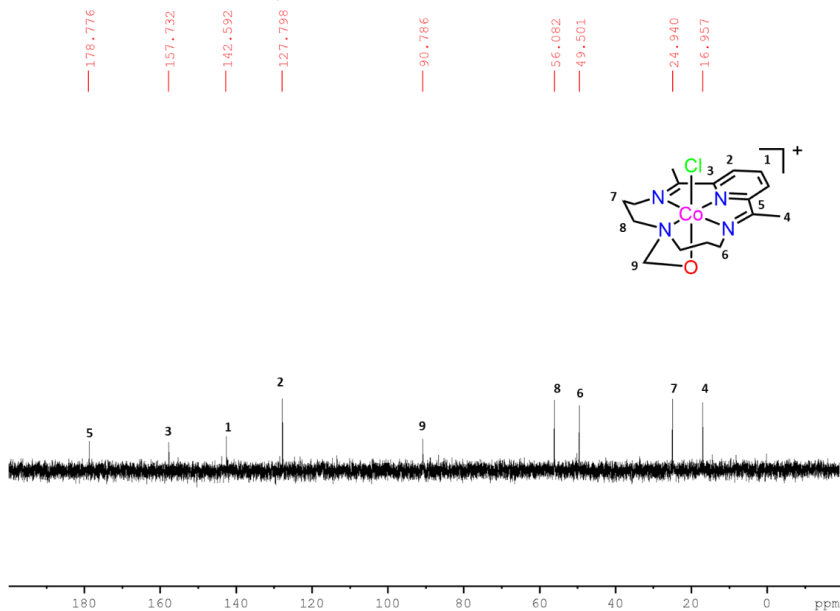
COSY (400MHz, MeOD-d₄) spectrum of **3**.



NMR spectra of 4



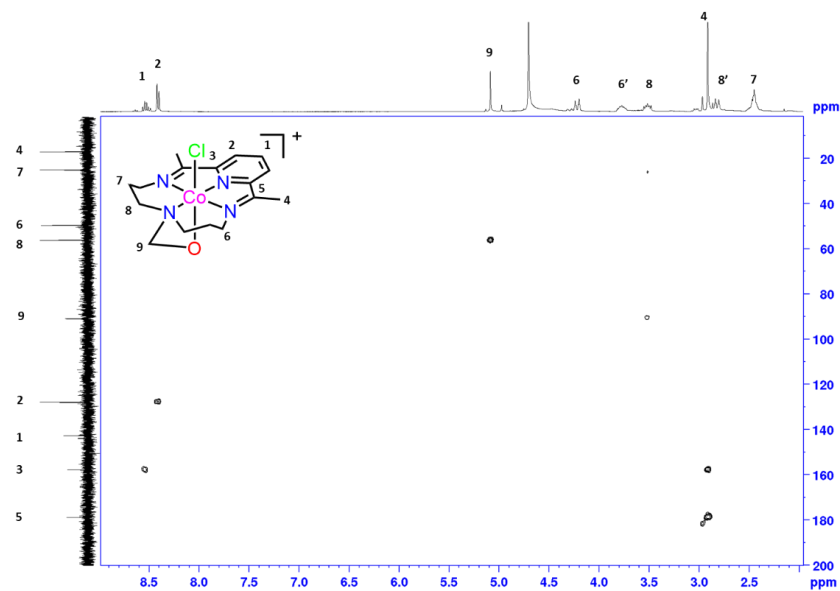
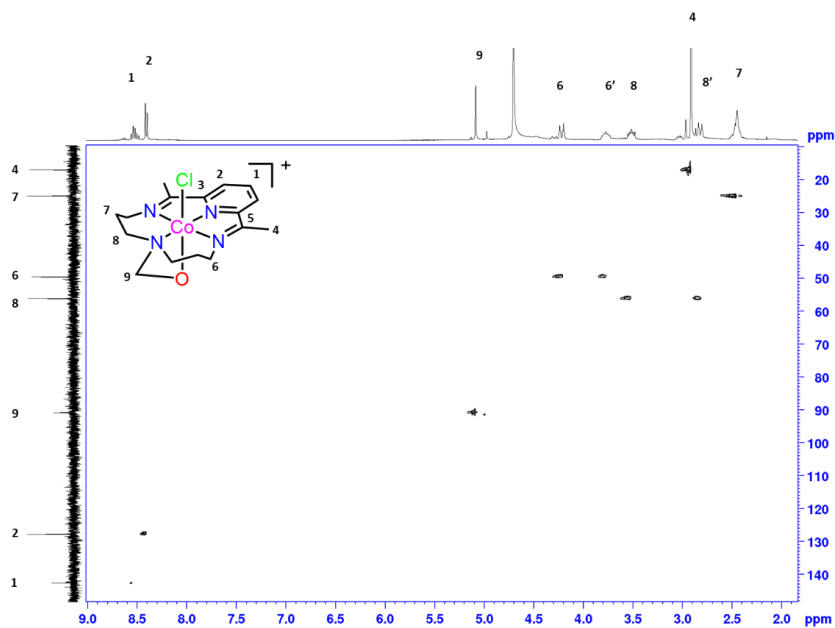
^1H NMR (500MHz, D_2O - d_2) spectrum of 4 in D_2O .

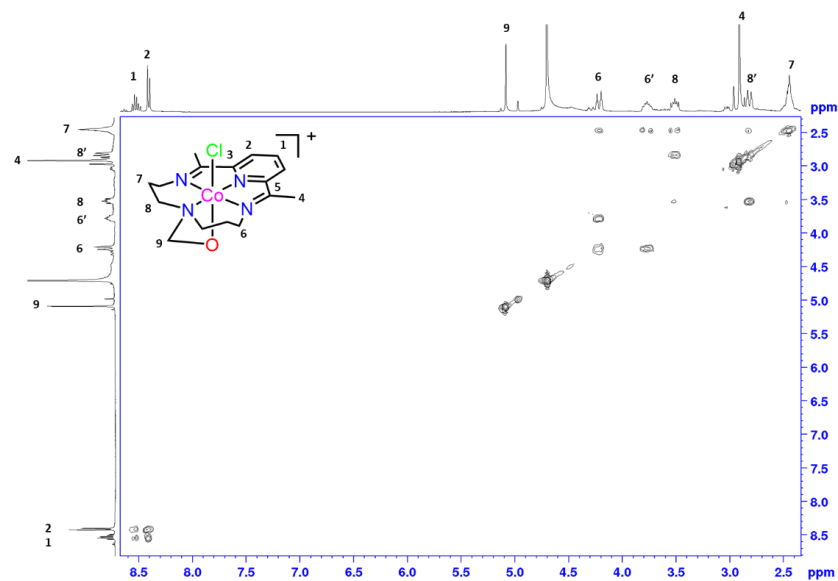


^{13}C NMR (400MHz, D_2O - d_2) spectrum of 4.



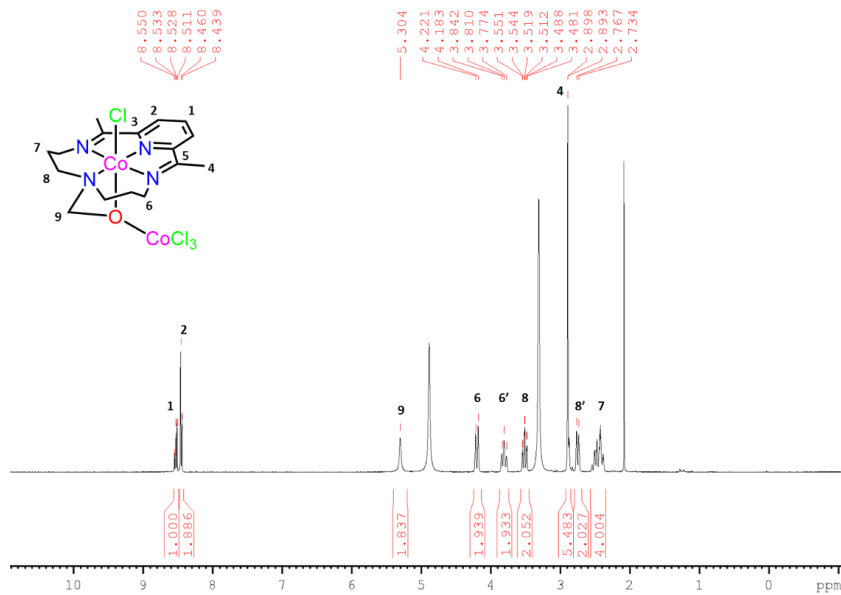
Factors influencing HE (photo)catalysis in cobalt macrocycles





COSY (400MHz, D₂O-d₂) spectrum of 4.

NMR spectra of 5

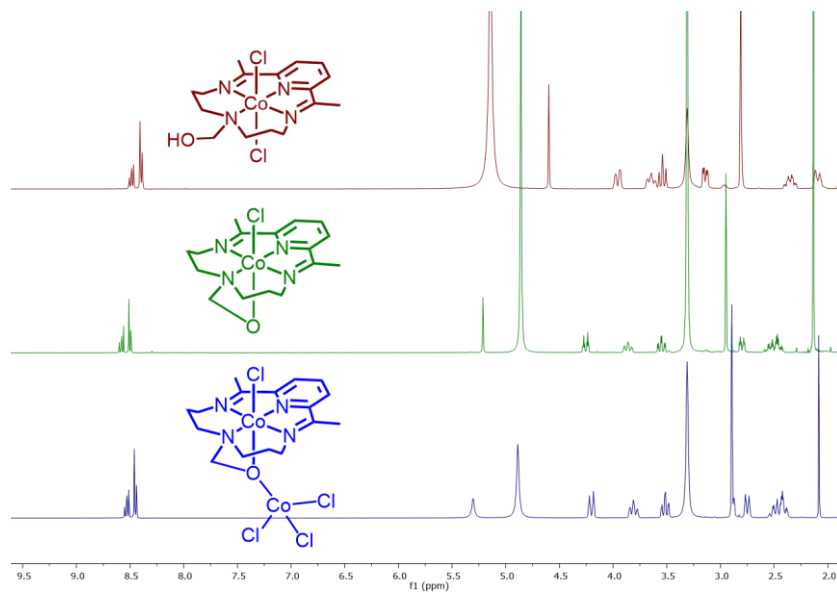


¹H NMR (400MHz, MeOD-d₄) spectrum of 5.



Factors influencing HE (photo)catalysis in cobalt macrocycles

Overlapping of ^1H NMR spectra of 3, 4 and 5



^1H NMR (400MHz, MeOD-d_4) spectra of 3, 4 and 5.

3.5.7. References

- (1) Molton, F.; Fortage, J.; Deronzier, A.; Blackman, A. G.; Stoll, T.; Collomb, M.-N.; Varma, S.; Castillo, C. E. Efficient Photocatalytic Hydrogen Production in Water Using a Cobalt(iii) Tetraaza-Macrocyclic Catalyst: Electrochemical Generation of the Low-Valent Co(i) Species and Its Reactivity toward Proton Reduction. *Phys. Chem. Chem. Phys.* **2013**, *15* (40), 17544. <https://doi.org/10.1039/c3cp52641k>.
- (2) Ahlrichs, R.; Bär, M.; Häser, M.; Horn, H.; Kölmel, C. Electronic Structure Calculations on Workstation Computers: The Program System Turbomole. *Chem. Phys. Lett.* **1989**, *162* (3), 165–169. [https://doi.org/10.1016/0009-2614\(89\)85118-8](https://doi.org/10.1016/0009-2614(89)85118-8).
- (3) Becke, A. D. Density-Functional Exchange-Energy Approximation with Correct Asymptotic Behavior. *Phys. Rev. A* **1988**, *38* (6), 3098–3100. <https://doi.org/10.1103/PhysRevA.38.3098>.
- (4) Perdew, J. P. Density-Functional Approximation for the Correlation Energy of the Inhomogeneous Electron Gas. *Phys. Rev. B* **1986**, *33* (12), 8822–8824. <https://doi.org/10.1103/PhysRevB.33.8822>.
- (5) Weigend, F.; Ahlrichs, R. Balanced Basis Sets of Split Valence, Triple Zeta Valence and Quadruple Zeta Valence. *Phys. Chem. Chem. Phys.* **2005**, *7*, 3297–3305. <https://doi.org/10.1039/b508541a>.
- (6) Grimme, S.; Antony, J.; Ehrlich, S.; Krieg, H. A Consistent and Accurate Ab Initio Parametrization of Density Functional Dispersion Correction (DFT-D) for the 94 Elements H-Pu. *J. Chem. Phys.* **2010**, *132* (15), 154104. <https://doi.org/10.1063/1.3382344>.
- (7) Klamt, A.; Schuurmann, G. COSMO: A New Approach to Dielectric Screening in Solvents with Explicit. *J. Chem. Soc. Perkin Trans* **1993**, *2*, 799–805. <https://doi.org/10.1039/P29930000799>.
- (8) Becke, A. D. Density-Functional Thermochemistry. III. The Role of Exact Exchange. *J. Chem. Phys.* **1993**, *98* (7), 5648–5652. <https://doi.org/10.1063/1.464913>.
- (9) Lee, C.; Yang, W.; Parr, R. G. Development of the Colle-Salvetti Correlation-Energy Formula into a Functional of the Electron Density. *Chem. Phys. Lett.* **1988**, *37* (2), 785–789. [https://doi.org/10.1016/0009-2614\(89\)85118-8](https://doi.org/10.1016/0009-2614(89)85118-8).
- (10) Eichkorn, K.; Treutler, O.; Öhm, H.; Häser, M.; Ahlrichs, R. Auxiliary Basis Sets to Approximate Coulomb Potentials (Chem. Phys. Letters 240 (1995) 283-290). *Chem. Phys. Lett.* **1995**, *242* (6), 652–660. [https://doi.org/10.1016/0009-2614\(95\)00838-U](https://doi.org/10.1016/0009-2614(95)00838-U).
- (11) Eichkorn, K.; Weigend, F.; Treutler, O.; Ahlrichs, R. Auxiliary Basis Sets



Factors influencing HE (photo)catalysis in cobalt macrocycles

- for Main Row Atoms and Transition Metals and Their Use to Approximate Coulomb Potentials. *Theor. Chem. Acc.* **1997**, 97 (1-4), 119–124. <https://doi.org/10.1007/s002140050244>.
- (12) Weigend, F. Accurate Coulomb-Fitting Basis Sets for H to Rn. *Phys. Chem. Chem. Phys.* **2006**, 8 (9), 1057–1065. <https://doi.org/10.1039/b515623h>.
- (13) Sierka, M.; Hogekamp, A.; Ahlrichs, R. Fast Evaluation of the Coulomb Potential for Electron Densities Using Multipole Accelerated Resolution of Identity Approximation. *J. Chem. Phys.* **2003**, 118 (20), 9136–9148. <https://doi.org/10.1063/1.1567253>.
- (14) Yamaguchi, K.; Jensen, F.; Dorigo, A.; Houk, K. N. A Spin Correction Procedure For Unrestricted HF and MP Wavefunctions for Singlet Diradicals and Polyradicals. *Chem. Phys. Lett.* **1988**, 149, 537–542.
- (15) Wittbrodt, J. M.; Schlegel, H. B. Some Reasons Not to Use Spin Projected Density Functional Theory. *J. Chem. Phys.* **1996**, 105 (15), 6574–6577. <https://doi.org/10.1063/1.472497>.
- (16) Plessow, P. Reaction Path Optimization without NEB Springs or Interpolation Algorithms. *J. Chem. Theory Comput.* **2013**, 9 (3), 1305–1310. <https://doi.org/10.1021/ct300951j>.
- (17) Call, A.; Franco, F.; Kandoth, N.; Fernández, S.; González-Béjar, M.; Pérez-Prieto, J.; Luis, J. M.; Lloret-Fillol, J. Understanding Light-Driven H₂ Evolution through the Electronic Tuning of Aminopyridine Cobalt Complexes. *Chem. Sci.* **2018**, 9 (9), 2609–2619. <https://doi.org/10.1039/c7sc04328g>.
- (18) Marenich, A. V.; Ho, J.; Coote, M. L.; Cramer, C. J.; Truhlar, D. G. Computational Electrochemistry: Prediction of Liquid-Phase Reduction Potentials. *Phys. Chem. Chem. Phys.* **2014**, 16 (29), 15068–15106. <https://doi.org/10.1039/c4cp01572j>.
- (19) Kelly, C. P.; Cramer, C. J.; Truhlar, D. G. Aqueous Solvation Free Energies of Ions and Ion-Water Clusters Based on an Accurate Value for the Absolute Aqueous Solvation Free Energy of the Proton. *J. Phys. Chem. B* **2006**, 110 (32), 16066–16081. <https://doi.org/10.1021/jp063552y>.
- (20) Wang, T.; Brudvig, G. W.; Batista, V. S. Study of Proton Coupled Electron Transfer in a Biomimetic Dimanganese Water Oxidation Catalyst with Terminal Water Ligands. *J. Chem. Theory Comput.* **2010**, 6 (8), 2395–2401. <https://doi.org/10.1021/ct1002658>.
- (21) Liao, R. Z.; Siegbahn, P. E. M. Quantum Chemical Modeling of Homogeneous Water Oxidation Catalysis. *ChemSusChem* **2017**, 10 (22), 4236–4263. <https://doi.org/10.1002/cssc.201701374>.
- (22) Schilling, M.; Lubner, S. Computational Modeling of Cobalt-Based Water



- Oxidation: Current Status and Future Challenges. *Front. Chem.* **2018**, *6* (April), 100. <https://doi.org/10.3389/fchem.2018.00100>.
- (23) Ho, J. Are Thermodynamic Cycles Necessary for Continuum Solvent Calculation of pKas and Reduction Potentials? *Phys. Chem. Chem. Phys.* **2015**, *17* (4), 2859–2868. <https://doi.org/10.1039/c4cp04538f>.
- (24) Huang, Y.; Nielsen, R. J.; Goddard, W. A.; Soriaga, M. P. The Reaction Mechanism with Free Energy Barriers for Electrochemical Dihydrogen Evolution on MoS₂. *J. Am. Chem. Soc.* **2015**, *137* (20), 6692–6698. <https://doi.org/10.1021/jacs.5b03329>.
- (25) Morris, R. H. Brønsted-Lowry Acid Strength of Metal Hydride and Dihydrogen Complexes. *Chem. Rev.* **2016**, *116* (15), 8588–8654. <https://doi.org/10.1021/acs.chemrev.5b00695>.





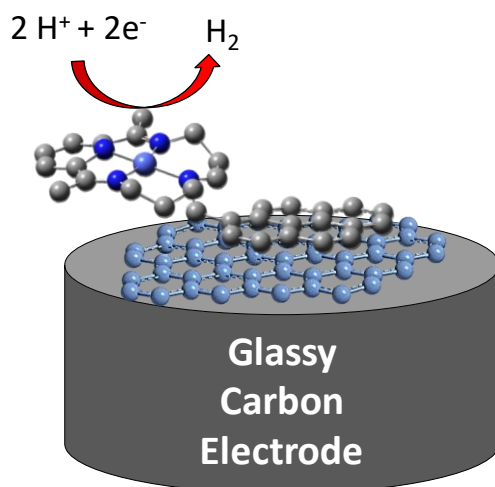
Chapter

4

A molecular cathode for hydrogen evolution catalysis

A cobalt macrocyclic complex bearing a pyrene moiety in the ligand scaffold was developed for proton reduction. Its electrochemical properties have been characterized showing important differences in its catalytic properties compared to its analogous catalyst without the pyrene group. The catalyst has been used to prepare molecular cathodes by anchoring it on graphene powder by π - π stacking. A solid state analysis as well as an electrochemical study of the complex in solution and on the electrode reveal a strong interaction between the dangling pyrene group and the Co metal center which strongly affects its catalytic properties. By using different electrochemical techniques we were able to determine the onset potential of the electrode as well as the faradaic efficiency of the overall catalytic process.

A molecular cathode for hydrogen evolution catalysis



Abstract



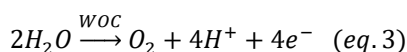
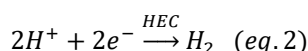
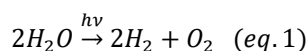
A cobalt based macrocyclic complex active for the hydrogen evolution catalysis, bearing a pyrene moiety in the ligand backbone (**Co-pyr**) has been synthesized and thoroughly characterized in the solid state by single crystal x-ray diffraction analysis and x-ray absorption spectroscopy and in solution through spectroscopic and electrochemical techniques. The pyrene group allows to use this catalyst in heterogeneous phase by allowing π - π stacking with graphene powder that is later dropcasted on conductive electrodes to form the molecular cathode GC@G-Co-Pyr. Electrochemical characterization of this hybrid electrode reveals that the pyrene moiety is not only giving the ability to anchor the catalyst on graphitic surfaces but also has a strong influence on the conformation of the complex and electronic effects on the cobalt metal center modifying its catalytic activity compared to its analogous homogeneous catalyst.

Contributions:

Sergi Grau Abarca synthesized and characterized all the compounds, carried out the photochemical, electrochemical and UV-vis spectroscopic experiments.

4.1 Introduction

In the field of light induced water splitting (eq. 1), the development of electrodes and photoelectrodes for the hydrogen evolution (HER) (eq. 2) and oxygen evolution reaction (OER) (eq. 3) is a topic of extensive research (Figure 6, Chapter 1).¹ A recent strategy in this line is the use of molecular catalysts (i.e. hydrogen evolution catalysts (HEC) and water oxidation catalysts (WOC)) that have shown high activity in homogeneous conditions.¹⁻⁵



In order to use such catalysts in the required heterogeneous phase, they need to be functionalized with an appropriate functional group that will be the link between the catalyst and the conductive or semiconductor support (Figure 1).⁶ The type of linkage will determine the nature of the support, for instance, carboxylate and phosphonate groups have been shown to attach on metal oxide conductors and semiconductors such as fluorine doped tin oxide (FTO) or titanium dioxide (TiO₂) via M-O covalent bond, a common strategy in dye-sensitized solar cell's field.⁷⁻¹³ Another strategy is to cover the (photo)electrode with polymers, where the catalyst can directly be linked.¹⁴⁻¹⁷ Alternatively, C-C bonds or π - π stacking interactions are used to attach molecular catalyst on carbon-based electrodes such as glassy carbon¹⁸⁻²²

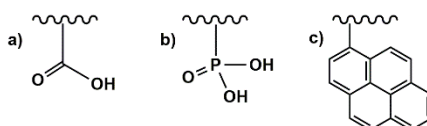


Figure 1. Binding moieties to anchor molecular catalyst to metal oxides via covalent bonds (a and b) and graphitic materials via π - π stacking interactions (c): a) Carboxylic Acid, b) Phosphonic Acid and c) Pyrene.

A molecular cathode for hydrogen evolution catalysis

In this work, we synthesize, characterize and study the electrochemical and photochemical activity towards HER of a cobalt macrocycle with a pyrene moiety that has been incorporated in the ligand scaffold with the aim of attaching the catalyst on carbon-based electrodes (**Co-Pyr**, Figure 2). The catalytic center of **Co-Pyr** is inspired by a previously reported highly active molecular catalyst (**Co-NH**, Figure 2 and Chapter 3).²³⁻²⁶ Thus, this catalyst is used to functionalize graphitic materials in order to prepare molecular electrodes active for HER in water. To compare and evaluate the structure, chemical and electrochemical properties in homogeneous phase, the analogous catalyst without pyrene moiety was used in this work (**Co-Me**, Figure 2).

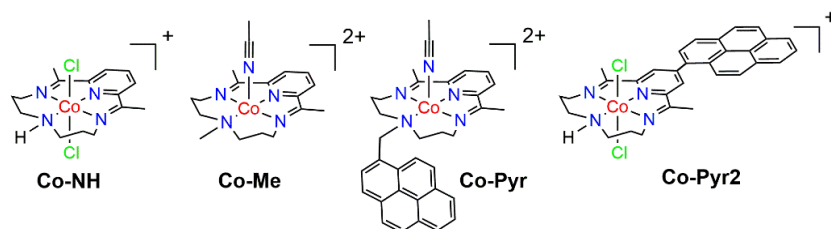
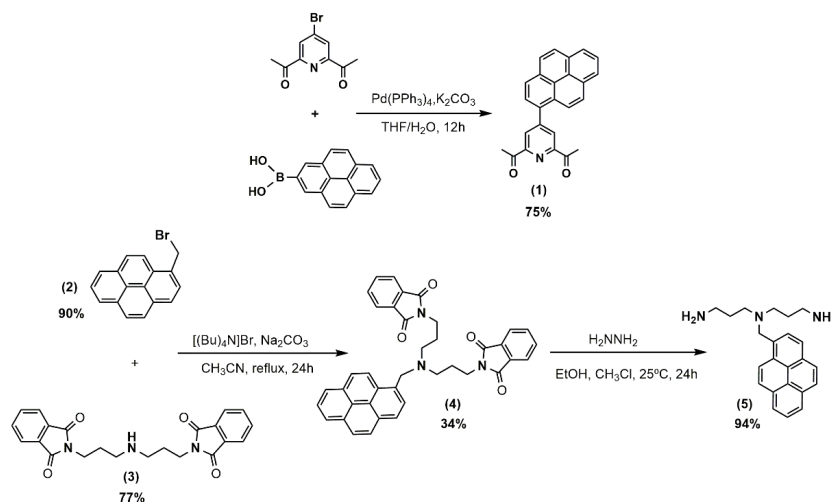


Figure 2. Structure of the hydrogen evolution catalyst **Co-Pyr** studied in this work and selected macrocyclic complexes.

4.2 Results and discussion

4.2.1 Synthesis, spectroscopic and structural characterization.

To anchor our catalyst on graphitic materials, two ligand precursors containing a pyrene group were synthesized (**1** and **5** in Scheme 1). The first one was prepared in one-step reaction from 4-bromo-2,6-diacetylpyridine and pyrene-1-boronic acid via Suzuki cross-coupling conditions in 75% yield. The second one, is based on a bis-(3-aminopropyl)amine scaffold functionalized with a methylenepyrene group (**5**, Scheme 1). The precursor 1-bromomethylpyrene **2** reacted with the protected bis-(3-aminopropyl)amine **3** via nucleophilic substitution obtaining compound **4** in 34% yield. The final ligand precursor **5** was isolated after deprotection using hydrazine in ethanol: CHCl_3 (9:2) mixture for 24h at room temperature with high yield (94%).

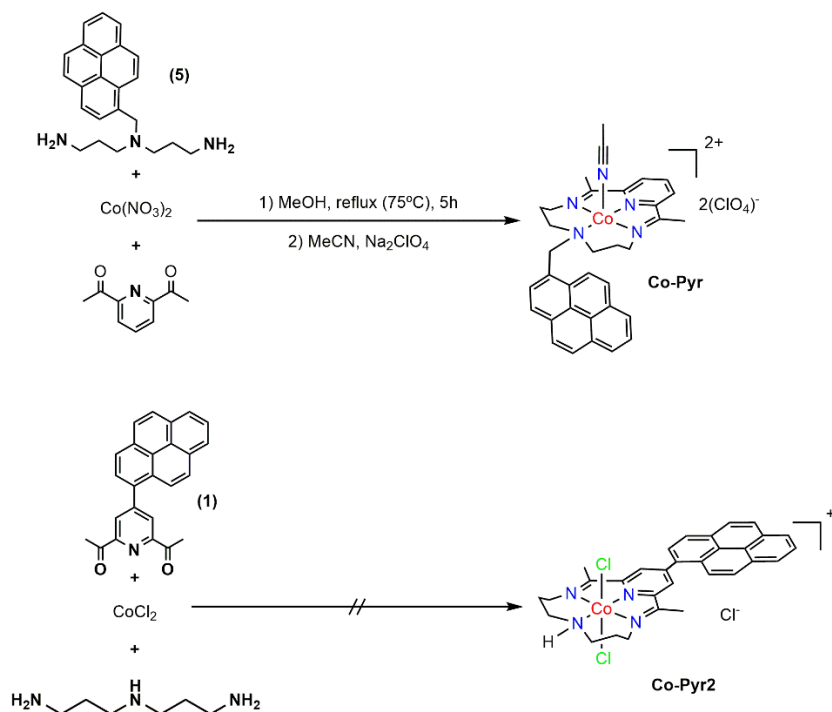


Scheme 1. Summary of the synthetic pathway followed in this work for the synthesis of ligand precursors **1** and **5**.

The synthesis of the cobalt complexes derived from ligand precursors **1** and **5** were attempted using a modified reported procedure²⁷⁻²⁹, which consists of a one-step template synthesis starting from 2,6-diacetylpyridine and the corresponding bis-(3-aminopropyl)amine derivative **5** to obtain **Co-Pyr** and 4-pyrene-2,6-diacetylpyridine **1** and bis-(3-aminopropyl)amine to obtain **Co-Pyr2** (Scheme 2).



A molecular cathode for hydrogen evolution catalysis



Scheme 2. Synthetic pathways followed to obtain HEC with a pyrene moiety.

Several attempts of preparing **Co-Pyr2** were carried out on without fruitful results. Due to the low solubility of **1** in EtOH/H₂O mixture, some modifications in the reaction conditions such as mixture of solvents, temperature and reaction time were done without getting the desired **Co-Pyr2**. We concluded that the addition of the pyrene moiety in the 2,6-diacetylpyridine ligand precursor hinders the condensation/template reaction due to the electron withdrawing character of the pyrene moiety.

On the other hand, complex **Co-Pyr** was successfully prepared in moderate yields (15-25%) when the reaction was performed in anhydrous MeOH conditions and under nitrogen atmosphere (Scheme 2). Single crystals of Co-Pyr suitable for x-ray diffraction (XRD) studies were obtained and two different views of the ORTEP plots are shown in Figure 3.

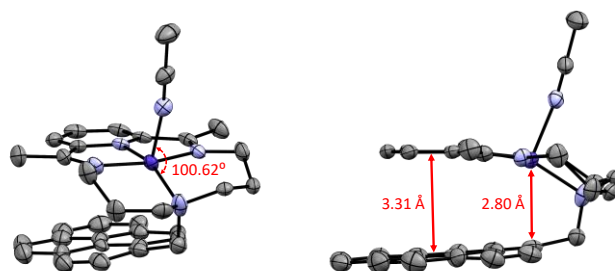


Figure 3. ORTEP plot at 50% probability of the cationic part of **Co-Pyr** with two different orientations. The H atoms as well as counter ions (ClO_4^-) have been omitted for clarity.

Co-Pyr is a Co^{II} penta-coordinated complex with a highly distorted square-based pyramidal geometry with an acetonitrile ligand occupying the axial position. An intramolecular π - π interaction between the pyridine ring of the equatorial ligand and the pyrene moiety distorts the geometry, forcing a more opened $\text{N}_{\text{MeCN}}\text{-Co-N}_{\text{amine}}$ angle for the **Co-Pyr** catalyst as compared to the analogous **Co-Me** ($100.62(14)^\circ$ and $95.56(6)^\circ$ respectively, Figure S2). On the other hand, bond distances $\text{Co-N}_{\text{MeCN}}$ and $\text{Co-N}_{\text{amine}}$ don't exhibit any remarkable differences between the two complexes. Besides the intramolecular π - π interaction with a distance of ca. 3.31 \AA , two intermolecular interactions between two pyrene groups and two pyridine groups of two different molecules are found in the crystal structure (ca. 3.34 and 3.37 \AA respectively, Figure S3). Interestingly, due to the intramolecular π - π interaction, the distance between the cobalt and the nearest carbon of the pyrene ring is only 2.80 \AA (Figure 3), a contact that has a strong electronic effect on the metal center that is manifested in the electrochemical properties and x-ray absorption spectroscopic energies of the complex as described and discussed in detail later on in this chapter.

The UV-Vis spectrum of **Co-Pyr** is presented in Figure S1. The Co^{II} species exhibits intense absorption bands between 250-400 nm, corresponding to π - π^* transitions of the ligands. In particular, **Co-Pyr** presents two strong peaks at 278 and 345 nm related to the pyrene moiety, which are not present for the **Co-Me** analog (compare blue and red traces in Figure S1, right). In the visible region, the two complexes show less intense absorptions with maxima at 449, 545 and 596 nm for **Co-Pyr** and 438 and 537 nm for **Co-Me**, corresponding to metal to ligand charge transfer (MLCT) bands and d-d transition bands.



A molecular cathode for hydrogen evolution catalysis

Interestingly, the UV-Vis spectrum of **Co-Pyr** is significantly different in pure water, pure MeCN and in a mixture water:MeCN (1:1), suggesting exchange of the acetonitrilo axial ligand by an aqua group upon dissolution in aqueous solutions (Figure S1, left). The same phenomenon has been observed for **Co-Me** (see Figure S6, Chapter 3).

4.2.2 Electrochemical characterization in organic media

The electrochemical properties of **Co-Pyr** were studied in MeCN-0.1M [(Bu)₄N]PF₆ by cyclic voltammetry (CV) and compared with those of **Co-Me**. The catalyst presents two chemically reversible metal centered one-electron waves belonging to Co^{III/II} and Co^{II/I} couples and one reversible wave assigned to reduction of the equatorial macrocyclic ligand L/L⁻ (see Figure 4 and Table S1 in the SI).



Co-Pyr shows a quasireversible wave associated to the Co^{II/I} couple with redox potential very close to the **Co-Me** wave ($E_{1/2} = -0.577\text{V}$ vs Fc⁺/Fc ($\Delta E = 105\text{mV}$) and $E_{1/2} = -0.555\text{V}$ vs Fc⁺/Fc ($\Delta E = 55\text{mV}$) respectively). The electrochemically irreversible but chemically reversible process belonging to Co^{III/II} couple features a large peak-to-peak separation. This process is most likely ruled by the same squared mechanism involving significant changes of geometry. The same mechanism was already proposed for **Co-Me** in Chapter 3 ($E_a = 0.986\text{V}$ and $E_c = 0.319\text{V}$ vs Fc⁺/Fc ($\Delta E = 647\text{mV}$)) (see Figure S2, Chapter 3). Finally, the wave associated to the quasireversible redox process of the equatorial ligand is only slightly shifted anodically compared to **Co-Me** ($E_{1/2} = -1.754\text{V}$ vs Fc⁺/Fc ($\Delta E = 106\text{mV}$) and $E_{1/2} = -1.776\text{V}$ vs Fc⁺/Fc ($\Delta E = 73\text{mV}$) respectively).

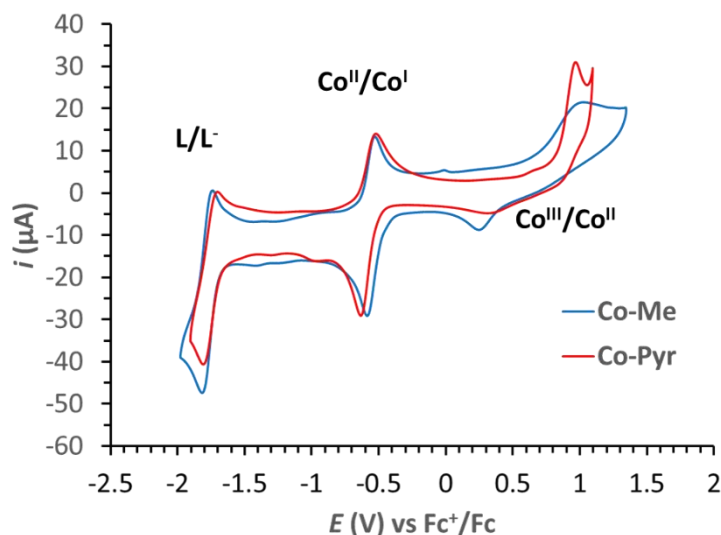


Figure 4. Cyclic Voltammometry experiments of 1mM Co-Pyr (red) and Co-Me (blue) in MeCN-0.1M [(Bu)₄N]PF₆. WE: GC Disk. CE: Pt Disk. Scan rate: 100mV/s. All potentials are referred versus ferrocene.



4.2.3 Electrochemical characterization in aqueous media

The electrochemical properties of **Co-Pyr** were tested in different pHs in order to evaluate its activity towards the proton reduction. It's known that the family of macrocyclic complexes shown in Figure 2 and discussed in Chapter 3 are active only in acidic pHs due to slow protonation of the active Co^I intermediate species (usually lower than 4.1)^{23,24,30}. Thus, the cyclic voltammometry experiments were recorded in the pH range between 2-7 (Figure 5). All redox potentials for experiments done in aqueous solutions are reported versus the normal hydrogen electrode (NHE).

A molecular cathode for hydrogen evolution catalysis

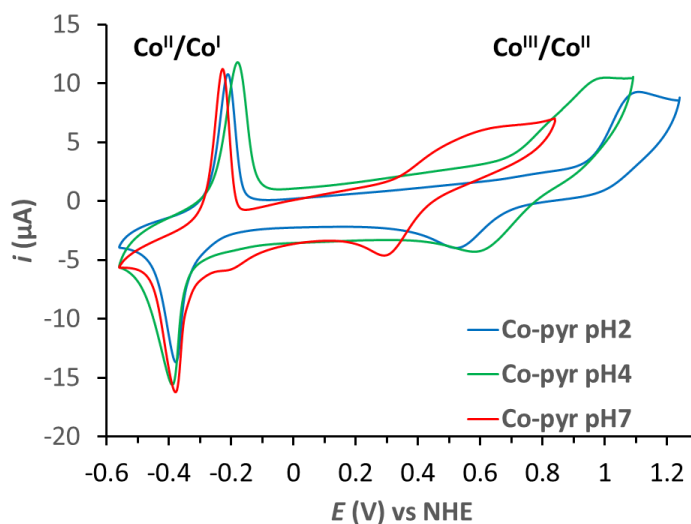


Figure 5. Cyclic Voltammometry experiments of 1mM Co-Pyr in pH 2 (phosphate buffer), pH 4 (Acetate buffer) and pH 7 (phosphate buffer). WE: GC Disk. RE: SCE. CE: Pt Disk. Scan rate 100 mV/s.



Using Glassy Carbon Electrode (GCE) as working electrode and a 1mM of **Co-Pyr** in aqueous solution, two redox waves associated to the one-electron-metal-centered processes can be observed (Figure 5). The $\text{Co}^{\text{II/I}}$ redox couple is pH independent (Table S2). The sharp peaks observed for this process are typical of adsorption phenomenon,³¹ suggesting that complex **Co-Pyr** attaches to the surface upon reduction, a process induced by the presence of the pyrene moiety in the ligand that can form π - π stacking interactions with the glassy carbon structure of the electrode. These results are in sharp contrast to the behavior of **Co-Pyr** in MeCN, where this adsorption process is not observed after several CV scans. Analysis of the i_p vs squared root of the scan rate plot reveals a linear behavior, suggesting that despite the adsorption process, it is still controlled by diffusion (Figure S4, bottom). The fact that the peaks do not increase along several scans indicates that all the absorbed catalyst during the cathodic scan are desorbed from the surface along the subsequent anodic scan. Moreover, the relatively large peak-to-peak separation of the oxidation and reduction process ($\Delta E = 150$ mV) suggests a strong interaction between electrode and the absorbed catalyst, requiring higher potentials to oxidize and desorb the **Co-Pyr**. The nature of this interaction is further analyzed by x-ray absorption spectroscopy studies in the next section.

The $\text{Co}^{\text{II/I}}$ redox potentials of **Co-Pyr** and **Co-Me** show a difference of 180 mV (-0.301 V and -0.482 V respectively, Figure 6). This anodic shift is attributed to the electron-withdrawing character of the pyrene moiety, which is prone to interact with the cobalt center as shown by the solid state structure of **Co-Pyr** (Figure 3). This electronic effect is not observed in MeCN, where the redox potentials of the $\text{Co}^{\text{II/I}}$ couple have essentially the same value for both catalysts (Figure 4). These results highlight the strong influence of the nature of the solvent, which can induce different solvation environments and make the complex adopt different conformations with or without the contact of the cobalt center with the pyrene moiety.

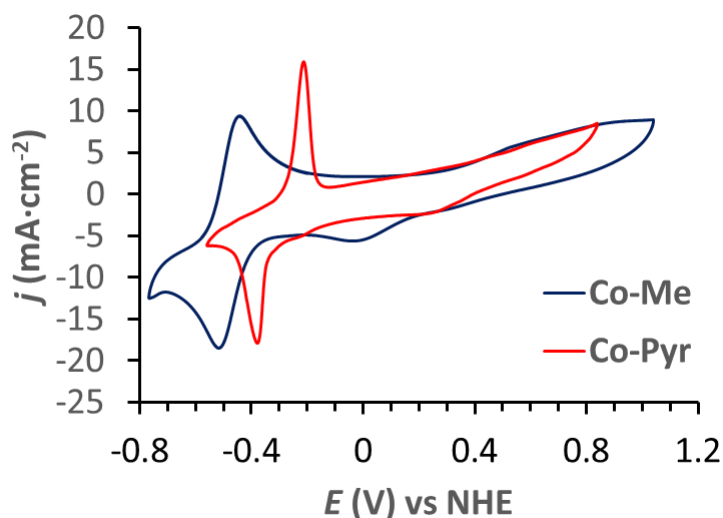


Figure 6. Cyclic Voltammetry experiments of 1mM **Co-Pyr** (red line) and 1mM **Co-Me** (blue line) in pH 7 (phosphate buffer). WE: GC Disk. RE: SCE. CE: Pt Disk. Scan rate 100 mV/s.

On the other hand, the $\text{Co}^{\text{II/III}}$ couple is pH dependent, controlled by diffusion and also shows the same square mechanism observed in MeCN ($\Delta E = 320\text{-}575\text{mV}$, Table S2). This pH dependency supports the hypothesis that the MeCN initially coordinated to the metal center is substituted by an aqua ligand as soon as it dissolves in aqueous media, as was also discussed above for the UV-Vis spectra of this compound in pure water, pure MeCN and mixture 1:1



A molecular cathode for hydrogen evolution catalysis

(water:MeCN) (Figure S1). Such a Co-OH₂ group could be involved in proton coupled electron transfer (PCET) process inducing changes in redox potential at different levels of protonation.³²

It is important to notice that no apparent catalytic wave was observed in neither pH 2 nor 4. In our previous work, we demonstrate that the rate-determining step for the hydrogen evolution reaction of this family of cobalt complexes is the protonation of the Co^I species (see Chapter 3). If the rate constant of this reaction is low, the timescale of the measurement doesn't give enough time to form the Co^{III}-H species and the following H₂ formation is hindered. Thus, cyclic voltammetry experiments with different scan rates (from 5 to 2000 mV/s) were recorded in order to check the activity of the catalyst at different time scales (Figure S4). Even at very low scan rates (5 mV/s) no apparent catalytic wave was observed at any pH as opposed to what was observed for the analogous **Co-Me** (see Figure S10, Chapter 3). Two main factors can be responsible for the lower reactivity of the Co^I species; *i*) the electron density of the cobalt center in **Co-Pyr** is significantly poorer as compared to the **Co-Me** in aqueous conditions, due to the cobalt-pyrene contact and *ii*) the adsorption phenomenon taking place on the surface of the electrode upon reduction from Co^{II} to Co^I, induces further changes in the coordination sphere that hinder the protonation step. In order to get more insights into the catalytic performance involved in the HER by **Co-Pyr**, homogenous photocatalytic experiments and heterogeneous electrocatalytic experiments were performed and are described in the next sections.



4.2.4 Hydrogen Evolution Photocatalysis

The HER ability of the catalyst was tested in a photochemical system using [Ru(bpy)₃]²⁺ as photosensitizer and a mixture 1:1 of ascorbic acid/sodium ascorbate (pH = 4.1) as sacrificial reducing agent and proton source that should produce hydrogen according to the sequence of reactions indicated in the mechanism scheme of Figure 7. The reaction was performed under 1 sun irradiation (*i.e.* 150W xenon lamp, AM 1.5G filter at 100 mW/cm²) and the amount of H₂ evolved was followed with a hydrogen Clark electrode.

As shown in Figure 7, complex **Co-Pyr** is an active catalyst that produces hydrogen for about one hour. However, it shows slower kinetics than its analog analogous **Co-Me** complex and a much lower stability completing 30 turnover numbers before deactivation as opposed to the 474 TONs achieved by **Co-Me** (Figure S5, supporting information). These results suggest a detrimental effect of the pyrene group in the activity of **Co-Pyr** in homogeneous photocatalytic HER, most likely induced by aggregation of catalytic centers. Indeed, structural and electrochemical experiments discussed above support the intermolecular affinity between molecules due to the highly conjugated nature of the ligand and solvation effects in aqueous solutions.

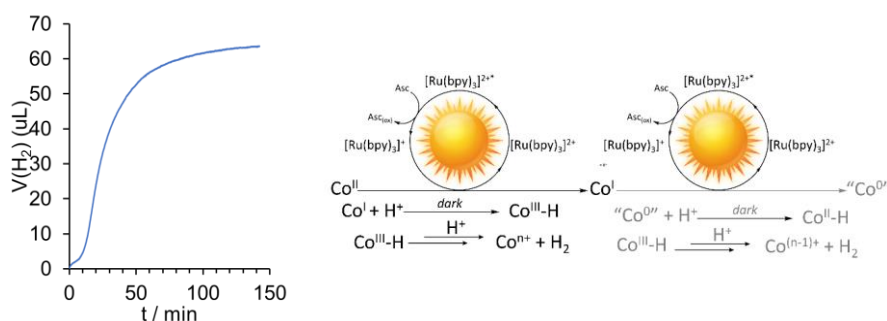


Figure 7. *Left*) Photochemical hydrogen production of **Co-Pyr** under 1 sun illumination. $[Co-Pyr]=0.05mM$, $[[Ru(bpy)_3](ClO_4)_2] = 0.5mM$ and $[sodium\ ascorbate] = [ascorbic\ acid] = 0.55M$. *Right*) Generic photocatalytic pathways towards hydrogen evolution catalysis by molecular cobalt complexes (See Chapter 3).

4.2.5 Hydrogen evolution heterogeneous catalysis: a molecular cathode

The complex **Co-Pyr** was used to functionalize graphitic materials via π - π interactions with the pyrene group with the aim of generating cathodes active for the HER. A schematic representation of the electrode preparation process is given in Figure 8A and the details are given in the SI. Briefly, it consists of preparing a suspension of commercially available graphene powder in a 1mM methanolic solution of **Co-Pyr**. After stirring the mixture overnight, the supernatant solution is separated by centrifugation and analyzed by UV-Vis spectroscopy. As shown in Figure 8B, the concentration of the **Co-Pyr** in methanol, decreased significantly, more than 80%, supporting the successful



A molecular cathode for hydrogen evolution catalysis

attachment of the complex on the graphene powder. The functionalized graphene (G-Co-Pyr) was cleaned with more methanol, dried, and re-dispersed in THF containing 10% (w/w) Nafion® with a final concentration of 1mg/mL. Next, this suspension was used to cover GCE of a Rotating Ring-Disk Electrode (RRDE) by dropcasting to produce cobalt functionalized glassy carbon electrodes (GC@G-Co-Pyr). Analogous electrodes were prepared using the graphene powder without the cobalt complex (GC@G).

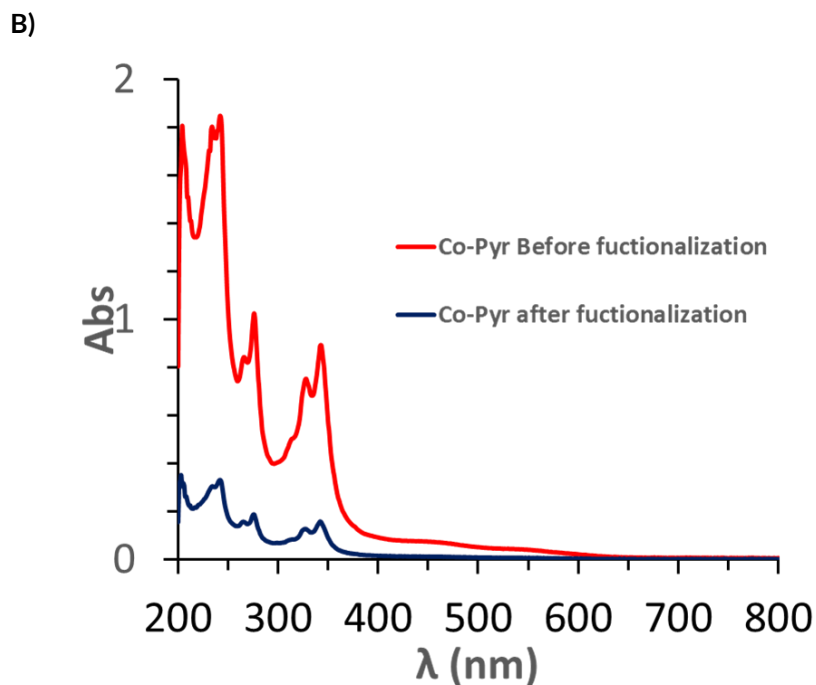
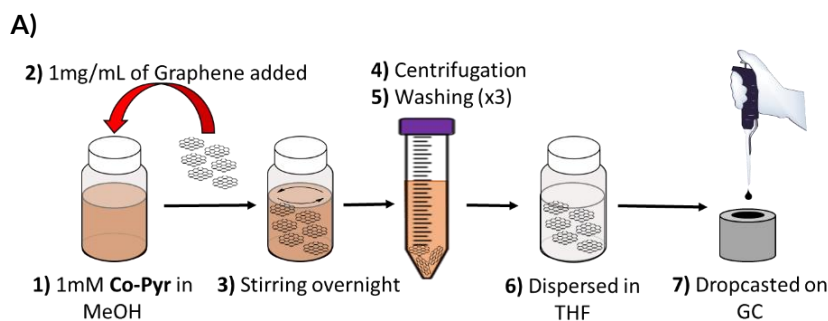


Figure 8. A) Steps followed to prepare GC@G-Co-Pyr. B) UV-vis spectra of Co-Pyr methanolic solution before the functionalization in graphene (red line) and after (blue line).

Figure 9 shows linear sweep voltammetry (LSV) experiments in pH 2 using the electrodes functionalized with the cobalt catalyst (GC@G-Co-Pyr). The first scan features a reductive peak at $E_{p,c,het} = -0.245$ V attributed to the $Co^{II/I}$ redox couple. This reductive peak is not reversible and doesn't appear in subsequent scans (Figure 9 and S6). Interestingly, the reduction potential of this peak is shifted anodically compared to the potential observed in homogenous phase $E_{p,c,hom} = -0.375$ V, indicating that once the catalyst is anchored on the graphene, the electron density on the metal center decreases (Figure S6). We attribute this result to the π - π interaction between the graphene and the pyrene moiety, which enhances the electron-withdrawing character of the conjugated system on the cobalt center. Upon reduction of the Co^{II} species, it is likely that the catalyst releases the acetonitrile axial ligand to give a square pyramidal cobalt center, favored by the d^8 electronic configuration of the metal. Such process implies significant conformational changes that could result into a stronger interaction between the complex and the graphitic structure to stabilize the reduced complex, either through the pyrene moiety, or even by direct contact of the cobalt center (Figure 9, right). In both cases, the resulting structure would lead to enhanced electronic coupling between the catalyst and the electrode. In this type of modified electrodes, the electronic structure of the catalyst is linked to the electronic structure of the graphitic electrode and the redox potential of the catalyst is shifted simultaneously with the fermi level of the conductive material when an external potential is applied. Thus, the redox features of the isolated molecular complex are lost. Such phenomena have recently been extensively studied by Prof. Surendranath for cathodes modified with rhodium molecular catalysts that are active for the carbon dioxide reduction.^{33,34} This hypothesis is fully consistent with the irreversibility of the $Co^{II/I}$ wave and the absence of the $Co^{III/II}$ wave in the solid state (Figure S6).



A molecular cathode for hydrogen evolution catalysis

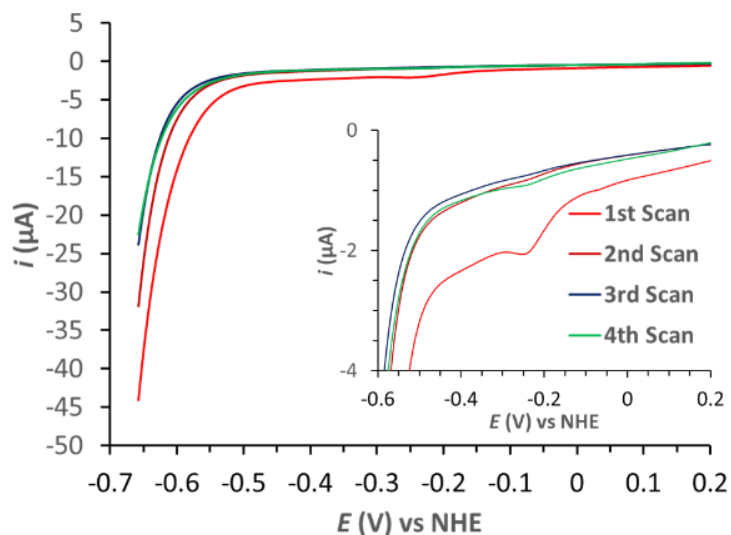


Figure 9. Top) Consecutive LSV experiments of GC@G-Co-Pyr at 1600 rpm in pH 2 phosphate buffer. RE: SCE. CE: Pt Disk. Scan rate 50 mV/s. Bottom) Proposed conformational changes of Co-Pyr anchored on graphene surface upon reduction.

Following the $\text{Co}^{\text{II/I}}$ reduction wave, the GC@G-Co-Pyr electrode shows a significant amount of current starting around $E_{\text{onset,het}} = -0.475$ V, that is not observed for the unfunctionalized electrode and that we attribute to the hydrogen evolution reaction (Figure 10, compare red and grey traces). This

value is 75 mV lower than that observed for its analogous homogeneous catalyst **Co-Me**, which has an $E_{\text{onset, hom(Co-Me)}} = -0.4$ V (see Chapter 3), although this comparison is not totally correct due to the big changes in conformation of the **Co-Pyr** once it is attached on the surface of the conductive material, as discussed above.

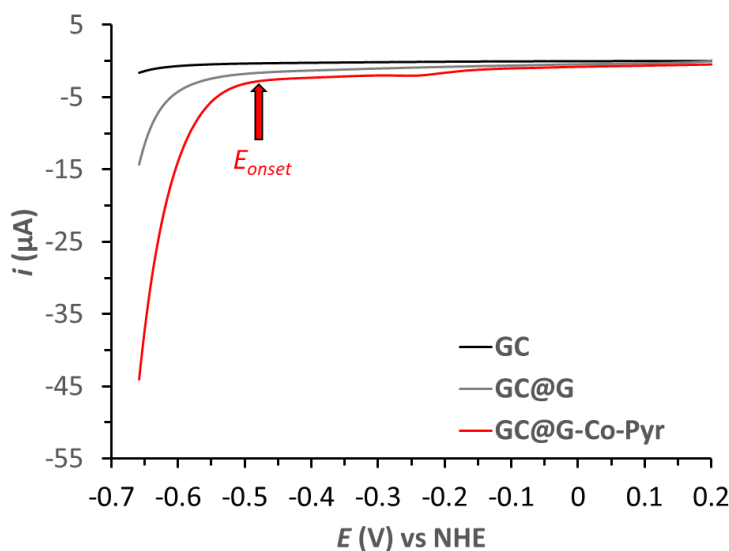


Figure 10. LSV of functionalized GC with Graphene (GC@GC, grey), G-Co-Pyr (GC@GC-Co-Pyr, red) and bare GC (black) at 1600 rpm in pH 2 phosphate buffer. RE: SCE. CE: Pt Disk. Scan rate 50 mV/s.

In order to ascertain if the current observed in electrochemical experiments was due to the reduction of water, further hydrogen detection experiments were performed. First, rotating ring disk electrode (RRDE) confirmed the production of hydrogen gas by the presence of oxidative current at the Pt Ring in the range of -0.45 to -0.56 V in pH 1 (Figure S8). From the response of the Pt Ring, the onset potential for HER of the molecular cathode GC@G-Co-Pyr is $E_{\text{onset}} = -0.45$ V, that corresponds to an overpotential of $\eta = 391$ mV in good agreement with the LSV of Figure 10. In addition, the Faradaic Efficiency (FE) of the HER was determined by using a glassy carbon plate (1 cm² approximately) covered with G-Co-Pyr by dropcasting, and submitted to a controlled potential electrolysis (CPE) at $E_{\text{app}} = -0.56$ V in a gas tight cell with two compartments. The evolution of the hydrogen was followed *in situ* by using



A molecular cathode for hydrogen evolution catalysis

a hydrogen Clark sensor electrode yielding a FE **93%** for 1h of experiments (Figure S9).

4.2.6 X-ray absorption spectroscopy analysis of Co-Pyr and GC@G-Co-Pyr

In order to get more insights into the structure of the **Co-Pyr** on the surface of graphitic materials, Co K-edge X-ray absorption spectroscopy experiments of **Co-Pyr** in solid state, in solution and on the surface of a glassy carbon electrode plate (GC_{plate}@G-**Co-Pyr**) were done in CLAEISS beamline at ALBA synchrotron in collaboration with Dr. D. Moonshiram (IMDEA Materiales, Madrid).

X-ray absorption near edge structure (XANES) and Extended X-ray absorption fine structure (EXAFS) analysis of the measurements are summarized in Figures 11-13, together with relevant data for the **Co-Me** analog that has a similar coordination sphere around the metal center. All measurements were obtained at 77 K with a defocused beam to minimize radiation change.



EXAFS spectra of **Co-Pyr** and **Co-Me** solid samples features prominent merged peaks corresponding to different Co-N bond distances (Figure 11, left). The fitting of the spectra clearly resolved 5 Co-N distances around 1.93-1.94 Å that is in good agreement with the distances obtained by single crystal x-ray diffraction analysis (see Tables S3-S4). Interestingly, XANES spectra revealed small changes in the first coordination sphere manifested in the shifts of the peaks in the lower energy region (7711-7717eV), as well as differences in the pre-edge features (Figure 11, right). The pre-edge region corresponds to the 1s → 3d quadrupole transitions and dipole allowed excitations of the Co core electrons into the valence 3d states hybridized with nitrogen p orbitals of the ligand.³⁵⁻³⁸ Thus, this changes are attributed to the larger N_{MeCN}-Co-N_{amine} angle as well as the more distorted squared base pyramid geometry of **Co-Pyr** compared to **Co-Me** (Figure 3 and Figure S2), which affect the hybridization of the nitrogen p orbitals of the macrocyclic equatorial ligand with the 3d orbitals of the cobalt center.

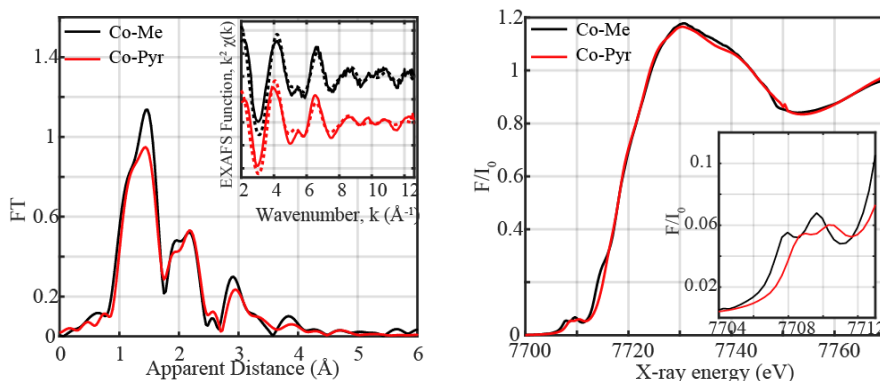


Figure 11. Left) Experimental Fourier transforms of k^2 -weighted Co EXAFS of **Co-Me** and **Co-Pyr** in solid state. Inset: EXAFS Function $Re[\chi(k)]$ of **Co-Me** and **Co-Pyr** experimental data (in solid lines) with fits (in dashed lines). Experimental spectra were calculated for k values of 2-12.6 \AA^{-1} . Right) Normalized Co K-edge XANES of **Co-Me** and **Co-Pyr** in solid state. Inset. Zoom-in of the pre-edge details.

EXAFS fits for the first coordination sphere and the entire spectra are shown in Table S3 in the supporting information. The changes detected in the experimental XANES and EXAFS spectra for the **Co-Pyr** and **Co-Me** complexes in solid state correlate very well with data obtained from XRD analysis and Free Energy Force Field (FEFF) simulations of density functional theory (DFT) optimized structures of the complexes (see Figure S11 and Tables S3-S4), showing that our theoretical methods including geometry optimization and XAS simulations reproduce the experimental data properly. These techniques can therefore be reliably used for analysis of the solution of the complexes and derived species of the cobalt catalyst generated both in solution and upon deposition on electrode surfaces.

EXAFS spectra analysis of **Co-Me** and **Co-Pyr** solutions in MeCN and water supports the substitution of the axial acetonitrilo ligand for aqua already suggested by UV-Vis spectroscopy (Figure 12 and Figure S1). The ligand exchange induces a decrease in the amplitude of the first coordination sphere peak of the EXAFS spectrum and an increase of the peak at around 2.4 \AA denoted by the black arrows in Figure 12 (right). Further analysis (Fit 8) showed an averaged Co-N distance of coordination number 4 at around 1.93 \AA and a lengthened Co-O distance at 2.45 \AA in agreement with DFT optimized



A molecular cathode for hydrogen evolution catalysis

structures of the **Co-Pyr** complex with an aqua ligand in the axial position (Figure S11, Table S3-S4).

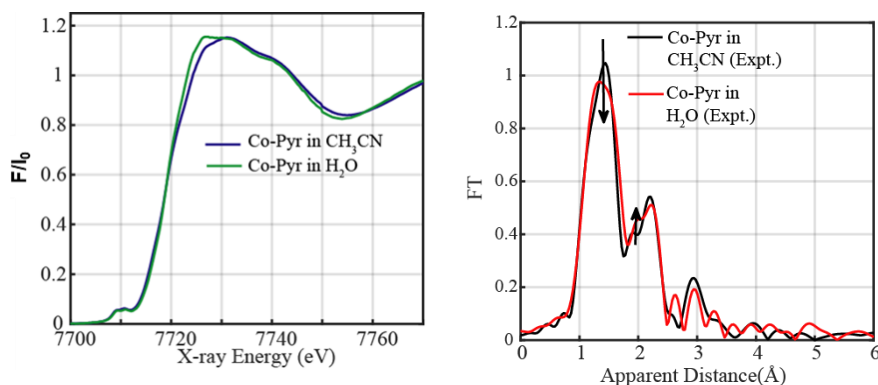


Figure 12. Left) Normalized Co-K edges XANES of **Co-Pyr** in CH_3CN and H_2O . Right) Experimental Fourier transforms of k^2 -weighted Co EXAFS of **Co-Pyr** in CH_3CN and H_2O .



XAS measurements of a freshly prepared $\text{GC}_{\text{plate}}@\text{G-Co-Pyr}$ sample confirmed the presence of the **Co-Pyr** on the surface of the electrode (Figure 13 A and B). Interestingly, the comparison of the XANES spectra of $\text{GC}_{\text{plate}}@\text{G-Co-Pyr}$ with **Co-Pyr** in the solid state or in solution shows an increased energy shift in the spectrum of around 1.2 eV, clearly reflecting the higher ionization energy required for ejecting a core 1s electron upon anchorage on the graphitic material (Figure 13 and Figure S12). This result is in good agreement with the anodic shift observed in the electrochemical experiments of **Co-Pyr** once it is absorbed onto graphene surface (Figure S6). Both experimental evidences point to an electron-acceptor character of the graphene, which is responsible for the decrease of the electron density on the cobalt metal center. Further DFT calculations will help to confirm the conformational change of the catalysts upon absorption on graphene surface, and how the electron density on the metal center is affected.

The GC_{plate}@G-Co-Pyr electrodes were analyzed by XANES and EXAFS after 5 CV cycles with different cathodic limits ($E = -0.66$ V and $E = -0.96$ V vs NHE) at pH 1 (Figure 13 C and D). The spectra showed distinct XANES and EXAFS characteristics as compared to the initial deposited complex, as expected from electrochemical experiments that shows the loss of the Co^{III} wave after the first scan. In particular, the EXAFS spectrum of the electrodes after catalysis at -0.660 V (*i.e.* $\eta = 601$ mV) clearly reveals two prominent peaks corresponding to two sets of distances in the first coordination sphere of the cobalt as opposed to the single set (with a shoulder) of the freshly prepared electrode (compare pink and blue lines in Figure 13D). This analysis suggests two things: i) the electronic environment around the cobalt center is significantly different after reduction and catalysis but at the same time the molecular entity of the complex seems to be maintained, and ii) the change in the first coordination sphere could be indicative of a close interaction of the Co center with the graphene surface (Figure 9, right). Additional experiments as well as DFT calculations are necessary to support these two statements.

The electrodes analyzed after catalysis with lower cathodic limit ($E = -0.96$ V, $\eta = 901$ mV) show a prominent peak at around 3 \AA in the EXAFS spectrum, likely attributable to a photo-electron scattered in a neighbor Co atom outside of the first coordination sphere (Figure 13 D, indicated with black arrow). This result indicates that the mononuclear structure of the complex is lost and higher nuclearity species are formed at such low potential.³⁹



A molecular cathode for hydrogen evolution catalysis

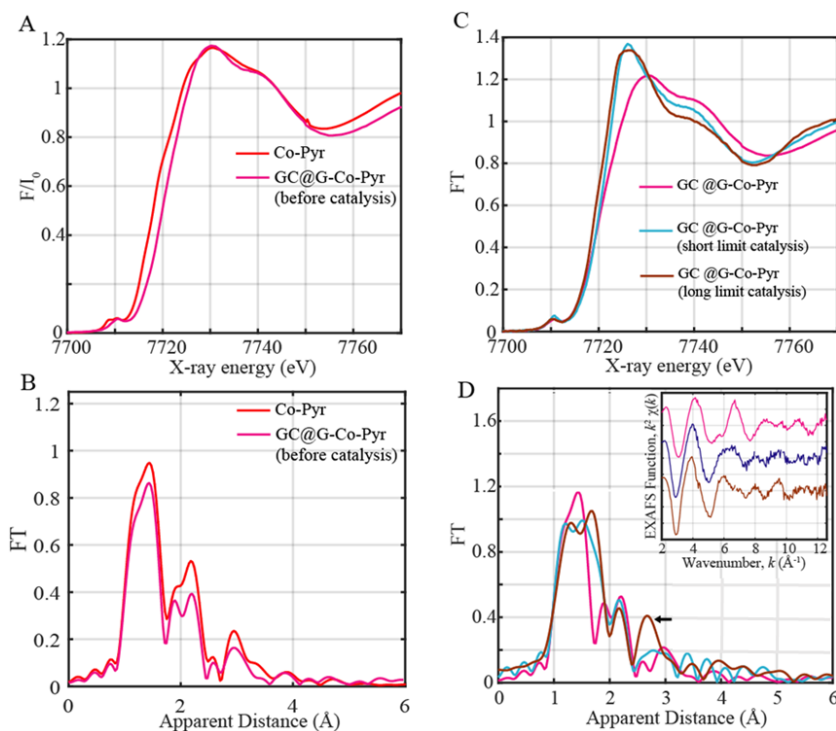


Figure 13. A) Normalized Co-K edges XANES and B) Experimental Fourier transforms of k^2 -weighted Co EXAFS of Co^{II} -Pyr (powder) and GC@G-Co-Pyr before catalysis. C) Normalized Co-K edge XANES and D) Experiment Fourier transforms of k^2 -weighted Co EXAFS of GC@G-Co-Pyr before and after catalysis (long and short range, corresponding to $E = -0.66$ V and $E = -0.96$ V, respectively). Experimental spectra were calculated for k values of 2-12.6 \AA^{-1} . A prominent peak is observed on the EXAFS spectrum of the the electrode GC@G-Co-Pyr after catalysis at long limit ($E = -0.96$ V) around 3 \AA suggesting the formation of polynuclear Co species.

4.3 Summary and conclusions

A molecular cobalt catalyst modified with a pyrene group (**Co-Pyr**) has been successfully synthesized and used to functionalize graphitic materials. Its structural, electrochemical and HER catalytic properties were described and compared with its analogous homogenous catalyst without the pyrene moiety (**Co-Me**).

Single crystal x-ray diffraction analysis of the complex shows that the pyrene group has a strong interaction with the cobalt metal center. This interaction has a strong effect in the electron density of the cobalt as confirmed by electrochemical experiments in aqueous solution, which show that the $\text{Co}^{\text{II/I}}$ reductive wave is anodically shifted as compared to that of the **Co-Me**. In contrast, the electrochemistry in acetonitrile solution show that both complexes **Co-Pyr** and **Co-Me** have almost identical electrochemistry. This result suggest that in organic solvents, the pyrene group is not interacting with the cobalt center but conformationally free. The high affinity of the pyrene group to form π -stacking interactions with other pyrene groups and with the cobalt have also a strong influence in the HER photocatalytic activity of **Co-Pyr** in the presence of $[\text{Ru}(\text{bpy})_3]^{2+}$ as photosensitizer and ascorbate as sacrificial agent. The system deactivates much faster than the **Co-Me**, presumably due to the formation of aggregates in aqueous conditions.

It was possible to fabricate molecular cathodes for the hydrogen evolution catalysis by drop-casting graphene functionalized with **Co-Pyr** on glassy carbon electrodes to form the hybrid cathode GC@G-**Co-Pyr**. Using Clark sensor and RRDE techniques, the production of H_2 was confirmed and the onset potential for HER in pH 1 was found to be $E_{\text{onset}} = -0.45 \text{ V vs NHE}$. This value is among the lowest overpotentials for molecular HER. The Faradaic efficiency of the process at $E = -0.56 \text{ V}$ was found to be 93%.

XAS measurements revealed that once the catalyst is anchored on the graphene surface, its first coordination sphere changes, as well as its redox properties. A higher ionization energy is needed for the GC@G-**Co-Pyr** as compared to that of powder **Co-Pyr** suggesting that the electron density on the cobalt is even lower once deposited on the electrode. After cathodic scans the molecular cathode changes completely its nature as proven by electrochemical



A molecular cathode for hydrogen evolution catalysis

experiments, which show that the initial Co^{II} reductive wave does not appear in subsequent scans, while the catalytic activity still remains. EXAFS spectra also show different features of the electrode before and after catalysis supporting this change in coordination sphere. In order to explain these results we propose significant geometry and coordination changes around the cobalt center upon reduction of the **GC@G-Co-Pyr**. The initial penta-coordinated Co^{II} complex attached to the electrode by the pyrene group is reduced to Co^{I} . This reduction induces the loss of the axial ligand (acetonitril or aqua) to form a square planar cobalt complex that can interact with the graphitic surface either through the planar pyrene group or through the planar cobalt center. In any case, the latter species has such a strong affinity to the graphitic that its redox behavior is now shifted simultaneously with the fermi level of the conductive material when an external potential is applied. Consequently, the redox features of the molecular catalyst as well as its catalytic activity are completely different than its homogeneous homolog. In order to reassert the latter hypothesis, further experiments and DFT calculations are necessary.



4.4 References

- (1) Matheu, R.; Garrido-Barros, P.; Gil-Sepulcre, M.; Ertem, M. Z.; Sala, X.; Gimbert-Suriñach, C.; Llobet, A. The Development of Molecular Water Oxidation Catalysts. *Nat. Rev. Chem.* **2019**, *3* (5), 331–341. <https://doi.org/10.1038/s41570-019-0096-0>.
- (2) Berardi, S.; Drouet, S.; Francàs, L.; Gimbert-Suriñach, C.; Guttentag, M.; Richmond, C.; Stoll, T.; Llobet, A. Molecular Artificial Photosynthesis. *Chem. Soc. Rev.* **2014**, *43* (22), 7501–7519. <https://doi.org/10.1039/c3cs60405e>.
- (3) Estes, D. P.; Grills, D. C.; Norton, J. R. The Reaction of Cobaloximes with Hydrogen: Products and Thermodynamics. *J. Am. Chem. Soc.* **2014**, *136* (50), 17362–17365. <https://doi.org/10.1021/ja508200g>.
- (4) Huo, P.; Uyeda, C.; Goodpaster, J. D.; Peters, J. C.; Miller, T. F. Breaking the Correlation between Energy Costs and Kinetic Barriers in Hydrogen Evolution via a Cobalt Pyridine-Diimine-Dioxime Catalyst. *ACS Catal.* **2016**, *6* (9), 6114–6123. <https://doi.org/10.1021/acscatal.6b01387>.
- (5) Artero, V.; Chavarot-Kerlidou, M.; Fontecave, M. Splitting Water with Cobalt. *Angew. Chemie - Int. Ed.* **2011**, *50* (32), 7238–7266. <https://doi.org/10.1002/anie.201007987>.
- (6) Reynal, A.; Durrant, J. R.; Pastor, E.; Orchard, K. L.; Willkomm, J.; Reisner, E. Dye-Sensitised Semiconductors Modified with Molecular Catalysts for Light-Driven H₂ Production. *Chem. Soc. Rev.* **2015**, *45* (1), 9–23. <https://doi.org/10.1039/c5cs00733j>.
- (7) Willkomm, J.; Muresan, N. M.; Reisner, E. Enhancing H₂ Evolution Performance of an Immobilised Cobalt Catalyst by Rational Ligand Design. *Chem. Sci.* **2015**, *6* (5), 2727–2736. <https://doi.org/10.1039/c4sc03946g>.
- (8) Materna, K. L.; Crabtree, R. H.; Brudvig, G. W. Anchoring Groups for Photocatalytic Water Oxidation on Metal Oxide Surfaces. *Chem. Soc. Rev.* **2017**, *46* (20), 6099–6110. <https://doi.org/10.1039/c7cs00314e>.
- (9) Lakadamyali, F.; Reynal, A.; Kato, M.; Durrant, J. R.; Reisner, E. Electron Transfer in Dye-Sensitised Semiconductors Modified with Molecular Cobalt Catalysts: Photoreduction of Aqueous Protons. *Chem. - A Eur. J.* **2012**, *18* (48), 15464–15475. <https://doi.org/10.1002/chem.201202149>.
- (10) Muresan, N. M.; Willkomm, J.; Mersch, D.; Vaynzof, Y.; Reisner, E. Immobilization of a Molecular Cobaloxime Catalyst for Hydrogen Evolution on a Mesoporous Metal Oxide Electrode. *Angew. Chemie - Int. Ed.* **2012**, *51* (51), 12749–12753. <https://doi.org/10.1002/anie.201207448>.
- (11) Moore, G. F.; Sharp, I. D. A Noble-Metal-Free Hydrogen Evolution Catalyst



A molecular cathode for hydrogen evolution catalysis

- Grafted to Visible Light-Absorbing Semiconductors. *J. Phys. Chem. Lett.* **2013**, *4* (4), 568–572. <https://doi.org/10.1021/jz400028z>.
- (12) Neale, N. R.; Steirer, K. X.; Yan, Y.; Gu, J.; Turner, J. A.; Young, J. L. Water Reduction by a P-GaInP₂ Photoelectrode Stabilized by an Amorphous TiO₂ Coating and a Molecular Cobalt Catalyst. *Nat. Mater.* **2015**, *15* (4), 456–460. <https://doi.org/10.1038/nmat4511>.
- (13) Chandrasekaran, S.; Kaeffer, N.; Cagnon, L.; Aldakov, D.; Fize, J.; Nonglaton, G.; Baleras, F.; Mailley, P.; Artero, V. A Robust ALD-Protected Silicon-Based Hybrid Photoelectrode for Aqueous Hydrogen Evolution. *Chem. Sci.* **2019**, *10*, 4469–4475. <https://doi.org/10.1039/c8sc05006f>.
- (14) Beiler, A. M.; Khusnutdinova, D.; Jacob, S. I.; Moore, G. F. Solar Hydrogen Production Using Molecular Catalysts Immobilized on Gallium Phosphide (111)A and (111)B Polymer-Modified Photocathodes. *ACS Appl. Mater. Interfaces* **2016**, *8* (15), 10038–10047. <https://doi.org/10.1021/acsami.6b01557>.
- (15) Krawicz, A.; Yang, J.; Anzenberg, E.; Yano, J.; Sharp, I. D.; Moore, G. F. Photofunctional Construct That Interfaces Molecular Cobalt-Based Catalysts for H₂ Production to a Visible-Light-Absorbing Semiconductor. *J. Am. Chem. Soc.* **2013**, *135* (32), 11861–11868. <https://doi.org/10.1021/ja404158r>.
- (16) Krawicz, A.; Cedeno, D.; Moore, G. F. Energetics and Efficiency Analysis of a Cobaloxime-Modified Semiconductor under Simulated Air Mass 1.5 Illumination. *Phys. Chem. Chem. Phys.* **2014**, *16* (30), 15818–15824. <https://doi.org/10.1039/c4cp00495g>.
- (17) Cedeno, D.; Krawicz, A.; Doak, P.; Yu, M.; Neaton, J. B.; Moore, G. F. Using Molecular Design to Control the Performance of Hydrogen-Producing Polymer-Brush-Modified Photocathodes. *J. Phys. Chem. Lett.* **2014**, *5* (18), 3222–3226. <https://doi.org/10.1021/jz5016394>.
- (18) Grau, S.; Berardi, S.; Moya, A.; Matheu, R.; Cristino, V.; Vilatela, J. J.; Bignozzi, C. A.; Caramori, S.; Gimbert-Suriñach, C.; Llobet, A. A Hybrid Molecular Photoanode for Efficient Light-Induced Water Oxidation. *Sustain. Energy Fuels* **2018**, *2* (9), 1979–1985. <https://doi.org/10.1039/c8se00146d>.
- (19) Creus, J.; Matheu, R.; Peñafiel, I.; Moonshiram, D.; Blondeau, P.; Benet-Buchholz, J.; García-Antón, J.; Sala, X.; Godard, C.; Llobet, A. A Million Turnover Molecular Anode for Catalytic Water Oxidation. *Angew. Chemie - Int. Ed.* **2016**, *55* (49), 15382–15386. <https://doi.org/10.1002/anie.201609167>.
- (20) Matheu, R.; Moreno-Hernandez, I. A.; Sala, X.; Gray, H. B.; Brunshwig, B. S.; Llobet, A.; Lewis, N. S. Photoelectrochemical Behavior of a Molecular Ru-Based Water-Oxidation Catalyst Bound to TiO₂-Protected Si Photoanodes. *J. Am. Chem. Soc.* **2017**, *139* (33), 11345–11348.



- <https://doi.org/10.1021/jacs.7b06800>.
- (21) Chen, Y.; Chen, H.; Tian, H. Immobilization of a Cobalt Catalyst on Fullerene in Molecular Devices for Water Reduction. *Chem. Commun.* **2015**, 51 (57), 11508–11511. <https://doi.org/10.1039/c5cc03856a>.
- (22) Andreiadis, E. S.; Jacques, P. A.; Tran, P. D.; Leyris, A.; Chavarot-Kerlidou, M.; Jusselme, B.; Matheron, M.; Pécaut, J.; Palacin, S.; Fontecave, M.; et al. Molecular Engineering of a Cobalt-Based Electrocatalytic Nanomaterial for H₂ Evolution under Fully Aqueous Conditions. *Nat. Chem.* **2013**, 5 (1), 48–53. <https://doi.org/10.1038/nchem.1481>.
- (23) McCrory, C. C. L.; Uyeda, C.; Peters, J. C. Electrocatalytic Hydrogen Evolution in Acidic Water with Molecular Cobalt Tetraazamacrocycles. *J. Am. Chem. Soc.* **2012**, 134 (6), 3164–3170. <https://doi.org/10.1021/ja210661k>.
- (24) Molton, F.; Fortage, J.; Deronzier, A.; Blackman, A. G.; Stoll, T.; Collomb, M.-N.; Varma, S.; Castillo, C. E. Efficient Photocatalytic Hydrogen Production in Water Using a Cobalt(III) Tetraaza-Macrocyclic Catalyst: Electrochemical Generation of the Low-Valent Co(I) Species and Its Reactivity toward Proton Reduction. *Phys. Chem. Chem. Phys.* **2013**, 15 (40), 17544. <https://doi.org/10.1039/c3cp52641k>.
- (25) Gimbert-Suriñach, C.; Albero, J.; Stoll, T.; Fortage, J.; Collomb, M.-N.; Deronzier, A.; Palomares, E.; Llobet, A. Efficient and Limiting Reactions in Aqueous Light-Induced Hydrogen Evolution Systems Using Molecular Catalysts and Quantum Dots. *J. Am. Chem. Soc.* **2014**, 136 (21), 7655–7661. <https://doi.org/10.1021/ja501489h>.
- (26) Moonshiram, D.; Gimbert-Suriñach, C.; Guda, A.; Picon, A.; Lehmann, C. S.; Zhang, X.; Doumy, G.; March, A. M.; Benet-Buchholz, J.; Soldatov, A.; et al. Tracking the Structural and Electronic Configurations of a Cobalt Proton Reduction Catalyst in Water. *J. Am. Chem. Soc.* **2016**, 138 (33), 10586–10596. <https://doi.org/10.1021/jacs.6b05680>.
- (27) Poon, C.-K.; Wan, W.-K.; Liao, S. S. T. Structural and Mechanistic Studies of Co-Ordination Compounds. Part 172 Preparation and Acid Hydrolysis of Some Cobalt(III) Complexes Containing the Quadridentate Macrocycle 2,7,12-Trimethyl-3,7,11,17-Tetra-azabicyclo[11.3.1]heptadeca-1(17),2,11,13,15-Pe. **1977**, 4–8.
- (28) Long, K. M.; Busch, D. H. Cobalt(II) Complexes of the Quadridentate Macrocycle 2,12-Dimethyl-3,7,11,17-tetraazabicyclo[11.3.1]heptadeca-1(17),2,11,13,15-Pentaene. **1970**, 9 (3).
- (29) Long, K. M.; Busch, D. H. Cobalt(III) Complexes of the Tetridentate Macrocycle 2, 12-Dimethyl-3, 7,11, 17-Tetraazabi-Cyclo(1 1.3.1)heptadeca-1(17), 2,11,13, 15-Pentaene. *J. Coord. Chem.* **1974**, 4 (2), 113–123. <https://doi.org/10.1080/00958977408075888>.



A molecular cathode for hydrogen evolution catalysis

- (30) Leung, C.-F.; Chen, Y.-Z.; Yu, H.-Q.; Yiu, S.-M.; Ko, C.-C.; Lau, T.-C. Electro and Photocatalytic Hydrogen Generation in Acetonitrile and Aqueous Solutions by a Cobalt Macrocyclic Schiff-Base Complex. *Int. J. Hydrogen Energy* **2011**, *36* (18), 11640–11645. <https://doi.org/10.1016/j.ijhydene.2011.06.062>.
- (31) Bard, A. J.; Faulkner, L. R. *Electrochemical Methods, Fundamentals and Applications*, 2nd ed.; Wiley, 2001; Vol. 60. <https://doi.org/10.1021/ed060pa25.1>.
- (32) Huynh, M. H. V.; Meyer, T. J. Proton-Coupled Electron Transfer. *Chem. Rev.* **2007**, *107* (11), 5004–5064. <https://doi.org/10.1021/cr0500030>.
- (33) Jackson, M. N.; Oh, S.; Kaminsky, C. J.; Chu, S. B.; Zhang, G.; Miller, J. T.; Surendranath, Y. Strong Electronic Coupling of Molecular Sites to Graphitic Electrodes via Pyrazine Conjugation. *J. Am. Chem. Soc.* **2018**, *140* (3), 1004–1010. <https://doi.org/10.1021/jacs.7b10723>.
- (34) Oh, S.; Gallagher, J. R.; Miller, J. T.; Surendranath, Y. Graphite-Conjugated Rhenium Catalysts for Carbon Dioxide Reduction. *J. Am. Chem. Soc.* **2016**, *138* (6), 1820–1823. <https://doi.org/10.1021/jacs.5b13080>.
- (35) De Groot, F.; Vankó, G.; Glatzel, P. The 1s X-Ray Absorption Pre-Edge Structures in Transition Metal Oxides. *J. Phys. Condens. Matter* **2009**, *21* (10). <https://doi.org/10.1088/0953-8984/21/10/104207>.
- (36) Vankó, G.; de Groot, F. M. F.; Huotari, S.; Cava, R. J.; Lorenz, T.; Reuther, M. Intersite 4p-3d Hybridization in Cobalt Oxides: A Resonant X-Ray Emission Spectroscopy Study. **2008**, 1–7.
- (37) Kau, L. shan; Spira-solomon, D. J.; Spira-solomon-penner-hahn, J. E.; Hodgson, K. O.; Solomon, E. I. X-Ray Absorption Edge Determination of the Oxidation State and Coordination Number of Copper: Application to the Type 3 Site in Rhus Vernicifera Laccase and Its Reaction with Oxygen. *J. Am. Chem. Soc.* **1987**, *109* (21), 6433–6442. <https://doi.org/10.1021/ja00255a032>.
- (38) Westre, T. E.; Kennepohl, P.; DeWitt, J. G.; Hedman, B.; Hodgson, K. O.; Solomon, E. I. A Multiplet Analysis of Fe K-Edge 1s → 3d Pre-Edge Features of Iron Complexes. *J. Am. Chem. Soc.* **1997**, *119* (27), 6297–6314. <https://doi.org/10.1021/ja964352a>.
- (39) Gimbert-Suriñach, C.; Moonshiram, D.; Francàs, L.; Planas, N.; Bernales, V.; Bozoglian, F.; Guda, A.; Mognon, L.; López, I.; Hoque, M. A.; et al. Structural and Spectroscopic Characterization of Reaction Intermediates Involved in a Dinuclear Co–Hbpp Water Oxidation Catalyst. *J. Am. Chem. Soc.* **2016**, *138* (47), 15291–15294. <https://doi.org/10.1021/jacs.6b08532>.



4.5 Supporting Information

4.5.1. Materials and Methods

Reagents

Buffer solutions were prepared with Na_2HPO_4 , NaH_2PO_4 , Acetic acid, Potassium Acetate and Trifluoromethanesulfonic Acid provided by Sigma-Aldrich. Nafion® perfluorinated resin solution (5%w/w) was supplied from Sigma-Aldrich.

X-ray Diffraction (XRD) equipment

XRD analysis was carried out with an automatic Philips X'pert $\theta/2\theta$ diffractometer using Cu KR radiation ($\lambda = 1.5416 \text{ \AA}$).

UV-Vis equipment

UV-Vis measurements were carried out on a Lambda 1050 PerkinElmer spectrophotometer equipped with a PMT, InGaAs and PbS detectors system, double beam optics, double monochromator and D2 and W light sources. Diffuse reflectance measurements were carried out in the same equip using 150 mm Integrating Sphere with PbS and PMT detectors.

Electrochemical equipment

Cyclic voltammetry (CV), linear sweep voltammetry (LSV) and Controlled Potential Electrolysis (CPE) were measured using a CHI660D potentiostat or CHI730D bipotentiostat.

The RRDE experiments were done using a CHI730D bipotentiostat and RRDE-3A from CH Instruments.

Glassy Carbon Disk electrodes, Platinum Disk Electrodes, RRDE (Pt-Pt and GC-Pt) and reference electrodes (SCE and AgCl/Ag) were purchased from IJ-Cambria Ltd. Pads and alumina for polishing were also purchased from the same company.

Glassy Carbon Plates (Sigradur K films 20mm x 10mm x 180 μm) were purchased from HTW.

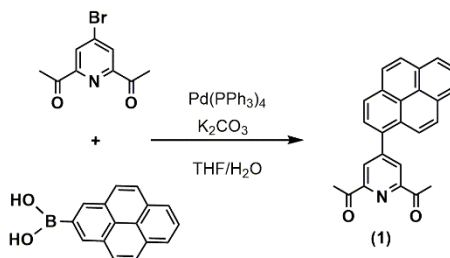


A molecular cathode for hydrogen evolution catalysis

Graphene (>98 wt%, D 2-10 μm , 1-3 layers) was purchased from Nanostructured & Amorphous Materials, Inc.

4.5.2. Synthesis and characterization of Co-Pyr

Synthesis of 4-pyren-2,6-diacetylpyridine, 1

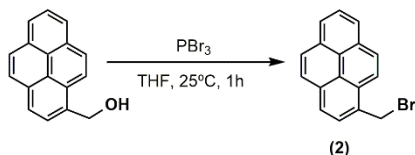


4-pyren-2,6-diacetylpyridine was prepared following a similar procedure reported in the literature.¹ 4-bromo-2,6-diacetylpyridine (400 mg, 1.65 mmol), pyrene boronic acid (406 mg, 1.65 mmol), and K₂CO₃ (228 mg, 1.65 mmol) were added into a Schlenk flask. Tetrakis(triphenylphosphine)palladium (190 mg, 0.165 mmol) was added inside a glove box. After that the degassed solid mixture was dissolved with a mixture of degassed water:THF (1:5, 80 mL). The mixture was heated up to 90°C under nitrogen atmosphere overnight under vigorous stirring. Then 60 mL of water was added and the mixture was extracted with THF (3 × 50 mL). The organic phase was dried with anhydrous MgSO₄ and filtered. The solvent was then evaporated to obtain a dark brown powder. The crude mixture was purified by column chromatography (silica gel) using dichloromethane:hexane (3:7–1:1–1:0). The target compound was obtained as a yellow powder (4.49 mg, 1.24 mmols, 75%).

¹H-NMR (400 MHz, CDCl₃): δ = 2.93 (s, 6H), 8.53 (s, 2H), 7.94–8.29 (m, 9H).

Mass Spectrometry: ESI⁺-MS m/z: calcd for [1-H]⁺ (C₂₅H₁₈NO₂⁺): m/z: 364.1, found m/z: 364.1.

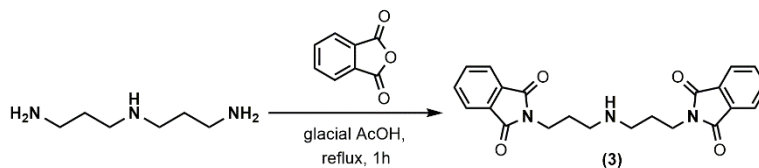
Synthesis of 1-bromomethylpyrene, 2



The synthesis was adapted from literature.² Phosphorus tribromide (1.2 mL, 12.9 mmol) was added to a solution of 1-pyrenemethanol (2.0 g, 8.6 mmol) in 10 mL dry THF. The resulting mixture was stirred for 1h at room temperature under N₂. 50mL of saturated sodium bicarbonate solution was added. The compound was extracted using DCM. The organic layer solution was dried using anhydrous magnesium sulfate and the solvent was removed under reduced pressure. 1-(bromomethyl)pyrene was obtained as a yellow greenish powder. The powder was purified by dissolving it in the minimum amount of DCM and precipitated adding hexane (2.29 g, Yield: 90%).

¹H NMR (400 MHz, CDCl₃): δ 8.39 (d, *J* = 9.2 Hz, 1H), 8.27 – 8.20 (m, 3H), 8.12 (d, *J* = 7.8 Hz, 1H), 8.09 (d, *J* = 9.0 Hz, 1H), 8.05 (s, 1H), 8.04 – 8.01 (m, 2H), 5.26 (s, 2H).

Synthesis of 2,2'-(azanediylbis(propane-3,1-diyl))bis(isoindoline-1,3-dione), 3



The protection of bis-(3-aminopropyl)amine was performed following a similar procedure described in the literature.^{3,4} A mixture of bis-(3-aminopropyl)amine (4 mL, 28 mmol) and phthalic anhydride (8.29 g, 56 mmol) in 43 mL glacial acetic acid was at refluxed for 1 hour under N₂ atmosphere.

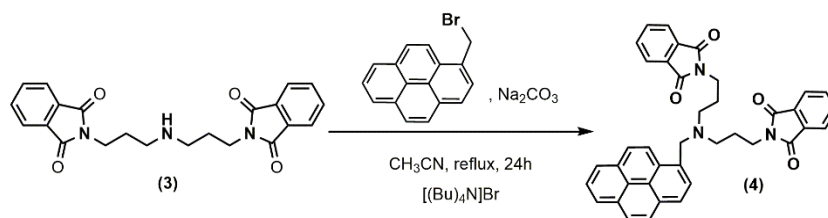


A molecular cathode for hydrogen evolution catalysis

The solvent was removed under reduced pressure and 56 mL of hot ethanol was added to the dry residue and stirred until an appearance of the solid. The final product was obtained as a white powder by filtration and washed with cold ethanol (8.54 g, Yield: 77%).

$^1\text{H NMR}$ (400 MHz, CDCl_3): δ 7.86 – 7.80 (m, $J = 5.5, 3.0$ Hz, 4H), 7.74 – 7.68 (m, $J = 5.5, 3.1$ Hz, 4H), 3.77 (t, $J = 6.8$ Hz, 4H), 2.69 (t, $J = 7.0$ Hz, 4H), 1.91 (p, $J = 6.9$ Hz, 4H).

Synthesis of 2,2'-(((pyren-1-ylmethyl)azanediyl)bis(propane-3,1-diyl))bis(isoindoline-1,3-dione), 4

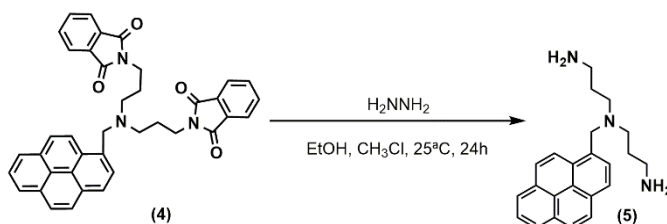


This reaction was performed following a similar procedure previously reported in the literature.⁴ A mixture of **1** (2.95g, 10 mmol), **2** (3.26g, 8.33 mmol), K_2CO_3 (2.86 g, 20.7 mmol) and tetrabutylammonium bromide (51 mg, 0.158 mmol) in 150 mL acetonitrile was refluxed for 24h. The solvent was evaporated under reduced pressure. The dry residue was treated with water and extracted with DCM (3 x 34 mL). The organic layer was dried using magnesium sulfate anhydrous and the solvent removed under reduced pressure. The final product was obtained as yellow crystals after recrystallization in 50:50 DCM: methanol. (1.70 g, Yield: 34%).

$^1\text{H NMR}$ (500 MHz, CDCl_3): δ 8.58 (d, $J = 9.2$ Hz, 1H), 8.17 – 8.12 (m, $J = 8.8$ Hz, 3H), 8.02 – 7.94 (m, 5H), 7.86 – 7.64 (m, $J = 5.4, 3.0$ Hz, 4H), 7.64 – 7.51 (m, 4H), 4.24 (s, 2H), 3.67 (t, 4H), 2.64 (t, $J = 7.0$ Hz, 4H), 1.94 (p, 4H).

^{13}C NMR (126 MHz, CDCl_3): δ 168.65, 133.97, 133.00, 132.39, 131.67, 131.33, 130.97, 130.08, 128.64, 127.80, 127.64, 127.29, 126.06, 125.35, 125.21, 125.14, 124.73, 124.42, 123.32, 66.21, 57.54, 51.58, 36.80, 26.32.

Synthesis of N^1 -(3-aminopropyl)- N^1 -(pyren-1-ylmethyl)propane-1,3-diamine, **5**



The deprotection of **4** was performed following the typical reaction described in the literature.⁴ A mixture of **4** (2.25 g, 3.71 mmol), and hydrazine monohydrate (2.4 mL, 49 mmol) in 90 mL ethanol and 20 mL chloroform was stirred at room temperature for 24 hours. The resulting white solid was filtered off and the filtrate was evaporated under reduced pressure. 75 mL chloroform were added to the dry residue and the suspension stirred for 24 hours. The white solid was filtered off and the filtrate was evaporated under reduced pressure to leave a yellow oil identified as the desired product **5** (1.20 g, Yield: 94%).

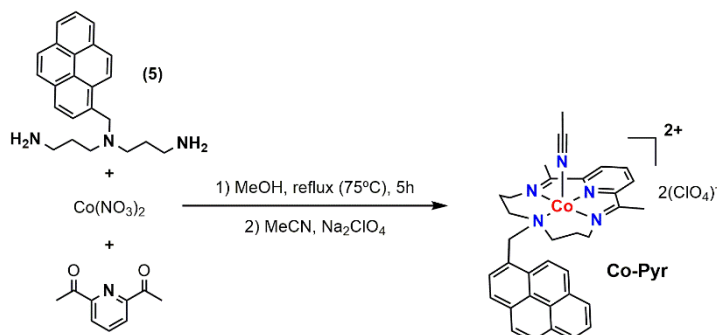
^1H NMR (500 MHz, CDCl_3): δ 8.53 (d, $J = 9.2$ Hz, 1H), 8.19 – 8.15 (m, 2H), 8.11 (t, $J = 8.5$ Hz, 2H), 8.04 (s, 2H), 8.02 – 7.97 (m, 2H), 4.23 (s, 2H), 2.66 (t, $J = 6.8$ Hz, 4H), 2.59 (t, 4H), 1.69 (p, 4H).

^{13}C NMR (126 MHz, CDCl_3): δ 133.44, 131.44, 130.99, 130.75, 129.82, 128.21, 127.57, 127.22, 127.16, 125.97, 125.11, 125.09, 124.92, 124.55, 124.03, 77.41, 77.16, 76.91, 57.77, 51.80, 40.57, 30.76.



A molecular cathode for hydrogen evolution catalysis

Synthesis of complex Co-Pyr



2,6-diacetyl-pyridine (257.3 mg, 1.577 mmol) and Co(NO₃)₂·6H₂O (459.0 mg, 1.577 mmol) were introduced into a double neck round bottom flask under N₂ and degassed anhydrous methanol (40mL) were added. The reaction mixture was heated to 75°C under N₂ and stirred until everything was dissolved, giving a pink-red solution. N¹-(3-aminopropyl)-N¹-(pyren-1-ylmethyl)propane-1,3-diamine (551.3 mg, 1.586 mmol) was dissolved in the minimum amount of dry and degassed DCM and added dropwise to the reaction mixture. The reaction mixture (dark red) was stirred and kept at 75°C for 5 hours under N₂. After 5hours, the condensation was complete. The solvent was removed under reduced pressure resulting in a dark red solid, and redissolved in dry and degassed MeCN giving a dark red-orange solution. The dark-red solution was filtered under N₂ and transferred into Schlenk flask containing NaClO₄ (381.4mg, 3.115mmol) dissolved in the minimum amount of MeCN, a white powder precipitates. The supernatant solution was filtered under N₂ and transferred to another Schlenk flask where the volume of MeCN was reduced under reduced pressure. Degassed and dry Et₂O was added to induce the precipitation of the reddish powder of Co-Pyr. For further purification, this powder was dissolved in EtOH, insoluble dark impurities separated from the solvent by filtration under air. The solvent of the filtrate was removed under reduced pressure and the resulting red solid redissolved in MeCN. Red-purple crystalline solid was obtained by precipitation when Et₂O was added (40mg,



0.514mmol, 25% yield). Single crystals suitable for XRD analysis were obtained by slow diffusion of THF in MeCN solution of **Co-Pyr**.

Anal. Calcd for $C_{34}H_{35}Cl_2CoN_5O_8$: C, 52.93; H, 4.57; N, 9.08. **Found**: C, 52.44; H, 4.92; N, 8.93.

ESI⁺-HRMS m/z: calcd for $[M^{2+}-CH_3CN+ClO_4^-]^+$ ($C_{32}H_{32}ClCoN_4O_4^+$): m/z: 630.1450, found m/z: 630.1455.

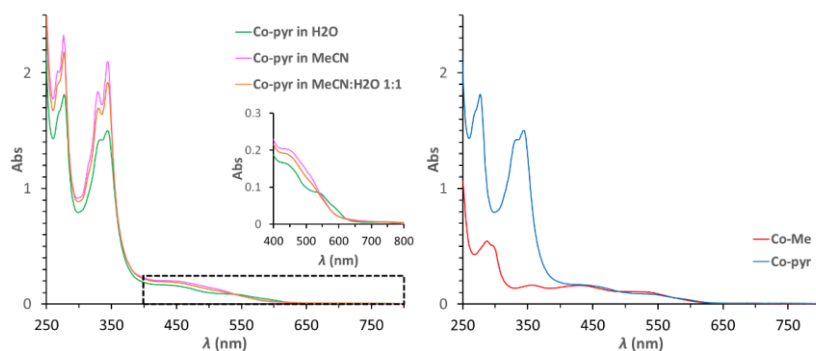


Figure S1 Left: UV-vis absorption spectra of 0.1mM of **Co-Pyr** in water, MeCN and mixture 1:1 (water, MeCN). Inset: magnification of the highlighted zone. **Right:** UV-vis spectra of 0.1mM of **Co-pyr** and 0.1mM of **Co-Me** in pure water.



A molecular cathode for hydrogen evolution catalysis

4.5.3. Single crystal x-ray diffraction structure of Co-Pyr

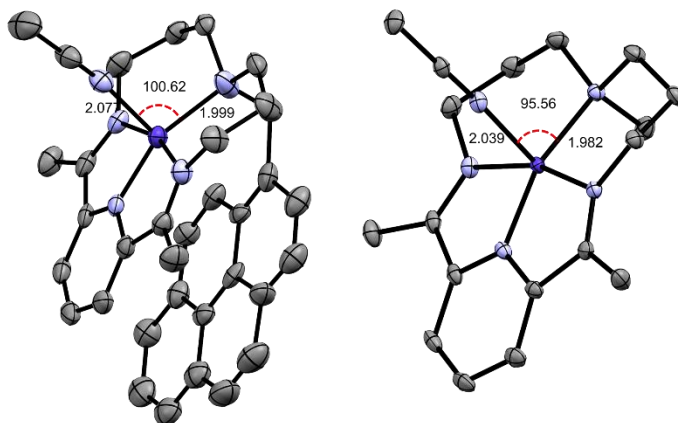


Figure S2. Comparison of angles and bond distances of Co-Pyr (left) and Co-Me (right).

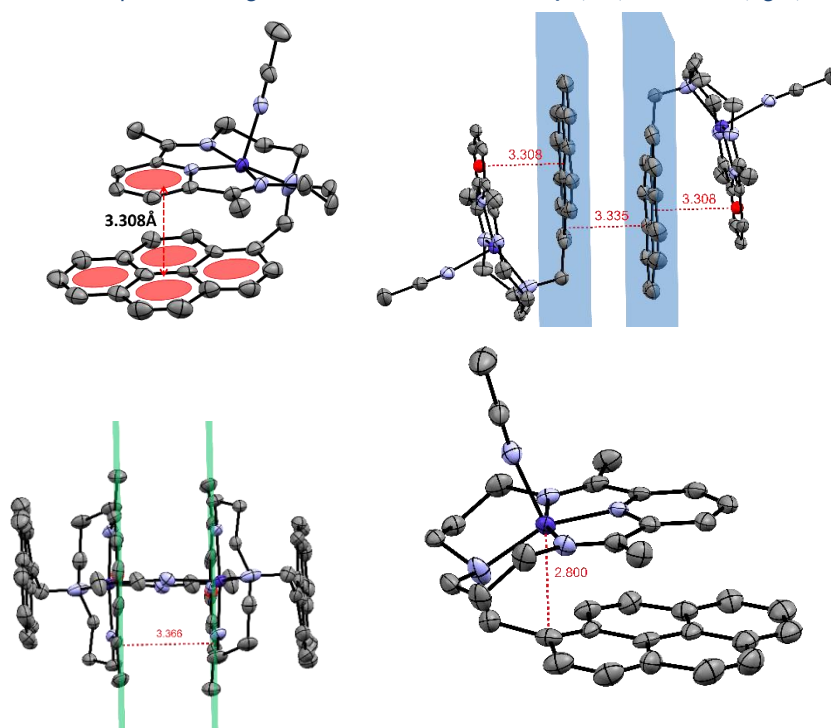


Figure S3. Representation of π - π interaction in Co-Pyr catalyst. The dashed red arrow represents the distance between the two planes (or atoms) formed by i) the pyridine ring of the macrocyclic ligand (green planes) and ii) the pyrene unit (blue plane).

4.5.4. Co-Pyr in homogeneous phase

All the potentials were converted to NHE using the following formula (aqueous media):

$$E_{NHE} = E + E_{ref}$$

Where E is the potential measured and E_{ref} is the equilibrium potential of the reference electrode at standard conditions (i.e. $E_{SCE} = +0.24$ V).

In organic media (MeCN), the potentials were referred versus the $E_{1/2}$ of ferrocene (Fc^+/Fc). This was determined by CV adding a small amount of internal standard ferrocene into the electrochemical cell at the end of each experiment, and taking that value as zero. The potentials were converted using the following formula:

$$E_{Fc^+/Fc} = E_{vs AgNO_3(0.01M)/Ag} - E_{1/2(Fc^+/Fc)}$$

Where $E_{vs AgNO_3(0.01M)/Ag}$ is the potential measured versus non-aqueous reference electrode and $E_{1/2(Fc^+/Fc)}$ is the potential of the ferrocene's reversible wave (experimentally measured at +0.095V).



Solvent:	L/L ⁻		II/I		III/II	
	$E_{1/2}$ (V)	ΔE (V)	$E_{1/2}$ (V)	ΔE (V)	$E_{1/2}$ (V)	ΔE (V)
Co-pyr	-1.754	0.106	-0.577	0.105	NA ^a	0.647
Co-Me	-1.776	0.073	-0.555	0.055	NA ^a	0.763

Table S1. Redox potentials of Co-Pyr in MeCN 0.1 M [(Bu)₄N]PF₆. Potentials referred to ferrocene. ^aSquared mechanism.

pH	II/I				III/II			
	E_c	E_a	$E_{1/2}$	ΔE	E_c	E_a	$E_{1/2}$	ΔE
2	-0.375	-0.206	-0.291	0.169	0.535	1.11	0.823 ^a	0.575
4	-0.386	-0.174	-0.280	0.212	0.602	0.99	0.796 ^a	0.388
7	-0.376	-0.226	-0.301	0.15	0.305	0.626	0.466 ^a	0.321

Table S2. Redox potentials of Co-Pyr in aqueous solution using GCE as WE. All potentials referred to NHE. ^aSquared mechanism.

A molecular cathode for hydrogen evolution catalysis

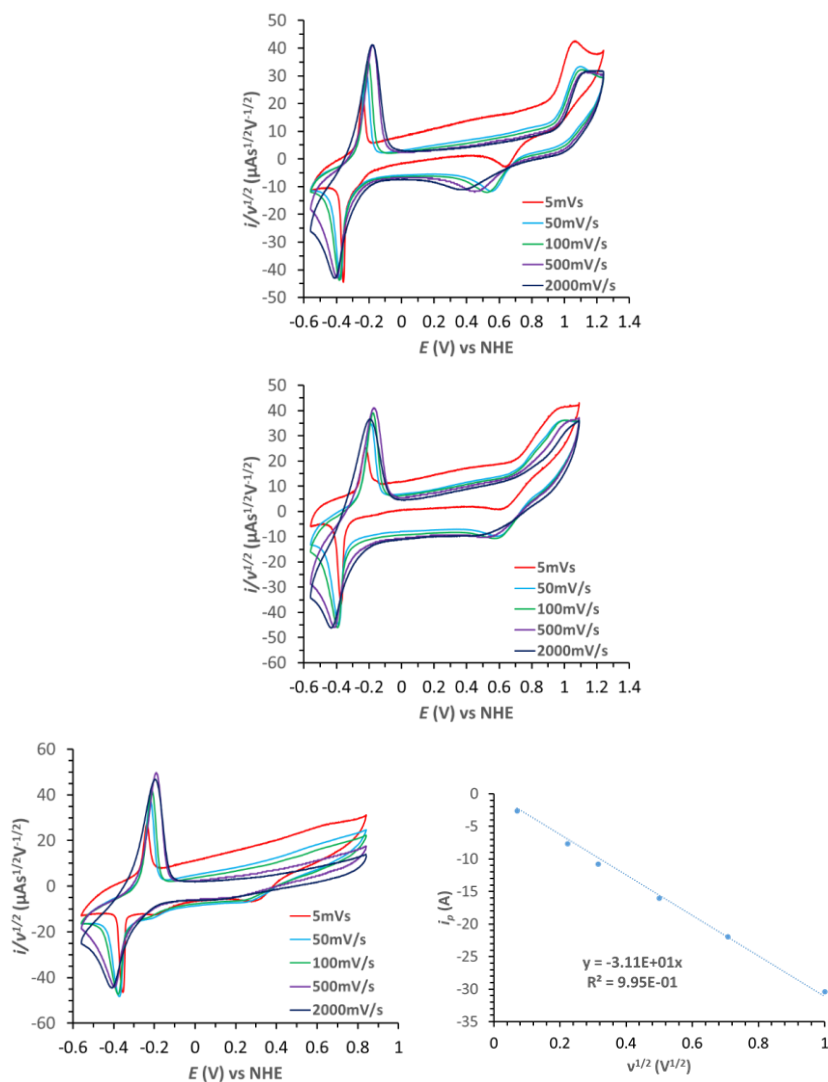


Figure S4. Cyclic Voltammeteries of 1mM of Co-Pyr using GCE as WE in pH 2 (top), pH 4 (middle) and pH 7 (bottom, left) with different scan rates. The intensity was divided by the squared root of the scan rate. Bottom right: Plot of i_p vs squared root of the scan rate.

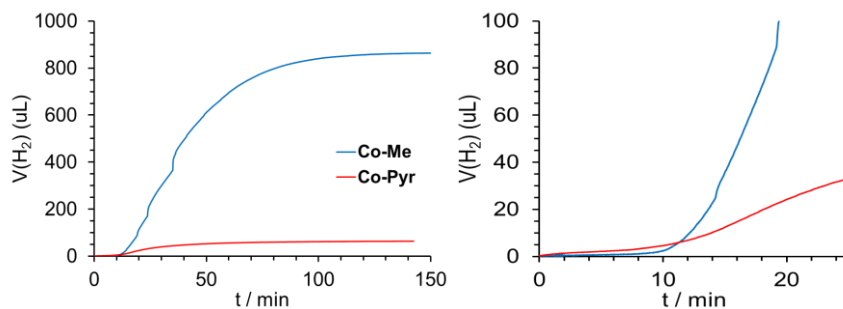


Figure S5. *Left)* Comparison of the photocatalytic activity of Co-Pyr and Co-Me under the same conditions (see experimental details). *Right)* Zoom in of the first 25 minutes of experiment.

4.5.5. Molecular electrode preparation and characterization

To prepare G-Co-pyr, 4 mg of commercially available graphene powder were dispersed in 4 mL of 1 mM Co-py methanolic solution and left stirring overnight in a 4 mL vial. For blank experiments, 4 mg of graphene were also dispersed in clean MeOH and stirred overnight. The day after, both dispersions were centrifuged at $4 \cdot 10^4$ rpm for 10 minutes. The supernatant solutions were separated with a Pasteur pipette and 4 mL of clean MeOH was added to the vials. The graphitic materials were stirred for 5 minutes and centrifuged again in the same conditions described before. The supernatant solution was removed and this cleaning process was repeated twice to remove all the Co-pyr that wasn't anchored to the graphene via π - π stacking interactions. After three cleaning cycles, the graphene and G-Co-pyr were dried using an air flow.

4 mL of clean THF were introduced into each vial containing the powder, together with 10 µL of Nafion® solution (5 wt%) to improve the post-adhesion of the graphene and G-Co-pyr onto GC surfaces. In order to obtain a homogeneous dispersion of the graphitic material in THF, the vials were sonicated for 10 minutes and kept under stirring during the drop casting process.

Before any functionalization, all GC Disks were polished with 0.1 µm alumina on a "nylon pad", rinsed with water, and polished again with 0.05 µm alumina on a "velvet pad". After the polishing procedure, the electrodes were rinsed



A molecular cathode for hydrogen evolution catalysis

with water, and sonicated inside MilliQ water for 3 minutes, rinsed with methanol, acetone and dried with air flow.

To get a homogeneous layer of Graphene or G-Co-pyr on GC disk surface, it was necessary to use 10 drops of 5 μL of the dispersion (it's necessary to wait until THF is completely dry to follow with the next drop). In the case of the GC plates used for the bulk electrolysis experiments (1 cm^2), 10 drops of 30 μL were used to obtain a fully covered surface.

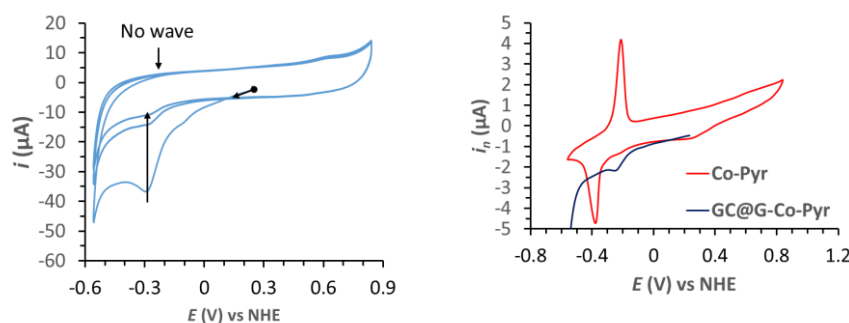


Figure S6. *Left*) CV of GC@G-Co-Pyr in pH 2. No oxidative wave is observed during the anodic scan. Scan rate 100 mV/s. *Right*) Comparison between Co-Pyr CV in homogeneous phase and LSV of GC@G-Co-Pyr. Scan rate 50 mV/s.

4.5.6. Rotating Ring Disk Electrode (RRDE) measurements

RRDE make possible the collection experiments, where the Disk generates species that can be observed at the Ring.⁵ Thus the Disk will reduce protons from the media and the Ring will oxidized it. To select the right potential to oxidase molecular hydrogen, we use Pt-Pt (Disk-Ring) electrode, since platinum is one of the best electrocatalyst to reduce/oxidase H_2 . From Figure S7, we identify at which potentials hydrogen evolution reactions take place (near to $E = -0.020$ V vs NHE).

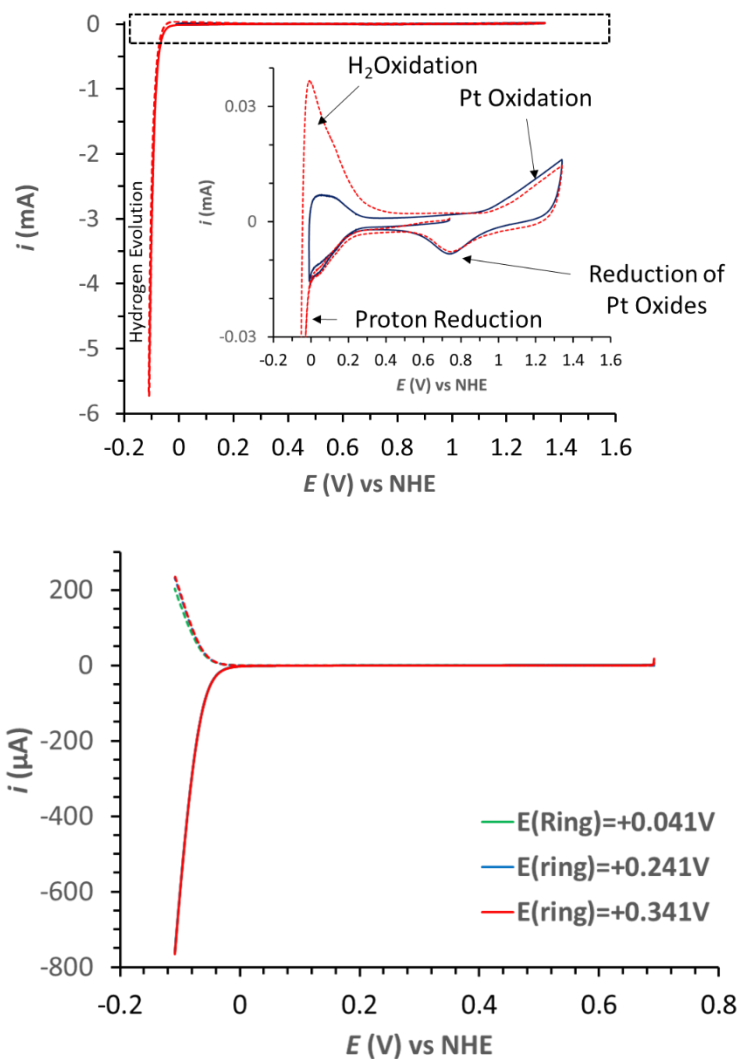


Figure S7. Top) Cyclic Voltammety of Pt Disk in pH 1. Solid line corresponds to Pt profile without reaching catalytic potentials. Dashed line corresponds to the same Pt Disk reaching catalytic potentials. Scan rate 50 mV/s. Inset: magnification of the zone inside the dashed square. **Bottom)** LSV of Pt-Pt RRDE. Solid line corresponds to i -V curve of a cathodic polarization of Pt Disk. Dashed line corresponds to the i -t of Pt ring at different constant potentials. Scan rate 5 mV/s.



A molecular cathode for hydrogen evolution catalysis

From Figure S7 we can also observe that Pt can oxidase H₂ at potentials higher than 0V vs NHE. Multiple Linear Sweep Voltammetry (LSV) with cathodic polarization of the Pt Disk were ran, selecting different constant potentials for Pt Ring in order to find the best potential to detect the presence of H₂.

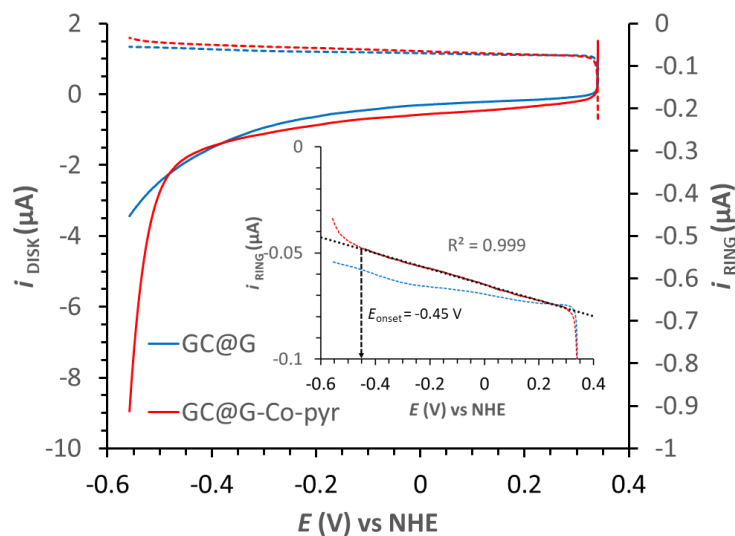


Figure S8. LSV of functionalized GC with Graphene (GC@GC, black) and G-Co-Pyr (GC@GC-Co-Pyr, red) at 1600 rpm in pH 1. Solid line corresponds to i -V curve of the LSV. Dashed line corresponds to the response of Pt disk at $E = +0.341\text{V}$ vs NHE. Inset: i - t curve of Pt disk. CE: Pt Disk. Scan rate 50 mV/s.

While the curves corresponding to the Disk were identical, one can observe from Figure S7 that the intensities of the Ring increases with the potential applied. To detect the onset potential of our G-Co-Pyr, $E = +0.341\text{V}$ (vs NHE) were used.

4.5.7. Determination of Faradaic Efficiency (FE)

The FE of the CPE is calculated using the following formula:

$$FE (\%) = \frac{n_{H_2 \text{ detected}}}{n_{H_2 \text{ theoretical}}} \cdot 100 \quad (\text{eq. 1})$$

Where $n_{H_2 \text{ detected}}$ is the number of mols molecular hydrogen that Clark Electrode and $n_{H_2 \text{ theoretical}}$ is the number of theoretical mols of H_2 calculated from the charge that pass through the electrode.

CP experiments were carried out in a gas-tight two-compartment cell with a 25mL headspace. The GC plate covered with G-Co-Pyr (see section 6) was placed in one compartment (WE) with AgCl/Ag (reference electrode). A Pt mesh was used as CE in the other compartment. Before any experiment, both compartments were degassed with N_2 for 30 minutes. The experiment were carried under stirring conditions. The Clark Electrode was placed in WE compartment after degassing the electrolyte.

Calibration slope is required to correlate the signal of the Clark Electrode and the amount of H_2 contained in the headspace.

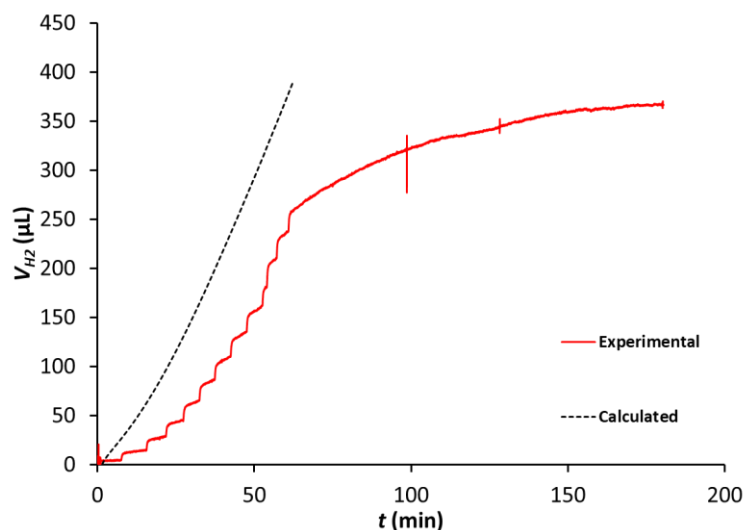


Figure S9. Molecular hydrogen evolved from the electrode measured by Clark at $E = -0.559 \text{ V}$ vs NHE for 1 hour.



A molecular cathode for hydrogen evolution catalysis

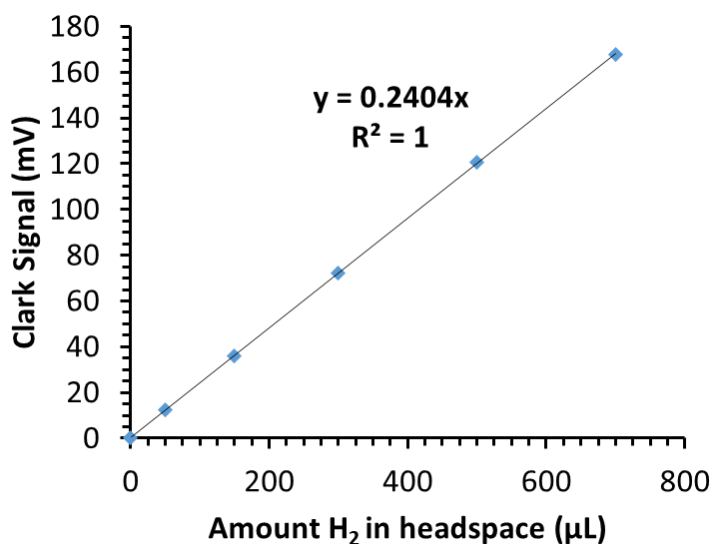


Figure S10. Experimental values used for calibration slope of Clark electrode.



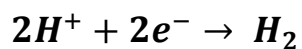
With the slope of the calibration, we can convert the Clark's values (mV) in volume of H₂. Using the perfect gases equation, we can obtain the number of moles of hydrogen gas produced by the electrode and measured in the headspace:

$$P \cdot V = n \cdot R \cdot T$$

$$n = \frac{P \cdot V}{R \cdot T} \quad (\text{eq. 2})$$

Where P is the pressure of the headspace (1 atm), R is the gas constant ($0.082 \frac{\text{atm} \cdot \text{L}}{\text{K} \cdot \text{mol}}$) and T the temperature (298.15 K).

To calculate the theoretical number of moles from the electrical charge transferred to the electrode:



$$n_{H_2 \text{ theoretical}} = \frac{C}{F \cdot n} \quad (\text{eq. 3})$$

Where C is the charge (in C) passed through the electrode, F is the faraday constant (96485C) and n the number of electrons involved to form one molecule of hydrogen.



A molecular cathode for hydrogen evolution catalysis

4.5.8. X-ray Absorption Spectroscopy (XAS) and Methods

X-ray absorption spectra were collected at the CLAES beamline at the ALBA synchrotron light source. The radiation was monochromatized using a pair of Si(111) crystals. The intensity of the X-rays were monitored by three ion chambers (I_0 , I_1 and I_2). I_0 placed before the sample was filled with 100% nitrogen while I_1 and I_2 placed after the sample were filled with 77 % N_2 and 23 % Kr. Co metal was placed between ion chambers I_1 and I_2 and its absorption was recorded with each scan for energy calibration. The samples were measured in customized PEEK sample holders and measured with a defocused beam spot size of $500 \times 500 \mu\text{m}$ using a liquid nitrogen cryostat cooled down to 77 K. Fluorescence absorption measurements were carried out with an Amptek silicon drift solid state detector (XR-100 SDD)⁶ placed at 90 degrees to the incoming beam. The silicon drift detector was placed on a motorized stage allowing the sample-detector distance to be easily changed between 30-110 mm⁶. Around 20-25 scans were collected on the solution and hybrid complexes, and care was taken to measure at different spots on the samples in order to minimize radiation damage. No more than 2 scans were taken in this instance on each spot on the solution and hybrid complexes. The solid cobalt complexes were on the other hand diluted with BN powder, pressed between kapton and mylar tape, and measured in the cryostat in transmission mode. All samples were also protected from the x-ray beam during spectrometer movements by a shutter synchronized with the scan program. Co XAS energy was calibrated by the first maxima in the second derivative of the Cobalt metal X-ray absorption near edge structure (XANES) spectrum.



Extended X-ray Absorption Fine Structure (EXAFS) Analysis

Athena software⁷ was used for data processing. The energy scale for each scan was normalized using copper metal standard. Data in energy space were pre-edge corrected, normalized, deglitched (if necessary), and background corrected. The processed data were next converted to the photoelectron wave vector (k) space and weighted by k . The electron wave number is defined as $k = [2m(E - E_0) / \hbar^2]^{1/2}$, E_0 is the energy origin or the threshold energy. K-space data were truncated near the zero crossings $k = 2$ to 12.6 \AA^{-1} for the solid, solution and hybrid complexes, in Co EXAFS before Fourier transformation.

The k-space data were transferred into the Artemis Software for curve fitting. In order to fit the data, the Fourier peaks were isolated separately, grouped together, or the entire (unfiltered) spectrum was used. The individual Fourier peaks were isolated by applying a Hanning window to the first and last 15% of the chosen range, leaving the middle 70% untouched. Curve fitting was performed using *ab initio*-calculated phases and amplitudes from the FEFF8⁸ program from the University of Washington. *Ab initio*-calculated phases and amplitudes were used in the EXAFS equation

$$\chi(k) = S_0^2 \sum_j \frac{N_j}{kR_j^2} f_{eff_j}(\pi, k, R_j) e^{-2\sigma_j^2 k^2} e^{\frac{-2R_j}{\lambda_j(k)}} \sin(2kR_j + \phi_j(k)) \quad (S2)$$

where N_j is the number of atoms in the j^{th} shell; R_j the mean distance between the absorbing atom and the atoms in the j^{th} shell; $f_{eff_j}(\pi, k, R_j)$ is the *ab initio* amplitude function for shell j , and the Debye-Waller term $e^{-2\sigma_j^2 k^2}$ accounts for damping due to static and thermal disorder in absorber-backscatterer distances. The mean free path term $e^{\frac{-2R_j}{\lambda_j(k)}}$ reflects losses due to inelastic scattering, where $\lambda_j(k)$, is the electron mean free path. The oscillations in the EXAFS spectrum are reflected in the sinusoidal term $\sin(2kR_j + \phi_j(k))$, where $\phi_j(k)$ is the *ab initio* phase function for shell j . This sinusoidal term shows the direct relation between the frequency of the EXAFS oscillations in k-space and the absorber-backscatterer distance. S_0^2 is an amplitude reduction factor.

The EXAFS equation⁹ (Eq. S2) was used to fit the experimental Fourier isolated data (q-space) as well as unfiltered data (k-space) and Fourier transformed data (R-space) using N , S_0^2 , E_0 , R , and σ^2 as variable parameters (Table S1). N refers to the number of coordination atoms surrounding Fe for each shell. The quality of fit was evaluated by R-factor and the reduced χ^2 value. The deviation in E_0 ought to be less than or equal to 10 eV. R-factor less than 2% denotes that the fit is good enough. R-factor between 2 and 5% denotes that the fit is correct within a consistently broad model. The reduced χ^2 value is used to compare fits as more absorber-backscatter shells are included to fit the data. A smaller reduced χ^2 value implies a better fit. Similar results were obtained from fits done in k, q, and R-spaces.



A molecular cathode for hydrogen evolution catalysis

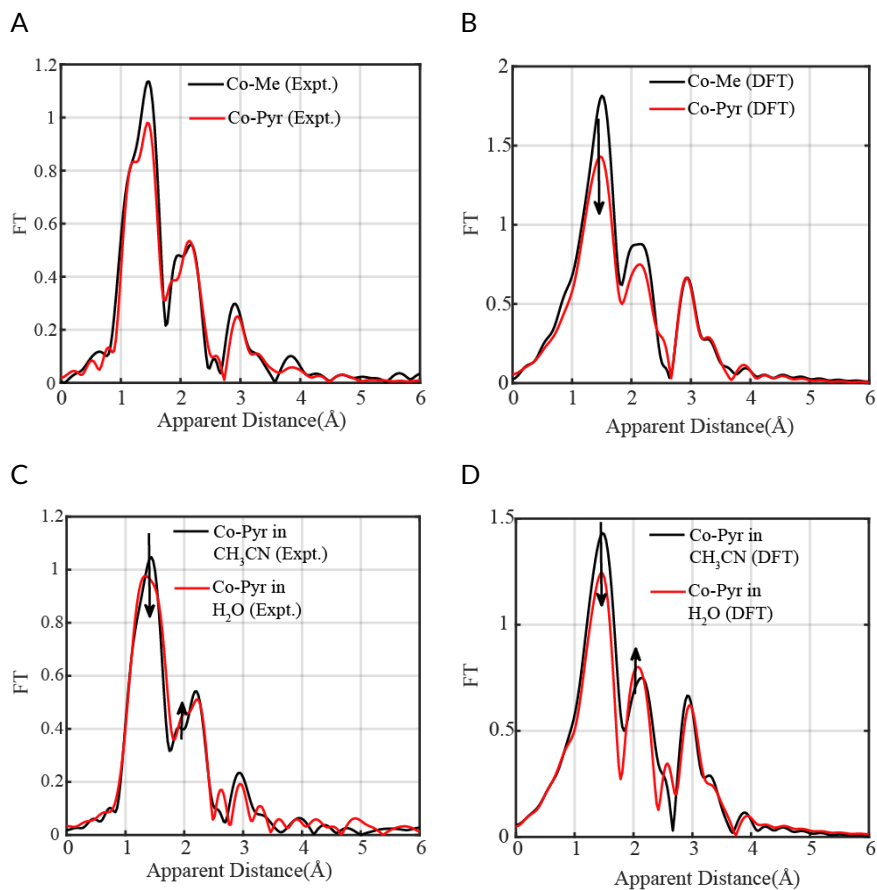


Figure S11. A) Experimental Fourier transforms of k^2 -weighted Co EXAFS of Co-Me and Co-Pyr powder samples. B) DFT calculated Fourier transforms of k^2 -weighted Co EXAFS of Co-Me and Co-Pyr powders. C) Experimental Fourier transforms of k^2 -weighted Co EXAFS of Co-Pyr in CH_3CN and H_2O . D) Theoretically calculated Fourier transforms of k^2 -weighted Co EXAFS of Co-Pyr in CH_3CN and H_2O .

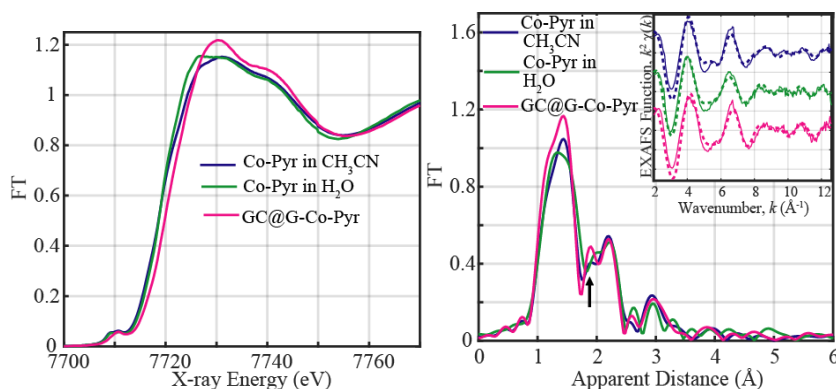


Figure S12. *Left)* Normalized Co-K edges XANES of Co-Pyr in CH₃CN and H₂O with GC@G-Co-Pyr. *Right)* Experimental Fourier transforms of k^2 -weighted Co EXAFS of Co-Pyr in CH₃CN, in H₂O and on electrode surface before catalysis. *Inset:* Back Fourier transformed experimental (solid lines) and fitted (dashed lines) $Re[\chi(k)]$ of Co-Pyr in CH₃CN, in H₂O and on electrode surface before catalysis. Experimental spectra were calculated for k values of 2-12.6 Å⁻¹.



Sample	Fit	Peak	Shell,N	R, Å	E ₀	ss. ² (10 ⁻³)	R-factor	Reduced Chi-square
Co-Me (solid)	1	I	Co-N,5	1.94	-2.7	11.4	0.0054	81
	2	All	Co-N,5	1.94	-3.6	12.5	0.0084	79
			Co-C,5	2.83	9.0			
			Co-C,14	3.08		25.5		
Co-Pyr (solid)	3	I	Co-N,5	1.94	-5.6	11.8	0.0066	2366
	4	All	Co-N,5	1.93	-6.5	12.7	0.0104	1784
			Co-C,6	2.83	11.6			
Co-C,15			3.14	0.2				
Co-Pyr (in CH ₃ CN)	5	I	Co-N,5	1.93	-5.1	10.9	0.0059	434
	6	All	Co-N,5	1.94	-5.4	11.5	0.0100	371
			Co-C,6	2.82	10.4			
Co-C,15			3.12	0.4				
Co-Pyr (in H ₂ O)	7	1	Co-N,5	1.96	-3.5	11.5	0.070	230
	8	All	Co-N,4	1.93	-8.1	9.7	0.0062	223
			Co-O,1	2.45	5.4			
			Co-C,6	2.77	13.3			
			Co-C,15	3.18		0.9		

Table S 3. EXAFS Fits parameters.

A molecular cathode for hydrogen evolution catalysis

	Co-N ₁	Co-N ₂	Co-N ₃	Co-N ₄	Co-N ₅	Co-O
Co-Me (XRD)	1.847	1.932	1.950	1.983	2.040	
Co-Pyr (XRD)	1.840	1.924	1.924	1.999	2.077	
Co-Me (DFT)	1.851	1.950	1.952	2.008	2.024	
Co-Pyr (DFT)	1.850	1.949	1.956	2.043	2.051	
Co-Me (in H ₂ O, DFT)	1.847	1.951	1.954	2.008		2.218
Co-Pyr (in H ₂ O, DFT)	1.846	1.954	1.961	2.029		2.374

Table S 4. XRD and DFT calculated parameters of all crystallized and calculated cobalt complexes.

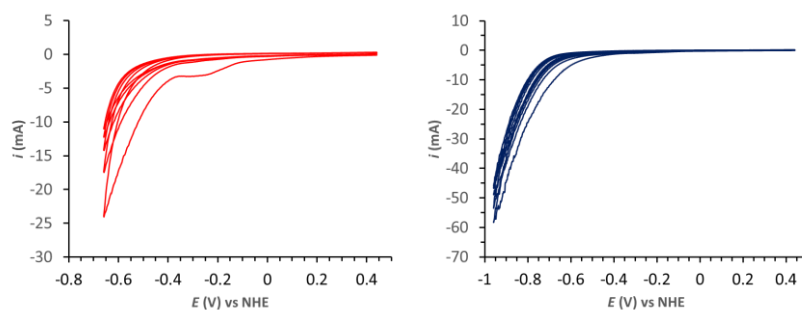


Figure S13. CV of GC@G-Co-Pyr in pH 1 with short cathodic limit (Left) and long cathodic limit (right) analyzed by XAS.



4.5.9. DFT optimization coordinates of Cobalt Complexes

The calculations were carried out using ORCA, the hybrid functional BP861,2 with the def2-TZVP3 triple-zeta basis sets.¹⁰⁻¹²

DFT optimization file of Co-Me in MeCN

Co	3.32031584905181	4.40560061883731	1.63933481670832
N	4.20738987467672	2.79053558481570	1.46760099345352
N	5.10499964216420	4.99134947544902	2.17075161533485
N	2.63887214816927	6.20269303571653	1.00380619811813
N	1.83786537632394	3.32519114931257	0.97837629638096
N	2.64422547649185	4.38795735252679	3.53012572622319
C	1.11966527270370	1.03630999422422	0.29592438218905
H	1.60728221923196	0.09149996915859	0.03703791641880
H	0.55098329000335	1.37162948093133	-0.58302869047047
H	0.39319601228281	0.82722068700975	1.09698446371658
C	2.11456753992304	2.06537819281269	0.73181806983831
C	3.53000094670392	1.73108454573879	0.95797554396883
C	4.20476866791782	0.53185232997459	0.70579033854119
H	3.67828191449103	-0.33208577144034	0.30271046238203
C	5.57644976035396	0.46100436398329	0.96967249550294
H	6.11820924404523	-0.46549098515180	0.77919459986631
C	6.26025177161474	1.57930813180306	1.45753898858553
H	7.33260229916260	1.52931033450676	1.64147754228665
C	5.54468244370616	2.75834949744253	1.69356086430065
C	6.03530774893338	4.06438167424940	2.16229856476575
C	7.45139783676312	4.26376583856169	2.60085611090853
H	8.06792033632802	3.38909271925175	2.37057087741973
H	7.50653270317080	4.43323914129132	3.68765900868408
C	7.90763767794496	5.13443014529583	2.10939141947295
C	5.360924886982753	6.32428589135227	2.71795202054903
H	6.43993530280766	6.51387234295137	2.79878484273310
H	4.95456818891482	6.33230342346377	3.74446527585687
C	4.70276366279156	7.43734632129924	1.90216983256132
H	4.93598134623598	8.38921540488377	2.40292340836554
H	5.16946984804053	7.51010412965391	0.90952933902964
C	3.18383451595711	7.35534167600457	1.801111102319918
H	2.73953879869639	7.28555350779918	2.80430946145514
H	2.80476579716295	8.28384232757783	1.34030081306822
C	1.13988161009062	6.31582225496018	1.03969511722366
H	0.87208802269257	7.29634970308455	0.60897638335823
H	0.84874726129728	6.33354010496077	2.09969960588208
C	0.37123572467972	5.22372210452553	0.30424918074462
H	-0.68954630190791	5.51740346047250	0.32133890579786
H	0.64535765993885	5.18177940209487	-0.75957968645937
C	0.46577132177477	3.83152344029694	0.93093078676226
H	0.10364040007872	3.87331262699136	1.97324119188203
H	-0.19132785228605	3.13729928604814	0.39008799425528
C	3.11600813321670	6.29725449655651	-0.41103734230324
H	2.80547792039883	7.25905907467577	-0.85261851695656
H	2.69425913785333	5.48305249430945	-1.00909933092552
H	4.20815139560692	6.22629673917165	0.45273250122940
C	2.29179468807100	4.29274452174482	4.63366636784914
C	1.85401285387014	4.17339929361674	6.01006372407845
H	2.65444022322950	4.49616520967837	6.69116745742542
H	1.59816816458384	3.12801406449357	6.23419132670119
H	0.96695125421827	4.79978919103096	6.18168471449941



A molecular cathode for hydrogen evolution catalysis

DFT optimization file of Co-Me in H₂O

Co	3.39561237850465	4.41039927141885	1.53635414172081
N	4.26810720783006	2.78761358891295	1.40786969179402
N	5.17732960959661	4.99696092044701	2.08443776556694
N	2.65955895801484	6.20583053927921	1.02090472692568
N	1.88252483602525	3.31516561077847	0.97154641966895
O	2.70334400403640	4.47413794941021	3.64256111780069
C	1.15381713467520	1.01325872574644	0.34505026687954
H	1.63414494370493	0.05891211439112	0.10961380628414
H	0.57733547818062	1.32533321298993	-0.53822343741929
H	0.43220773472703	0.83076858190137	1.15727748828494
C	2.15603986527117	2.05042216585898	0.73916186433302
C	3.57911747955526	1.71971374895539	0.93425521891210
C	4.24737270606752	0.51537171832870	0.68856529872137
H	3.71241452223121	-0.35568002376772	0.31324261429931
C	5.62466292932229	0.44831654949806	0.92397538675861
H	6.16187750118029	-0.48155400285823	0.73764323543051
C	6.31877360655382	1.57303597226325	1.38243702577837
H	7.39407916254652	1.52346536090736	1.54818739434189
C	5.60832825360597	2.75625460961056	1.61354961732275
C	6.10657469625468	4.06706762568782	2.06828789771750
C	7.52730226275631	4.26662123222449	2.48837070960941
H	8.13038608843704	3.37288741558857	2.30100057225827
H	7.59497378246429	4.49485718720551	3.56334815298693
H	7.99111722302348	5.10458384433227	1.94786892378743
C	5.45577536952568	6.33106305964863	2.62709345066606
H	6.53620154640584	6.53022758858684	2.63625705021913
H	5.12495211579680	6.33084225506224	3.68160657557616
C	4.73430847040714	7.44951178943334	1.87634549669701
H	4.97104349208755	8.39062765274111	2.39514962772119
H	5.15283360096207	7.56461737405513	0.86630604644651
C	3.21484247529737	7.33545979533047	1.84587565753731
H	2.82077769745623	7.20648905276382	2.86415476272641
H	2.79251268950522	8.27298022818217	1.44618836192184
C	1.16073409747362	6.29259524956379	1.11343563957603
H	0.86327688903018	7.28463016077324	0.73226556773062
H	0.90713345771606	6.26755245238365	2.18348911592144
C	0.38526468775098	5.21833961957242	0.35962569943405
H	-0.67725776855193	5.50180837426438	0.40781265272992
H	0.63634161420528	5.21187036181234	-0.71051444987871
C	0.50175129659841	3.80783886242702	0.93685390457265
H	0.12408715810829	3.80718868405785	1.97601516318492
H	-0.14427885681647	3.12287452177798	0.37111374663907
C	3.08673738457753	6.35795051723450	-0.40545959896996
H	2.74805782754254	7.32897862336154	-0.80290351356319
H	2.65639281765251	5.55885495368303	-1.01793304451217
H	4.17780970014517	6.30575801375567	-0.48579651762244
H	3.36443581793057	4.33705516858115	4.34575489829930
H	1.92616405462795	3.95764172183708	3.92427780718295



DFT optimization file of Co-Pyr in CH₃CN

Co	4.33972764596002	14.79563172475207	8.16130485825791
N	2.81609321072002	15.44973651424553	9.19701411672891
N	5.83788173801308	15.71560118175147	9.21746946768247
N	5.45648332893647	13.73487224517862	6.96748911356203
N	3.08744070233263	13.52989399096053	7.66038811863079
N	4.05954614932481	16.25418242747475	6.75807524214416
C	2.82290532311510	16.73570461328731	9.89652492556277
H	1.97992279490883	16.79899193903604	10.59908280573942
H	2.66484341363150	17.51992992563850	9.13482450748287
C	6.77012573604445	14.17851034850058	6.49856968857191
H	6.58660534667865	14.89577478134086	5.67850639275837
H	7.33159306723759	13.33893044850417	6.06496160904613
C	4.88142460474059	12.67733430972602	6.44229418260055
C	5.52472272718319	11.75810674989595	5.45145031128462
H	5.76285780389561	12.28673006845112	4.51551243577707
H	4.87126874504460	10.91713289527978	5.20086538773870
H	6.46546430103083	11.34567854105702	5.84383764241673
C	3.49019538087637	12.49881557655290	6.87612461694710
C	2.59613115637290	11.46527793571305	6.57405482092352
H	2.90213447563968	10.63295011278330	5.94260456215093
C	1.30283566186945	11.51344155858076	7.10338154600460
H	0.59304157797103	10.71810081725320	6.87601103598911
C	0.91977877847099	12.57166980693388	7.93394717225398
H	-0.08154149543460	12.60178963472282	8.36014950633099
C	1.84787303012789	13.58216639163846	8.21119433664977
C	1.69947760878687	14.76799260955854	9.06295760853435
C	0.38438299931288	15.15085584323390	9.66745522795008
H	0.02909657137046	16.11199972058351	9.26589694949795
H	0.45979514163018	15.26200551962556	10.75962675844890
H	-0.38540187946733	14.40045188093022	9.46089332872875
C	4.12671197502196	17.00396229748594	10.64394550443738
H	4.03500707092252	17.99502020672020	11.11403475569915
H	4.22998823139887	16.29506491024685	11.47896096983520
C	5.38136059284209	17.03949286952290	9.77689628540927
H	5.21931905950589	17.70964299257102	8.92061096965593
H	6.21544015779275	17.45980445519012	10.36464460080717
C	6.98153075015790	16.02807885213553	8.29046194604105
H	6.60556323077824	16.75171472081935	7.55280633479787
H	7.75659534461292	16.54340748804237	8.88444705307190
C	7.61903988112460	14.83982759767389	7.58173735373247
H	8.52912536240705	15.21660175411424	7.08985071068239
H	7.95857705591325	14.08511404240702	8.30132138141397
C	6.32746354389714	14.85773060541260	10.38985645058795
H	5.72838995546031	15.15312045134356	11.25926317924969
H	7.35763070602689	15.17536020354689	10.60053865319406
C	6.21432178610939	13.35878204140924	10.23940405939209
C	4.92192427959648	12.79801053672598	10.25461946661312
H	4.06882821763040	13.45404600627189	10.44660227893889
C	4.70505016130245	11.43194424876486	10.11850395537784
H	3.69170104542099	11.02795542968105	10.16107439581673
C	5.79111303024286	10.54581904986406	9.98968749290756
C	7.12358580239158	11.07489223203233	10.05766020395615
C	7.34186983140519	12.49034854042634	10.20634790516091
C	8.69959653853334	12.94205128085932	10.34397227137447
H	8.90735441821842	13.99727723991600	10.52428481556962
C	9.75846698916319	12.07562720256609	10.30054718228274
H	10.77511858960713	12.45283331891079	10.42688374336359
C	9.56860640487109	10.67263580887727	10.11205926142244
C	8.23115165657939	10.17824403999246	10.00032784006910



A molecular cathode for hydrogen evolution catalysis

C	8.01419793820345	8.77139017697240	9.84510117304545
C	9.12467840494959	7.90941922469220	9.78807018637503
H	8.95801691329516	6.83695753914896	9.66881569354403
C	10.42666647437139	8.40519554591298	9.789194733846453
H	11.27254287475898	7.71847943676487	9.85120636727213
C	10.64903680352009	9.77051081978572	10.05705731238382
H	11.66662563228522	10.15335966423395	10.15185883457496
C	6.66994972152588	8.28235702214646	9.76810203607605
H	6.51120409078744	7.20734941267111	9.66096044672272
C	5.60302901644652	9.13348026829276	9.84616875047143
H	4.58356768108145	8.74440150428548	9.81285174768130
C	3.78847713680500	16.98943046433195	5.89909177289749
C	3.45428016416687	17.90732570673294	4.82779480082682
H	4.12020221130331	17.74488507379710	3.96847522813172
H	3.56433545280592	18.94666088055842	5.16964692427259
H	2.41535216845471	17.74862672295218	4.50533209000389

DFT optimization file of Co-Pyr in H₂O

Co	4.47600463064460	14.74106601453045	8.27598196770392
N	2.91679252125887	15.47459963457335	9.21157961116049
N	5.94287490073118	15.74381327895211	9.25618904561101
N	5.58420927713768	13.75277390639018	7.00541823785905
N	3.18934841722013	13.58515841201349	7.63116632032550
O	4.23098157191584	16.50095617978393	6.70105486926286
C	2.91549236437404	16.73308752698165	9.96674339076191
H	2.08709987213326	16.74537902587446	10.68981794481736
H	2.71853056174577	17.55104932580086	9.25035106926023
C	6.92531008348410	14.15963860174021	6.57014762435713
H	6.79041436234184	14.82562970232349	5.697208095642597
H	7.49411736357867	13.29039548124556	6.20981429483233
C	4.98888079409421	12.74024283536329	6.41568851754299
C	5.62829269235033	11.85318265468471	5.39526953202116
H	5.92236810589258	12.42315830368859	4.50015081559613
H	4.95472174973480	11.05315048677646	5.07344842471313
H	6.53990427883294	11.38461127177634	5.79525129628326
C	3.57859148654676	12.58617173832899	6.80168808858331
C	2.65536936396026	11.61174853716554	6.40464517303328
H	2.95047489396548	10.80485774867089	5.73583858296390
C	1.34370130681611	11.68918462744704	6.88356351424834
H	0.61084749431702	10.94033959194935	6.58323787939716
C	0.96838870174883	12.72237348889651	7.74856601398250
H	-0.05089451681453	12.78007939543338	8.12684240057764
C	1.92672516405887	13.67324084910873	8.11858570208197
C	1.78329699742180	14.83867703042919	9.00231302260134
C	0.45688630083338	15.25342235793928	9.55595792553024
H	0.17392885538574	16.25668845713381	9.20276892995734
H	0.47762393838791	15.29305548952792	10.65624674043804
H	-0.33758191377226	14.56114616349898	9.26101407658291
C	4.22778087053084	17.00221364236155	10.69544899399910
H	4.13167860636886	17.98378962627698	11.18412026677882
H	4.35371397903592	16.28142078748925	11.51729068946957
C	5.46455892332360	17.06449983786812	9.80600720254160
H	5.27465028045715	17.71939647600372	8.94374831455599
H	6.29853093236809	17.50884992341718	10.37532081878452
C	7.05965721658875	16.07228212897882	8.30052275042864
H	6.64255943322043	16.75137437277508	7.54262566257892
H	7.81652725992025	16.64407051306272	8.86475046193811
C	7.73878100236248	14.87950195451286	7.64102637854906

H	8.64743938905160	15.25983883886551	7.14982057232271
H	8.08496447074450	14.15822777131980	8.39130101953423
C	6.47574442349799	14.90396426101131	10.41836993017446
H	5.92988572944144	15.22315169712528	11.31439396972423
H	7.52281377069108	15.19527778514454	10.57302806135259
C	6.30463568125469	13.41107844513148	10.26623971607805
C	4.98492416441363	12.91171015152540	10.24205391122431
H	4.16105254865268	13.59325721924257	10.47261401334735
C	4.71022711444973	11.55523138444052	10.08208688582188
H	3.67949667120818	11.19601429705874	10.10125175829038
C	5.75743867539234	10.62454840965466	9.96771347921032
C	7.11200065407966	11.09287069271454	10.06968349585499
C	7.39146764254066	12.49604893885722	10.23942427106557
C	8.76510025193695	12.88744938684873	10.40440595261705
H	9.01556346256573	13.92982413825283	10.60323533808422
C	9.78396865967761	11.97459752698791	10.37063977870875
H	10.81425341972571	12.30407936760246	10.51779635465098
C	9.53464358522531	10.58249930046342	10.16725131145238
C	8.17835341947195	10.14861750317911	10.02590253200924
C	7.90141311509369	8.75347333716403	9.85621637142632
C	8.97251748673082	7.84321288284047	9.81604678128341
H	8.76078062254622	6.78001394982758	9.68669177429429
C	10.29297237255241	8.28008878515504	9.94855935187643
H	11.10796345142843	7.55627637616479	9.92030605038996
C	10.57376680236657	9.63351829747526	10.12661467001305
H	11.60576064379757	9.96874098066255	10.24378320773050
C	6.53810694115652	8.32535648524410	9.74836373964038
H	6.33412209821022	7.25925410647977	9.63119365581405
C	5.50919324437164	9.22223565920927	9.80921075202236
H	4.47436654598346	8.87960492099885	9.75226827861377
H	3.36405539033371	16.93800463434020	6.62040690814408
H	4.52446742690475	16.36605508823692	5.78184259909114



A molecular cathode for hydrogen evolution catalysis

4.5.10. References

- (1) Kwon, J.; Hong, J. P.; Lee, S.; Hong, J. I. 4,4'-Di(pyren-1-Yl)-1,1'-Biphenyl as an Efficient Material for Organic Light-Emitting Diodes and Thin-Film Transistors. *New J. Chem.* **2013**, *37* (9), 2881–2887. <https://doi.org/10.1039/c3nj00295k>.
- (2) Huang, K. W.; Wu, Y. R.; Jeong, K. U.; Kuo, S. W. From Random Coil Polymers to Helical Structures Induced by Carbon Nanotubes and Supramolecular Interactions. *Macromol. Rapid Commun.* **2013**, *34* (19), 1530–1536. <https://doi.org/10.1002/marc.201300533>.
- (3) Ng, C. Y.; Motekaitis, R. J.; Martell, A. E. New Multidentate Ligands. 18. Synthesis of L, 4-Bis(bis(2-aminoethyl)aminomethyl)benzene: Binuclear Chelating Tendencies and Mixed-Ligand Binuclear Chelate Formation. *Inorg. Chem.* **1979**, *18* (11), 2982–2986. <https://doi.org/10.1021/ic50201a008>.
- (4) Arbuse, A.; Font, M.; Martínez, M. A.; Fontrodona, X.; Prieto, M. J.; Moreno, V.; Sala, X.; Llobet, A. DNA-Cleavage Induced by New Macrocyclic Schiff Base Dinuclear Cu(I) Complexes Containing Pyridyl Pendant Arms. *Inorg. Chem.* **2009**, *48* (23), 11098–11107. <https://doi.org/10.1021/ic901488j>.
- (5) Bard, A. J.; Faulkner, L. R. *Electrochemical Methods, Fundamentals and Applications*, 2nd ed.; Wiley, 2001; Vol. 60. <https://doi.org/10.1021/ed060pa25.1>.
- (6) Simonelli, L.; Marini, C.; Olszewski, W.; Ávila Pérez, M.; Ramanan, N.; Guilera, G.; Cuartero, V.; Klementiev, K. CLAESS: The Hard X-Ray Absorption Beamline of the ALBA CELLS Synchrotron. *Cogent Phys.* **2016**, *3* (1), 1–10. <https://doi.org/10.1080/23311940.2016.1231987>.
- (7) Ravel, B.; Newville, M. ATHENA, ARTEMIS, HEPHAESTUS: Data Analysis for X-Ray Absorption Spectroscopy Using IFEFFIT. *J. Synchrotron Radiat.* **2005**, *12* (4), 537–541. <https://doi.org/10.1107/S0909049505012719>.
- (8) Rehr, J. J.; Albers, R. C.; Zabinsky, S. I. High-Order Multiple-Scattering Calculations of X-Ray-Absorption Fine Structure. *Phys. Rev. Lett.* **1992**, *69* (23), 3397–3400. <https://doi.org/10.1103/PhysRevLett.69.3397>.
- (9) D. C. Koningsberger, R. P. *X-Ray Absorption: Principles, Applications, Techniques of EXAFS, SEXAFS and XANES*; D. C. Koningsberger, R. P., Ed.; New York: Wiley, c1988, 1988.
- (10) Becke, A. D. Density-Functional Exchange-Energy Approximation with Correct Asymptotic Behavior. *Phys. Rev. A* **1988**, *38* (6), 3098–3100. <https://doi.org/10.1103/PhysRevA.38.3098>.
- (11) Perdew, J. P. Density-Functional Approximation for the Correlation Energy of the Inhomogeneous Electron Gas. *Phys. Rev. B* **1986**, *33* (12), 8822–8824. <https://doi.org/10.1103/PhysRevB.33.8822>.
- (12) Weigend, F.; Ahlrichs, R. Balanced Basis Sets of Split Valence, Triple Zeta Valence and Quadruple Zeta Valence. *Phys. Chem. Chem. Phys.* **2005**, *7*, 3297–3305. <https://doi.org/10.1039/b508541a>.



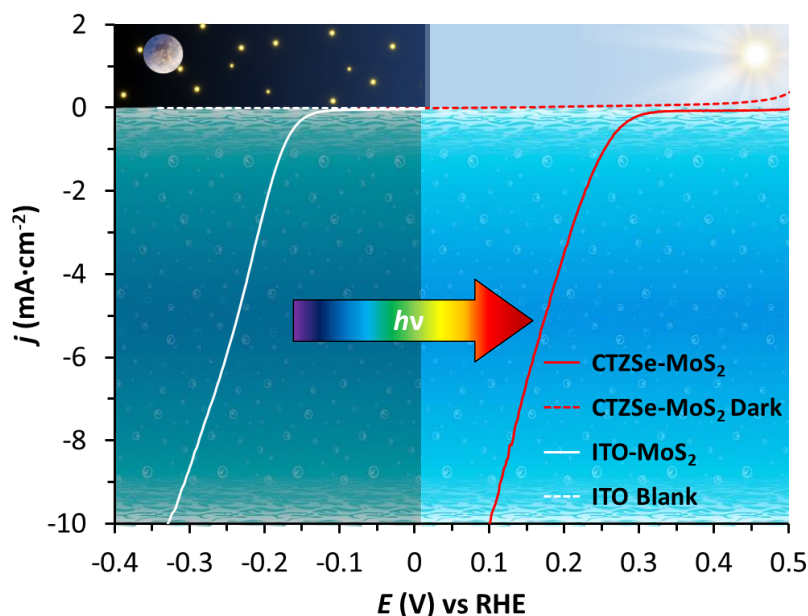
Chapter

5

Photocathodes based on $\text{Cu}_2\text{ZnSnSe}_4$ for the Hydrogen Evolution Reaction

A methodology to electrodeposit amorphous MoS_2 on ITO electrodes have been developed that allows us to fuctionalize p-type semiconductor kesterite (CZTSe) very active for proton reduction catalysis. The prepared non-noble metal photocathode features an excelent performance in pH 2, able to reach $-10 \text{ mA}\cdot\text{cm}^{-2}$ at 100 mV before the thermodynamic potential. Moreover, the photocathode is able to sustain high current densities without any loss in activity for at least one hour.

Photocathodes based on $\text{Cu}_2\text{ZnSnSe}_4$ for HER



Abstract



In this work, a multilayered p-type photoabsorber based on kesterite $\text{Cu}_2\text{ZnSnSe}_4$ (Mo/CZTSe/CdS/ZnO/ITO) have been functionalized with inexpensive and easily scalable amorphous MoS_2 electrocatalyst by photoelectrodeposition. The resulting photocathodes feature a high catalytic current density at 0 V vs RHE (-18 mA/cm^2) and have been able to perform HER under 1 sun illumination at -10 mA/cm^2 above thermodynamic potential of the H^+/H_2 couple for 1 hour without loss in activity. As far as we know, this is the first example in the literature of a kesterite based photocathode prepared without any precious metal as HER catalyst that reaches high current densities with high conversion efficiencies. The MoS_2 layer is key not only to catalyze the HER but also to protect the photoabsorber from the corrosive electrolyte solution.

Contributions:

Sergi Grau Abarca functionalized ITO and CZTSe (photo)cathodes, and carried out the electrochemical, photoelectrochemical and spectroscopic experiments. He also collaborated in the preparation of the CZTSe absorbers and the acquisition of SEM images.

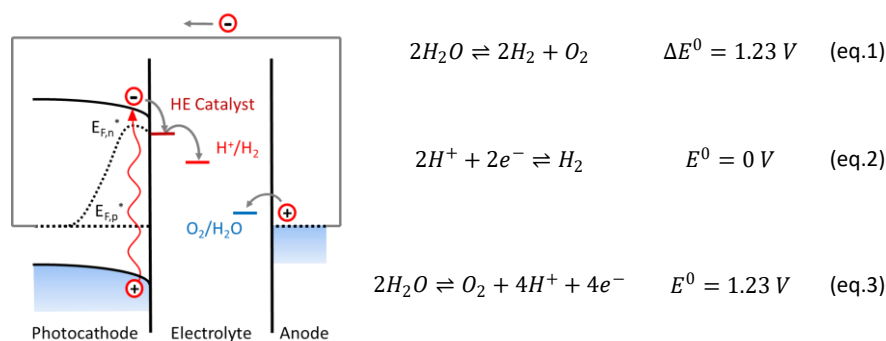
5.1 Introduction

Since 2000, the worldwide energy consumption have been increasing with an average rate of 2.3%.¹ This increase was mainly supplied by fossil fuels leading in a rise of CO₂ atmospheric levels, reaching the historical value of 407.4 ppm in 2018.² It is predicted that the energy consumption will continue to increase even more in the future and for this reason, it is imperative to find other sources of energy, renewable and environmentally friendly to supply humankind energy needing.

Artificial photosynthesis is a general term that includes light induced water splitting reactions or light driven CO₂ reduction. Both processes are important because they store the energy of the sunlight producing clean fuels (e.g. H₂) and they reduce the CO₂ atmospheric levels.^{3,4} One common strategy for the hydrogen production is the use of the photoelectrochemical cell (PEC), where the photoelectrodes harvest the light, separate the electron-hole pair and perform water oxidation (photoanode) and hydrogen evolution (HE) (photocathode) reactions (see example in Scheme 1).⁵ Thermodynamically, water splitting reaction requires 1.23 V (eq. 1) plus the overpotential associated to kinetic barrier of each half-reactions (eq. 2 and 3). To minimize the overpotential required for Hydrogen Evolution Reaction (HER, eq. 2) and Oxygen Evolution Reaction (OER, eq. 3) it's necessary to use selective and efficient catalysts for each reaction.



Photocathodes based on $\text{Cu}_2\text{ZnSnSe}_4$ for HER



Scheme 1. Diagram of a PEC where the photocathode performs HER and a metallic anode performs OER, where HE is Hydrogen Evolution, $E_{F,h}^*$ is quasi-fermi level of holes and $E_{F,e}^*$ is quasi-fermi level of electrons.

Platinum (Pt) is the best catalyst for HER known to date, able to reduce protons to molecular hydrogen with almost no overpotential, but is scarce and expensive.^{6,7} For these reasons, the scientific community has been investigating for a long time cheap and earth abundant materials active for HER. Among them a remarkable material is MoS_2 , which was not investigated as a HER catalyst due to his low activity as bulk material until Hinnemann *et al.* reported in 2005 that MoS_2 nanoparticles were active HER catalysts.⁸ Further theoretical studies reveled that only the edge sites and sulfur S vacancies were the active sites on the crystallographic edges of the MoS_2 nanoparticles.⁸⁻¹⁰ Later, Jaramillo *et al.* proved it experimentally showing that the catalytic current in HER was proportional to the length of the edges in MoS_2 crystalline nanoparticles, instead of the geometrical area.¹¹ Since then, several theoretical and experimental studies with different synthetic approaches to obtain MoS_2 active for HER with different nanostructures as well as amorphous MoS_2 thin films have been published.¹²⁻¹⁷ On the other hand, only a few examples can be found in the literature where MoS_2 HER electrocatalyst is combined with semiconductors to build photocathodes.¹⁸⁻²⁰

During the last decades, quaternary salts of the family of p-type kesterites with stoichiometry $\text{Cu}_2\text{ZnSn}(\text{S}/\text{Se})_4$ have been widely used as photocathodes for the HER. They have been explored for their high performance as photoabsorbers



in photovoltaic devices with efficiencies in the range up to 12.7% and V_{oc} of 513.7 mV.²¹ In addition, they are made from non-critical raw materials (earth abundant materials or materials that are not used in large scale in industry to produce goods, i.e. inexpensive) and low-toxicity elements.

Mainly, in the literature one can find sulfur based kesterites as photocathodes Cu_2ZnSnS_4 that are commonly abbreviated as CZTS. In 2008 Scragg *et al.* obtained p-type CZTS annealing Cu/Zn/Sn electroplated stacks on Mo-coated glass under sulfur atmosphere.²² Domen *et al.* prepared in 2010 a CZTS photocathode with an additional n-type CdS layer to create a p-n junction and a TiO_2 top layer to protect the absorbers from the electrolyte and HER platinum nanoparticles on the surface. This improved the performance and reached an impressive current density of -9.0 mA/cm^2 at the thermodynamic potential ($E_{OV \text{ vs RHE}}$) at pH 9.5.²³ Later, in 2015, the same group prepared Mo/CZTS/CdS/ In_2S_3 /Pt able to reach -9.30 mA/cm^2 at the $E_{OV \text{ vs RHE}}$ at pH 6.5.²⁴ Two years later, Zhigang *et al.* used a similar photocathode configuration improving the performance with the addition of Ge and reaching -11.1 mA/cm^2 at the $E_{OV \text{ vs RHE}}$ at pH 6.5.²⁵ A recent paper has used selenium based thin-film kesterites as photocathodes containing a top layer of TiO_2 and Pt on the surface showing current densities of -37 mA/cm^2 at $E_{OV \text{ vs RHE}}$ in pH 0.²⁶

Despite all these promising advances, there is still a lack of an efficient and stable $Cu_2ZnSn(S/Se)_4$ photocathode that is made of inexpensive catalysts, as they are all based on platinum particles. In addition, the stability of the reported examples is most of the time an overlooked parameter that should not be ignored in a field where long-term performance is key to bring light-induced water splitting devices into the market. In this work, CZTSe based p-type photoabsorbers are combined with MoS_2 electrocatalyst layers to build a powerful photocathode for the HER. The two key components have been selected for **i)** their high performance as light absorbers (CZTSe) and catalytic activity (MoS_2) and **ii)** for the optimum band alignment of the semiconductor^{21,27,28} with the overpotential of the electrocatalyst,^{8,11,15-17,19} that should favor charge separation and fast catalysis leading to high performance.



Photocathodes based on $\text{Cu}_2\text{ZnSnSe}_4$ for HER

5.2 Results and Discussion

5.2.1 Preparation of CZTSe absorber layer

The preparation of the multilayered photoabsorber based on $\text{Cu}_2\text{ZnSnSe}_4$ electrodes were performed in collaboration with Dr. Edgardo Saucedo and Professor Dr. Alejandro Perez-Rodriguez in the *Institut de Recerca en Energia de Catalunya* (IREC), during a 1 week stay in their laboratories. Additional samples were directly provided by the IREC research group following the same procedure.²⁹

The photoabsorber consists of a carefully designed multilayered configuration that can be formulated as $\text{Mo}/\text{MoSe}_2/\text{Cu}_2\text{ZnSnSe}_4/\text{CdS}/\text{ZnO}/\text{ITO}$ (where ITO is indium doped tin oxide). Detailed description of the preparation of the samples is given in the supporting information. Additionally, more details on the baseline absorber synthesis can be found in references ^{30,31}. Briefly, it consists of selenization of $\text{Cu}/\text{Zn}/\text{Sn}$ stacks, that have been previously deposited by sputtering on Molybdenum-coated soda-lime glass (also prepared by sputtering). The resulting $\text{Mo}/\text{MoSe}_2/\text{Cu}_2\text{ZnSnSe}_4$ samples were dipped in a chemical bath for n-type CdS deposition, followed by the sputtering deposition of ZnO and ITO in order to complete the devices. Finally, all the devices were subjected to a soft post-deposition annealing at 250 °C for 15 minutes on a hotplate in air atmosphere to improve cathode performance. For the sake of simplicity, the full photoabsorber $\text{Mo}/\text{MoSe}_2/\text{Cu}_2\text{ZnSnSe}_4/\text{CdS}/\text{ZnO}/\text{ITO}$ will be regarded as CZTSe in the rest of the chapter. Powder x-ray diffraction, resonance Raman spectroscopy and transmission electron microscopy analysis of the prepared samples confirmed the crystallinity and purity of the $\text{Cu}_2\text{ZnSnSe}_4$ photoabsorber layer with no secondary phases. Composition, morphology and grain size were also as previously reported.^{26,29}

Optical band gap of CZTSe/CdS/ZnO/ITO were measured using UV-vis Diffuse Reflectance Spectroscopy (DRS) and External Quantum Efficiency (EQE) experiments obtaining the results summarized in Table 1 (see Figures S1 and S11B):



Method	CZTSe (eV)	CdS (eV)	ZnO (eV)	ITO (eV)
DRS (this work)	0.94-1.35	2.0-2.1	3.0-3.4	2.9
EQE (this work)	1.05	---	---	---
Literature ^{32,33}	0.95	2.4	3.3	2.8

Table 1. Band gap values obtained from DRS and EQE compared data from the literature.

Due to the post deposition annealing, some S^{2-} migrate from CdS to ZnO and CZTSe layers, doping the absorber, as well as Cu^+ ions doping CdS layer, phenomena that have proven to be beneficial for the device efficiency.³⁴ In Figure S1, a representative Tauc plot obtained from DRS spectrum shows seven transitions corresponding to CZTSe (pure, $E_g = 0.94$ eV), CZTSSe ($E_g = 1.35$ eV), two for CdS ($E_g = 2.1-2.0$ eV), two for ZnO/ZnS ($E_g = 3.0-3.4$ eV)³⁵ and one for ITO ($E_g = 2.9$ eV). Interestingly, CdS and ZnO features double peaks (green dashed lines in Figure S1), very likely due the shallow doping during the post deposition annealing, thus corresponding one to the pure material and the other to the doped material layers.

5.2.2 Optimization of the MoS₂ electrocatalyst layer

Molybdenum sulfide MoS_x ($x = 2$ or 3) can be prepared by electrodeposition from the precursor $(NH_4)_2MoS_4$ into conductive substrates in three different ways: i) cathodic deposition, ii) anodic deposition and iii) cyclic deposition¹²⁻¹⁴. The last two approaches were ruled out due to the required oxidation potential, which could lead to the chemical decomposition of the CZTSe absorber during the photoelectrochemical deposition. Thus, in this work, all the electrodes were prepared by the cathodic deposition approach on indium tin oxide (ITO) in galvanostatic mode. Detailed description of the MoS₂ electrodeposition procedure can be found in the SI. Briefly, it consists of a cathodic electrodeposition from an electrochemical bath containing $[(NH_4)_2MoS_4] = 30$ mM and ionic strength $I = 0.1$ M in galvanostatic mode (fixed current density $j = -7.5 \cdot 10^{-5}$ A/cm²). The process was done under weak argon bubbling to avoid the formation of molybdenum oxides and the loading of the molybdenum sulfide deposited was controlled by the total amount of charge passed through the electrochemical system. The potential required to prepare



Photocathodes based on $\text{Cu}_2\text{ZnSnSe}_4$ for HER

the catalyst lays beyond the HER potential and produces concomitant hydrogen gas evolution during the deposition process (Figure S9).¹⁶

Table 2, Figure 1 and Figure S2 summarize the results of the activity of MoS_2 -coated ITO electrodes (ITO- MoS_2 hereafter) towards HER in pH 2 phosphate buffer solution with different loadings of the electrocatalyst. The overpotential required to reach -1 mA/cm^2 decreases with increasing amount of MoS_2 while the current density at $E_{-0.3\text{V vs RHE}}$ increases with higher amount of catalyst. As shown in Figure S3 the MoS_2 films are not transparent and therefore are expected to influence the light absorbing process once deposited on the CZTSe photoabsorber. Although the best performing electrode is the one with a charge loading of 0.1 C/cm^2 , it is also the electrode with a lower degree of transmittance (10-55 % in the range of 350-800nm). Therefore, the ITO- MoS_2 electrode with $Q = 0.05 \text{ C/cm}^2$ with $E_{(\text{at } j = -1 \text{ mA/cm}^2)} = -0.180 \text{ V}$ and $j_{(\text{at } E = -0.3 \text{ V})} = -9.46 \text{ mA/cm}^2$ was selected as a good compromise between high activity (Figure 1) and high transparency (Table S3).



Charge passed (C/cm^2)	E for $j = -1 \text{ mA/cm}^2$	j at $E_{\text{vs RHE}} = -0.3 \text{ V}$
0.01	-0.205 V	$-7.37 \text{ mA}\cdot\text{cm}^{-2}$
0.02	-0.195 V	$-8.45 \text{ mA}\cdot\text{cm}^{-2}$
0.05	-0.175 V	$-9.46 \text{ mA}\cdot\text{cm}^{-2}$
0.1	-0.165 V	$-9.96 \text{ mA}\cdot\text{cm}^{-2}$

Table 2. Overpotential (at $j = -1 \text{ mA/cm}^2$) and current density (at $\eta = 300 \text{ mV}$) values of the ITO- MoS_2 samples with different loadings of HER catalyst.

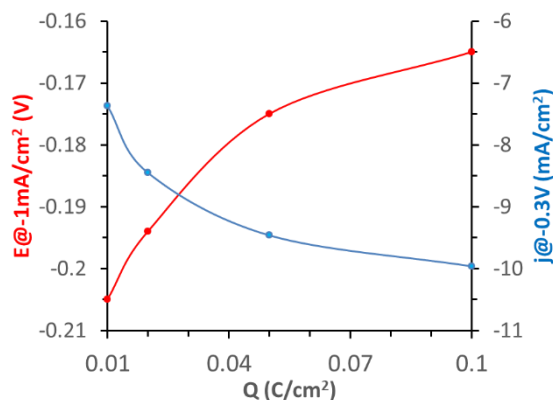


Figure 1. Potential required to reach -1 mA/cm^2 (red dots, left y axis) and j reached at -0.3 V (blue dots, right y axis) versus MoS_2 loading.

All the ITO-MoS₂ electrodes prepared by cathodic deposition show a reduction process at potentials between -0.025 and -0.150 V vs RHE, before the hydrogen evolution reaction, attributed to the reduction of the MoS₃ to MoS₂ during the first Linear Sweep Voltammetry (LSV) scan. This event was not observed again in subsequent scans of the LSV experiments on the same sample (Figure 2, compare red and blue traces)^{12,14}.

The activity of the ITO-MoS₂ electrodes is highly dependent on the pH of the electrolyte solution, showing drastic decrease of the cathodic current associated to the HER in pH values higher than 2 (Figure S4). ITO-MoS₂ electrodes tested in pH higher than 10 were unstable and the catalyst peeled off very quickly from the electrode surface. This result is in sharp contrast to other reported amorphous MoS₂ based electrodes for HER in the literature where are very active in extreme pH values (0 and 14).³⁶ We attribute these results to the lower adhesion of our MoS₂ to the ITO substrate.

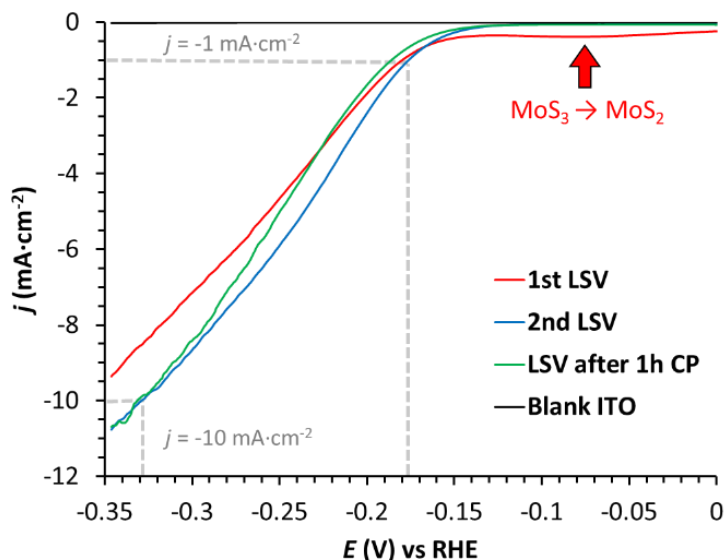


Figure 2. LSV of ITO-MoS₂ with a $Q = 0.05 \text{ C/cm}^2$ loading at pH 2. Counter electrode: Pt mesh. Reference electrode: AgCl/Ag. Scan rate: 5 mV/s. Experiments recorded under stirring conditions. *iR* drop corrected at 85%.



Photocathodes based on $\text{Cu}_2\text{ZnSnSe}_4$ for HER

LSV experiments in Figure 2 show that ITO-MoS₂ electrodes with a 0.05 C/cm² loading feature an overpotential of -175 mV and -330 mV vs RHE to reach -1 mA/cm² and -10 mA/cm² respectively at pH 2. A chronopotentiometry (CP) experiment at -10 mA/cm² was ran for 1 hour, without showing any significant loss of activity (Figure 3, left). The averaged overpotential required to sustain -10 mA/cm² for the whole experiment was -328 mV vs RHE, in good agreement with the LSV results and indicating that the scan rate used to run the LSV were close to the stationary conditions. In order to check the faradaic efficiency (FE), the experiment was repeated in a two-compartment electrochemical cell, monitoring the amount of hydrogen evolved from the cathode by using a Clark electrode sensor, obtaining 100% efficiency (Figure 3, right, see also details in the SI). The activity of the electrode after this test was also checked by LSV without remarkable losses of current densities (Figure 2, compare blue and green traces).

Long-term CP tests up to 10h were ran to assess the stability of the ITO-MoS₂ electrodes. The catalytic activity started to decrease linearly after 1 hour of electrolysis until the 5th hour. At this time the required potential to run $j = -10$ mA/cm² is $E = -0.6$ V as opposed to the $E = -0.33$ V required during the first hour (Figure S5). After 5h, the HER activity of the electrode decreases drastically requiring lower potentials to sustain the selected current density.

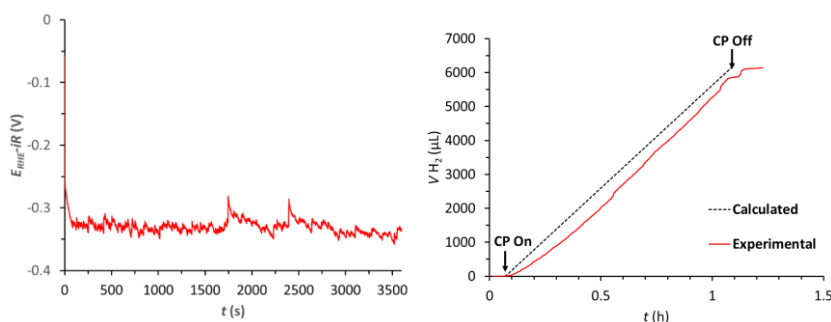


Figure 3. *Left*) CP of ITO-MoS₂ in pH 2 at -10 mA/cm² in a two-compartment electrochemical cell. Counter electrode: Pt mesh. Reference electrode: AgCl/Ag. *i*R drop corrected at 85%. *Right*) Amount of molecular hydrogen evolved during CP experiments (red line) and the calculated from the charge transferred (black dashed line).

In order to get insights into the deactivation processes during electrolysis, the morphology of the electrodes before and after catalysis were analyzed by Scanning Electronic Microscopy (SEM).

Top view SEM images confirm homogeneous and continuous MoS_2 films covering completely the ITO surface after deposition of the electrocatalyst (Figure 4A and Figure S6). Only small cracks in the amorphous MoS_2 layer can be observed, that are likely produced by the mechanical stress due the expansion of the hydrogen bubbles during the electrodeposition process.

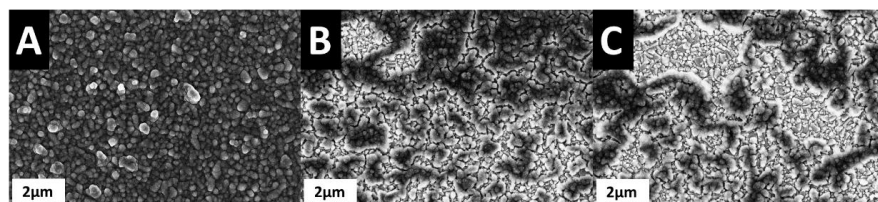


Figure 4. Top view SEM images of ITO- MoS_2 electrodes as prepared (A), after 1h of CP (B) and after 10h of CP (C).

After 1h of electrolysis, the SEM images show small regions where the initial cracks start to get wider, starting to expose ITO underlayer to the electrolyte (Figure 4B). The cracks become even larger after 10h of experiment when the ITO is mostly exposed and only little amount of the MoS_2 layer is left (Figure 4C). Interestingly, the shape of some of the cracks suggest a peeling due to mechanical stress from a gas bubble rather than a chemical process (Figure S7). It is important to notice that the images of the damaged regions shown in Figure 3B and 3C were chosen from the most affected zones and they are not representative of the whole surface, where the ITO- MoS_2 mainly looks intact (Figure S8).



Photocathodes based on $\text{Cu}_2\text{ZnSnSe}_4$ for HER

5.2.3 MoS_2 modified CTZSe and HER photoelectrochemical performance

The CZTSe absorbers were functionalized with MoS_2 using the methodology developed in the previous section adapted to the photoelectrochemical properties of these photoelectrodes. The cathodic photoelectrodeposition of the MoS_2 HER catalyst onto the ITO top layer of the photoabsorber was done in galvanostatic mode under 2 sun illumination due to the strong absorption of light by the electrochemical bath ($[(\text{NH}_4)_2\text{MoS}_4]=30\text{mM}$). The (photo)electrodeposition of MoS_2 in galvanostatic mode allows consistent rate of growth of the catalyst film on ITO, and on CZTSe samples, despite the fact that the actual applied potential to make the HER catalyst layer growth is different due to the distinct photovoltage generated by different samples of CZTSe under light irradiation. Figure S9 shows the $E-t$ curves of MoS_2 deposition from representative ITO and CZTSe (photo)electrodes. The catalyst deposition using this method is very reproducible, giving identical $E-t$ curves for ITO sample and only slight differences in $E-t$ curves are observed for the CZTSe samples. Detailed description of the photocathodes' preparation and photoelectrodeposition of MoS_2 can be found in the SI.



The photoelectrochemical activity of the CZTSe- MoS_2 electrodes towards HER were tested in pH 2 phosphate buffer solution under 1 sun illumination. Analogous to the ITO- MoS_2 electrodes described in section 5.3.2, the CZTSe- MoS_2 photocathodes also showed a reduction process before the HER catalysis assigned to the MoS_3 to MoS_2 transformation at potentials from 0.4 to 0.25 V vs RHE during the first LSV scan (Figure S10). CZTSe covered with MoS_2 features an onset potential and overpotential of +254 mV and +100 mV to achieve -1 mA/cm^2 and -10 mA/cm^2 respectively (Figure 5, red line). No dark-current was observed in the range of potentials used. Due to the high overpotential required for producing molecular hydrogen for raw CZTSe photocathode no photocurrent was detected below 0 V vs RHE without the MoS_2 modification (see black dashed line in Figure 5).

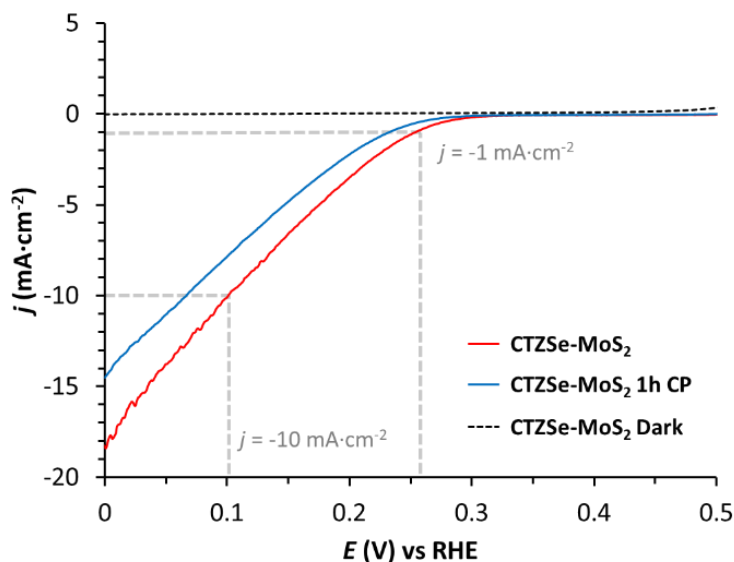


Figure 5. LSV of CZTSe-MoS₂ in pH 2 under 1 sun illumination (red line), in dark conditions (black dashed line) and after 1 h of CP at -10 mA/cm² (blue line). Counter electrode: Pt mesh. Reference electrode: AgCl/Ag. Scan rate: 5 mV/s. LSV recorded under stirring conditions. iR drop corrected at 85%.

By comparing the LSV of the ITO-MoS₂ and the CTZSe-MoS₂ electrodes we can observe the onset potential for HER is anodically shifted by approximately +430 mV. This value is close to the Open Circuit Potential (V_{oc}) obtained from the J - V curve of an equivalent photovoltaic device, indicating minimum losses in photovoltage (V_{ph}) by the presence of the MoS₂ layer, suggest we are at the limit of the capabilities of the photoabsorber (Figure 6 and S11, left). Remarkably, the high current densities obtained for our CTZSe-MoS₂ electrode are amongst the best performing photocathodes for the hydrogen evolution reaction described in the literature (Table 3 and S1).



Photocathodes based on $\text{Cu}_2\text{ZnSnSe}_4$ for HER

Material	HEC	pH	j_{ov} ($\text{mA}\cdot\text{cm}^{-2}$)	$j_{@10\text{mA}/\text{cm}^2}$ (V)	E_{onset} (V)	Stability	Year	Ref
Mo/CZTS/Cds/TiO ₂	Pt	9.5	-9.0	--	+0.60	--	2010	23
Mo/CZTS/Cds/ In ₂ S ₃	Pt	6.5	-9.3	--	+0.64	2h	2015	24
Mo/Ge-CZTS/Cds/In ₂ S ₃	Pt	6.5	-11.1	+0.100	+0.60	2h	2017	25
Mo/CZTSe/Cds/ZnO/ITO/TiO ₂	Pt	0	-37.0	+0.27	+0.45	1h	2018	26
Mo/CZTS/Cds/ZnS	Pt	6.5	-8.0	--	+0.65	2h	2019	37
Mo/CZTSe/Cds/ZnO/ITO	MoS ₂	2	-18.1	+0.100	+0.30	3.5h	2019	This work

Table 3. Comparison of the best CZTS/Se base photocathodes with our work.

Among the most recent CZTS/Se photocathodes reported, ours is the only one that does not use noble-metal HEC, reaching the impressive current density of $-18.1 \text{ mA}/\text{cm}^2$ at the thermodynamic H^+/H_2 potential in mild conditions, only overcome by Ros *et al.* photocathode²⁶ that used Pt as HEC in pH 0. It is important to notice that unlike ours, some of the reported photocathodes had never measured the evolved molecular hydrogen, giving the chance to overestimate the performance of the photocathode (by assigning all the measured current to the generation of H_2 and not possible internal redox inside the material).

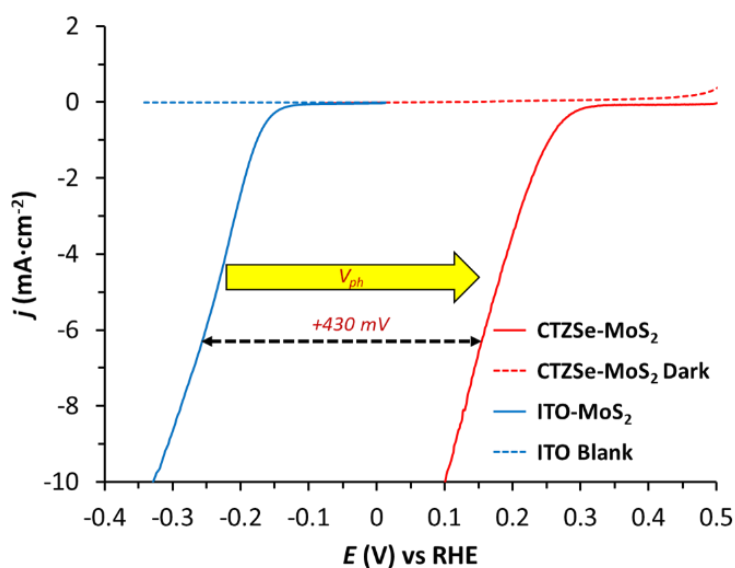


Figure 6. LSV of ITO-MoS₂ and CZTSe-MoS₂ with the same loading of catalyst. Scan rate: 5 mV/s. LSV recorded under stirring conditions. *iR* drop corrected at 85%.

CP experiments at -10 mA/cm^2 were ran in a two-compartment cell under 1 sun illumination, obtaining an averaged potential of $+0.86 \text{ V}$ vs RHE for one hour with FE of 100% (Figure 7 and S12, right). As shown in Figure 7 (left) no loss in activity was observed during this lapse of time (no increase in the required potential). A LSV experiment of the photocathodes after CP shows a slight decrease in activity requiring an overpotential of $+233 \text{ mV}$ and $+66 \text{ mV}$ to get -1 mA/cm^2 and -10 mA/cm^2 respectively (Figure 5, compare red and blue lines).

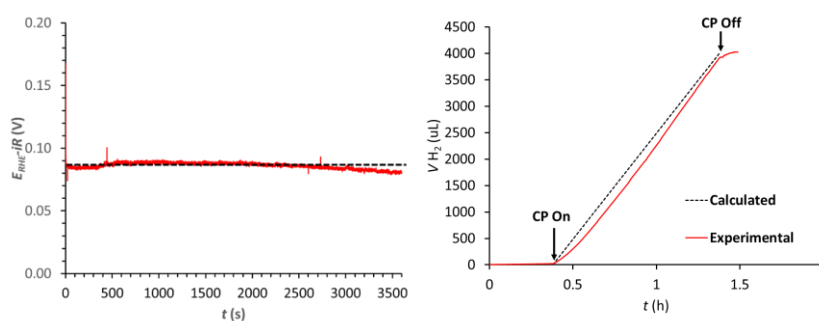


Figure 7. *Left)* CP of CZTSe-MoS₂ in pH 2 at -10 mA/cm^2 in a two-compartment photoelectrochemical cell. Dashed black line indicates the averaged potential during the CP experiment ($E = +0.86 \text{ V}$). *Right)* Amount of molecular hydrogen evolved (red line) and the calculated from the charge transferred (black dashed line).



Longer CP experiments (Figure 8) show that our photocathode is able to produce molecular hydrogen at -10 mA/cm^2 for 2h without any significant loss in activity (i.e. $1.2 \mu\text{L}(\text{H}_2)/\text{cm}^2\cdot\text{s}$) and able to perform HER below the thermodynamic potential for 3.5 hours. After the first two hours, the potential required to sustain -10 mA/cm^2 increases linearly, increasing the potential by ca. 44 mV/h , a similar trend that was observed for the ITO-MoS₂ electrodes. Interestingly, the MoS₂ layer seems to last longer when it is on the surface of the photoelectrode (2h) than when it is on the ITO surface (1h) before losing activity. This result might be attributed to the distinct nature of the ITO surface when it is deposited onto CZTSe electrode than when it is deposited directly onto glass, resulting in better adhesion to the surface in the former case.

Photocathodes based on $\text{Cu}_2\text{ZnSnSe}_4$ for HER

Due to the low stability of the ITO layer directly immersed in pH 2³⁸⁻⁴⁰ it was not possible to measure more than two scans with raw CZTSe because of the fast degradation of the photoabsorber. Thus, the amorphous MoS_2 layer not only reduces the overpotential for HER, but also protects the ITO and the absorber layers from the electrolyte, preventing its corrosion and dissolution.

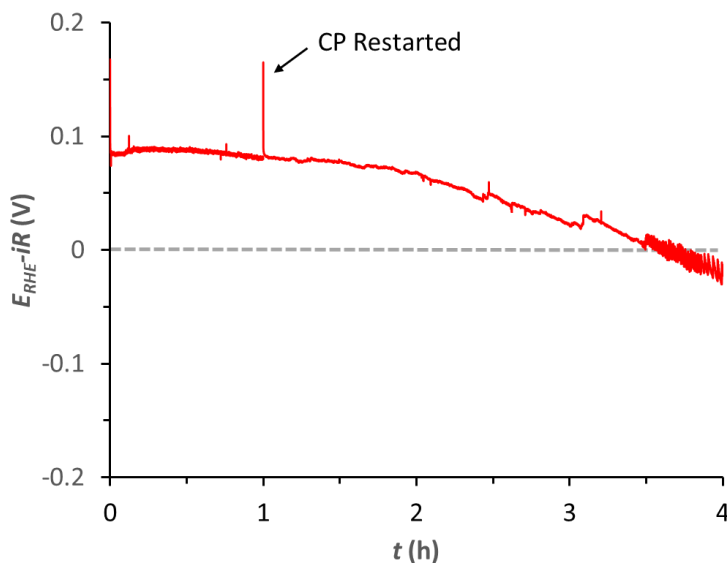


Figure 8. CP of CZTSe-MoS₂ in pH 2 at -10 mA/cm² in a two-compartment photoelectrochemical cell.

In order to rule out the loss of activity due to dissolution of the photoabsorber material, aging experiments consisting of immersing the CZTSe-MoS₂ photoelectrodes in pH 2 for 5 hours were performed, from which no change in activity was observed (Figure S13). Therefore, the loss of activity can be attributed to the depletion of electroactive material by mechanical stress from the evolution of H₂ bubbles, as suggested also for the parent ITO-MoS₂ electrodes.

SEM images of the CZTSe-MoS₂ electrodes show the homogeneity and compactness of the top layer before and after catalytic tests, despite the small cracks already mentioned for the analogous ITO-MoS₂ electrodes in section

5.3.2 (Figure 9, A and D). While the top-view SEM images did not show any change in the morphology, cross-sections of the photocathodes as prepared and after 1 hour of CP revealed that the MoS₂ layer became thinner (Figure 9, D and E) from 150-250 nm to 80-130 nm. The electrocatalyst layer became even thinner with the extended CP, reaching 60-90nm of thickness after 5 hours. No peeled regions were found during the surface analysis as opposed to what was observed for the ITO-MoS₂ electrodes suggesting that the mechanical stability in this case is better. On the other hand, the other layers (Mo/MoSe₂/CZTSe/ZnO/ITO) look intact, highlighting once more the stabilizing role of the MoS₂ electrocatalytic layer.

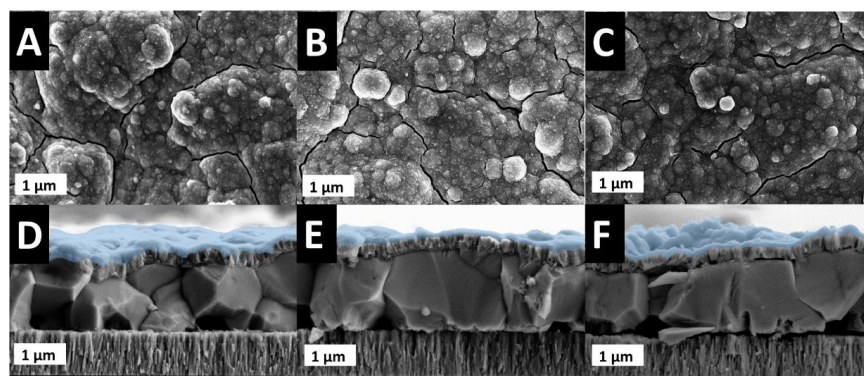


Figure 9. Top view and cross section of SEM images of CZTSe-MoS₂ as prepared (A and D), after 1h of CP (B and E) and after 5h (C and F). In cross-section images, MoS₂ layer was colored with blue.



Photocathodes based on $\text{Cu}_2\text{ZnSnSe}_4$ for HER

5.3 Summary and Conclusions

In this chapter the preparation of a highly active photocathode for HER is described. It is based on the modification of a kesterite thin-film photoabsorber with a multilayered architecture ($\text{Mo}/\text{MoSe}_2/\text{Cu}_2\text{ZnSnSe}_4/\text{CdS}/\text{ZnO}/\text{ITO}$, abbreviated CZTSe) and an amorphous electrocatalytic MoS_2 top layer.

An electrodeposition procedure based on galvanostatic methods has been developed, which allowed us to prepare ITO-MoS_2 electrocathodes and CZTSe-MoS_2 photocathodes in a very reliable and reproducible manner.

Photoelectrochemical experiments show that the CZTSe-MoS_2 electrode can perform the HER at +0.3 V vs RHE in pH 2 (+0.254 V to reach $1 \text{ mA}\cdot\text{cm}^{-2}$). This accounts for the decrease of 430 mV in overpotential compared to the ITO-MoS_2 electrode. This value, in good agreement with the photovoltage of an analogous photovoltaic device made of the same absorber.

In addition, the stability of the CZTSe-MoS_2 photocathode has been studied in detail, finding that it is able to perform HER for two hours without any significant loss of activity. Moreover, it is able to keep the hydrogen production for more than 3.5 hours below the thermodynamic potential ($E = 0\text{V}$ vs RHE). Longer reaction times induce loss of the electroactive layer caused by the expansion of microbubbles on the surface of the photocathode as demonstrated by SEM images. A similar phenomenon has been observed for the ITO-MoS_2 . In sharp contrast, the photoactive CZTSe layer remains intact, highlighting the key role of the MoS_2 film in isolating it from the electrolyte.

All these results allow us to conclude that, amorphous MoS_2 obtained by (photo)electrodeposition is a very good catalyst for HER, inexpensive and easy to prepare that not only reduces the overpotential for HER but also protects the sensitive photoactive underlayers of the photocathode from the corrosive electrolyte.



5.4 References

- (1) BP Statistical Review of World Energy. *Statistical Review of World Energy June 2018*; BP p.l.c., 1 St James's Square, London, SW1Y 4PD, UK, 2018.
- (2) IEA. *Global Energy & CO₂ Status Report*; 2018.
- (3) Barber, J. Photosynthetic Energy Conversion: Natural and Artificial. *Chem. Soc. Rev.* **2009**, 38 (1), 185–196. <https://doi.org/10.1039/b802262n>.
- (4) Nathan S. Lewis. Research Opportunities to Advance Solar Energy Utilization. *Science (80-.)*. **2016**, 351 (6271), 353–364. <https://doi.org/10.1126/science.aad1920.22>.
- (5) Walter, M. G.; Warren, E. L.; Mckone, J. R.; Boettcher, S. W.; Mi, Q.; Santori, E. A.; Lewis, N. S. Solar Water Splitting Cells. *Chem. Rev.* **2010**, 110, 6446–6473.
- (6) Saurat, M.; Bringezu, S. Of Europe , Part 1 Global Supply , Use in Industry , and Shifting. *J. Ind. Ecol.* **2008**, 12 (5/6), 754–767. <https://doi.org/10.1111/j.1530-9290.2008.00087.x>.
- (7) Alonso, E.; Field, F. R.; Kirchain, R. E. Platinum Availability for Future Automotive Technologies. *Environ. Sci. Technol.* **2012**, 46 (23), 12986–12993. <https://doi.org/10.1021/es301110e>.
- (8) Chorkendorff, I.; Jørgensen, K. P.; Nielsen, J. H.; Hinnemann, B.; Moses, P. G.; Nørskov, J. K.; Hørch, S.; Bonde, J. Biomimetic Hydrogen Evolution: MoS₂ Nanoparticles as Catalyst for Hydrogen Evolution. *J. Am. Chem. Soc.* **2005**, 127 (15), 5308–5309. <https://doi.org/10.1021/ja0504690>.
- (9) Li, G.; Zhang, D.; Qiao, Q.; Yu, Y.; Peterson, D.; Zafar, A.; Kumar, R.; Curtarolo, S.; Hunte, F.; Shannon, S.; et al. All The Catalytic Active Sites of MoS₂ for Hydrogen Evolution. *J. Am. Chem. Soc.* **2016**, 138 (51), 16632–16638. <https://doi.org/10.1021/jacs.6b05940>.
- (10) He, Z.; Que, W. Molybdenum Disulfide Nanomaterials: Structures, Properties, Synthesis and Recent Progress on Hydrogen Evolution Reaction. *Appl. Mater. Today* **2016**, 3, 23–56. <https://doi.org/10.1016/j.apmt.2016.02.001>.
- (11) Chorkendorff, I.; Bonde, J.; Jorgensen, K. P.; Hørch, S.; Jaramillo, T. F.; Nielsen, J. H. Identification of Active Edge Sites for Electrochemical H₂ Evolution from MoS₂ Nanocatalysts. *Science (80-.)*. **2007**, 317 (5834), 100–102. <https://doi.org/10.1126/science.1141483>.
- (12) Vrabel, H.; Hu, X. Growth and Activation of an Amorphous Molybdenum Sulfide Hydrogen Evolving Catalyst. *ACS Catal.* **2013**, 3 (9), 2002–2011. <https://doi.org/10.1021/cs400441u>.



Photocathodes based on $\text{Cu}_2\text{ZnSnSe}_4$ for HER

- (13) Merki, D.; Fierro, S.; Vrabel, H.; Hu, X. Amorphous Molybdenum Sulfide Films as Catalysts for Electrochemical Hydrogen Production in Water. *Chem. Sci.* **2011**, 2 (7), 1262–1267. <https://doi.org/10.1039/c1sc00117e>.
- (14) Morales-Guio, C. G.; Hu, X. Amorphous Molybdenum Sulfides as Hydrogen Evolution Catalysts. *Acc. Chem. Res.* **2014**, 47 (8), 2671–2681. <https://doi.org/10.1021/ar5002022>.
- (15) Albu-Yaron, A.; Lévy-Clément, C.; Katty, A.; Bastide, S.; Tenne, R. Influence of the Electrochemical Deposition Parameters on the Microstructure of MoS_2 Thin Films. *Thin Solid Films* **2000**, 361, 223–228. [https://doi.org/10.1016/S0040-6090\(99\)00838-X](https://doi.org/10.1016/S0040-6090(99)00838-X).
- (16) Ponomarev, E. A.; Hodes, G. Electrochemical Deposition of MoS_2 Thin Films by Reduction of Tetrathiomolybdate. *Thin Solid Films* **1996**, 280, 186–189.
- (17) Huang, Y.; Nielsen, R. J.; Goddard, W. A.; Soriaga, M. P. The Reaction Mechanism with Free Energy Barriers for Electrochemical Dihydrogen Evolution on MoS_2 . *J. Am. Chem. Soc.* **2015**, 137 (20), 6692–6698. <https://doi.org/10.1021/jacs.5b03329>.
- (18) King, L. A.; Hellstern, T. R.; Park, J.; Sinclair, R.; Jaramillo, T. F. Highly Stable Molybdenum Disulfide Protected Silicon Photocathodes for Photoelectrochemical Water Splitting. *ACS Appl. Mater. Interfaces* **2017**, 9 (42), 36792–36798. <https://doi.org/10.1021/acsami.7b10749>.
- (19) Shearer, M. J.; Jin, S.; Ding, Q.; Liang, D.; Cabán-Acevedo, M.; Daniel, A. S.; English, C. R.; Meng, F.; Hamers, R. J. Efficient Photoelectrochemical Hydrogen Generation Using Heterostructures of Si and Chemically Exfoliated Metallic MoS_2 . *J. Am. Chem. Soc.* **2014**, 136 (24), 8504–8507. <https://doi.org/10.1021/ja5025673>.
- (20) Morales-Guio, C. G.; Thorwarth, K.; Niesen, B.; Liardet, L.; Patscheider, J.; Ballif, C.; Hu, X. Solar Hydrogen Production by Amorphous Silicon Photocathodes Coated with a Magnetron Sputter Deposited Mo_2C Catalyst. *J. Am. Chem. Soc.* **2015**, 137 (22), 7035–7038. <https://doi.org/10.1021/jacs.5b03417>.
- (21) Dhawale, D. S.; Ali, A.; Lokhande, A. Impact of Various Dopant Elements on the Properties of Kesterite Compound for Solar Cell Application: A Status Review. *Sustain. Energy Fuels* **2019**. <https://doi.org/10.1039/C9SE00040B>.
- (22) Scragg, J. J.; Dale, P. J.; Peter, L. M.; Zoppi, G.; Forbes, I. New Routes to Sustainable Photovoltaics: Evaluation of $\text{Cu}_2\text{ZnSnS}_4$ as an Alternative Absorber Material. *Phys. Status Solidi Basic Res.* **2008**, 245 (9), 1772–1778. <https://doi.org/10.1002/pssb.200879539>.
- (23) Yokoyama, D.; Minegishi, T.; Jimbo, K.; Hisatomi, T.; Ma, G.; Katayama, M.; Kubota, J.; Katagiri, H.; Domen, K. H_2 Evolution from Water on



- Modified $\text{Cu}_2\text{ZnSnS}_4$ Photoelectrode under Solar Light. *Appl. Phys. Express* **2010**, 3 (10), 2–4. <https://doi.org/10.1143/APEX.3.101202>.
- (24) Minegishi, T.; Harada, T.; Kuang, Y.; Jiang, F.; Ikeda, S.; Gunawan; Domen, K. Pt/ In_2S_3 /CdS/ $\text{Cu}_2\text{ZnSnS}_4$ Thin Film as an Efficient and Stable Photocathode for Water Reduction under Sunlight Radiation. *J. Am. Chem. Soc.* **2015**, 137 (42), 13691–13697. <https://doi.org/10.1021/jacs.5b09015>.
- (25) Wen, X.; Luo, W.; Guan, Z.; Huang, W.; Zou, Z. Boosting Efficiency and Stability of a $\text{Cu}_2\text{ZnSnS}_4$ Photocathode by Alloying Ge and Increasing Sulfur Pressure Simultaneously. *Nano Energy* **2017**, 41 (May), 18–26. <https://doi.org/10.1016/j.nanoen.2017.09.006>.
- (26) Ros, C.; Andreu, T.; Giraldo, S.; Izquierdo-Roca, V.; Saucedo, E.; Morante, J. R. Turning Earth Abundant Kesterite-Based Solar Cells Into Efficient Protected Water-Splitting Photocathodes. *ACS Appl. Mater. Interfaces* **2018**, 10 (16), 13425–13433. <https://doi.org/10.1021/acscami.8b00062>.
- (27) Chen, S.; Wang, L. W. Thermodynamic Oxidation and Reduction Potentials of Photocatalytic Semiconductors in Aqueous Solution. *Chem. Mater.* **2012**, 24 (18), 3659–3666. <https://doi.org/10.1021/cm302533s>.
- (28) Haight, R.; Barkhouse, A.; Gunawan, O.; Shin, B.; Copel, M.; Hopstaken, M.; Mitzi, D. B. Band Alignment at the $\text{Cu}_2\text{ZnSn}(\text{S}_x\text{Se}_{1-x})_4$ /CdS Interface. *Appl. Phys. Lett.* **2011**, 98 (25), 253502. <https://doi.org/10.1063/1.3600776>.
- (29) Neuschitzer, M.; Moises, E.-R.; Guc, M.; Prieto, J.; Giraldo, S.; Forbes, I.; Alejandro, P.-R.; Saucedo, E. Revealing the Beneficial Effects of Ge Doping on $\text{Cu}_2\text{ZnSnSe}_4$ Thin Film Solar Cells. *J Mater Chem* **2018**, 6 (25), 11759–11772. <https://doi.org/10.1039/C8TA02551G>.
- (30) Giraldo, S.; Neuschitzer, M.; Thersleff, T.; López-Marino, S.; Sánchez, Y.; Xie, H.; Colina, M.; Placidi, M.; Pistor, P.; Izquierdo-Roca, V.; et al. Large Efficiency Improvement in $\text{Cu}_2\text{ZnSnSe}_4$ Solar Cells by Introducing a Superficial Ge Nanolayer. *Adv. Energy Mater.* **2015**, 5 (21), 1501070. <https://doi.org/10.1002/aenm.201501070>.
- (31) Giraldo, S.; Saucedo, E.; Neuschitzer, M.; Oliva, F.; Placidi, M.; Alcobé, X.; Izquierdo-Roca, V.; Kim, S.; Tampo, H.; Shibata, H.; et al. How Small Amounts of Ge Modify the Formation Pathways and Crystallization of Kesterites. *Energy Environ. Sci.* **2018**, 11 (3), 582–593. <https://doi.org/10.1039/c7ee02318a>.
- (32) Kaur, K.; Kumar, N.; Kumar, M. Strategic Review of Interface Carrier Recombination in Earth Abundant Cu-Zn-Sn-S-Se Solar Cells: Current Challenges and Future Prospects. *J. Mater. Chem. A* **2017**, 5 (7), 3069–3090. <https://doi.org/10.1039/C6TA10543B>.
- (33) Li, S.; Ghinea, C.; Bayer, T. J. M.; Motzko, M.; Schafranek, R.; Klein, A. Electrical Properties of (Ba, Sr) TiO_3 Thin Films with Pt and ITO Electrodes:



Photocathodes based on $\text{Cu}_2\text{ZnSnSe}_4$ for HER

- Dielectric and Rectifying Behaviour. *J. Phys. Condens. Matter* **2011**, *23* (33). <https://doi.org/10.1088/0953-8984/23/33/334202>.
- (34) Neuschitzer, M.; Sanchez, Y.; Olar, T.; Thersleff, T.; Lopez-Marino, S.; Oliva, F.; Espindola-Rodriguez, M.; Xie, H.; Placidi, M.; Izquierdo-Roca, V.; et al. Complex Surface Chemistry of Kesterites: Cu/Zn Reordering after Low Temperature Postdeposition Annealing and Its Role in High Performance Devices. *Chem. Mater.* **2015**, *27* (15), 5279–5287. <https://doi.org/10.1021/acs.chemmater.5b01473>.
- (35) Torabi, A.; Staroverov, V. N. Band Gap Reduction in ZnO and ZnS by Creating Layered ZnO/ZnS Heterostructures. *J. Phys. Chem. Lett.* **2015**, *6* (11), 2075–2080. <https://doi.org/10.1021/acs.jpcclett.5b00687>.
- (36) Morales-Guio, C. G.; Liardet, L.; Mayer, M. T.; Tilley, S. D.; Grätzel, M.; Hu, X. Photoelectrochemical Hydrogen Production in Alkaline Solutions Using Cu_2O Coated with Earth-Abundant Hydrogen Evolution Catalysts. *Angew. Chemie - Int. Ed.* **2015**, *54* (2), 664–667. <https://doi.org/10.1002/anie.201410569>.
- (37) Wang, K.; Huang, D.; Yu, L.; Gu, H.; Ikeda, S.; Jiang, F. Environmentally Friendly $\text{Cu}_2\text{ZnSnS}_4$ -Based Photocathode Modified with a ZnS Protection Layer for Efficient Solar Water Splitting. *J. Colloid Interface Sci.* **2019**, *536*, 9–16. <https://doi.org/10.1016/j.jcis.2018.10.032>.
- (38) Senthilkumar, M.; Mathiyarasu, J.; Joseph, J.; Phani, K. L. N.; Yegnaraman, V. Electrochemical Instability of Indium Tin Oxide (ITO) Glass in Acidic pH Range during Cathodic Polarization. *Mater. Chem. Phys.* **2008**, *108* (2-3), 403–407. <https://doi.org/10.1016/j.matchemphys.2007.10.030>.
- (39) Benck, J. D.; Pinaud, B. A.; Gorlin, Y.; Jaramillo, T. F. Substrate Selection for Fundamental Studies of Electrocatalysts and Photoelectrodes: Inert Potential Windows in Acidic, Neutral, and Basic Electrolyte. *PLoS One* **2014**, *9* (10). <https://doi.org/10.1371/journal.pone.0107942>.
- (40) Geiger, S.; Kasian, O.; Mingers, A. M.; Mayrhofer, K. J. J.; Cherevko, S. Stability Limits of Tin-Based Electrocatalyst Supports. *Sci. Rep.* **2017**, *7* (1), 1–8. <https://doi.org/10.1038/s41598-017-04079-9>.



5.5 Supporting information

5.5.1 Materials and Methods

Reagents

Buffer solutions were prepared with Na_2HPO_4 , NaH_2PO_4 and Na_2SO_4 from Sigma-Aldrich. $(\text{NH}_4)_2[\text{MoS}_4]$ and Indium leads were supplied from Sigma-Aldrich.

Mo/Cu/Zn/Sn stacks were sputtered using elemental targets of Mo (99.95%), Cu (99.99%), Zn (99.99%) and Sn (99.99%) supplied by PhotonExport. Ge nanolayers were thermally evaporated from Ge chips (99.999%) supplied by Sigma-Aldrich.

The reactive annealings were performed using Se powder (99.999%, 200 mesh) and Sn powder (99.995%, 100 mesh) from Alfa Aesar.

CdS buffer layers were deposited by chemical bath deposition (CBD) using the following reagents: $\text{Cd}(\text{NO}_3)_2$ (cadmium nitrate), $\text{SC}(\text{NH}_2)_2$ (thiourea), $\text{Na}_3\text{C}_3\text{H}_5\text{O}(\text{COO})_3$ (sodium citrate), and NH_3 (ammonia) from Alfa Aesar.

The chemical etchings of the absorbers were performed using a $(\text{NH}_4)_2\text{S}$ (22% (w/w)) aqueous solution prepared from commercial $(\text{NH}_4)_2\text{S}$ (44% (w/w)) supplied by Alfa-Aesar.

i-ZnO/ITO window layers were sputtered using ZnO (99.99%) and $\text{In}_2\text{O}_3\text{-SnO}_2$ ITO (99.99%) targets from PhotonExport.



Photocathodes based on $\text{Cu}_2\text{ZnSnSe}_4$ for HER

Solar cells fabrication

The CZTSe films were prepared by a sequential process onto Mo-coated soda-lime glass substrates. For this purpose, Zn-rich and Cu-poor Cu/Zn/Sn stacks ($\text{Cu}/(\text{Zn}+\text{Sn}) = 0.75$ and $\text{Zn}/\text{Sn} = 1.10$ determined with calibrated X-ray fluorescence (Fischerscope XVD)) were deposited using DC magnetron sputtering (Alliance Ac450). Additionally, very thin Ge layers were thermally evaporated prior to the stack deposition (10 nm Ge on the Mo) and on top of the metallic stack (5 nm Ge), as reported elsewhere¹. Then, the whole precursor stack was subsequently annealed in a Se + Sn atmosphere (100 mg of Se and 5 mg of Sn), using graphite boxes (69 cm³ in volume) in a conventional tubular furnace (Hobersal). The selenization was performed in a two-step process: the first one at 400 °C (heating rate of 20 °C/min) for 30 minutes and 1.5 mbar of Ar pressure, followed by a second step at 550 °C (heating rate of 20 °C/min) for 15 minutes and 1 bar of Ar pressure, with a natural cooling down to room temperature. To complete the devices, a CdS buffer layer (50 nm) was grown by chemical bath deposition, preceded by a chemical etching in $(\text{NH}_4)_2\text{S}$ solution in order to remove possible secondary phases and to passivate the absorbers surface. Just after CdS growth, the solar cells were completed by DC-pulsed sputtering deposition of i-ZnO (50 nm) and $\text{In}_2\text{O}_3\text{-SnO}_2$ (ITO, 200 nm or 400 nm) as transparent conductive window layer (Alliance CT100).



Scanning Electron Microscopy

Scanning electron microscopy (SEM) images were obtained with a ZEISS Series Auriga micro- scope using 5 kV accelerating voltage.

UV-Vis Spectrometer

UV-Vis measurements were carried out on a Lambda 1050 PerkinElmer spectrophotometer equipped with a PMT, InGaAs and PbS detectors system, double beam optics, double monochromator and D2 and W light sources. Diffuse reflectance measurements were carried out in the same equip using 150mm Integrating Sphere with PbS and PMT detectors.

EQE measurements

External quantum efficiency (EQE) measurements were performed using a Bentham PVE300 system calibrated with Si and Ge photodiodes.

(Photo)Electrochemical equipment

Linear sweep voltammetry (LSV) and Chronopotenciometry (CP) were measured using a CHI660D potentiostat.

Platinum Disk/Mesh Electrodes and reference electrodes (SCE and AgCl/Ag) were purchased from IJ-Cambria Ltd.

All solutions used in this work were degassed for 20min with Argon before any measurement.

Photoelectrochemical experiments were ran under simulated 1 sun irradiation (100 mW/cm²), using ABET 150LS Xenon lamps as a source of light with AM1.5 filter. The irradiation was calibrated with a handmade Si diode before any experiment.

To convert the potentials versus Reversible Hydrogen Electrode the following equation was used:⁵

$$E_{RHE} = E + E_{ref} + 0.059 \cdot pH$$

Where E is the potential applied and E_{ref} is the potential of the reference electrode used during the measurements vs NHE .

Hydrogen detector

Selective hydrogen Clark electrode (model H2-NP, Unisense) was used as a detector to quantify the amount of molecular hydrogen evolved from the (photo)electrodes.

5.5.2 Optical Band gap determination

Optical band gap of CZTSe/CdS/ZnO/ITO were measured using the diffuse reflectance UV-vis spectra of the sample. Kubelka-Munk equation (eq 1) can be used to extract the absorption coefficient (α) from the diffuse reflectance spectra:²



Photocathodes based on $\text{Cu}_2\text{ZnSnSe}_4$ for HER

$$f(R) = \frac{(1-R)^2}{2R} = \frac{\alpha}{s} \quad (\text{eq. 1})$$

Where R is diffuse reflectance values at given wavelength and s is the scattering coefficient.

Assuming that s is wavelength independent, we can consider that $f(R)$ is directly proportional to α , and $f(R)$ can be used in place of α to make the Tauc plot (eq 2):

$$\alpha h\nu \propto (h\nu - E_g)^{\frac{1}{n}} \quad (\text{eq. 2})$$

Where E_g is band gap energy (in eV) and n can take value of $\frac{1}{2}$ for the direct and allowed transition.

Plotting $(\alpha h\nu)^2$ vs $h\nu$ (Tauc plot) E_g value can be calculated extrapolating the linear region to the baseline (Figure S11). The values obtained using this method gives an E_g value of 0.96-1.3 eV for CZTSe, 2.1 eV for CdS, 2.9 eV for ITO and 3.4 eV for ZnO, that is in good agreement with the reported values in the literature.^{3,4}



The band gap was also estimated from EQE measurements by derivative way. Since most of the photons with energy higher than band gap will be absorbed by the absorber, EQE should show an abrupt change at the position of the band gap, so at that position the change rate of EQE should be the largest. Thus, differentiate the EQE curve and then fit the corresponding valley with Gauss mode in ORIGIN software to get the center position X_c , known as the inflection point. Finally use the following equation to calculate the E_g :

$$E_g(\text{eV}) = \frac{1239.84}{X_c} \quad (\text{eq. 3})$$

With a $X_c=1172.81$, the estimated value for E_g is 1.05 eV (see Figure S11 C).

5.5.3 MoS_2 (photo)electrodeposition

Clean glass coated with ITO were cutted in approximated 1,25cmx1,25cm pieces. The electrical connection between copper wire and the electrode were made with solder (USS-9210 MBR electronics) using cerasolzer (Alloy #CS186 MBR electronics). The electrical connection as well as the edges of the electrode were covered with non transparent epoxy resin in order to isolate it

from the solution. The electrode's area were calculated using J-Image (free software).

The electrochemical bath were prepared with a composition of 30mM of $(\text{NH}_4)_2[\text{MoS}_4]$ and 0.1M Na_2SO_4 as supporting electrolyte with MilliQ water. The solution was kept under Argon bubbling to prevent the formation of Molybdenum oxides and used as prepared.

Galvanostatic mode were chose to electroplate cathodically the amorphous MoS_2 , selecting $j = -7.5 \cdot 10^{-5} \text{ A/cm}^2$. By controlling the time of the electrodeposition different thickness of the catalyst layer can be obtained. In this work, the charge passed through the electrodes was 0.05 C/cm^2 corresponding to 200 nm of thickness approximately (confirmed by SEM, Figure 7). After the electrodeposition, the electrodes were cleaned with MilliQ water and dried under air flow.

For the photocathodes, the same methodology were used with some modifications. Before making the electrical contact, the four edges of photoelectrode were scratched, removing the material to expose Molybdenum back contact (approximately 0.5-1mm of wideness). As a soldering material, Indium leads were used. The photoelectrochemical deposition conditions of the catalyst were exactly the same than ITO electrodes, but lighting the electrochemical cell with 2 sun irradiation (the high concentration of $(\text{NH}_4)_2[\text{MoS}_4]$ gives a strong dark red color to the solution, and higher intensity of light is required to allow the photoelectrodeposition).

In the Figure S6 the E-t deposition curve is shown for some of the electrodes/photoelectrodes used in this work. It's important to notice that the potential required to reach the selected j for the photocathodes were shifted anodicly around 550mV compared with ITO electrodes due the photovoltage generated by the semiconductor.

5.5.4 Calculation of Faradaic Efficiency (FE)

The FE of the CP is calculated using the following formula:⁵

$$FE (\%) = \frac{n_{\text{H}_2 \text{ detected}}}{n_{\text{H}_2 \text{ theoretical}}} \cdot 100 \quad (\text{eq. 1})$$



Photocathodes based on $\text{Cu}_2\text{ZnSnSe}_4$ for HER

Where $n_{\text{H}_2 \text{ detected}}$ is the number of mols of molecular hydrogen that Clark Electrode have detected and $n_{\text{H}_2 \text{ theoretical}}$ is the number of theoretical mols of H_2 calculated from the charge that pass through the electrode.

Clark electrode measures partial pressure of H_2 in the headspace of the electrochemical cell. Calibration slope is required to correlate the signal of the Clark Electrode and the amount of H_2 contained in the headspace.

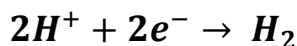
After the CP, the cell is degased with N_2 for 30 min, and different known amounts of H_2 gas were injected in the head space using a Hamilton syringe. Ploting the reponse of the Clark sensor versus the hydrogen volume added is it possible to obatin a calibration line (Figure S9). With the slope of the calibration, we can convert the Clark's values (mV) in volume of H_2 . Using the perfect gases equation, we can obtain the number of moles of hydrogen gas produced by the electrode and measured in the headspace:

$$P \cdot V = n \cdot R \cdot T$$


$$n = \frac{P \cdot V}{R \cdot T} \quad (\text{eq. 2})$$

Where P is the pressure of the headspace (1atm), R is the gas constant ($0.082 \frac{\text{atm} \cdot \text{L}}{\text{K} \cdot \text{mol}}$) and T the temperature (298.15K).

To calculate the theoretical number of moles from the electrical charge transferred to the electrode:



$$n_{\text{H}_2 \text{ theoretical}} = \frac{C}{F \cdot n} \quad (\text{eq. 3})$$

Where C is the charge (in C) passed through the electrode, F is the faraday constant (96485C) and n the number of electrons involved to form one molecule of hydrogen (2).

5.5.4 Figures

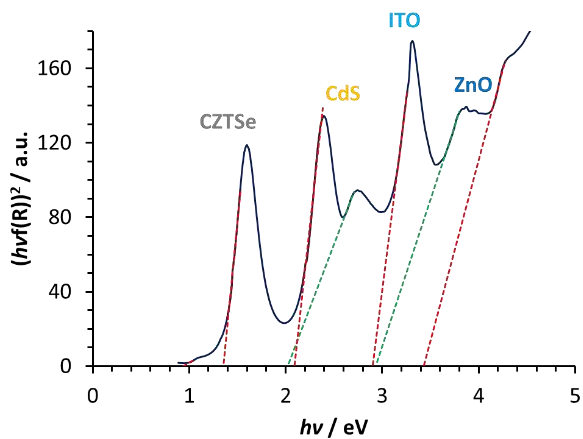


Figure S1. Tauc plot of Mo/CZTSe/CdS/ZnO/ITO for direct and allowed transitions.

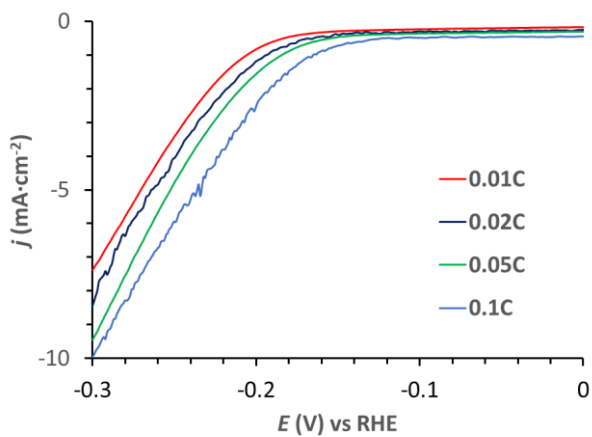


Figure S2. LSV of ITO covered with different amounts of MoS₂ in pH 2. Counter electrode: Pt mesh. Reference electrode: SCE. Scan rate: 5mV/s. iR drop corrected at 85%.



Photocathodes based on $\text{Cu}_2\text{ZnSnSe}_4$ for HER

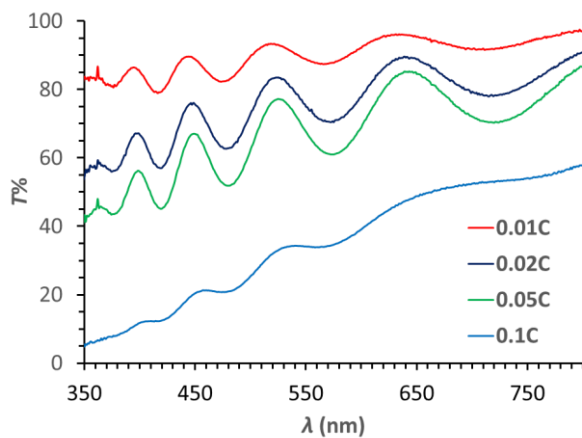


Figure S3. Transmittance spectra of ITO coated with different amounts of amorphous MoS_2 .

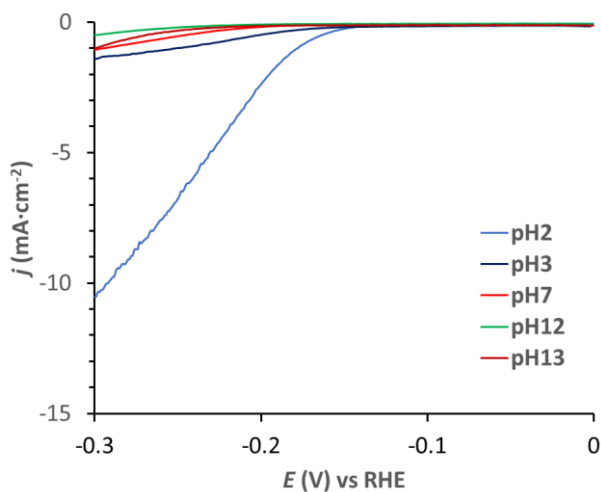


Figure S4. LSV of ITO- MoS_2 in different pHs. Scan rate 5mV/s.



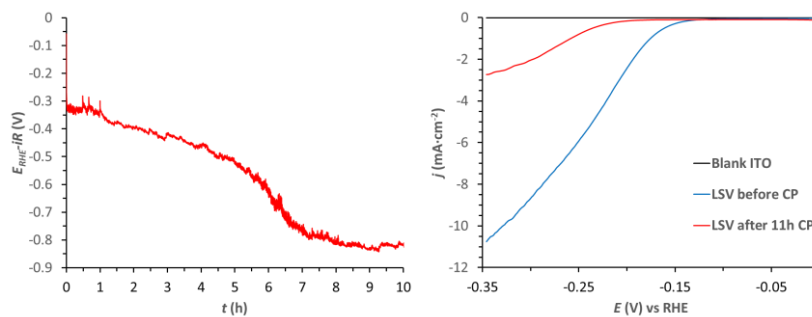


Figure S5. Left) CP of ITO-MoS₂ in pH 2 under stirring conditions. Right) LSV before and after 11h of CP in pH 2. iR drop corrected at 85%.

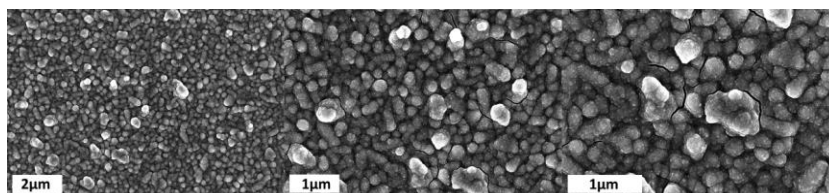


Figure S6. SEM images of ITO-MoS₂ (Top view) with different magnification.

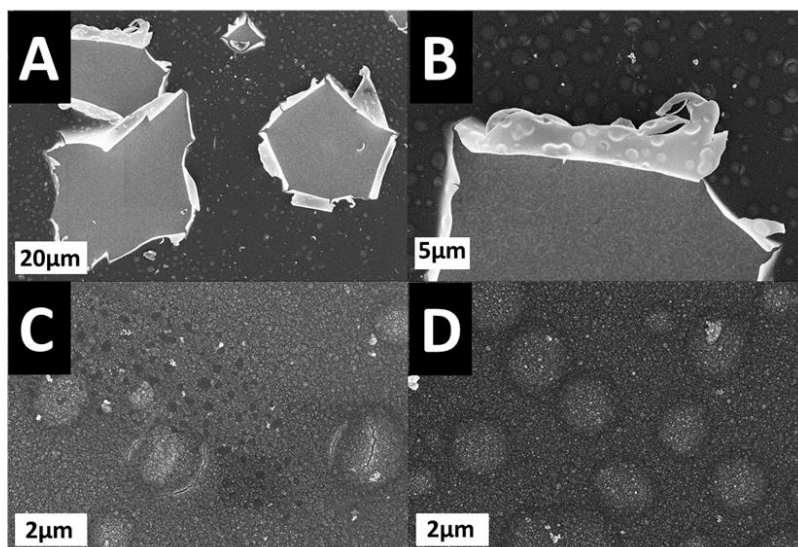


Figure S7. SEM images of the most damaged areas of ITO-MoS₂ after 5h of CP, suggesting hydrogen bubbles as responsible for the peeling of the MoS₂ layers.



Photocathodes based on $\text{Cu}_2\text{ZnSnSe}_4$ for HER

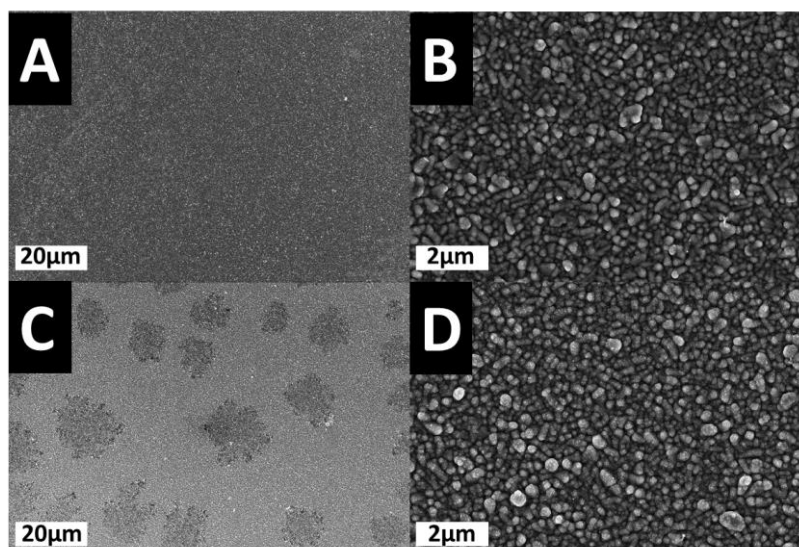


Figure 58. SEM images of non-damaged areas of ITO- MoS_2 after 1h of CP (A and B) and after 10h (C and D).

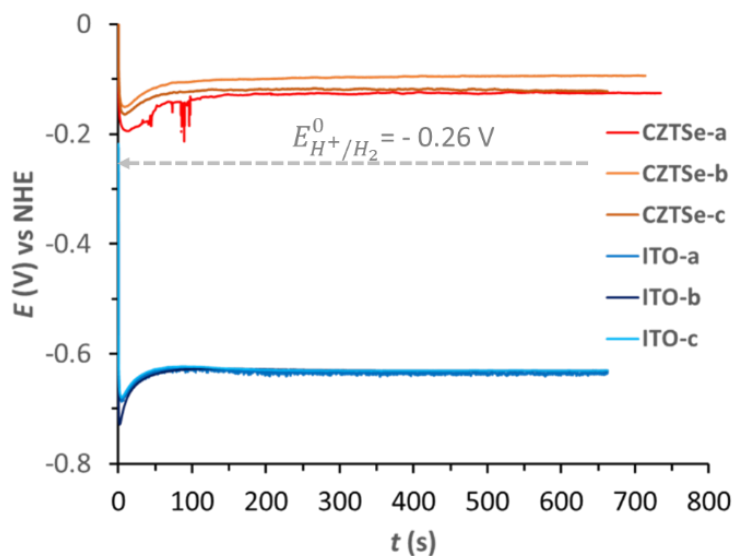


Figure 59. E - t curve (photo)electrodeposition of MoS_2 on ITO and Mo/CZTSe/CdS/ZnO/ITO (photo)cathodes. Dashed gray line indicates redox potential for HER at pH 4.5 (electrodeposition conditions).

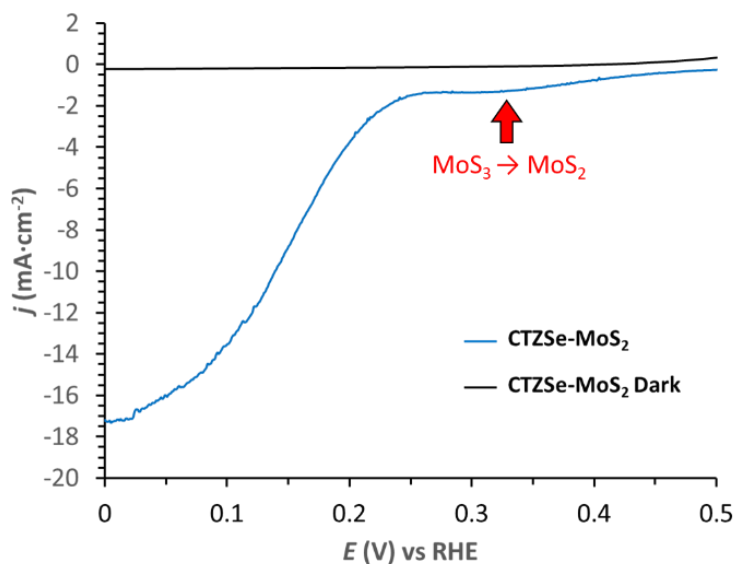


Figure S10. 1st LSV of CZTSe-MoS₂ in pH 2. Counter electrode: Pt mesh. Reference electrode: SCE. Scan Rate: 5mV/s. Stirring Conditions. iR drop corrected at 85%.

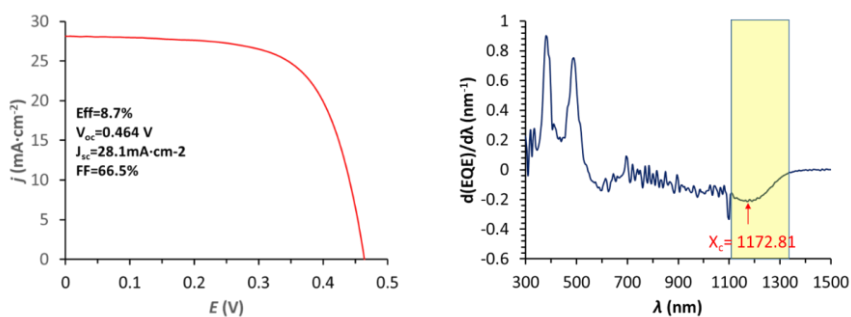


Figure S11. Left) Photovoltaic J-V curve of Mo/CZTSe/CdS/ZnO/ITO device used in this work. Right) First derivative of EQE of Mo/CZTSe/CdS/ZnO/ITO used to estimate E_g .



Photocathodes based on $\text{Cu}_2\text{ZnSnSe}_4$ for HER

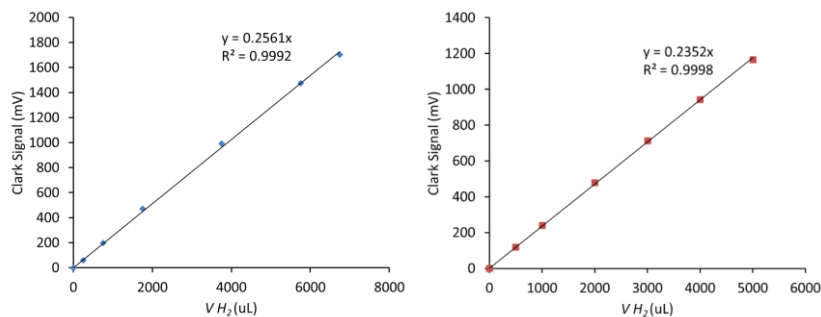


Figure S12. Calibration slope for calculating the FE of the CP experiments in a two-compartment (photo)electrochemical cell for the ITO- MoS_2 electrodes related to CP in Figure 3 of the main manuscript (Left) and CZTSe- MoS_2 photoelectrodes related to CP in Figure 7 of the main manuscript (Right).

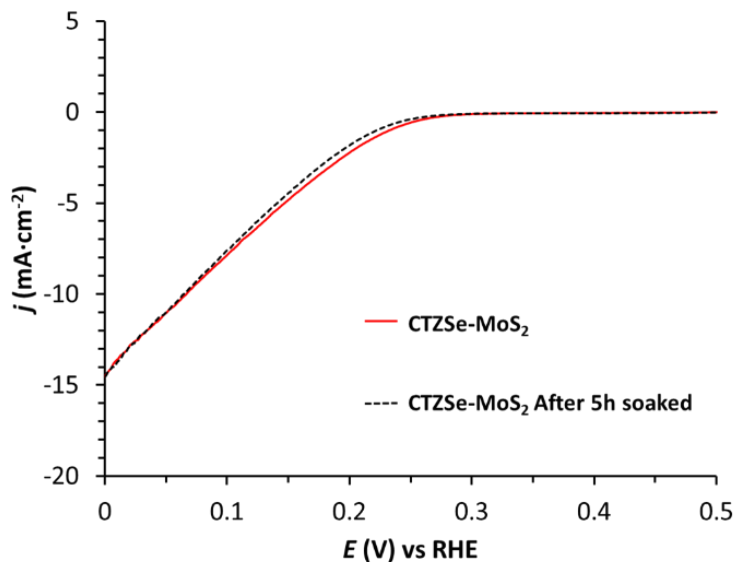


Figure S13. Polarization curve of CZTSe- MoS_2 (red line) and the same photocathode after 5h soaked in pH 2 (dashed black line).

Material	Catalyst	pH	j_{0V} (mA·cm ⁻²)	$j_{@10mA/cm^2}$ (V)	E_{onset} (V)	Stability	Year	Ref
Mo/CZTS/CdS/TiO ₂	Pt	9.5	-9.0	--	+0.60	--	2010	6
Mo/CZTS/CdS/In ₂ S ₃	Pt	6.5	-9.3	--	+0.64	2h	2015	7
Mo/Ge-CZTS/CdS/In ₂ S ₃	Pt	6.5	-11.1	+0.10	+0.60	2h	2017	8
Mo/CZTSe/CdS/ZnO/ITO/TiO ₂	Pt	0	-37.0	+0.27	+0.45	1h	2018	9
Mo/CZTS/CdS/ZnS	Pt	6.5	-8.0	--	+0.65	2h	2019	10
Mo/CuInS ₂ /In ₂ S ₃	Pt	6.5	-15.0	+0.26	+0.72	3h	2014	11
Mo/CuInS ₂ /TiO ₂	Pt	10	-13.0	+0.15	+0.60	1h	2014	12
Mo/(Ag,Cu)GaSe ₂ /CuGa ₃ Se ₅ /CdS	Pt	10	-8.8	--	+1.0	20 days	2015	13
Mo/Cu(In,Ga)Se ₂ /Ti/Mo	Pt	6.8	-30.0	+0.42	+0.63	10 days	2015	14
Ti/p-Si	1T-MoS ₂	0	-17.6	--	+0.25	3h	2014	15
Cu ₂ O/AZO/TiO ₂	MoS ₂	14	-6.3	--	+0.48	10h	2015	16
Si/SiO ₂ /Mo ₂ Si/Mo ₂ O	MoS ₂	0	-15.7	+0.09V	+0.31	64d	2017	17
Mo/CZTSe/CdS/ZnO/ITO	MoS ₂	2	-18.1	+0.100	+0.30	3.5h	2019	This work

Table S 1. Relevant work on photocathodes using CZTS/Se as absorber, CIS/CIGS and photocathodes with MoS₂ as HER electrocatalyst.



Photocathodes based on $\text{Cu}_2\text{ZnSnSe}_4$ for HER

5.5.5 References

- (1) Giraldo, S.; Saucedo, E.; Neuschitzer, M.; Oliva, F.; Placidi, M.; Alcobé, X.; Izquierdo-Roca, V.; Kim, S.; Tampo, H.; Shibata, H.; et al. How Small Amounts of Ge Modify the Formation Pathways and Crystallization of Kesterites. *Energy Environ. Sci.* **2018**, *11* (3), 582–593. <https://doi.org/10.1039/c7ee02318a>.
- (2) Wood, D. L.; Tauc, J. Weak Absorption Tails in Amorphous Semiconductors. *Phys. Rev. B* **1972**, *5* (8), 3144–3151. <https://doi.org/10.1103/PhysRevB.5.3144>.
- (3) Kaur, K.; Kumar, N.; Kumar, M. Strategic Review of Interface Carrier Recombination in Earth Abundant Cu-Zn-Sn-S-Se Solar Cells: Current Challenges and Future Prospects. *J. Mater. Chem. A* **2017**, *5* (7), 3069–3090. <https://doi.org/10.1039/C6TA10543B>.
- (4) Li, S.; Ghinea, C.; Bayer, T. J. M.; Motzko, M.; Schafrank, R.; Klein, A. Electrical Properties of (Ba, Sr)TiO₃ Thin Films with Pt and ITO Electrodes: Dielectric and Rectifying Behaviour. *J. Phys. Condens. Matter* **2011**, *23* (33). <https://doi.org/10.1088/0953-8984/23/33/334202>.
- (5) Bard, A. J.; Faulkner, L. R. *Electrochemical Methods, Fundamentals and Applications*, 2nd ed.; Wiley, 2001; Vol. 60. <https://doi.org/10.1021/ed060pa25.1>.
- (6) Yokoyama, D.; Minegishi, T.; Jimbo, K.; Hisatomi, T.; Ma, G.; Katayama, M.; Kubota, J.; Katagiri, H.; Domen, K. H₂ Evolution from Water on Modified $\text{Cu}_2\text{ZnSnS}_4$ Photoelectrode under Solar Light. *Appl. Phys. Express* **2010**, *3* (10), 2–4. <https://doi.org/10.1143/APEX.3.101202>.
- (7) Minegishi, T.; Harada, T.; Kuang, Y.; Jiang, F.; Ikeda, S.; Gunawan; Domen, K. Pt/In₂S₃/CdS/ $\text{Cu}_2\text{ZnSnS}_4$ Thin Film as an Efficient and Stable Photocathode for Water Reduction under Sunlight Radiation. *J. Am. Chem. Soc.* **2015**, *137* (42), 13691–13697. <https://doi.org/10.1021/jacs.5b09015>.
- (8) Wen, X.; Luo, W.; Guan, Z.; Huang, W.; Zou, Z. Boosting Efficiency and Stability of a $\text{Cu}_2\text{ZnSnS}_4$ Photocathode by Alloying Ge and Increasing Sulfur Pressure Simultaneously. *Nano Energy* **2017**, *41* (May), 18–26. <https://doi.org/10.1016/j.nanoen.2017.09.006>.
- (9) Ros, C.; Andreu, T.; Giraldo, S.; Izquierdo-Roca, V.; Saucedo, E.; Morante, J. R. Turning Earth Abundant Kesterite-Based Solar Cells into Efficient Protected Water-Splitting Photocathodes. *ACS Appl. Mater. Interfaces* **2018**, *10* (16), 13425–13433. <https://doi.org/10.1021/acsami.8b00062>.
- (10) Wang, K.; Huang, D.; Yu, L.; Gu, H.; Ikeda, S.; Jiang, F. Environmentally Friendly $\text{Cu}_2\text{ZnSnS}_4$ -Based Photocathode Modified with a ZnS Protection Layer for Efficient Solar Water Splitting. *J. Colloid Interface Sci.* **2019**, *536*, 9–16. <https://doi.org/10.1016/j.jcis.2018.10.032>.



- (11) Gunawan; Septina, W.; Harada, T.; Nose, Y.; Ikeda, S. Investigation of the Electric Structures of Heterointerfaces in Pt- and In₂S₃-Modified CuInS₂ Photocathodes Used for Sunlight-Induced Hydrogen Evolution. *ACS Appl. Mater. Interfaces* **2015**, *7* (29), 16086–16092. <https://doi.org/10.1021/acsami.5b04634>.
- (12) Yamada, T.; Hisatomi, T.; Nakabayashi, M.; Minegishi, T.; Ma, G.; Zhao, J.; Gunawan; Shibata, N.; Katayama, M.; Zhong, M.; et al. Enhancement of Solar Hydrogen Evolution from Water by Surface Modification with CdS and TiO₂ on Porous CuInS₂ Photocathodes Prepared by an Electrodeposition-Sulfurization Method. *Angew. Chemie Int. Ed.* **2014**, *53* (44), 11808–11812. <https://doi.org/10.1002/anie.201406483>.
- (13) Zhang, L.; Minegishi, T.; Nakabayashi, M.; Suzuki, Y.; Seki, K.; Shibata, N.; Kubota, J.; Domen, K. Durable Hydrogen Evolution from Water Driven by Sunlight Using (Ag,Cu)GaSe₂ Photocathodes Modified with CdS and CuGa₃Se₅. *Chem. Sci.* **2015**, *6* (2), 894–901. <https://doi.org/10.1039/c4sc02346c>.
- (14) Kumagai, H.; Minegishi, T.; Sato, N.; Yamada, T.; Kubota, J.; Domen, K. Efficient Solar Hydrogen Production from Neutral Electrolytes Using Surface-Modified Cu(In,Ga)Se₂ Photocathodes. *J. Mater. Chem. A* **2015**, *3* (16), 8300–8307. <https://doi.org/10.1039/c5ta01058f>.
- (15) Shearer, M. J.; Jin, S.; Ding, Q.; Liang, D.; Cabán-Acevedo, M.; Daniel, A. S.; English, C. R.; Meng, F.; Hamers, R. J. Efficient Photoelectrochemical Hydrogen Generation Using Heterostructures of Si and Chemically Exfoliated Metallic MoS₂. *J. Am. Chem. Soc.* **2014**, *136* (24), 8504–8507. <https://doi.org/10.1021/ja5025673>.
- (16) Morales-Guio, C. G.; Liardet, L.; Mayer, M. T.; Tilley, S. D.; Grätzel, M.; Hu, X. Photoelectrochemical Hydrogen Production in Alkaline Solutions Using Cu₂O Coated with Earth-Abundant Hydrogen Evolution Catalysts. *Angew. Chemie - Int. Ed.* **2015**, *54* (2), 664–667. <https://doi.org/10.1002/anie.201410569>.
- (17) King, L. A.; Hellstern, T. R.; Park, J.; Sinclair, R.; Jaramillo, T. F. Highly Stable Molybdenum Disulfide Protected Silicon Photocathodes for Photoelectrochemical Water Splitting. *ACS Appl. Mater. Interfaces* **2017**, *9* (42), 36792–36798. <https://doi.org/10.1021/acsami.7b10749>.





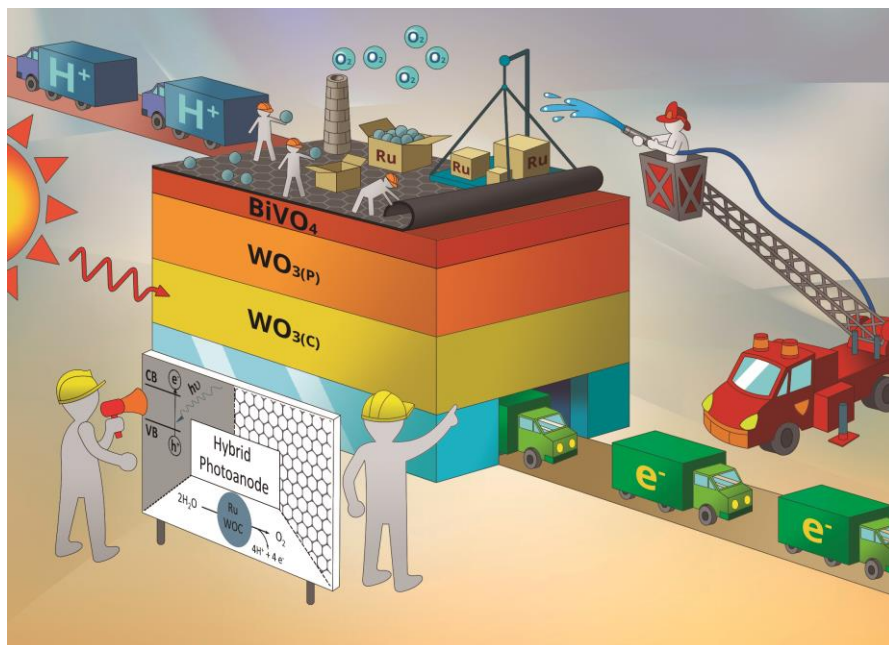
Chapter

6

A hybrid molecular photoanode for efficient light-induced water oxidation

The catalytic activity towards water oxidation of a heterostructured $\text{WO}_3/\text{BiVO}_4$ based photoanode has been carried out by the addition of a carbon nanotube fiber decorated with the state-of-the-art molecular catalysts for water oxidation, increasing the photocurrent at low potentials where the bare material can not oxidize water at all. The photoelectrochemical experiment probed that the molecular catalyst is producing oxygen from water. A detailed EIS study of the photoanode has been done, providing a valuable information to rationalize the electrical properties that affect the photoelectrochemical performance.

A hybrid molecular photoanode for efficient light-induced WO



Abstract

A hybrid photoanode, made of a multilayered heterostructured $\text{WO}_3/\text{BiVO}_4$ semiconductor and a molecular water oxidation catalyst $\text{Ru}(\text{tda})(\text{py-pyr})_2$ (Ru-WOC, where tda is [2,2':6',2''-terpyridine]-6,6''-dicarboxylato and py-pyr is 4-(pyren-1-yl)-N-(pyridin-4-ylmethyl)butanamide), is described. Both elements are linked by a highly conductive carbon nanotubes fibre film (CNT_f), which acts as charge transfer and anchoring platform, where the catalyst is attached through π - π stacking interactions. Photoelectrochemical characterization of the resulting electrodes shows that the full photoanode $\text{WO}_3/\text{BiVO}_4/\text{CNT}_f/\text{Ru-WOC}$ outperforms the bare $\text{WO}_3/\text{BiVO}_4$ electrode at a potential range of 0.3 V to 0.8 V vs NHE at pH 7, with current densities enhanced by 0.05 to 0.29 mA/cm^2 . Bulk electrolysis experiments and oxygen gas measurements prove that the enhanced photocurrent is due to the catalytic water oxidation reaction. Detailed electrochemical impedance spectroscopy (EIS) analysis is used to investigate the role of the multiple layers involved in the process. The $\text{CNT}_f/\text{Ru-WOC}$ interface is responsible of increasing charge accumulation and also reducing recombination phenomena. On one hand, the CNT_f is able to hold the charge coming from the light absorbed by the $\text{WO}_3/\text{BiVO}_4$ semiconductor, as shown by the high capacitive



values observed for a $\text{WO}_3/\text{BiVO}_4/\text{CNT}_f$ electrode in the whole range of studied potentials (0.15-0.85 V vs NHE). On the other hand, the Ru-WOC transfers the charge to the solution by performing fast water oxidation catalysis. This is supported by the low resistivity shown by the full $\text{WO}_3/\text{BiVO}_4/\text{CNT}_f/\text{Ru-WOC}$ electrode at low potentials ($E < 0.5$ V vs NHE). The robustness and high catalytic rate of the Ru-WOC ensures the proper performance of the hybrid photoelectrode device. The latter is particularly important as it opens an avenue of opportunities to improve the performance of photoanodes for the water oxidation reaction based on the easy modification of ligands of the molecular catalyst to tune its structural, electronic and catalytic properties. This is a unique advantage with regard to the commonly used catalysts based on metal oxide or oxy(hydroxides), with limited tunability.

Contributions:

Sergi Grau Abarca carried out the electrochemical, photoelectrochemical and UV-vis spectroscopic experiments, as well as the preparation of the molecular photoanode with the fuctionalized CNT_f with Ru-WOC.

6.1 Introduction

The conversion of solar energy is on the focus of worldwide scientific research with the aim to turn into a more sustainable energy management of our society. While photovoltaic (PV) and solar thermal technologies are a reality with solar panels generating part of global energy production, the conversion of solar energy into clean fuels is still in a laboratory-scale stage.¹ The latter strategy offers a solution to the mismatch between sunlight intermittence and energy needs by converting the sunlight energy into storable chemical bonds. One of the reasons that hinders the implementation of such technology is the difficulty to find an efficient light absorbing material coupled to active electrocatalysts, either connected through wires in a typical PV-electrochemical (PV-EC) configuration or via semiconductor-electrolyte interfaces.¹⁻³ The system needs to effectively absorb light and produce long lived separated charges to facilitate fast electron and hole transfer to catalysts



A hybrid molecular photoanode for efficient light-induced WO

in order to drive the desired chemical reactions. In this regard, the water oxidation reaction is one of the limiting process within such a complex system due to high demands needed for efficient catalysts, namely, a high thermodynamic potential and large kinetic complexity. Indeed the latter complexity is a consequence of the need to transfer four electrons and four protons from two water molecules together with the generation of an O-O bond (Figure 1).⁴⁻⁶ For this reason, great efforts are devoted nowadays to the field of solar-to-fuel conversion, specifically to find highly performant electroanodes and photoanodes for the water oxidation reaction.^{2,7-9}

Tungsten oxide (WO_3) and bismuth vanadate (BiVO_4) are two promising semiconductor materials with suitable band gap and valence band position to carry out photoinduced water oxidation.^{7,8} In particular, BiVO_4 has shown excellent photocurrent densities at potentials close to and even lower than the thermodynamic value. However, the performances of BiVO_4 photoanodes are still far from its theoretical maximum capacities.^{7,8} This problem is associated with the slow charge carrier mobility as well as slow kinetics of the water oxidation reaction at the surface of the electrode. Four main strategies have been used to overcome these unfavorable phenomena: i) doping with metallic elements (particularly good results obtained with W and Mo),¹⁰ ii) tuning morphology and nanostructure of the material,¹⁰⁻¹² iii) formation of heterojunctions with other semiconductors (e.g. WO_3)^{13,14} or conductive materials (e.g. graphene)^{7,15} and iv) modifying the surface of the photoelectrode with suitable water oxidation catalysts (metal oxides or oxy(hydroxides)).^{16,17} While the first three strategies (i-iii) are designed to enhance charge carrier mobility, charge separation and/or avoid recombination, the latter strategy (iv) is mainly addressed to reduce the high kinetic barrier associated with the water oxidation reaction. Interestingly, recent works point to the poor effect of metal oxide derivatives as water oxidation catalysts.^{17,18} Instead, they attribute the enhancement of the photocurrent densities to higher charge separation efficiency obtained with the presence of the metallic oxide deposited on the surface of the photoanode.^{17,18} These observations are in agreement with the intrinsic limited catalytic activity of metal oxides such as cobalt oxide that competes with the catalysis by the BiVO_4 itself. In contrast to metal oxide catalysts, molecular water oxidation catalysts (WOC) have experienced a tremendous



improvement in catalytic rates, achieving maximum turnover frequencies that are three to four orders of magnitude higher than the best water oxidation catalysts based on oxides. Indeed, molecular water oxidation catalysts outperform the naturally occurring Oxygen Evolving Complex in Photosystem II, responsible for oxygen release in the natural photosynthetic process in plants, by two orders of magnitude.^{5,6,19} More recently, strategies to anchor these molecular catalysts on electrode surfaces have been developed, maintaining the high catalytic activity observed in homogeneous conditions and in some cases even increasing their performance.²⁰⁻²²

In this work, we couple a $\text{WO}_3/\text{BiVO}_4$ photoanode with a highly active molecular WOC with the aim of enhancing the kinetics of the chemical reaction, minimizing recombination and oxide degradation, and thus improving the overall performance of the photoelectrode. A carbon nanotube fibre interlayer film between the photoactive material and the catalyst is used as highly conductive platform that facilitates the anchoring of the functionalized molecular WOC and allows fast charge transfer between the two key components (semiconductor and catalyst) of the photoelectrode (Figure 1).

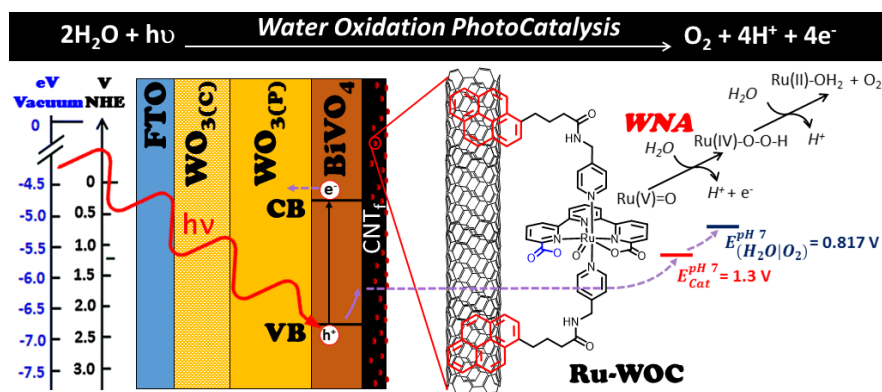


Figure 1. Hybrid photoanode design studied in this work. $\text{WO}_3(\text{c})$ = compact tungsten oxide film, WO_3 = mesoporous tungsten oxide layer, Ru-WOC = molecular ruthenium water oxidation catalyst with pyrene groups in red and dangling carboxylate group in blue, WNA = water nucleophilic attack, $E(\text{cat})$ = oxidation potential of catalyst to give the Ru(V)-oxo active species, $E(\text{H}_2\text{O}/\text{O}_2)$ = thermodynamic potential of water oxidation at pH 7.



A hybrid molecular photoanode for efficient light-induced WO

6.2 Results

6.2.1 Fabrication of the hybrid photoanode

The multilayer architecture of the $\text{WO}_3/\text{BiVO}_4$ photoactive material used in this study is shown in Figure 1. It is made of three well defined layers, namely, a compact thin film of tungsten oxide ($\text{WO}_{3(\text{C})}$), a mesoporous layer of the same material ($\text{WO}_{3(\text{P})}$)²³ and a top layer of porous BiVO_4 .¹⁶ The inner compact layer of $\text{WO}_{3(\text{C})}$ is essential for isolating the back FTO contact from the electrolyte solution, avoiding dark currents associated with shunt phenomena. This effect is clearly seen in Figure S5, which shows that in the absence of light the electrode $\text{WO}_{3(\text{C})}/\text{WO}_{3(\text{P})}/\text{BiVO}_4$ does not show any current in the whole potential range while the electrode that lacks the WO_3 compact underlayer ($\text{WO}_{3(\text{P})}/\text{BiVO}_4$) shows significant dark currents from 0.75 V vs NHE. On the other hand, the heterostructured $\text{WO}_3/\text{BiVO}_4$ porous material has shown improved performance as compared to bare BiVO_4 photoanodes.^{13,14} This improvement is attributed to the good band alignment and synergistic effects between the two semiconductors, leading to higher charge separation efficiencies.¹⁴ Detailed structural, electrochemical and optical characterization of the photoanodes used in this work is given in Figures S1-S5 in the supporting information.



The water oxidation catalyst, Ru-WOC in Figure 1, was selected for its high activity both in homogeneous and in heterogeneous conditions.^{19,20,22} This catalyst is known to operate via an electrophilic Ru(V)-oxo species that suffers a water nucleophilic attack (WNA) by a water molecule forming an hydroperoxo key derivative with a newly formed O-O bond. The high catalytic rate that characterizes this catalyst is attributed to the role of the dangling carboxylate group assisting the O-O bond formation step (Figure 1, blue moiety of the Ru-WOC complex).²⁴ Several reports describe the direct attachment of molecular catalysts on semiconducting materials, usually by using phosphonates or carboxylate groups.^{25,26,27} In the present case, when the Ru-WOC is attached to the $\text{WO}_3/\text{BiVO}_4$ photoanode, no improvement of the performance of the electrode is observed. This result is due to deactivation of the dangling carboxylate group, which interacts directly with the metal oxide hindering its proper activation.²⁷ This can be avoided by using a conductive

support that isolates the catalyst from the photoelectrode surface. The support should guarantee fast charge transfer from the semiconductor to the catalyst, while maintaining the ruthenium catalytic centre unaltered. In this regard, carbon nanostructures such as graphene, single or multiwalled carbon nanotubes are good candidates for their unique properties including high surface area, high thermal and electrical conductivity as well as chemical inertness. In particular, carbon nanotube fibres (CNT_f) are excellent conductive platforms. They are macroscopic arrays of CNTs combining surface area around 250 m²/g, electrical conductivity of 3.5 × 10⁵ S/m, high electrochemical stability²⁸ and the possibility to produce them in a kilometer/day scale,²⁹ for example as free-form electrodes. In this direction, the hybrid molecular photoanode device is prepared following a new strategy; an approximately 1 × 1 cm² of WO₃/BiVO₄ photoanode is covered with an approximately 0.9 × 0.9 cm² of a CNT_f film with a thickness of around 5 μm, estimated based on fibre linear density, winding rate and spinning time.²⁹ Next, the resulting WO₃/BiVO₄/CNT_f is soaked in a 1mM methanolic solution of the Ru-WOC precursor overnight to allow for the chemical attachment of the ruthenium complex on the surface of the electrode via π-π interactions of the pyrene groups of the complex and the graphitic structure of the CNT_f (Figure 1). After this treatment, the electrodes are rinsed with clean methanol to make sure that excess of the homogeneous catalyst is removed and carefully dried with an air flow. In order to estimate the loading of the catalyst on the surface of the electrode, analogous experiments with non-photoactive ITO/CNT_f electrodes were done. Analysis of the current underneath the Ru(III/II) wave in the cyclic voltammetry (CV) of the resulting ITO/CNT_f/Ru-WOC electrodes allow us to calculate the amount of catalyst precursor on the CNT_f film, giving values up to $\Gamma = 15$ nmol/cm², comparable to those observed in previous studies that used multiwalled carbon nanotubes (Figure S9).^{20,22} This confirms that the free-standing format and high surface area of CNT_f makes them an attractive conducting support in heterogeneous catalysis.



A hybrid molecular photoanode for efficient light-induced WO

6.2.3 Photoelectrochemical performance

The photoelectrochemical performance of the photoanodes was tested in a typical one-compartment three-electrodes photoelectrochemical cell, as described in detail in the supporting information. The CNT_f are extremely black layers that completely block incoming light, therefore all the photoelectrochemical results presented in this study are based on back illumination of the photoelectrodes. The photoelectrochemical behaviour of the bare WO₃/BiVO₄ photoanodes improves over consecutive linear sweep voltammetry (LSV) experiments as shown in Figure S8. Thus, all electrodes were exposed to an electrochemical pre-treatment until a constant photocurrent response was achieved previous to any modification (usually 3-5 LSV cycles).

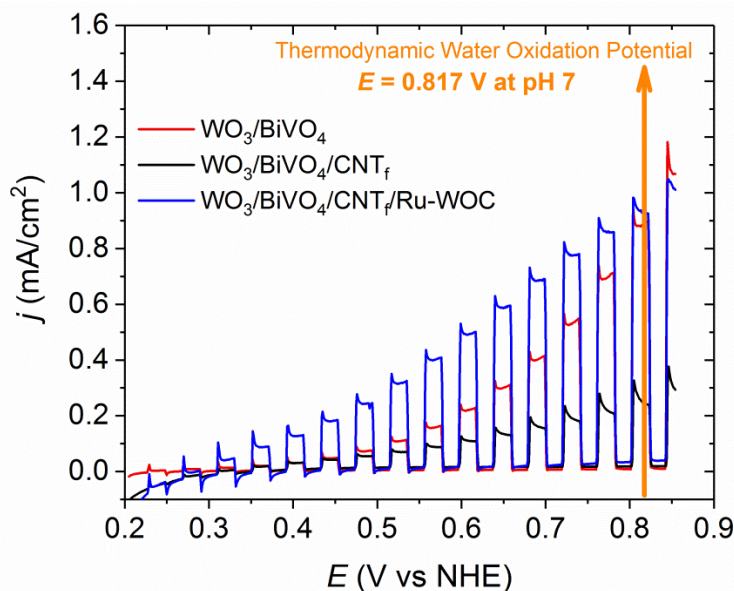


Figure 2. IR drop compensated chopped light LSV (5 mV/s) of different photoanodes in pH 7 phosphate buffer. WO₃/BiVO₄ (red), WO₃/BiVO₄/CNT_f (black) and WO₃/BiVO₄/CNT_f/Ru-WOC (blue).

Figure 2 shows the chopped light LSV performance of a WO₃/BiVO₄ photoanode and that of a WO₃/BiVO₄/CNT_f analogue in pH 7 buffered solution, showing a significant decrease of the photocurrent when the CNT_f is

present (compare red and black traces). This result is in agreement with the CNT_f film blocking the BiVO_4 active centres responsible for the water oxidation catalysis. Thus, while the CNT_f film is highly conductive, it is unable to perform the chemical reaction, in other words it does not act as water oxidation catalysts under these conditions. On the other hand, the presence of the Ru-WOC on the surface of the electrode significantly improves the performance of the photocurrent, particularly in the range of 0.3 V to 0.8 V vs NHE (compare blue trace with black and red traces in Figure 2). The improvement goes from 0.05 mA/cm^2 at 0.3 V up to 0.29 mA/cm^2 at 0.7 V vs NHE. In order to make sure that this enhancement is due to the catalyst and not to the methanolic solution treatment during catalyst deposition, we did analogous blank tests. Specifically, $\text{WO}_3/\text{BiVO}_4/\text{CNT}_f$ electrodes were soaked in clean methanol overnight and subsequently dried. The resulting treated electrodes did not show a significant improvement of the performance, confirming that the increased photocurrent observed in Figure 2 is due to the presence of the catalyst (Figure S10).

Bulk electrolysis experiments show that the full electrode $\text{WO}_3/\text{BiVO}_4/\text{CNT}_f/\text{Ru-WOC}$ outperforms the bare $\text{WO}_3/\text{BiVO}_4$ electrode (Figure 3, blue and red traces, respectively). We attribute this photocurrent enhancement to the higher catalytic activity of Ru-WOC compared to BiVO_4 . The integrity of the molecular water oxidation catalyst after bulk electrolysis experiments was tested by carefully removing the $\text{CNT}_f/\text{Ru-WOC}$ film from the surface of the $\text{WO}_3/\text{BiVO}_4$ electrode and placing it on a clean ITO electrode. As depicted in Figure S9, the fingerprint of the ruthenium complex is still intact on the film.



A hybrid molecular photoanode for efficient light-induced WO

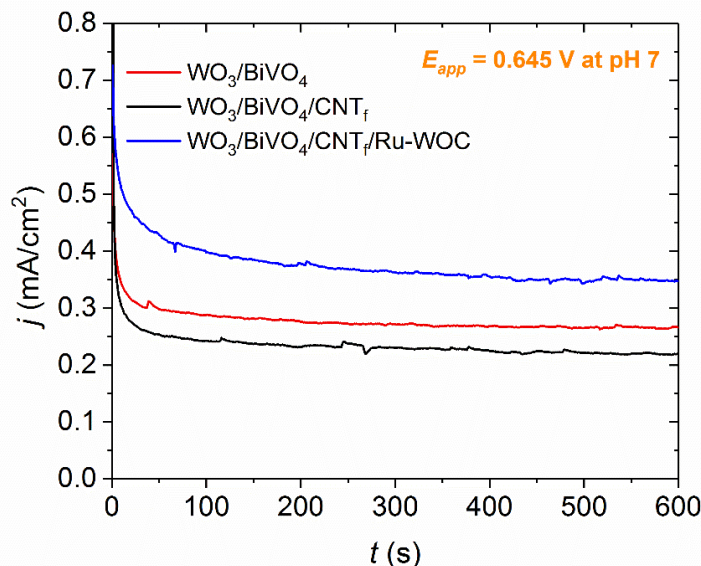


Figure 3. Bulk electrolysis experiment at applied potential $E_{app} = 0.645$ vs NHE in pH 7 phosphate buffer, IR drop was not compensated. $\text{WO}_3/\text{BiVO}_4$ (red), $\text{WO}_3/\text{BiVO}_4/\text{CNT}_f$ (black) and $\text{WO}_3/\text{BiVO}_4/\text{CNT}_f/\text{Ru-WOC}$ (blue).

Oxygen detection experiments were done to prove that the enhanced photocurrent obtained with the $\text{WO}_3/\text{BiVO}_4/\text{CNT}_f/\text{Ru-WOC}$ electrode is due to water oxidation catalysis. An adapted Generator-Collector device was used, which is inspired by previously reported procedures that have been built for related photoelectrochemical systems (Figure 4 and Figures S11-S13 in the supporting information).^{30,31} In particular, a slow scan rate LSV on the desired photoelectrode (Generator) is performed while a controlled potential electrolysis in a closely positioned FTO electrode (Collector) is simultaneously run. In the Collector electrode, the generated oxygen is reduced after diffusion through the solution from the Generator electrode. Thus, the current observed in the controlled potential electrolysis experiment is a measure of the evolved gas due to the water oxidation reaction on the photoelectrode. This method allows us to measure the oxygen gas *in situ* and to control at what potential the chemical reactions starts. As shown in Figure 4 and Figure S12, the oxygen evolution reaction for the full hybrid electrode $\text{WO}_3/\text{BiVO}_4/\text{CNT}_f/\text{Ru-WOC}$ starts at a potential 140 mV lower than that of the bare electrode $\text{WO}_3/\text{BiVO}_4$



(ca. 0.41 V for the former and 0.55 V for the latter). The faradaic efficiency calculated for these experiments are 94% for $\text{WO}_3/\text{BiVO}_4/\text{CNT}_f/\text{Ru-WOC}$ and 97% for $\text{WO}_3/\text{BiVO}_4$ (Figure S13). The delay in detecting the oxygen is attributed to the diffusion process of the oxygen gas from the generator electrode to the collector electrode (0.3 V from LSV in Figure 2 vs 0.41 V from G-C method in Figure 4 and Figure S12).

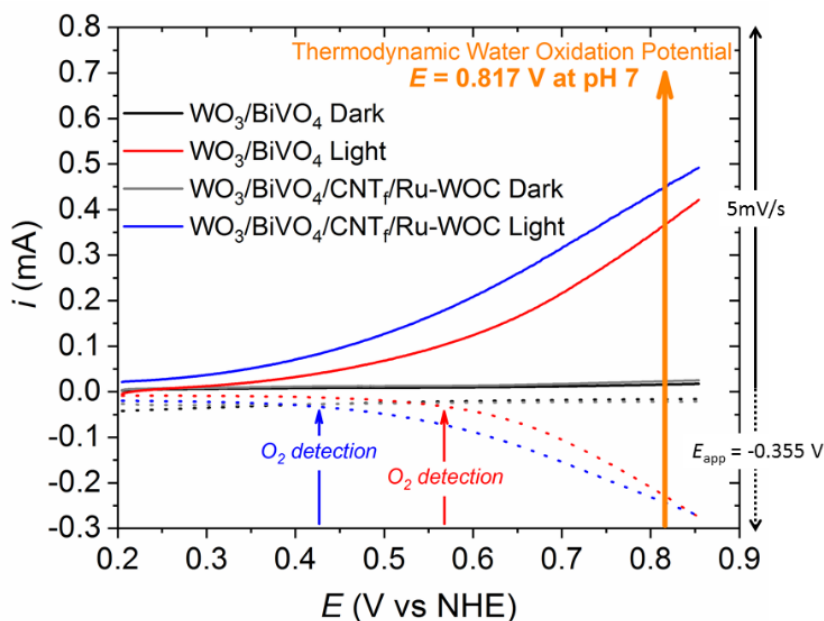


Figure 4. Oxygen gas detection experiments using an adapted Generator-Collector method performed in pH 7.^{30,31} Solid lines correspond to LSV (5 mV/s) performed on the photoanode electrode (Generator). The dotted lines correspond to the in situ current observed on the Collector electrode due to O_2 reduction (Controlled Potential Electrolysis at $E_{\text{app}} = -0.355$ V vs NHE, see details in the supporting information). $\text{WO}_3/\text{BiVO}_4$ in the dark (black), $\text{WO}_3/\text{BiVO}_4$ under 1 sun illumination (red), $\text{WO}_3/\text{BiVO}_4/\text{CNT}_f/\text{Ru-WOC}$ in the dark (grey) and $\text{WO}_3/\text{BiVO}_4/\text{CNT}_f/\text{Ru-WOC}$ under 1 sun illumination (blue).



A hybrid molecular photoanode for efficient light-induced WO

6.2.4 Electrochemical impedance spectroscopy analysis

In order to get further insights into the role of the different interfaces involved in the photocurrent generation, electrochemical impedance spectroscopy (EIS) experiments under illumination and different applied biases were carried out. The results have been fitted using a circuital model adapted from reported works (Figure 5A).^{14,32,33} Briefly, it consists of a serial resistance of the electrochemical cell (R_1), in series with a R_2 -CPE₂ mesh and an extended element (TL). The latter is commonly used to represent the transmission line of mesoporous films ($\text{WO}_3/\text{BiVO}_4$ in our case), through which the photogenerated carriers travel overcoming the transport resistance (R_{tr}) between the fused nanoparticles. The approximation of a negligible capacitance contribution between the particles is generally used. Furthermore, the model includes a resistive contribution (R_{ct}) due to the charge carrier recombination (which eventually influences the charge transfer to the electrolyte), as well as a capacitive contribution accounting for the accumulation of photogenerated charges in the film (CPE_{film}). On the other hand, the R_2 -CPE₂ mesh has been introduced to take into account the FTO/ WO_3 interface or the CNT_f /electrolyte interface when the CNT_f are present.



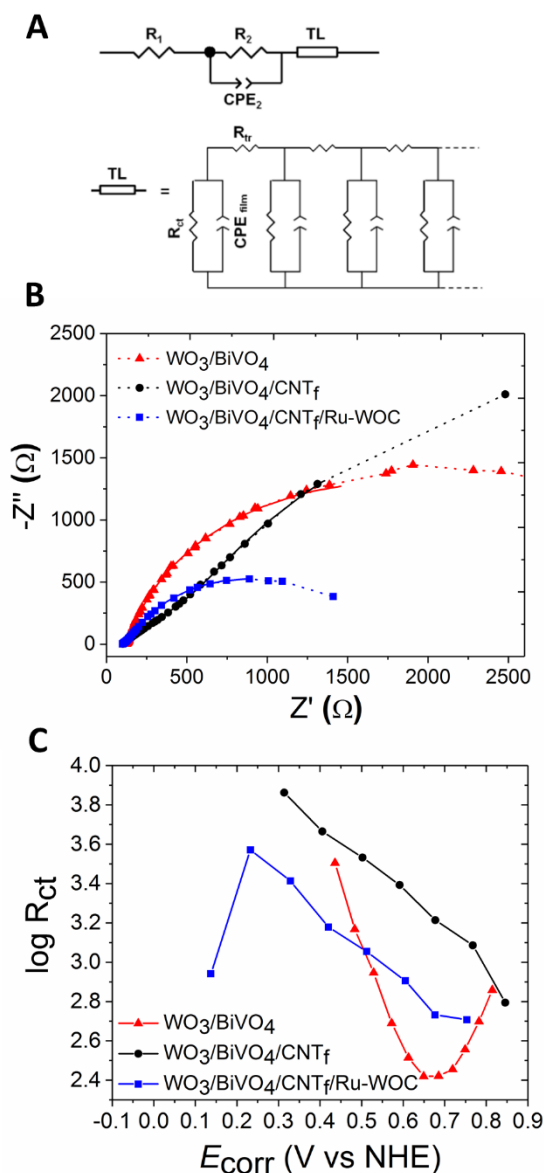


Figure 5. A) Equivalent circuit used to fit the EIS data of the photoanodes. B) complex plane Nyquist plots for the different electrodes measured under 1 sun illumination in pH 7 phosphate buffer at 0.440 V vs NHE. The corresponding fits are also reported as thick solid lines. C, $\log R_{ct}$ vs potential. Legend code: $\text{WO}_3/\text{BiVO}_4$ (red), $\text{WO}_3/\text{BiVO}_4/\text{CNT}_f$ (black) and $\text{WO}_3/\text{BiVO}_4/\text{CNT}_f/\text{Ru-WOC}$ (blue).



A hybrid molecular photoanode for efficient light-induced WO

The experimental Nyquist plots of the different photoanodes, together with the corresponding fittings, are reported in Figure 5B and Figure S14, evidencing the good agreement provided by the selected circuit model. The major contribution of the total resistance is given by R_{ct} , which follows the same dependence from the applied bias of the inverse of the differential resistance (Figure S15). The exact values, obtained for the different resistive and capacitive contributions, are reported in Table S1 and Table S2, respectively.

In the model, R_{ct} represents the recombination through the nanostructured film, and therefore its contribution is expected to decrease for systems that can effectively transfer charge to the electrolyte and perform fast water oxidation catalysis. Figure 5C reports the bias dependence of the logarithm of R_{ct} and gives a quantification of this recombination phenomenon. The presence of the Ru-WOC coupled to the CNT_f reduces the R_{ct} value of the corresponding photoanode by *ca.* three times in the whole range of potential (compare blue and black traces). The charge transfer rate to the aqueous electrolyte is indeed expected to be lower for the $WO_3/BiVO_4/CNT_f$ electrodes without the molecular catalyst, due to the hydrophobicity of the CNT_f layer and the blockage of the active catalytic sites of $BiVO_4$. On the other hand, with regard to the bare $WO_3/BiVO_4$ electrode, the enhancement of the charge transfer by the Ru-WOC is only improved at low potentials, as evidenced by the crossing point of the blue and red traces in Figure 5C. Furthermore, it is worth noting that the $WO_3/BiVO_4$ electrode shows a bell-shaped behaviour (red trace in Figure 5C) with a minimum around 0.69 V vs NHE, *i.e.* at the inflection point of the LSV curve of the photoelectrode (Figure S14). With regard to other resistive contributions, the resistance that we associate with the inert FTO/ WO_3 interface for bare $WO_3/BiVO_4$ is $< 15 \Omega$ and it is substantially independent on the applied bias, as expected when the interface is not directly involved in the photocurrent generation mechanism.¹⁴ On the other hand, for the $WO_3/BiVO_4/CNT_f$ electrodes, the R_2 values are much higher (in the range of 330–625 Ω), as well as bias-dependent. Thus, in this case, the R_2 -CPE₂ mesh has been assigned to the CNT_f /electrolyte interface, whose higher resistive contribution covers the one due to the FTO/ WO_3 interface, that was considered in the first place. This characteristic can be seen in the Nyquist plots, resulting in an additional arc for the $WO_3/BiVO_4/CNT_f$ electrode (Figure



5B, black trace). When the latter is coupled with the Ru-WOC, the R_2 values (assigned by analogy to the functionalized CNT_f /electrolyte interface decrease by at least one order of magnitude ($< 25\Omega$) with respect to the non-catalytic $\text{WO}_3/\text{BiVO}_4/\text{CNT}_f$, as expected from the improved surface kinetics in the presence of the catalyst, which also induces wetting of the porous CNT_f layer. Furthermore, the R_2 values are bias dependent for $\text{WO}_3/\text{BiVO}_4/\text{CNT}_f/\text{Ru-WOC}$, with a minimum at 0.64 V vs NHE, close to the inflection point of the LSV curve (Figure S14 and S15E). More information on the nanofibres/electrolyte interface can be extracted from the capacitance values given by CPE_2 , which follows a similar potential dependence for both $\text{WO}_3/\text{BiVO}_4/\text{CNT}_f$ and $\text{WO}_3/\text{BiVO}_4/\text{CNT}_f/\text{Ru-WOC}$ (Figure S16). These results support the hypothesis of reduced electron recombination with surface trapped holes (that may translate into $\text{WO}_3/\text{BiVO}_4$ defects, oxidized CNT_f or oxidized catalyst) as the potential increases.

In the case of the $\text{WO}_3/\text{BiVO}_4$ electrodes, the logarithm of the capacitance associated to the charge accumulation in the film (CPE_{film}) displays a linear dependence on the applied bias, as soon as the surface states have been emptied by the voltage, at approximately 0.54 V vs NHE (Figure S17). This behaviour is typical of a chemical capacitor, as expected for this kind of electrodes.³⁴ A higher CPE_{film} value has been observed for $\text{WO}_3/\text{BiVO}_4/\text{CNT}_f/\text{Ru-WOC}$ photoanodes, confirming that in the presence of the catalyst a higher charge can be accumulated and then transported to the electrolyte. It is worth noting that the higher CPE_{film} values for $\text{WO}_3/\text{BiVO}_4/\text{CNT}_f/\text{Ru-WOC}$ correspond to lower R_{ct} values in the 0.15-0.50 V vs NHE range, *i.e.* where the photocurrent response is anticipated with respect to the bare $\text{WO}_3/\text{BiVO}_4$ electrode (compare red and blue traces in Figure 5C and Figure S17). Furthermore, we observe that CPE_{film} follows same bias dependence for $\text{WO}_3/\text{BiVO}_4/\text{CNT}_f/\text{Ru-WOC}$ and $\text{WO}_3/\text{BiVO}_4$ electrodes at high potentials (> 0.59 V vs NHE), while for lower values it results essentially constant, as also observed in the case of $\text{WO}_3/\text{BiVO}_4/\text{CNT}_f$. The higher CPE_{film} values obtained in the latter case suggest a significant charge accumulation on the CNT_f layer (or on BiVO_4 states covered by CNT_f), which can be followed by a good charge transfer to the electrolyte only when the WOC is coupled to them.



A hybrid molecular photoanode for efficient light-induced WO

6.3 Discussion

Figure 1 shows the potential values required to oxidize the molecular catalyst attached on the surface of the $\text{WO}_3/\text{BiVO}_4/\text{CNT}_f/\text{Ru-WOC}$ photoanode and generate the Ru(V)=O active species ($E_{(\text{RuV/IV})} = 1.3\text{V vs NHE}$). This potential should be easily overcome by the oxidative power of the low BiVO_4 valence band upon illumination ($E_{\text{VB, pH 7}} = 2.2\text{-}2.4\text{ V vs NHE}$).³⁵ Once the Ru(V)=O species is formed, the water oxidation catalytic process is triggered and occurs at a maximum rate of almost 8000 cycles per second.^{19,20} Thus, upon illumination, the electrode $\text{WO}_3/\text{BiVO}_4/\text{CNT}_f/\text{Ru-WOC}$ should be able to perform oxygen evolution catalysis. Figure 2 proves that indeed the $\text{WO}_3/\text{BiVO}_4/\text{CNT}_f/\text{Ru-WOC}$ shows enhanced photocurrent at potentials lower than the $\text{WO}_3/\text{BiVO}_4$ and $\text{WO}_3/\text{BiVO}_4/\text{CNT}_f$ electrodes (compare blue with red and black traces). Bulk electrolysis and oxygen measurement experiments confirmed that the enhanced photocurrent is sustained over several minutes and that the current is due to oxygen gas formation (Figure 3 and 4). More importantly, the oxygen gas is detected at approximately 0.41 V vs NHE using the catalyst modified electrode $\text{WO}_3/\text{BiVO}_4/\text{CNT}_f/\text{Ru-WOC}$, 140 mV before the bare photoanode $\text{WO}_3/\text{BiVO}_4$ (Figure 4 and Figure S12) with faradaic efficiencies close to 100%. These results not only prove that the Ru-WOC performs the reaction but also, that the charge is efficiently transferred all the way through the multilayered architecture of the photoanode, *i.e.*, from the inner semiconductor, to the CNT fibres and finally to the catalyst. In this regard, the CNT fibres form an effective and stable interlayer with excellent charge transfer abilities. In addition, their work function above the conduction band of BiVO_4 might contribute to charge separation by preventing recombination phenomena.³⁶ Also, the CNT_f layer constitute an excellent platform for the easy anchoring of molecular catalysts.

EIS analysis allowed us to differentiate two potential ranges in which the $\text{CNT}_f/\text{Ru-WOC}$ interface have distinct influence on the overall catalytic performance. At high potentials, although the charge accumulation capacity of the complete photoanode $\text{WO}_3/\text{BiVO}_4/\text{CNT}_f/\text{Ru-WOC}$ is higher than that of simple $\text{WO}_3/\text{BiVO}_4$, the recombination is also higher, resulting in similar performance (Figures 5C and Figure S17, $E > 0.5\text{ V vs NHE}$). At this potential



range, the water oxidation catalysis by the Ru-WOC starts competing with the catalysis by the BiVO₄ active centres of the bare WO₃/BiVO₄ electrode, that are available in higher quantities in the absence of carbon nanotube fibres. On the other hand, at low potentials the full electrode WO₃/BiVO₄/CNT_f/Ru-WOC outperforms the WO₃/BiVO₄ photoanode, as a result of higher charge accumulation capacity and lower recombination phenomena (Figure 5C and Figure S17, $E < 0.5$ V vs NHE). This is particularly remarkable at the 0.3-0.5 V vs NHE range where the WO₃/BiVO₄ photoanode has practically no activity (Figure 1). This is a consequence of the high kinetic barrier of the water oxidation catalysis at BiVO₄ catalytic centres, which require higher potential to perform the reaction and avoid recombination phenomena. In sharp contrast, the specially designed Ru-WOC is able to perform the catalytic reaction at a potential as low as 0.3 V vs NHE, that is, *ca.* 300 mV higher than the semiconductor capacities ($E = -0.05$ V vs NHE, Figures S5). This value is close to those obtained for the best BiVO₄ based photoanodes described to date with onset potentials for the water oxidation catalysis in the range of -0.2 V to 0.2 V vs NHE.^{7,8,11,12,17,18,37,38,39} Among them, the best performing examples contain metal oxides (ruthenium, iron, cobalt or nickel) as water oxidation catalyst on the surface of the photoelectrode.^{11,12,17,18,37,38,39} Only limited examples of photoanodes modified with molecular catalysts have been reported with less efficiency than that of the photoanode WO₃/BiVO₄/CNT_f/Ru-WOC reported in this work.^{40,41,42} Importantly, the photoelectrode reported here can perform the reaction 510 mV below the thermodynamic potential of the water oxidation reaction at pH 7, allowing for the overlap with state of the art photocathodes for the overall unassisted water splitting reaction.^{37,39} This work highlights the promising role of robust and fast true molecular water oxidation catalysts on enhancing photoanode performance.



A hybrid molecular photoanode for efficient light-induced WO

6.4 Summary and conclusions

The preparation of a multilayer heterostructured $\text{WO}_3/\text{BiVO}_4$ photoanode containing two layers of WO_3 (compact and mesoporous) and a porous BiVO_4 film is described. The resulting photoactive material is covered by a highly conductive carbon nanotube fibre (CNT_f) that is able to accumulate charge but unable to perform the water oxidation reaction. Finally, the surface of the CNT_f is functionalized with a molecular catalyst precursor (Ru-WOC) modified with pyrene groups forming π - π stacking bonds. The Ru-WOC takes the charge accumulated on the CNT_f and rapidly transfers it to the solution by performing the water oxidation reaction. The system works at low potentials, where the bare $\text{WO}_3/\text{BiVO}_4$ is not active at all for the oxygen evolution reaction. However, at high potentials, the beneficial influence of the $\text{CNT}_f/\text{Ru-WOC}$ interfaces is not sufficient to overcome the good performance of the bare $\text{WO}_3/\text{BiVO}_4$. All these results have been rationalized by means of EIS experiments that prove the advantage of using a highly active molecular catalyst to trigger the water oxidation reaction all the way down to 510 mV below the thermodynamic potential of the reaction. Further improvements on the current molecular based photoanode can be focused on increasing the catalyst loading that should lead to enhanced current density at low potentials.



6.5 References

1. N. S. Lewis, *Science*, 2016, 351.
2. K. Sivula and R. van de Krol, *Nat. Rev. Mater.*, 2016, **1**, 15010.
3. J. H. Montoya, L. C. Seitz, P. Chakthranont, A. Vojvodic, T. F. Jaramillo and J. K. Nørskov, *Nat. Mater.*, 2016, **16**, 70.
4. X. Sala, I. Romero, M. Rodríguez, L. Escriche and A. Llobet, *Angew. Chem. Int. Ed.*, 2009, **48**, 2842.
5. S. Berardi, S. Drouet, L. Francàs, C. Gimbert-Suriñach, M. Guttentag, C. Richmond, T. Stoll and A. Llobet, *Chem. Soc. Rev.*, 2014, **43**, 7501.
6. P. Garrido-Barros, C. Gimbert-Suriñach, R. Matheu, X. Sala and A. Llobet, *Chem. Soc. Rev.*, 2017, **46**, 6088.
7. H. L. Tan, R. Amal and Y. H. Ng, *J. Mater. Chem. A*, 2017, **5**, 16498.
8. S. S. M. Bhat and H. W. Jang, *ChemSusChem*, 2017, **10**, 3001.
9. C. C. L. McCrory, S. Jung, I. M. Ferrer, S. M. Chatman, J. C. Peters and T. F. Jaramillo, *J. Am. Chem. Soc.*, 2015, **137**, 4347.
10. Z.-F. Huang, L. Pan, J.-J. Zou, X. Zhang and L. Wang, *Nanoscale*, 2014, **6**, 14044.
11. T. W. Kim and K.-S. Choi, *Science*, 2014, **343**, 990.
12. Y. Kuang, Q. Jia, H. Nishiyama, T. Yamada, A. Kudo and K. Domen, *Adv. En. Mat.*, 2016, **6**, 1501645.
13. S. J. Hong, S. Lee, J. S. Jang and J. S. Lee, *Energy Environ. Sci.*, 2011, **4**, 1781.
14. X. Shi, I. Herranz-Cardona, L. Bertoluzzi, P. Lopez-Varo, J. Bisquert, J. H. Park and S. Gimenez, *Phys. Chem. Chem. Phys.*, 2016, **18**, 9255.
15. M.-Q. Yang, N. Zhang, M. Pagliaro and Y.-J. Xu, *Chem. Soc. Rev.*, 2014, **43**, 8240.
16. J. A. Seabold and K.-S. Choi, *J. Am. Chem. Soc.*, 2012, **134**, 2186.
17. Y. Ma, A. Kafizas, S. R. Pendlebury, F. Le Formal and J. R. Durrant, *Adv. Funct. Mater.*, 2016, **26**, 4951.
18. C. Zachaus, F. F. Abdi, L. M. Peter and R. van de Krol, *Chem. Sci.*, 2017, **8**, 3712.



A hybrid molecular photoanode for efficient light-induced WO

19. R. Matheu, M. Z. Ertem, J. Benet-Buchholz, E. Coronado, V. S. Batista, X. Sala and A. Llobet, *J. Am. Chem. Soc.*, 2015, **137**, 10786.
20. J. Creus, R. Matheu, I. Peñafiel, D. Moonshiram, P. Blondeau, J. Benet-Buchholz, J. García-Antón, X. Sala, C. Godard and A. Llobet, *Angew. Chem. Int. Ed.*, 2016, **55**, 15382.
21. P. Garrido-Barros, C. Gimbert-Suriñach, D. Moonshiram, A. Picón, P. Monge, V. S. Batista and A. Llobet, *J. Am. Chem. Soc.*, 2017, **139**, 12907.
22. R. Matheu, I. A. Moreno-Hernandez, X. Sala, H. B. Gray, B. S. Brunshwig, A. Llobet and N. S. Lewis, *J. Am. Chem. Soc.*, 2017, **139**, 11345.
23. V. Cristino, S. Marinello, A. Molinari, S. Caramori, S. Carli, R. Boaretto, R. Argazzi, L. Meda and C. A. Bignozzi, *J. Mater. Chem. A*, 2016, **4**, 2995.
24. R. Matheu, M. Z. Ertem, C. Gimbert-Suriñach, J. Benet-Buchholz, X. Sala and A. Llobet, *ACS Catal.*, 2017, **7**, 6525.
25. M. K. Brennaman, R. J. Dillon, L. Alibabaei, M. K. Gish, C. J. Dares, D. L. Ashford, R. L. House, G. J. Meyer, J. M. Papanikolas and T. J. Meyer, *J. Am. Chem. Soc.*, 2016, **138**, 13085-13102.
26. M. Wang, Y. Yang, J. Shen, J. Jiang and L. Sun, *Sustainable Energy Fuels*, 2017, **1**, 1641.
27. L. Francàs, C. Richmond, P. Garrido-Barros, N. Planas, S. Roeser, J. Benet-Buchholz, L. Escriche, X. Sala and A. Llobet, *Chem. Eur. J.*, 2016, **22**, 5261.
28. E. Senokos, V. Reguero, J. Palma, J. J. Vilatela and R. Marcilla, *Nanoscale*, 2016, **8**, 3620.
29. V. Reguero, B. Alemán, B. Mas and J. J. Vilatela, *Chem. Mater.*, 2014, **26**, 3550.
30. B. D. Sherman, M. V. Sheridan, C. J. Dares and T. J. Meyer, *Anal. Chem.*, 2016, **88**, 7076-7082.
31. J. T. Kirner and R. G. Finke, *ACS Appl. Mater. Interfaces*, 2017, **9**, 27625.
32. J. Bisquert, *Phys. Chem. Chem. Phys.*, 2000, **2**, 4185.
33. J. Bisquert, G. Garcia-Belmonte, F. Fabregat-Santiago and A. Compte, *Electrochem. Commun.*, 1999, **1**, 429.
34. J. Bisquert, *Phys. Chem. Chem. Phys.*, 2003, **5**, 5360.
35. J. K. Cooper, S. Gul, F. M. Toma, L. Chen, P.-A. Glans, J. Guo, J. W. Ager, J. Yano and I. D. Sharp, *Chem. Mater.*, 2014, **26**, 5365.



36. A. Moya, N. Kemnade, M. R. Osorio, A. Cherevan, D. Granados, D. Eder and J. J. Vilatela, *J. Mater. Chem. A*, 2017, **5**, 24695.
37. F. Jiang, Gunawan, T. Harada, Y. Kuang, T. Minegishi, K. Domen and S. Ikeda, *J. Am. Chem. Soc.*, 2015, **137**, 13691.
38. F. Lin, D. Wang, Z. Jiang, Y. Ma, J. Li, R. Li, C. Li, *Energy Environ. Sci.* 2015, **5**, 6400.
39. P. Bornoz, F. F. Abdi, S. D. Tilley, B. Dam, R. van de Krol, M. Graetzel, K. Sivula, *J. Phys. Chem. C* 2014, **118**, 16959.
40. K. S. Joya, N. Morlanés, E. Maloney, V. Rodionov, K. Takanahe, *Chem. Commun.* 2015, **51**, 13481.
41. W. Li, S. W. Sheehan, D. He, Y. He, X. Yao, R. L. Grimm, G. W. Brudvig, D. Wang, *Angew. Chem. Int. Ed.* 2015, **54**, 11428.
42. B. Liu, J. Li, H.-L. Wu, W.-Q. Liu, X. Jiang, Z.-J. Li, B. Chen, C.-H. Tung, L.-Z. Wu, *ACS Appl. Mater. Interfaces* 2016, **8**, 18577.



A hybrid molecular photoanode for efficient light-induced WO

6.6 Supporting information

6.6.1 Materials and Methods

Reagents

Buffer solutions were prepared with Na_2HPO_4 , NaH_2PO_4 from Sigma-Aldrich. Metallic W (99.95%, Alfa Aesar), hydrogen peroxide (30%, Honeywell Fluka) and Triton X-100 (Fluka) were used as received. The molecular ruthenium precursor of Ru-WOC was prepared following a described procedure in the literature.¹ ITO substrates were purchased from Delta Tech (Corning® alkaline earth boroaluminosilicate glass, 50 x 75 x 1.1 mm, indium tin oxide coated on surface, $R_s = 4 - 10 \Omega/\text{sq}$), FTO substrates were purchased from Pilkington (FTO TEC 8, $8 \Omega/\text{sq}$).

Atomic force microscopy (AFM) images were collected using a Digital Instruments Nanoscope III scanning probe Microscope (Digital Instruments, CA). The instrument was equipped with a silicon tip (RTESP-300 Bruker) and operated in tapping mode. Surface topographical analysis of raw AFM images was carried out with NanoScope analysis 1.5 program.

Scanning Electron Microscopy (SEM) images were obtained using a Zeiss Evo 40 electron microscope.



X-ray Diffractometry (XRD) analysis was carried out with an automatic Philips X'pert $\theta/2\theta$ diffractometer using Cu KR radiation ($\lambda = 1.5416 \text{ \AA}$).

UV-Vis measurements were carried out on a Lambda 1050 PerkinElmer spectrophotometer equipped with a PMT, InGaAs and PbS detectors system, double beam optics, double monochromator and D2 and W light sources. Diffuse reflectance measurements were carried out in the same equip using 150mm Integrating Sphere with PbS and PMT detectors.

Electrochemical equipment

Cyclic voltammetry (CV), linear sweep voltammetry (LSV) and bulk electrolysis (BE) were measured using a CHI660D potentiostat or CHI730D bipotentiostat.

The oxygen evolution experiments based on the Generator-Collector method were done using a CHI730D bipotentiostat.

Electrochemical Impedance Spectroscopy (EIS) analyses were performed using a PGSTAT-302N potentiostat, equipped with a FRA2.v10 frequency response analyzer and controlled by Nova 1.10. An Abet solar simulator, equipped with an AM1.5G filter and calibrated to 0.1 W/cm^2 using a Newport 1918-C Power Meter, was used as the illumination source. The illuminated photoanodes were sampled in the selected potential ranges (0.14-0.94 V vs NHE) at 50 or 100 mV intervals. A 10 mV amplitude sinusoidal perturbation, whose angular frequency ω ranged between 50000 and 0.05 Hz, was used (single-sine frequency scan mode for $\omega > 2.6 \text{ kHz}$ and 5-sine frequency scan mode for $\omega < 2.6 \text{ kHz}$). The EIS data were fitted by means of the equivalent circuit reported in Figure S13 using the ZView software with typical relative errors lower than 10%.

6.6.2. Preparation of $\text{WO}_3/\text{BiVO}_4$ photoanodes

0.46 g of metallic W were added to 5 mL of 30% H_2O_2 and stirred until the dissolution was completed. 2 drops of Triton-X were then added, and the resulting solution was spin coated (at 1000 rpm for 9 s, then at 2000 rpm for 20 s) on the top of cleaned FTO slides. Three spin coating cycles were performed, each one followed by an annealing step at 550°C for 15 min. The AFM characterization of the resulting electrodes confirms the compact nature of the so-deposited WO_3 film (Figure S1). Mesoporous WO_3 was then formed on the top of the WO_3 compact underlayer, by spin-coating a colloidal precursor (prepared following literature procedures)² at 600 rpm for 6 s, then at 2000 rpm for 20 s. Six spin coating cycles were performed, each one followed by an annealing step at 550°C for 30 min. Finally, BiVO_4 was electrodeposited on the top of the so-produced electrodes, following an adapted literature procedure.³ Figures S2-S5 summarize the optical, electrochemical, structural and morphological characterization of the full $\text{WO}_{3(\text{C})}/\text{WO}_{3(\text{P})}/\text{BiVO}_4$ photoelectrode.



A hybrid molecular photoanode for efficient light-induced WO

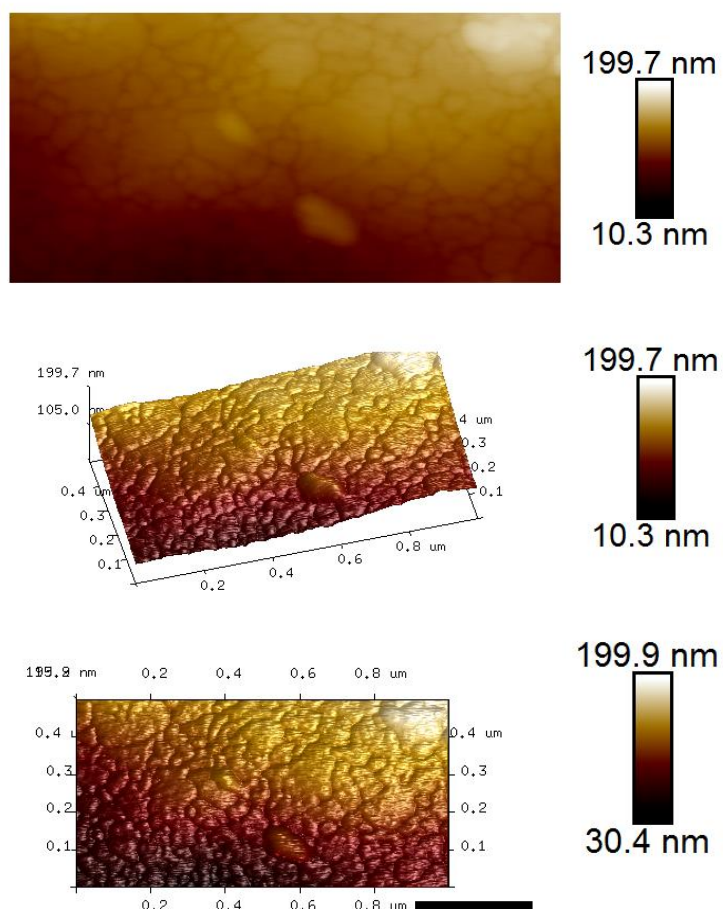


Figure S1. AFM images of the WO_3 compact underlayer deposited on FTO.



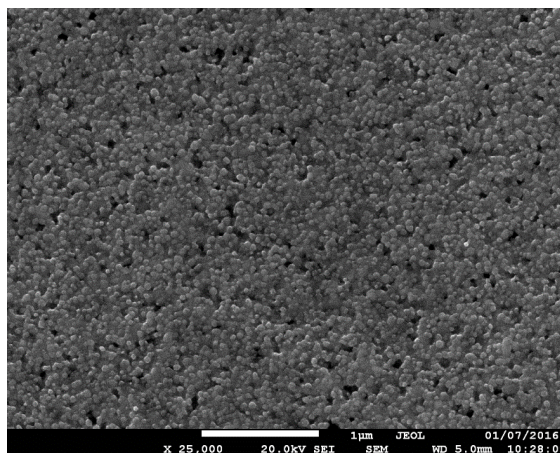


Figure S2. SEM image of a $\text{WO}_3(\text{C})/\text{WO}_3(\text{P})/\text{BiVO}_4$ photoelectrode evidencing the WO_3 particles (with diameters of 50-70 nm) homogeneously covered by BiVO_4

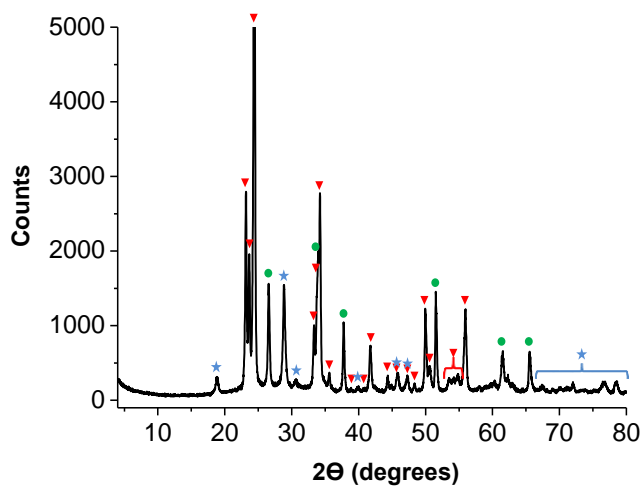


Figure S3. Grazing incidence XRD diffractogram of $\text{WO}_3(\text{C})/\text{WO}_3(\text{P})/\text{BiVO}_4$ photoelectrode. Red triangles: WO_3 ; grey stars: BiVO_4 ; green circles: FTO.



A hybrid molecular photoanode for efficient light-induced WO

6.6.3. Band Gap measurements

In order to determine the optical band gap of $\text{WO}_3/\text{BiVO}_4$ the diffuse reflectance UV-vis spectra were measured. Kubelka-Munk equation (eq 1) can be used to extract the absorption coefficient (α) from the diffuse reflectance spectra:⁴

$$f(R) = \frac{(1-R)^2}{2R} = \frac{\alpha}{s} \quad (\text{eq 1})$$

Where R is diffuse reflectance values at given wavelength and s is the scattering coefficient.

Assuming that s is wavelength independent, we can consider that $f(R)$ is directly proportional to α , and $f(R)$ can be used in place of α to make the Tauc plot (eq 2):

$$\alpha h\nu \propto (h\nu - E_g)^{\frac{1}{n}} \quad (\text{eq 2})$$

Where E_g is band gap energy (in eV) and n can take value of $\frac{1}{2}$ for the direct and allowed transition.

Plotting $(\alpha h\nu)^2$ vs $h\nu$ (Tauc plot) E_g value can be calculated extrapolating the linear region to the baseline (Fig S4). The value obtained using this method gives an E_g value of 2.6 eV that is in good agreement with the reported values for BiVO_4 thin films (2.5-2.6 eV).⁵

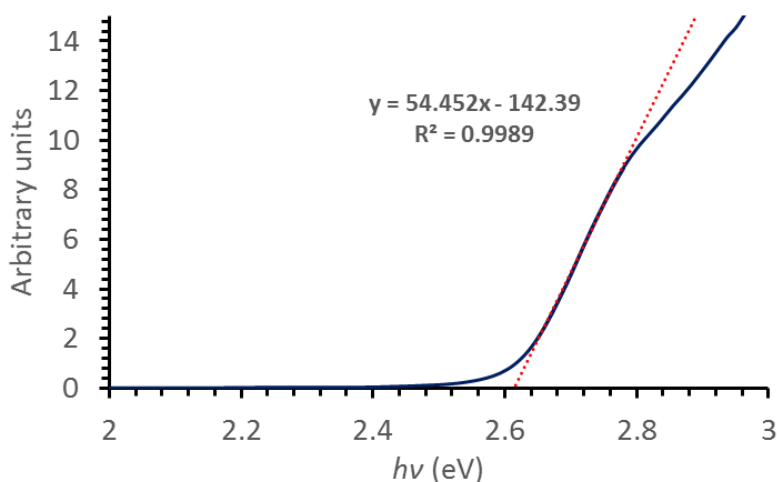


Figure S4. Tauc plot and corresponding fitting.

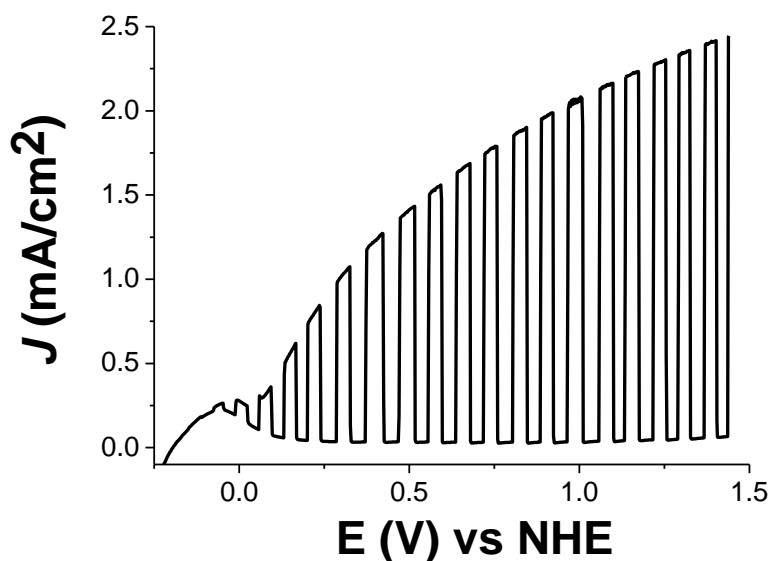


Figure S5. Chopped light LSV of a $\text{WO}_3(\text{C})/\text{WO}_3(\text{P})/\text{BiVO}_4$ electrode in the presence of a sacrificial agent (0.1 M Na_2SO_3 at pH 7), scan rate = 10 mV/s. The onset of the transient photocurrent (at ca. -0.05 V vs NHE) gives an estimation of the conduction band position. The dark current is negligible in all the explored potential range, supporting the efficiency of the WO_3 compact underlayer.

6.6.4. Fabrication of carbon nanotube fibers (CNT_f)

The CNT fiber layer consisted of a thin planar array of multiple CNT fibers overlaid as a non-woven unidirectional fabric. The CNT fibres were produced by directly spinning of a CNT aerogel from the gas-phase during CNT growth by chemical vapour deposition at 1250°C.⁶ Butanol, ferrocene, thiophene and hydrogen were used as carbon source, catalyst promoter and carrier gas, respectively. Their concentration was fixed to produce CNTs of few layers (3-5) length of around a millimeter. In the fiber, the CNTs are strongly associated in bundles that thus enable swift stress and charge transfer. Yet, the bundles are imperfectly packed and lead to a large mesoporosity and high surface area.



A hybrid molecular photoanode for efficient light-induced WO

6.6.5. Preparation of $\text{WO}_3/\text{BiVO}_4/\text{CNT}_f/\text{Ru-WOC}$ photoanodes

First, the $\text{WO}_3/\text{BiVO}_4$ photoanodes were cleaned with deionized water and dried with airflow. CNT_f is an extremely thin black foil (Figure S6, pic 1), placed between two protective paper foils. The most convenient way to cut it is using scissors before removing the paper foils (Figure S6, pic 3). After removing the paper (Figure S6, pic 5), the piece of appropriate size is placed on the surface of the photoanode with Teflon tweezers. Finally, a drop of acetone is added, wetting the whole fiber (Figure S6, pic 7). It is advisable to hold the edges of the CNT_f when acetone is added to prevent the CNT_f getting folded or rolled up (Figure S6, pic 6). The position of the CNT_f can be readjusted while still being wet (Figure S6, pic 8). Rolling a glass pipette to pull out the excess of acetone helps to get a flat and well attached CNT_f layer (Figure S6, pic 9-11). With the addition of acetone the CNT_f is contracted and gets attached on the photoelectrode surface in a relatively stable way. It is important that the CNT_f doesn't touch the edge of the BiVO_4 photoanode (or uncovered FTO), otherwise CNT_f may be in contact with FTO, creating a short-circuit between the back contact (FTO) and the layer in contact with the electrolyte ($\text{CNT}_f/\text{Ru-WOC}$) (Figure S6, pic 11 and 12).



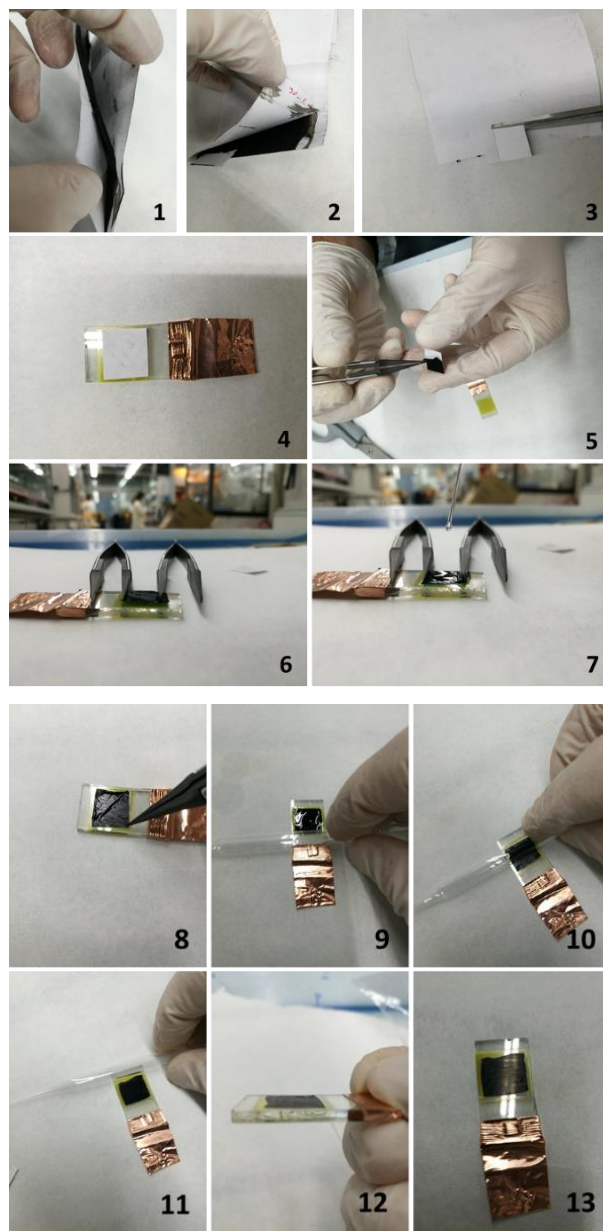


Figure S6. Deposition of CNT_f films on the WO₃/BiVO₄ photoanodes.



A hybrid molecular photoanode for efficient light-induced WO

6.6.6. Photoelectrochemistry (PEC)

All the electrochemical and photoelectrochemical experiments were performed in a pH 7 phosphate buffer (Ionic strength = 0.5 M) and using a hand-made Teflon cell (Figure S7). Platinum coil was used as counter electrode and Hg/HgSO₄ or SCE as reference electrodes (the potentials were converted to NHE by applying a correction of +0.645 V or +0.240 respectively). The teflon cell allows to illuminate the sample either from the front or from back. In our system, we use only back illumination since the carbon nanotube fibers (CNT_f) are black and opaque. The cell also allows to perfectly control the photoanode's area exposed to the electrolyte and to the light and corresponds to a 0.5 cm² area.

A Xenon Lamp (Abet LS150) with a UV-light filter (cutoff <400nm) was used as a source of light unless otherwise stated. The light intensity reaching the electrode was calibrated to 1 sun by means of a silicon photodiode, independently calibrated using a solar simulator (AM1.5G of solar irradiation with a total light intensity of 100 mW/cm²).

To perform the chopped light LSV, automated handmade chopper was used, changing between dark and light conditions every 5 seconds.



Figure S7. Photoelectrochemical cell used in this work.

6.6.7. Oxygen detection experiments using the Generator-Collector method^{7,8}

The Generator-Collector method consists of placing two electrodes very near to each other. One of them will perform water oxidation (Generator) while the other is set to reduce the oxygen that is produced (Collector) (Figure 11, Left).

In our setup, the photoanode (e.g. $\text{WO}_{3(\text{C})}/\text{WO}_{3(\text{P})}/\text{BiVO}_4/\text{CNTf}/\text{Ru-WOC}$) acts as an oxygen Generator. The Collector electrode consist of a clean FTO (sonicated for 15 minutes in a saturated solution of KOH in 2-propanol, rinsed with water and annealed for 30 min at 500°C). To select the optimal potential to reduce molecular oxygen in solution, several CVs in pH 7 were performed in aired and degassed solutions (Fig S11, Right). A reduction peak controlled by diffusion can be observed in aired solution, reaching the maximum intensity at -0.355 V vs NHE .

Both electrodes are placed together with the conductive part facing the inner part of the set-up. Two small pieces of coverslip (Menzel-Gläser, 130-140 μm of thickness) are used to keep a constant distance between both electrodes. Then the electrodes are covered with parafilm leaving lateral apertures in both sides to allow the solution to fill the inner space by capillarity forces (Fig S11, Left). Finally, the reference electrode is placed as near as possible to one lateral aperture.

To determine at witch potential the $\text{WO}_{3(\text{C})}/\text{WO}_{3(\text{P})}/\text{BiVO}_4/\text{CNTf}/\text{Ru-WOC}$ and $\text{WO}_{3(\text{C})}/\text{WO}_{3(\text{P})}/\text{BiVO}_4$ (Generators) start to produce molecular oxygen, LSV at 5 mV/s under 1 sun illumination were performed in a degassed pH 7 solution while the Collector performs a controlled potential electrolysis at -0.355 V vs NHE .



A hybrid molecular photoanode for efficient light-induced WO

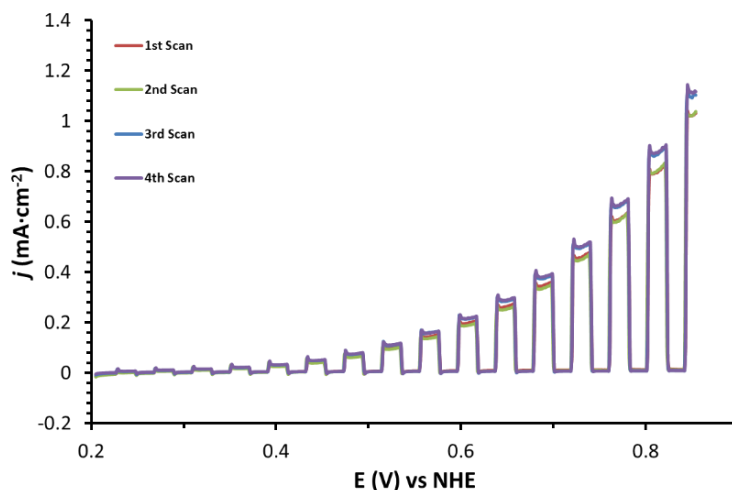


Figure S8. Consecutive LSV experiments (scan rate = 5 mV/s) of $\text{WO}_3/\text{BiVO}_4$ photoanodes showing an improving of its performance. All electrodes were submitted to such consecutives LSV until they were identical (usually takes 3-5 scans). After these LSV pre-treatment the photoanode is ready to be covered with CNT_f .

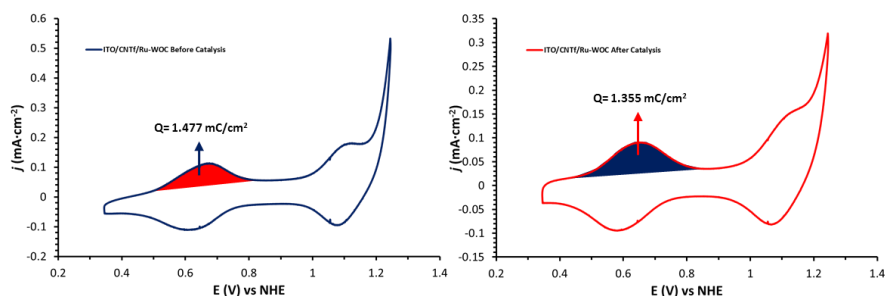


Figure S9. CV (5 mV/s) of a ITO/ CNT_f /Ru-WOC electrode. **Left)** as deposited. **Right)** After a bulk electrolysis of a $\text{WO}_3/\text{BiVO}_4/\text{CNT}_f$ /Ru-WOC photoanode and subsequent transfer of the CNT_f /Ru-WOC film on a clean ITO substrate. The surface coverage (Γ) of the Ru-WOC on the FTO/ CNT_f electrodes was estimated by applying the formula Γ ($\text{mol}\cdot\text{cm}^{-2}$) = $Q / (n \cdot S \cdot F)$, where Q is the charge under the Ru(III/II) oxidation wave, n is the number of electrons involved in the electron transfer ($1 e^-$ in this case), S is the surface of the electrode (0.5 cm^2) and F is the Faradaic constant.

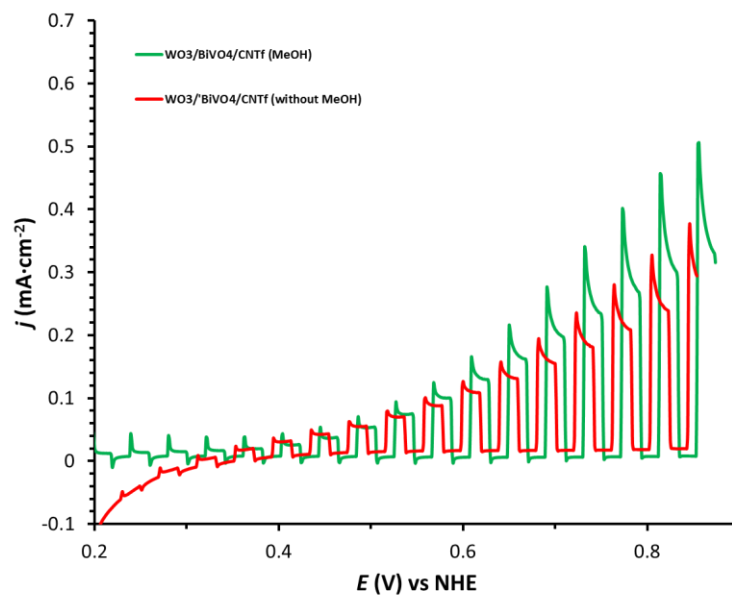


Figure S10. Comparison of the performance of a $\text{WO}_3/\text{BiVO}_4$ photoanode with (green) and without (red) treatment with methanol.



A hybrid molecular photoanode for efficient light-induced WO

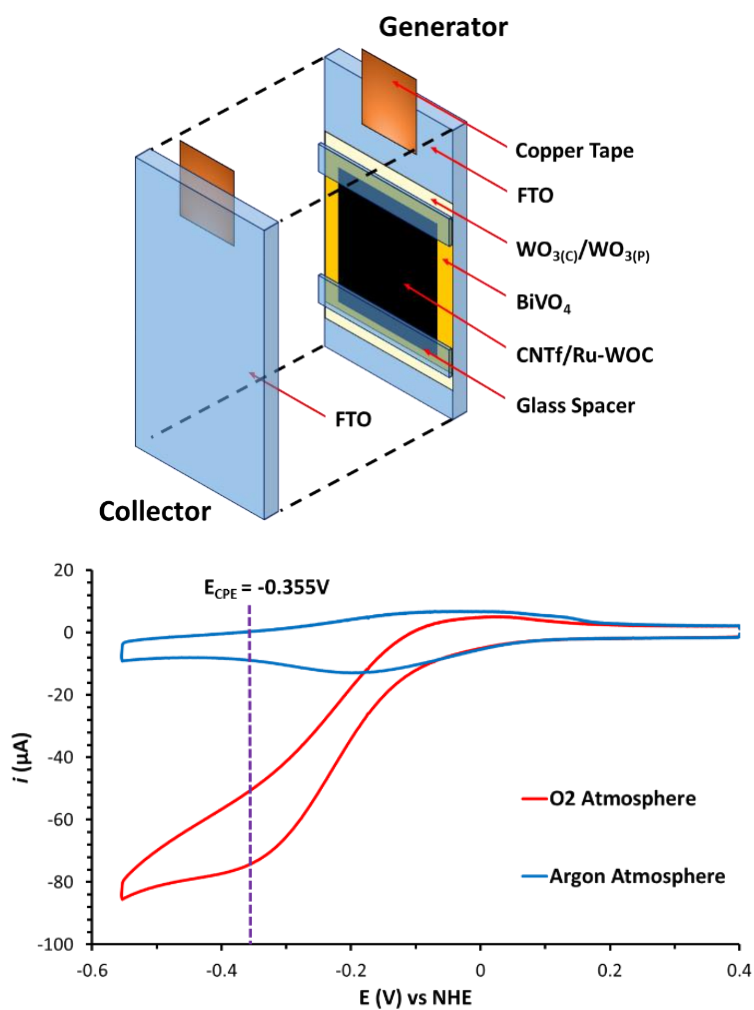


Figure S11. Top) Scheme of Generator-Collector system used in this work. **Bottom)** Cyclic voltammograms of an FTO working electrode in pH 7 under argon or oxygen atmosphere to set the potential for oxygen reduction in the collector electrode.

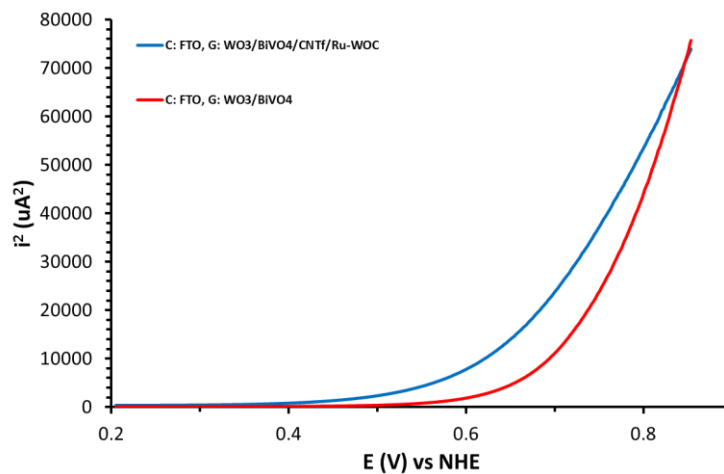


Figure S12. Plot of i^2 vs applied potential of a controlled potential electrolysis experiment using the Generator(G)-Collector(C) Method (from Figure 4 of main manuscript).



A hybrid molecular photoanode for efficient light-induced WO

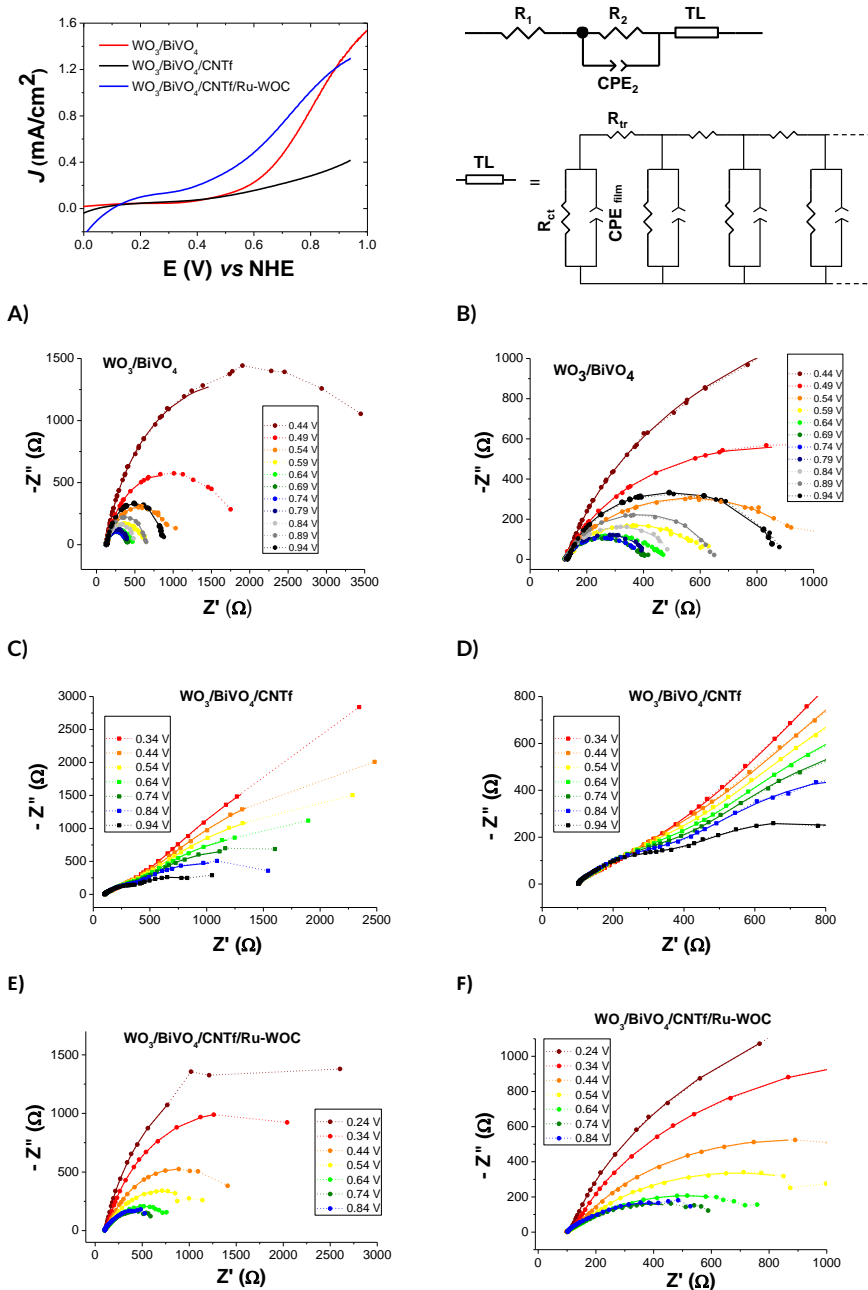


Figure S13. Top) left, J-V curves of the different photoanodes recorded at pH 7 under 1 sun illumination ($0.1 \text{ W}/\text{cm}^2$ AM1.5G). $\text{WO}_3/\text{BiVO}_4$ (red), $\text{WO}_3/\text{BiVO}_4/\text{CNTf}$ (black) and $\text{WO}_3/\text{BiVO}_4/\text{CNTf}/\text{Ru-WOC}$ (blue). Right, Equivalent circuit used to fit the EIS data of the photoanodes. Bottom) Complex plane Nyquist plots for $\text{WO}_3/\text{BiVO}_4$ (A, zoomed in B), $\text{WO}_3/\text{BiVO}_4/\text{CNTf}$ (C, zoomed in D) and $\text{WO}_3/\text{BiVO}_4/\text{CNTf}/\text{Ru-WOC}$ (E, zoomed in F) photoanodes recorded phosphate buffer (pH 7) under 1 sun illumination and different applied biases (all values vs NHE). The corresponding fits are also reported as thick solid lines.

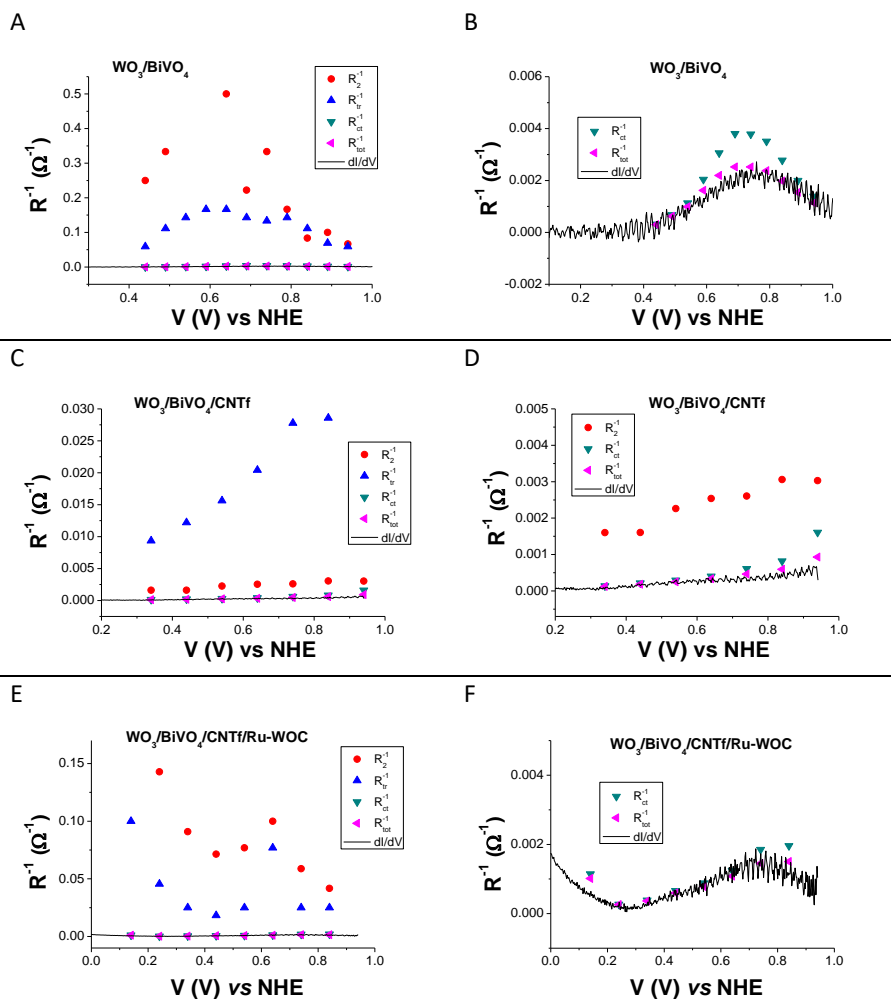


Figure S14. Applied bias dependence of R_{tot}^{-1} (pink triangles), R_2^{-1} (red circles), R_{tr}^{-1} (blue triangles) and R_{ee}^{-1} (green reverted triangles) for $\text{WO}_3/\text{BiVO}_4$ (A, zoomed in B), $\text{WO}_3/\text{BiVO}_4/\text{CNT}_f$ (C, zoomed in D) and $\text{WO}_3/\text{BiVO}_4/\text{CNT}_f/\text{Ru-WOC}$ (E, zoomed in F) photoanodes recorded at pH 7 under 1 sun. The resistance values are obtained from the fitting of the EIS data with the equivalent circuit reported in Figure S12 (top). The corresponding derivatives of the J-V curves in Figure S13 (di/dV) are reported as gray solid lines.



A hybrid molecular photoanode for efficient light-induced WO

Table S1. Resistance values obtained for all the reported photoanodes after the EIS data fit with the equivalent circuit reported in Figure S13.

Electrode	E (V) vs NHE	R ₁ (Ω)	R ₂ (Ω)	R _{tr} (Ω)	R _{ct} (Ω)	R _{tot} (Ω)
WO ₃ /BiVO ₄	0.44	121	4	17	3200	3342
"	0.49	121	3	9	1472	1605
"	0.54	121	1	7	884	1013
"	0.59	121	1.5	6	490	618.5
"	0.64	121	2	6	327	456
"	0.69	122	4.5	7	263	396.5
"	0.74	122	3	7.5	264	396.5
"	0.79	123	6	7	285	421
"	0.84	124	12	9	360	505
"	0.89	125	10	14.5	500	649.5
"	0.94	126	15	17	721	879
WO ₃ /BiVO ₄ /CNTf	0.34	96	625	107	7273	8101
"	0.44	97	623	82	4625	5427
"	0.54	97	442	64	3408	4011
"	0.64	97	394	49	2469	3009
"	0.74	99	384	36	1636	2155
"	0.84	98	327	35	1219	1679
"	0.94	99	330	24	622	1075
WO ₃ /BiVO ₄ /CNTf/Ru-WOC	0.14	98	5	10	873	986
"	0.24	98	7	22	3729	3856
"	0.34	97	11	40	2590	2738
"	0.44	96	14	55	1510	1675
"	0.54	96	13	40	1133	1282
"	0.64	97	10	13	804	924
"	0.74	92	17	40	540	689
"	0.84	92	24	40	510	666



Table S2. Capacitance values obtained for all the reported photoanodes after the EIS data fit with the equivalent circuit reported in Figure S13.

Electrode	E (V) vs NHE	CPE ₂ (F)	CPE _{film} (F)
WO₃/BiVO₄	0.44	9.9E-5	1.95E-4
"	0.49	1E-4	2.11E-4
"	0.54	3.78E-5	2.61E-4
"	0.59	4.49E-5	2.34E-4
"	0.64	2.72E-5	1.84E-4
"	0.69	1.47E-5	1.34E-4
"	0.74	3.19E-5	1.16E-4
"	0.79	3.37E-5	9.16E-5
"	0.84	3.01E-5	7.57E-5
"	0.89	9.23E-4	6.84E-5
"	0.94	1.32E-5	5.75E-5
WO₃/BiVO₄/CNTf	0.34	5.55E-4	6.23E-4
"	0.44	4.66E-4	6.64E-4
"	0.54	3.46E-4	6.44E-4
"	0.64	2.82E-4	6.9E-4
"	0.74	2.39E-4	7.33E-4
"	0.84	1.99E-4	7.86E-4
"	0.94	1.99E-4	1.15E-3
WO₃/BiVO₄/CNTf/Ru-WOC	0.14	2.73E-4	5.37E-4
"	0.24	3.67E-4	4.71E-4
"	0.34	4.08E-4	4.73E-4
"	0.44	2.87E-4	4.85E-4
"	0.54	8.68E-5	4.59E-4
"	0.64	4.4E-5	4.03E-4
"	0.74	4.45E-5	2E-4
"	0.84	3.2E-5	1.11E-4



A hybrid molecular photoanode for efficient light-induced WO

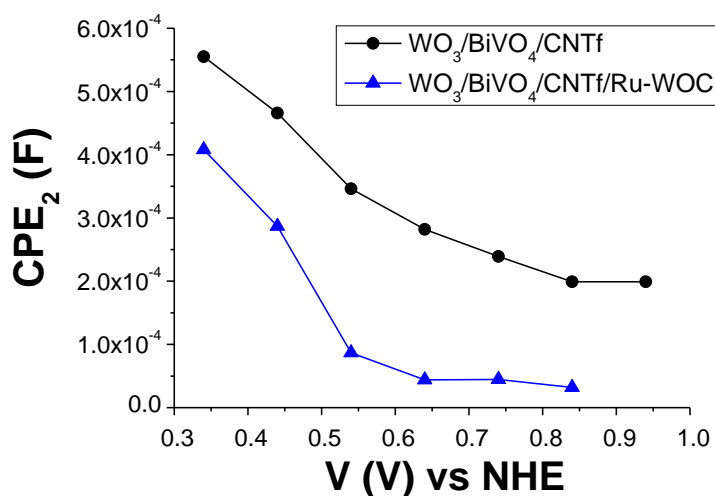


Figure S15. Dependency of the CPE₂ capacitance on the applied potential for WO₃/BiVO₄/CNT_f (black) and WO₃/BiVO₄/CNT_f/Ru-WOC (blue).

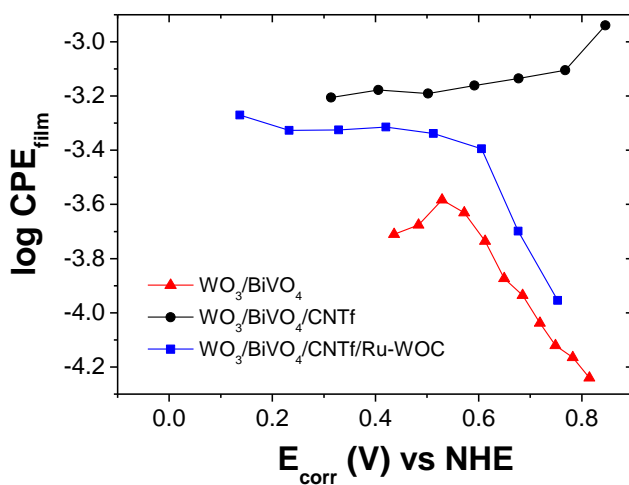


Figure S16. Dependency of the logarithm of the CPE_{film} capacitance on the applied potential corrected for the iR drop.



6.6.8 References

- (1) Creus, J.; Matheu, R.; Peñafiel, I.; Moonshiram, D.; Blondeau, P.; Benet-Buchholz, J.; García-Antón, J.; Sala, X.; Godard, C.; Llobet, A. *Angew. Chem. Int. Ed.* **2016**, *55*, 15382.
- (2) Cristino, V.; Marinello, S.; Molinari, A.; Caramori, S.; Carli, S.; Boaretto, R.; Argazzi, R.; Meda, L.; Bignozzi, C. A. *J. Mater. Chem. A* **2016**, *4*, 2995.
- (3) Pihosh, Y.; Turkevych, I.; Mawatari, K.; Uemura, J.; Kazoe, Y.; Kosar, S.; Makita, K.; Sugaya, T.; Matsui, T.; Fujita, D.; Tosa, M.; Kondo, M.; Kitamori, T. *Sci. Rep.* **2015**, *5*, 11141.
- (4) Chen, Z. D., H. N.; Miller, E.; Springer: 2013.
- (5) Hong, S. J.; Lee, S.; Jang, J. S.; Lee, J. S. *Energy Environ. Sci.* **2011**, *4*, 1781.
- (6) Reguero, V.; Alemán, B.; Mas, B.; Vilatela, J. J. *Chem. Mater.* **2014**, *26*, 3550.
- (7) Sherman, B. D.; Sheridan, M. V.; Dares, C. J.; Meyer, T. J. *Anal. Chem.* **2016**, *88*, 7076.
- (8) Kirner, J. T.; Finke, R. G. *ACS Appl. Mater. Interfaces* **2017**, *9*, 27625.





Chapter

7

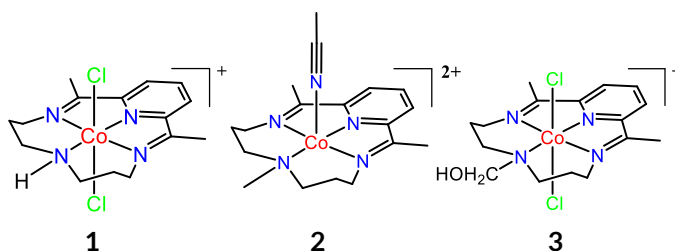
General Conclusions

Considering the general objectives proposed in Chapter 2 of the present thesis and according to the experimental results obtained, the general conclusions are summarized in this chapter.

General Conclusions

Chapter 3:

- Two new cobalt macrocyclic complexes (**2** and **3**), that are active for the hydrogen evolution reaction, have been prepared and fully characterized by spectroscopic and electrochemical techniques in order to study the effect of proton relay groups in the second coordination sphere of the cobalt center.



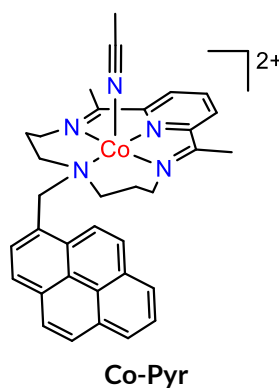
- The electrochemical experiments carried out with **1**, **2** and **3** revealed that the proton substitution in the amine (**1**) for methyl (**2**) and hydroxymethyl (**3**) groups has a strong effect on the electronic properties of the Co metal center shifting the redox Co^{III/I} couple to anodic potentials. Moreover the DFT calculations revealed that the pK_a of the Co^{III} hydride of **2** and **3** are more acidic than **1**. The high acidity of the Co^{III} hydrides species difficults its formation from the protonation of the Co^I species, that is the gate of the catalytic cycle for HER. This is reflected in the fact that catalysts **2** and **3** are only active at low pH (pH 2) while **1** is active at pH lower than 4. These results allow us to conclude that in the electrochemical scenario, the rate determining step of the overall catalytic cycle is the protonation of the Co^I species.



- The photochemical experiments carried out with **1**, **2** and **3** revealed a different trend in the catalytic rate than that observed in the electrochemical experiments. We have determined that the reduced photosensitizer $[\text{Ru}(\text{bpy})_3]^+$ has enough potential to reduce the catalysts by two consecutive electron transfers to form a formal "Co⁰" species. In this scenario, the formation of the Co^{II}-H species is not the rate determining step. DFT calculations of putative transition states for the H-H bond formation have been calculated and are in agreement with experimental results.

Chapter 4:

- A new cobalt macrocyclic complex with a pyrene moiety **Co-Pyr** to promote the absorption on graphitic surfaces have been synthesized and fully characterized by spectroscopic and electrochemical techniques.



General Conclusions

- Electrochemical experiments revealed that the pyrene moiety in the ligand framework not only makes the absorption of the catalyst in graphitic surfaces possible but also changes the electronic properties of the Co metal center hindering the catalytic activity. This is mainly due to the affinity of the pyrene group to form intermolecular π - π interactions with other molecules forming aggregates or intramolecularly with the cobalt center. The latter is supported by the single crystal x-ray diffraction analysis of the complex which shows a Co-Pyrene contact of 2.80 Å.
- Molecular electrodes active for the hydrogen evolution reaction have been prepared by decorating graphene powder with the molecular catalyst **Co-Pyr**.
- XANES and EXAFS analysis of the catalyst in the solid state, in solution and anchored on graphitic surfaces revealed a strong interaction between the conductive material and the molecular complex.

Chapter 5:

- An easy, rapid and reproducible methodology to electroplate amorphous MoS₂ on conductive surfaces has been developed allowing us to prepare cathodes and photocathodes active for the hydrogen evolution reaction. The performance of this new photocathode is among one of the best free-noble metal photocathodes reported to date.
- The photocathode is able to perform $-10 \text{ mA}\cdot\text{cm}^{-2}$ at $E = +0.86 \text{ V}$ vs RHE for at least 1 hour without any drop of activity. The loss in activity in the extended stability test are attributed to the loss of amorphous MoS₂ by the mechanical stress of the growth of hydrogen bubbles.



Chapter 6:

- A methodology to attach highly conductive carbon nanotube fibers (CNT_f) onto metal oxides surfaces have been developed. CNT_f have been proved to be an excellent graphitic support to attach molecular catalysts by π - π stacking interactions.
- Three types of photoanodes made: **i)** bare $\text{WO}_3/\text{BiVO}_4$, **ii)** $\text{WO}_3/\text{BiVO}_4/\text{CNT}_f$ and **iii)** $\text{WO}_3/\text{BiVO}_4/\text{CNT}_f/\text{Ru-WOC}$ (where Ru-WOC is ruthenium molecular water oxidation catalyst) have been characterized by photoelectrochemistry, Atomic Force Microscopy (AFM), UV-vis spectroscopy and Electrochemical Impedance Spectroscopy (EIS).
- The addition of the CNT_f fuctionalized with Ru-WOC leads to enhanced photocurrent at low potentials where the bare photoanode is not active at all. However, at high potentials the $\text{CNT}_f/\text{Ru-WOC}$ layer is not enough to overcome the good performance of the bare $\text{WO}_3/\text{BiVO}_4$.
- All the results obtained have been rationalized by means of EIS experiments that prove the benefits of using a highly active molecular catalyst to trigger the water oxidation reaction all the way down to 510 mV below the thermodynamic water oxidation potential.





Annexes

Glossary of terms and abbreviations

bpp ⁻	3,5-bis(2-pyridyl)pyrazolate
bpy	2,2'-bipyridine
MeCN	Acetonitrile
C _{DL}	Double Layer Capacitance
COSY	Correlation Spectroscopy
CPE	Controlled Potential Electrolysis
C _s	Specific Capacitance
CB	Conduction Band
CV	Cyclic Voltammetry
BDD	Boron Doped Diamond
d	doublet
δ	Chemical shift
DCM	Dichloromethane
DFT	Density Functional Theory
dmsO	Dimethyl sulfoxide
DPV	Differential Pulse Voltammetry
E	Potential
ECSA	Electrochemically Active Surface Area
ε	Extinction Coefficient
E _{1/2}	Half wave potential
ESI-MS	Electrospray Ionization Mass Spectrometry
FE	Faradaic Efficiency
FOWA	Foot of the Wave Analysis
GC	Glassy Carbon
H2bda	[2,2'-bipyridine]-6,6'-dicarboxylic acid
HER	Hydrogen Evolution Reaction
HEC	Hydrogen Evolution Catalyst
hν	Light
J	Coupling constant
λ	Wavelength
M	Molar
I	Ionic force
I2M	Bimolecular Interaction Mechanism
i	Current
j	Current density
m/z	Mass-to-Charge ratio
MLCT	Metal to Ligand Charge Transfer
MS	Mass Spectrometry
MSE	Mercury-mercurous Sulfate Electrode
m	Multiplet
η	Overpotential
NHE	Normal Hydrogen Electrode
NMR	Nuclear Magnetic Resonance
NOESY	Nuclear Overhauser Spectroscopy



NPs	Nanoparticles
OEC	Oxygen Evolving Center
PCET	Proton Coupled Electron Transfer
PEC	Photoelectrochemical cell
PEM	Proton Exchange Membrane
Ph	Phenyl
ppm	Parts per million
PS	Photosensitizer
PSI	Photosystem I
PSII	Photosystem II
PT	Proton Transfer
PV	Photovoltaic
py	Pyridine
rds	Rate determining step
RDV	Rotating Disk Voltammetry
RF	Roughness Factor
RT	Room Temperature
RRDE	Rotating Ring Disk Electrode
S	Surface of the electrode
s	Singlet
SCE	Saturated Calomel Electrode
t	Triplet
TBAPF ₆	Tetra(N-butyl)ammonium hexafluorophosphate
tda	[2,2':6',2''-terpyridine]-6,6''-dicarboxylato
TEA	Trimethylamine
TOF	Turnover Frequency
TON	Turnover Number
trpy	2,2':6',2''-terpyridine
UV-vis	Ultraviolet-visible Spectroscopy
v	Scan rate
VB	Valance Band
vs	versus
WNA	Water Nucleophilic attack
WO	Water Oxidation
WOC	Water Oxidation Catalyst





UNIVERSITAT ROVIRA I VIRGILI

MOLECULAR PHOCATODES AND PHOTOANODES FOR LIGHT DRIVEN WATER SPLITTING

Sergi Grau Abarca

UNIVERSITAT ROVIRA I VIRGILI

MOLECULAR PHOCATODES AND PHOTOANODES FOR LIGHT DRIVEN WATER SPLITTING

Sergi Grau Abarca

UNIVERSITAT ROVIRA I VIRGILI

MOLECULAR PHOCATODES AND PHOTOANODES FOR LIGHT DRIVEN WATER SPLITTING

Sergi Grau Abarca



UNIVERSITAT
ROVIRA i VIRGILI



Institut
Català
d'Investigació
Química